NIRS—M—74

特別研究「重粒子線等の医学利用に関する調査研究」論文集

第 4 集

(昭和62年4月—63年3月)

放射線医学総合研究所

Collected Papers of Project Research
"Medical Use of Accelerated Heavy Ions"

No. 4

(April 1987 — March 1988)

March, 1989

National Institute of Radiological Sciences
9-1,Anagawa 4-chome, Chiba-shi, 260 Japan

序

昭和62年度は重粒子線がん治療装置の詳細設計が行なわれた年である。治療装置の基本設計が行なわれた段階で，重粒子線の供給を安定させ，ビームを効率的に利用するため，主加速器シンクロトロンのリングを二重にすることが決った。主リングを二重にして実用されている加速器はこれまでに例がなく，設計の基本が定まるまでにかなり厳しい論議が交された。しかし，直交二門照射が同時に行なえる放射線治療技術上画期的なシステムが導入できたことの他，放射化ビーム（radioactive beam）を診断・治療に応用するための研究にも見通しが得られたことは装置を有効利用する上で大きなメリットとなった。

昭和62年12月末に「重粒子線がん治療装置」の建設が局長折衝の段階を経て決った。これで，世界では初めての医療用重粒子加速器による治療が平成5年度中に開始できることになった。

しかし，重粒子線がん治療装置を利用して行なわれる研究には，放射線医学それ自身の運命がかかっていると言っても過言ではない。質の向上がさらに求められる診療のために重粒子線を役立てたいものである。

特研班長　**恒元　博**

目　　　　次

RADIATION RESEARCH **112**, 426–435 (1987)

Radial Dose Distribution for 18.3 MeV/n α Beams in Tissue-Equivalent Gas

TATSUAKI KANAI AND KIYOMITSU KAWACHI

Division of Physics, National Institute of Radiological Sciences, 9-1 Anagawa 4 chome, Chiba-shi, Chiba 260, Japan

KANAI, T., AND KAWACHI, K. Radial Dose Distribution for 18.3 MeV/n α Beams in Tissue-Equivalent Gas. *Radiat. Res.* **112**, 426–435 (1987).

Experimental measurements of the radial restricted linear energy transfer (LET$_r$) for α beams of 18.3 MeV/n in tissue-equivalent gas were presented. The radial dose distribution for the α beam was deduced from the restricted LET measurements. A differential W value for the α particle in the tissue-equivalent gas was also deduced. The result for the differential W value was 29.0 ± 0.9 eV/ion pair. The radial dose varied according to an inverse-square function with distance from the track center for radii larger than 0.026 μm. The maximum extension of the track, the penumbra radius, as 2.73 ± 1.67 μm, which was less than predicted by calculations (7–9 μm).

INTRODUCTION

Linear energy transfer (LET) is considered to be a good index for the biological effectiveness of radiation (*1, 2*). Many authors, however, have pointed out that more detailed track structure should be known to understand the relation between physical quantities and radiation effects on living cells (*3–6*). Since the first derivation of the radial dose distribution by Katz and Butts (*7*), many experiments have been conducted on the spatial dose distribution on the nanometer scale by Varma, Baum, and colleagues (*8–11*), Menzel and Booz (*12*), Hodges and Marshall (*13*), and Kwok *et al.* (*14*). On the other hand, theoretical works using the Monte Carlo method have been developed to examine the track structure during the past 10 years by Berger (*15*), Paretzke (*16*), Hamm *et al.* (*17*), and Zaider *et al.* (*18*). Katz *et al.* (*3*), Chatterjee *et al.* (*19, 20*), Fain *et al.* (*21*), and Kiefer and Straaten (*22*) have developed ion track structure models using relatively simple assumptions. The experiments on track structure have been made at low or high incident energies of the heavy ion beams. A theoretical conclusion that radial dose varies according to an inverse-square function with radial distance was confirmed by the experiments in (*9*) and (*11*). However, a penumbra radius and a core radius or those shapes were not uniquely determined by those experiments. They are very important quantities for the analysis of inactivation cross sections of living cells and for determining the extension of the critical target in cells.

In this paper, we report the results of measurements of distance-restricted LET obtained using tissue-equivalent gas for α beams of medium energy (18.3 MeV/n). Also, radial doses have been calculated from the LET measurements. From a com-

0033-7587/87 $3.00

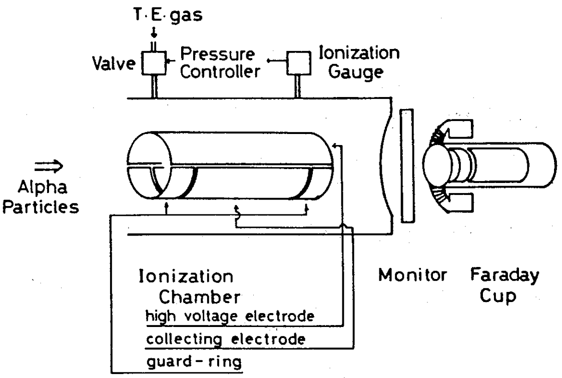

FIG. 1. Schematic diagram of the experimental arrangement.

parison of ionization current in a large ionization chamber with a calculated stopping power, a differential *W* value for the α ions in tissue-equivalent gas has been determined.

EXPERIMENTAL METHOD

The experimental arrangement consisted of a collimator, a cylindrical ionization chamber placed in a large vacuum chamber, a beam current monitor, and a Faraday cup as shown in Fig. 1. An 18.5 MeV/n α beam, accelerated by the NIRS (National Institute of Radiological Sciences) cyclotron, was delivered into a large vacuum chamber which was separated by a 30 μm aluminum entrance window from the beam transport system. A Mylar sheet 17 μm thick was attached to the entrance window to minimize errors due to differences in secondary electron production between the window and the gas. The beam was collimated by the entrance window in 1 mm diameter. The beam size at an exit window of a beam current monitor was less than 5 mm in diameter. The large vacuum chamber was filled with Rossi-type tissue-equivalent gas (a mixture of 64.4% methane, 32.4% CO_2, and 3.2% nitrogen, by vol) (*23*). The pressure in the large vacuum chamber was automatically controlled by a pressure control system which consisted of an electric piezo leak valve and an ionization pressure gauge. The absolute pressure was monitored by two Baratron gauges (10^{-3} to 10 Torr and 0 to 1000 Torr).

The thickness of the aluminum exit window was 50 μm. The parallel plate ionization chamber was placed just downstream of the exit window for monitoring the number of the incident α particles. Aluminized 2.5-μm polyester films were used for the collecting and high voltage electrodes of the ionization chamber. Total thickness of the polyester of the ionization chamber was 15 μm. The output of the ionization chamber was calibrated by a Faraday cup.

Calibration of the Monitor

The Faraday cup consisted of a collecting electrode, a guard ring, a magnetic coil, and a vacuum chamber. The diameter of the entrance window was 40 mm. The aluminum suppression ring was 45 mm long and 45 mm in diameter; the Faraday cup was 120 mm long and 40 mm in diameter. The vacuum chamber was evacuated to around 10^{-3} Torr by a rotary vacuum pump. A magnetic field of around 150 G was applied near the guard ring to keep secondary electrons from entering into or ejecting from the Faraday cup.

Figure 2 shows Faraday cup output versus the guard-ring voltage. The α particles passing through the crylindrical ionization chamber were fully collected by the Faraday cup because the beam size is sufficiently small compared with the Faraday cup, and beam loss due to nuclear collisions in vacuum windows, ionization monitors, and air could be neglected. The Faraday cup output decreased when minus bias was applied to the guard ring. The output increased when plus bias was applied to the guard ring. Secondary electrons produced by the vacuum window and the Faraday cup itself or the ionizations of the residual gas in the vacuum chamber affected the Faraday cup measurement. According to an analysis of the efficiency of a

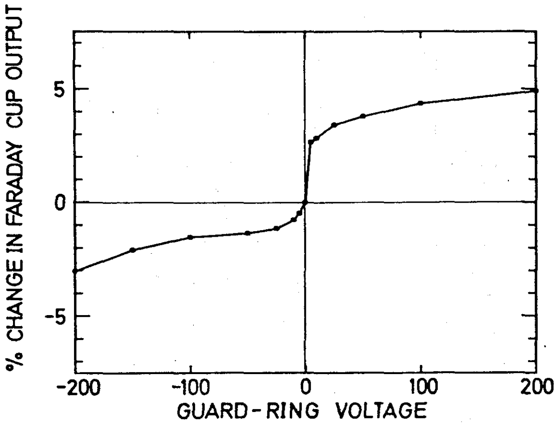

FIG. 2. The percentage change in the output of the Faraday cup as the guard-ring voltage is varied.

Faraday cup in high-energy proton beam dosimetry by Verhey *et al.* (*24*), the Faraday cup output at zero guard-ring voltage was used for calibrating the ionization chamber monitor although their Faraday cup was different from ours. We have assigned a 1% uncertainty to this quantity.

The Cylindrical Ionization Chamber

The cylindrical ionization chamber is illustrated in Fig. 1. The cylinder was divided by a plane which includes the central axis of the cylinder. One part of the divided cylinder served as a high-voltage electrode. The other part of the cylinder was divided into three parts by planes which were perpendicular to the central axis of the cylinder. The central part of the divided cylinder was a collecting electrode, and the other parts on both sides served as guard electrodes for shaping electric field. The closest gap between the high voltage electrode and the collecting electrode was 5 mm. The guard electrodes were placed 1 mm apart from the collecting electrode. The cylinder was 40 cm long and 14 cm in diameter and was made from carbon. The length of the guard electrodes was 4.9 cm. Thus the sensitive volume of the cylindrical ionization chamber was considered to be 30 cm long × 14 cm in diameter.

Figure 3 shows saturation curves of the cylindrical ionization chamber under high pressures of tissue-equivalent gas. Solid lines represent the saturation curves when plus ions are collected, and dashed lines represent those when electrons are collected. The shapes of the saturation curves of the ion current were similar to each other. The same behavior was obtained for those of electron currents. The voltages above which the ionization currents saturated were roughly proportional to the gas pressure. The saturated curves for plus and minus polarity of the bias differed from each other in shape, especially at low bias voltages. The saturation electron currents were around 2% lower than the saturation in ion currents. The ion currents were used to calculate the restricted LET in this work. Figure 4 shows the saturation curves at low tissue-equivalent gas pressures. Solid and dashed lines represent ion and electron current outputs of the ionization chamber, respectively. The electron and ion currents coincided with each other at saturated voltages. At pressures below 0.0272 Torr, the electron currents were much greater than the ion currents and both currents did not satuate.

General recombination effects can be neglected for these beam intensities, gas pressures, and electric fields.

RESTRICTED LET AND RADIAL DOSE DISTRIBUTION

From the saturation currents, LETs restricted to various radii were calculated. The ionization charge measured by the cylindrical ionization chamber corresponds to the number of ion pairs formed in a cylindrical volume, radius $R = 7$ cm and length $L = 30$ cm, at various gas pressures when the incident beam passes through the central

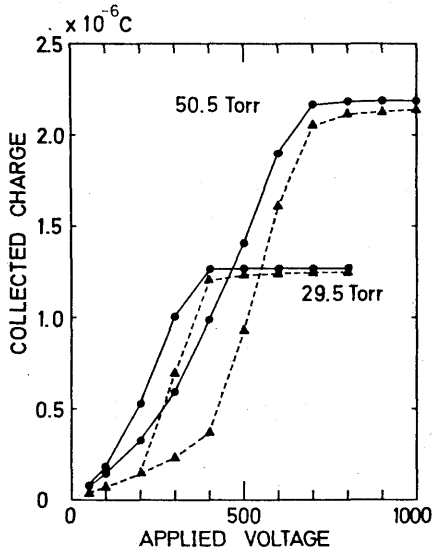

FIG. 3. The charge measured by the cylindrical ionization chamber versus voltage applied to the high-voltage electrode (at high pressures). Solid curves represent the positive ion current, and dashed curves represent the electron current.

axis of the cylinder. The ionization charge was converted to the energy absorbed in the cylinder per α article track, E_{gas}, as

$$E_{\text{gas}} = Q \cdot w/(N \cdot e), \tag{1}$$

where Q is the ionization charge measured by the cylindrical ionization chamber, w

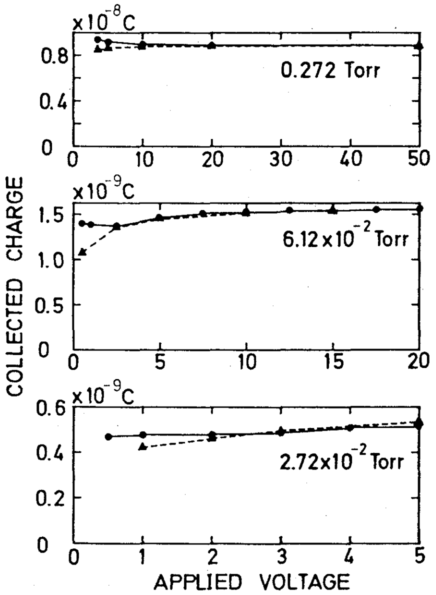

FIG. 4. The charge measured by the cylindrical ionization chamber versus voltage applied to the high-voltage electrode (at low pressures). Solid curves represent the positive ion current, and dashed curves represent the electron current.

is a differential W value of the tissue-equivalent gas for the α beam, N is the number of the incident α particles, and e is the charge of electron.

To deduce the radial dose distribution in tissue, we assumed a simulated small tissue cylinder of radius r and length l. The energy absorbed in the small tissue cylinder, E_{tissue}, should be equal to the energy absorbed in the gas-filled cylinder, E_{gas}, if the gas-filled cylinder can stimulate the small tissue cylinder. The energy deposition in the gas or tissue cylinder per incident α particle is expressed by a product of two parts, a total energy loss of the α particle in passing through the cylinder and a ratio of the energy deposition in the cylinder to the total energy losses of the α particles, as

$$E_{\mathrm{gas}} = \{\mathrm{LET}_R/(S)_{\mathrm{gas}}\}(S/\rho)_{\mathrm{gas}}\rho_{\mathrm{gas}}L \tag{2}$$

$$E_{\mathrm{tissue}} = \{\mathrm{LET}_r/(S)_{\mathrm{tissue}}\}(S/\rho)_{\mathrm{tissue}}\rho_{\mathrm{tissue}}l, \tag{3}$$

where LET_R and LET_r are the LET of the alpha particle in the gas and tissue restricted to radial distance R and r from the particle track, respectively. $(S)_{\mathrm{gas}}$ and $(S/\rho)_{\mathrm{gas}}$ are stopping power and mass stopping power of the α particle in the gas, respectively, ρ_{gas} is the density of the gas. For a determination of the simulated radius r and length l of the tissue cylinder, we assumed that the first and second terms in Eqs. (2) and (3) were the same in both substances:

$$\mathrm{LET}_R/(S)_{\mathrm{gas}} = \mathrm{LET}_r/(S)_{\mathrm{tissue}} \tag{4}$$

$$(S/\rho)_{\mathrm{gas}}\rho_{\mathrm{gas}}L = (S/\rho)_{\mathrm{tissue}}\rho_{\mathrm{tissue}}l. \tag{5}$$

Varma *et al.* pointed out that there might be differences in δ-ray emission and electron transport properties of the two media beyond differences in density (*9*). Assuming the number of δ rays is proportional to the energy loss of the α particles, the difference in the α-ray emission is corrected by Eq. (5). Thus the mass stopping power in the conversion Eq. (5) should be that of α particles in our formalism.

Concerning the difference in secondary electron transport properties between the gas and tissue, energy losses and deflection of the δ rays in traversing the gas and tissue should be the same after the conversion. The energy loss can be corrected by the following equation (*11*):

$$\rho_{\mathrm{tissue}}r = (S/\rho)_{\mathrm{gas/tissue}}\rho_{\mathrm{gas}}R. \tag{6}$$

Thus the stopping power ratio in Eq. (6) should be that of electrons.

For the deflection of electrons, a scattering power should be considered. The mean square scattering angle after traversal of a thickness X of the scattering substance of density ρ, $\langle\theta\rangle_X$, is proportional to $(Z^2/A)\rho\, X$, where Z is the charge and A the mass number of the scattering substance (*25*). The mean deflection distance, $\langle Y^2\rangle_X$, is given by $X^2\langle\theta^2\rangle_X/3$, which is proportional to $(Z^2/A)\rho\, X^3$ in substances of density ρ. Multiplying by the square of density, ρ^2, one can get the relation

$$\rho^2\langle Y^2\rangle_X \sim (Z^2/A)(\rho X)^3. \tag{7}$$

Substituting the relation (6) for the conversion into Eq. (7), we can conclude that the difference of the electron transport properties cannot be corrected by Eq. (6) if the following relation does not hold in the two media:

$$(Z^2/A)_{\text{gas}}/(S/\rho)_{\text{gas}} = (Z^2/A)_{\text{tissue}}/(S/\rho)_{\text{tissue}}. \quad (8)$$

In our simulation experiment, the tissue-equivlent gas was used for the gas substance to prevent the above error in the conversion. Thus 1 was used for the stopping power ratio in Eqs. (5) and (6).

Then, substituting Eqs. (2), (4), and (5) into Eq. (1), LET_r can be expressed as

$$\text{LET}_r = \{(Qw/NLe)(S/\rho)_{\text{tissue/gas}}\}\rho_{\text{tissue}}/\rho_{\text{gas}}. \quad (9)$$

The LET_r as a function of the restricted radius r was differentiated to obtain a radial dose distribution perpendicular to the incident α-particle path:

$$D(r) = \{d(\text{LET}_r)/dr\}/2\pi r. \quad (10)$$

RESULTS AND DISCUSSION

First we derived the differential W value, w, of the α particle for tissue-equivalent gas using the absolute α-particle number, N, which was measured by using the Faraday cup. Quotients of $Q/(N \cdot e)$ by $\rho_{\text{gas}}L$ were saturated for pressures greater than 50.5 Torr. The average number of the saturated ion pairs was 395.2 ± 0.685 ion pairs/(10^{-4}g/cm^2); this can be regarded as the number of ion pairs which contributed from the unrestricted radius around the ion path. The stopping power was calculated using a code developed by Steward and Wallace (*26*). The mean excitation energies for methane, carbon dioxide, and nitrogen recommended by ICRU (*27*) were adapted for the calculation of the mass stopping power of each gas. A sum of the fractions by weight of the mass stopping powers of these gases was taken as the mass stopping power of the tissue-equivalent gas. The incident energy of the α particle at the entrance of the cylindrical ionization chamber was 18.33 MeV/n, which was deduced from the residual range measurements, the accelerated energy of 18.5 MeV/n, and an energy degradation calculation. The calculated mass stopping power in the tissue-equivalent gas was 11.46 keV/(10^{-4}g/cm^2). From the above calculation, the w value of 18.33 MeV/n α particles for tissue-equivalent gas was 11.46 keV/395.2 ion pairs = 29.0 ± 0.05 eV. Considering the uncertainties of the Faraday cup measurement (estimated as 1%), the mass stopping power calculation (estimated as 1%), and the ionization charge measurements in the cylindrical chamber (estimated as 1%), it was conclusively estimated that $w = 29.0 \pm 0.9$ eV. The W value of high-energy photons or electrons for tissue-equivalent gas is 29.2 eV/ion pair (*28*). Therefore, the w value of high-energy heavy-charged particles may be equal to the W value of high-energy photons.

In deriving the restricted LET, we used the W value of 29.0 eV. The energy spectra of the δ rays in different cylindrical shells coaxial with the ion's path varies with radial distance, and the w value of electrons depends on their energy. Thus the value of LET_r deduced with the constant W value may be underestimated near the ion's path. However, for electrons with energy greater than around 100 eV, the W value is not so dependent on its energy (*28*). The range of the 100 eV electrons is estimated to be 1 nm. Thus the effect of the variation of the W value will be very small in the distances observed.

The mylar sheet was attached to the entrance window to avoid a large error due to the incomplete secondary electron equilibrium. Low-energy electrons produced by

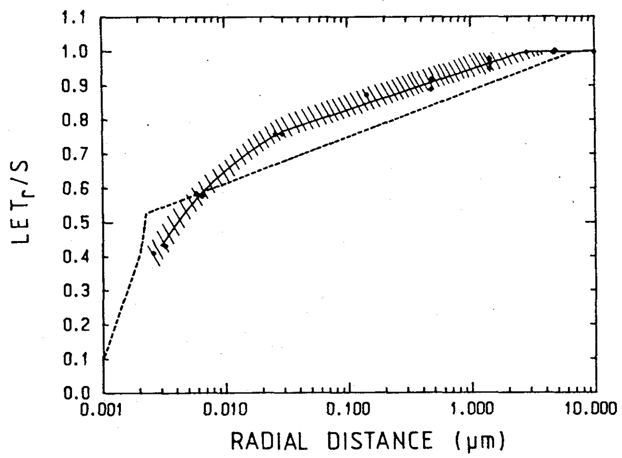

FIG. 5. The restricted LET expressed as percentage unrestricted LET for 18.3 MeV/n α particles in tissue-equivalent gas. The radial distances were those at unit density. The solid line represents the results of the least-squares fit of the data. The shaded area shows a 68% confidence band of the fitted curve. The dashed curve was calculated by the method of Chatterjee and Schaefer (*20*).

the mylar sheet cannot reach the cylindrical chamber. The number of high-energy electrons is roughly proportional to $(Z/A)\,(S/\rho)$ of the target materials (*10*). Assuming straight paths for the secondary electrons, we estimated that the error induced from the difference of quantities of high-energy electron production was about 5% at lowest gas pressure. At the gas pressure which corresponded to 0.01 μm radius, the error was 3%; for 0.1 μm radius it was 1%.

Figure 5 shows the results of the normalized LET ($=\mathrm{LET}_r/(S)_{\mathrm{tissue}}$ from Eq. (4)) as a function of radial distances. The radial distances were converted to those at unit density ($\rho_{\mathrm{tissue}} = 1.0$ Eqs. (6) and (9)). The experimental and theoretical work of many authors (*9, 11, 20–22*) has determined that the radial dose varies according to an inverse-square function with a radial distance from the track center. For comparison, the experimental data which correspond to radii longer than 0.026 μm were fitted to the following equations:

$$\mathrm{LET}_r/(S)_{\mathrm{tissue}} = A\{1 - \mathrm{K}\cdot\ln(r_p/r)\} \qquad \text{for } r < r_p \tag{11}$$

$$\mathrm{LET}_r/(S)_{\mathrm{tissue}} = A \qquad \text{for } r > r_p. \tag{12}$$

The errors in LET_r and the radial distance r were taken into account in the nonlinear least-squares fit of the parameters A, K, and r_p to the Eqs. (11) and (12). The derived parameters were

$$\begin{aligned} A &= 0.998 \pm 0.018 \\ K &= 0.051 \pm 0.008 \\ r_p &= 2.73 \ \ \pm 1.67\ \mu\mathrm{m}. \end{aligned} \tag{13}$$

The best fit value of A was different from unity by 0.2%. The difference is because

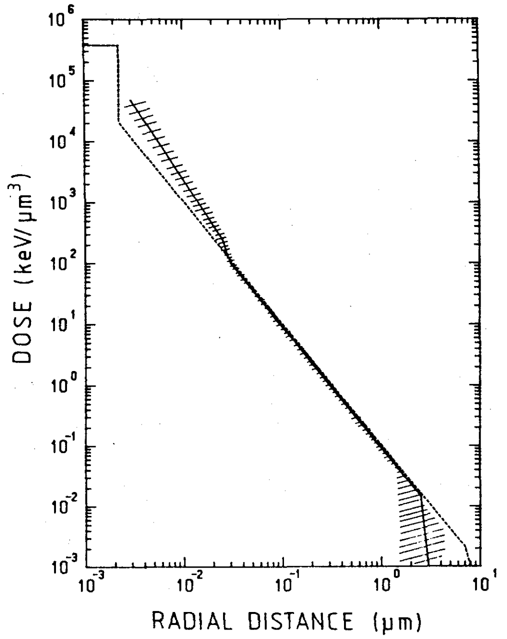

FIG. 6. The dose as a function of radial distance for 18.3 MeV/n α particles in tissue-equivalent gas. The radial distances were those at unit density. The solid curve was obtained from the restricted LET measurements (solid curve in Fig. 5) by Eq. (10). The shaded area shows a 68% confidence band of the deduced line. The dashed curve was calculated by the method of Chaterjee and Schaefer (*20*).

the observed LET$_r$ varied smoothly near the penumbra radius, r_p. Contribution of the dose beyond r_p was negligible compared to the total energy loss, so we defined the penumbra radius as the r_p deduced.

To deduce the radial dose distribution, $D(r)$, the experimental data which corresponded to radii smaller than 0.026 μm were fitted to a third-order polynomial function of log (r). The solid curve shown in Fig. 5 is the fitted curve. The shaded area in Fig. 5 shows a 68% confidence band of the fitted curve.

The radial dose distribution was obtained by substituting the LET function into Eq. (10). The solid curve in Fig. 6 shows the obtained radial dose distribution. The radial distances were those at unit density. The shaded area in Fig. 6 shows a 68% confidence band of the fitted curve.

The dashed curves in Figs. 5 and 6 show theoretical results of Chatterjee and Shaefer (*20*) for the normalized LET$_r$ and $D(r)$, respectively. Their formula for the calculation used water, and in the present experiments tissue-equivalent gas was used. The differences of LET$_r$ and $D(r)$ between the two materials are not two large.

A penumbra radius of 2.73 ± 1.67 μm, beyond which no dose is contributed from the track, was estimated by this experiment. The penumbra radius calculated by Chatterjee and Schaefer (*20*) is 7.1 μm for 18.33 MeV/n α beams and that calculated by Kiefer and Straaten (*22*) is 8.65 μm. Those values are fairly large compared with our result.

For radii larger than 0.026 μm, the simple equation (11) can reproduce the experimental results of the restricted LET. For these radii, the radial dose can be expressed by the inverse square of the radius as

$$d(r) = k(z/\beta)^2/r^2, \tag{14}$$

where k is constant, z is the charge of the incident particle, and β is the ratio of the incident particle velocity to a light velocity. k obtained from this experiment was $(1.42 \pm 0.25) \times 10^{-4}$ Gy·(μm)^3. This value is very close to the values, ranging from 1.25 to 1.5×10^{-4} Gy·(μm)^3, that have been obtained by others (*9, 11, 20–22*).

Chatterjee and Shaefer (*20*) predicted a distinguished core. Figure 6 shows that the core may have a more extended structure than Chatterjee and colleagues predicted. Zaider and Rossi (*6*) compared their results of Monte Carlo calculation for the track structure with the theoretical results of Chatterjee and Shaefer. The Monte Carlo calculation also showed that the core extended more and the penumbra radius seemed to be smaller than Chatterjee's result.

It can be concluded that the penumbra radius obtained by the present experiments was smaller than that predicted by calculations; that the energy deposited in a cylindrical region from the obtained penumbra radius to the theoretical penumbra radius was about 5% of the total energy loss of the α particles; and that the excess energy was deposited near the core.

ACKNOWLEDGMENTS

We thank H. Ogawa, K. Tashiro, N. Suzuki, M. Tazawa, and the cyclotron crew at NIRS for their offering a steady beam during the experiment. We also thank Dr. A. Shiragai for his helpful discussions.

RECEIVED: February 16, 1987; REVISED: May 18, 1987

REFERENCES

1. G. W. BARENDSEN, Impairment of the proliferative capacity of human cells in culture by alpha particles with differing linear-energy transfer. *Int. J. Radiat. Biol.* **8**, 453–466 (1964).

2. A. M. KELLERER and H. H. ROSSI, The theory of dual radiation action. *Curr. Top. Radiat. Res. Q* **8**, 85–158 (1972).

3. R. KATZ, B. ACKERSON, M. HOMAYOONFAR, and S. C. SCHARMA, Inactivation of cells by heavy ion bombardment. *Radiat. Res.* **47**, 402–425 (1971).

4. A. M. KELLERER and H. H. ROSSI, A generalized formation of dual radiation action. *Radiat. Res.* **75**, 471–488 (1978).

5. E. A. BLAKELY, C. A. TOBIAS, T. C. H. YANG, K. C. SMITH, and J. T. LYMAN, Inactivation of human kidney cells by high-energy monoenergetic heavy-ion beam. *Radiat. Res.* **80**, 122–160 (1979).

6. M. ZAIDER and H. H. ROSSI, Dual radiation action and the initial slope of survival curves. *Radiat. Res.* **104**, S-68–S-76 (1985).

7. R. KATZ and J. J. BUTTS, Width of ion and monopole tracks in emulsion. *Phys. Rev.* B **137**, 198–203 (1965).

8. C. L. WINGATE and J. W. BAUM, Measured radial distribution of dose and LET for alpha and proton beams in hydrogen and tissue-equivalent gas. *Radiat. Res.* **65**, 1–19 (1976).

9. M. N. VARMA, J. W. BAUM, and A. V. KUEHNER, Energy deposition by heavy ions in a "tissue equivalent" gas. *Radiat. Res.* **62**, 1–11 (1975).

10. M. N. VARMA, H. G. PARETZKE, J. W. BAUM, J. T. LYMAN, and J. HOWARD, Dose as a function of radial distance from a 930 MeV ^{4}He ion beam. In *Proceedings, Fifth Symposium on Microdosimetry, Verbania-Pallanza, Italy* (J. Booz, H. G. Ebert, and B. G. R. Smith, Eds), pp. 76–95. Commission of the European Communities, Luxembourg, 1976.

11. M. N. VARMA and J. W. BAUM, Energy deposition in nanometer regions by 377 MeV/nucleon ^{20}Ne ions. *Radiat. Res.* **81**, 355–363 (1980).

12. H. G. MENZEL and J. BOOZ, Measurement of radial deposition spectra for P and D in T.E.G. In *Proceedings, Fifth Symposium on Microdosimetry, Verbania-Pallanza, Italy* (J. Booz, H. G. Ebert, and B. G. R. Smith, Eds), pp. 61&73. Commission of the European Communities, Luxembourg, 1976.

13. D. C. HODGES and M. MARSHALL, A low-pressure cloud chamber to study the spatial distribution of ionizations. *J. Phys. E.* **10,** 342–350 (1977).

14. C. S. KWOK, T. BUDD, and M. MARSHALL, Track studies in a tissue-equivalent gas and water vapor with a low-pressure cloud chamber. In *Proceedings, Seventh Symposium on Microdosimetry, Oxford* (J. Booz, H. G. Ebert, and H. D. Hartfield, Eds.), pp. 347–357. Harwood, London, 1981.

15. M. J. BERGER, Some new transport calculations of the deposition of energy in biological materials by low-energy electrons. In *Proceedings, Fourth Symposium on Microdosimetry, Verbania-Pallanza, Italy* (J. Booz, H. G. Ebert, R. Eickel, and W. Walker, Eds.), pp. 695–711. Commission of the European Communities, Luxembourg, 1974.

16. H. G. PARETZKE, Comparison of track structure calculations with experimental results. In *Proceedings, Fourth Symposium on Microdosimetry, Verbania-Pallanza, Italy* (J. Booz, H. G. Ebert, R. Eickel, and W. Walker, Eds.), pp. 141–165. Commission of the European Communities, Luxembourg, 1974.

17. R. N. HAMM, H. A. WRIGHT, R. H. RITCHIE, J. E. TURNER, and T. P. TURNER, Monte Carlo calculation of transport of electrons through liquid water. In *Proceedings, Fifth Symposium on Microdosimetry, Verbania-Pallanza, Italy* (J. Booz, H. G. Ebert, and B. G. R. Smith, Eds.), pp. 1037–1050. Commission of the European Communities, Luxembourg, 1976.

18. M. ZAIDER, D. J. BRENNER, and W. E. WILSON, The applications of track calculations to radiobiology. 1. Monte Carlo Simulation of proton tracks. *Radiat. Res.* **95,** 231–247 (1983).

19. A. CHATTERJEE, H. D. MACCABEE, and C. A. TOBIAS, Radial cutoff LET and radial cutoff dose calculations for heavy charged particles in water. *Radiat. Res.* **54,** 479–494 (1973).

20. A. CHATTERJEE and H. J. SHAEFER, Microdosimetric structure of heavy ion tracks in tissue. *Radiat. Environ. Biophys.* **13,** 215–227 (1976).

21. J. FAIN, M. MONNIN, and M. MONTRET, Spatial energy distribution around heavy-ion path. *Radiat. Res.* **57,** 379–389 (1974).

22. J. KIEFER and H. STRAATEN, A model of ion track structure based on classical collision dynamics. *Phys. Med. Biol.* **31,** 1201–1209 (1986).

23. H. H. ROSSI and G. FAILLA, Tissue-equivalent ionization chambers. *Nucleonics* **14(2),** 32–36 (1956).

24. L. J. VERHEY, A. M. KOEHLER, J. C. MCDONALD, M. GOITEIN, I-CHANG MA, R. J. SCHNEIDER, and M. WAGNER, The determination of absorbed dose in a proton beam for purposes of charged-particle radiation therapy. *Radiat. Res.* **79,** 34–54 (1979).

25. B. B. ROSSI, In *High Energy Particles.* Prentice–Hall, New York, 1952.

26. P. STEWARD and R. WALLACE, *Calculations of Stopping Power and Range Energy Values for any Heavy Ion in Nongaseous Media.* Report UCRL-17314, Lawrence Berkeley Laboratory, University of California, 1966.

27. ICRU, *Stopping Powers for Electrons and Positrons.* Report 37, International Commission on Radiation Units and Measurements, Washington, DC, 1984.

28. D. COMBECHER, Measurement of *W* values of low-energy electrons in several gases. *Radiat. Res.* **84,** 189–218 (1980).

CRP.REPORT FOR 1987 FOR RESEARCH AGREEMENT No.4706/CF

Measurement of Relative Neutron Sensitivity of Non-hydrogenous Ionization Chambers

K.Kawashima, K.Hoshino, T.Hiraoka
Y.Noda, Y.Nakamura and Y.Kumamoto
National Institute of Radiological Sciences

1. INTRODUCTION

NIRS has been installed a Thomson-CSF isochronous cyclotron Model 70 in March 1974. Since November 1975, the NIRS-Chiba Isochronous Cyclotron has been used three times weekly for the clinical trials of fast neutron radiotherapy. Neutron beams are produced by bombarding 30 MeV deuterons on a thick beryllium target with a current of 30μA.

Neutron dosimetry intercomparison has been made between Japan and USA at NIRS on April in 1976 [1]. In the intercomparison, in spite of good agreement in total dose, fairly large discrepancy was found not only in correction factor for ion recombination loss but also in relative neutron sensitivity of non-hydrogenous dosemeters.

In neutron dosimetry intercomparison using ionization chambers, there may be two kinds of factors that affect the final results. One is the basic constants used in the calculation of the dose, such as W-value, stopping power ratios and kerma values. The other class of factors is the physics ones, such as composition of chamber wall, chamber size, gas composition and saturation characteristics of the ion chambers. Some of these factors are unique to the chambers. Therefore, when a chamber with different characteristics is used, those factors must be taken into account. Specially, relative neutron sensitivity of non-hydrogenous chamber is very much affected by both two kinds of factors. To determine the neutron sensitivities experimentally, the lead attenuation method developed by Waterman et al [2] was used.

2. METHODS & MATERIALS

a) Neutron beam production and dosimetric characterisics

The neutron beam is produced at a thick beryllium target by bombarding 30 MeV deuterons with a current of 30μA. Measurements were made using a fixed vertical beam with a collimator system shown in figure 1. Dose profiles in air and depth dose characteristics in a phantom are shown in figures 2 and 3.

b) Estimation of neutron sensitivity, kT, for TE chamber

Assuming the spectrum for d(30)Be+neutrons showing in figure 4 and using kerma factors published in ICRU Report 26 [3], the average value of kT for TE ionization chamber is estimated to be 0.980 according to the following equation,

$$kT = \int kT(E)\phi(E)\ K(E)\ dE \ / \int \phi(E)\ K(E)\ dE$$

where K is a kerma factor and ϕ is a fluence of neutron.

C) Neutron sensitivity of ionization chamber

The equation for the response, R, of any dosemeter to a mixed field is given by

$$R = hDg + kDn$$

Hence, D refers to the tissue dose, and h and k represent the dosemeter response per unit tissue dose of gamma-rays and neutrons, respectively.

Neutron sensitivity function relative to cobalt-60 γ-rays as a function of neutron energy has been obtained by the methods of Kuchnir et al [4] and of Waterman et al [5]. In their methods, a pure neutron field is simulated by the difference between measurements made at two angles in a n-γ mixed field in which the γ-ray component is isotropic. A sophisticated technique for measuring neutron spectra is also necessary. The lead filtration method, on the other hand, developed by Attix et al [6] and modified by Waterman et al [2] is also used to measure the relative neutron sensitivity with a ionization chamber.

The spectral difference method [4][5] provides the n/γ sensitivity of either a TE or a non-hydrogenous dosemeter as a function of neutron energy. The ratio of the response for neutrons to that for photons, k/h for a particular neutron beam can be determined from the n/γ sensitivity function if the energy spectrum is known. On the other hand, the lead filtration method directly provides k/h, for a non-hydrogenous dosemeter relative to that of a TE ionization chamber for a particular neutron beam, without any knowledge on neutron spectrum.

d) Measurement of k_U by improved lead filtration method

Using the lead filtration method, we measured the n/γ sensitivity of non-hydrogenous ionization chambers exposed to the neutron beam from 30 MeV deuterons on beryllium. These chambers were (1)a 2 ml magnesium spherical chamber with flowing argon gas(Mg-Ar);(2) a 1.6 ml graphite thimble chamber with air;(3) a 0.1 ml graphite thimble chambers with air;(4) a 1.3 ml thimble chamber having a wall of mixture of graphite with teflon, with air and with flowing carbon dioxide gas; and (5) a 3 ml thimble chamber of a wall of mixture of graphite with teflon, with air and with flowing carbon dioxide gas (C+Teflon-air or C+Teflon-CO2). A 1 ml tissue equivalent spherical chamber with flowing tissue equivalent gas (TE-TEgas) was used with each of the non-hydrogenous chambers.

A lead filter of 5 cm thick is placed just behind the second γ-ray shutter as shown in figure 1. A field size used is 3x4 cm at a distance of 175 cm from the beryllium target. The ionization chamber is scanned to obtain a dose profile at a distance of 200 cm from the target perpendicularly to the neutron beam .

A value of k/h for the dosemeter response to background was obtained by using the extrapolation of the tails of the beam scans to the beam axis, as indicated by the dashed lines in figure 5. The net response, R, of the dosemeter in the unfiltered beam which is obtained from the reading in the center, R_c, minus the extrapolated values R_b, is due to the gamma and neutron radiations which come from the collimator aperture alone namely, a D_g and aD_n. Then the response, R, is given by

$$R = R_c - R_b = h\ aD_g + k\ aD_n$$

Similarly,the net dosemeter response, R',in the filtered beam is

$$R' = R_c' - R_b' = hA\ aD_g + k\ aD_n'$$

The solution for k/ h is given by

$$k_U/h_U = (k_T/h_T)(h_T/h_U)(AR_U - R_U')/(AR_T - R_T')$$

where A is attenuation factor by the lead filter, that is, $A=\exp(-\mu x)$. μ is usually taken to be the total absorption coefficient for 4 MeV gamma-ray in lead and x is the thickness of the lead filter. T and U denote TE chamber and non-hydrogenous chamber, respectively. The gamma-ray sensitivity, h, can be obtained by exposing a ionization chamber to cobalt-60 gamma field in which the dose or dose rate is known precisely.

3. RESULTS AND DISCUSSION

Typical scanned dose distributions in air with and without a lead filter are shown in figure 5. Background doses in the beam axis were les than 2% in any . cases. Low background doses provides us reliable results on k_U. Observed values for various chambers with standard deviations are shown in table 1, with theoretical k_U' for infinitesimal cavity size of a chamber and k_U'' for infinite cavity size. The values of gamma -ray sensitivity , k_U' and k_U'', are given theoretically by

$$k' = \frac{(W_g)_c}{(W_g)_n} \cdot \frac{(S_{w,g})_c}{(S_{w,g})_n} \cdot \frac{(K_{t,w})_c}{(K_{t,w})_n}$$

and

$$k'' = \frac{(W_g)_c}{(W_g)_n} \cdot (S_{w,g})_c \cdot \frac{(K_{t,w})_c}{(K_{t,g})_n}$$

where S refers to a mass stopping power.

The observed values of k_U which are averages of four experiments over a year should be between k_U' and k_U''. The results reasonably agree with theoretical calculations.

REFERENCES

1) Kawashima,K. et al, Jpn.Radiol.Phys.,1,31-40,1981
2) Waterman,F.W. et al, Phys.Med.Biol.,22,880-888,1977
3) ICRU,ICRU Report 26,1977
4) Kuchnir,F.T. et al, Radiology,116,217-219,1975
5) Waterman,F.W. et al, Phys.Med.Biol.,24,721-733,1979
6) Attix,F.H. et al,Proc.2nd Symp.on Neutron Dosimetry in Biology and Medicine, EUR5273 d-e-f,329-340,1975

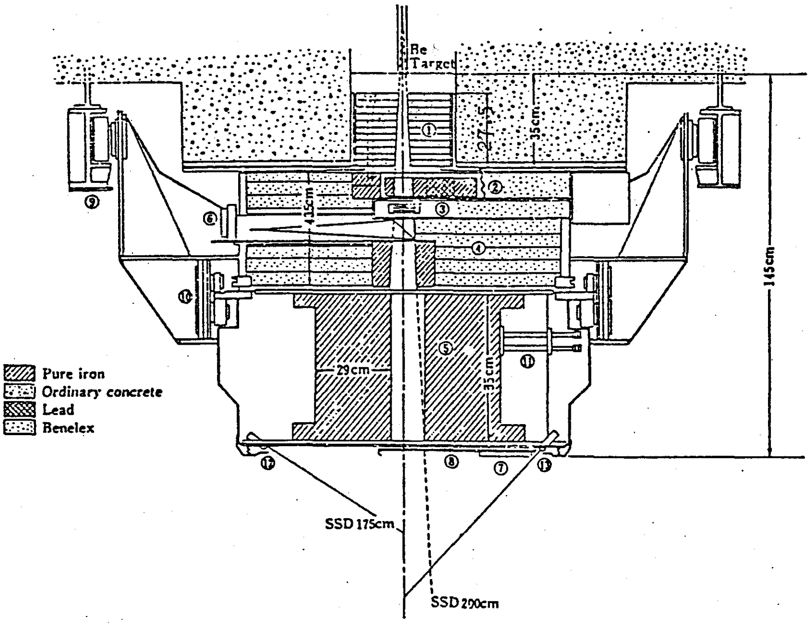

Fig. 1. Schematic drawing of collimator and shielding.

1. First collimator.
2. First gamma-ray shutter.
3. Neutron beam monitor (Transmitted type ionization chamber).
4. Second collimator.
5. Third collimator. Field size definition is provided by 8 couples of iron leaves which are usually motor driven.
6. Field illumination lamp system.
7. Second gamma-ray shutter.
8. Openig window for neutron beams.
9. Gantry.
10. Turning gear. This provides to rotate the complete collimator system around beam axis.
11. Motor driving system of multi-leaves collimator.
12. Source-skin distance indicator lamp (SSD = 175 cm)
13. Source-skin distance indicator lamp (SSD = 200 cm)

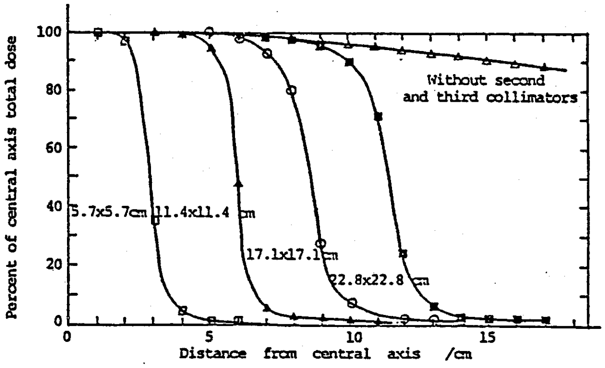

Fig. 2 Beam profiles in air for 5.7×5.7cm, 11.4×11.4cm, 17.1×17.1cm and 22.4×22.4cm square field and open field (without second and third colli mator) at 200cm from Be-taregt.

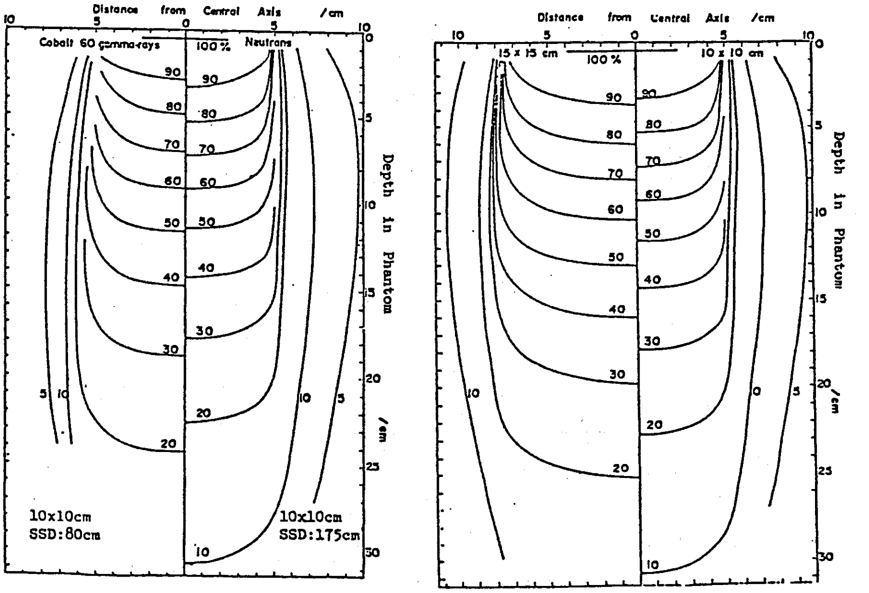

Fig. 3 Isodose curves in TE phantom.[14)]

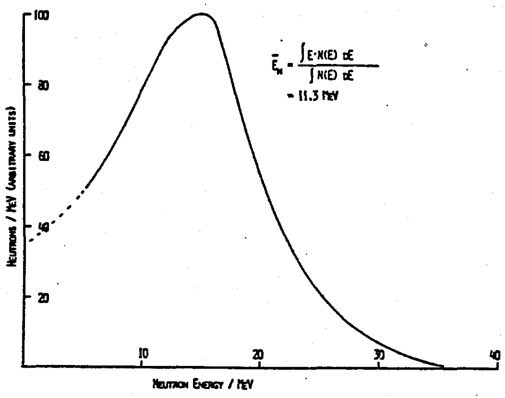

Fig.4 The estimated neutron spectrum for d(30)Be-neutrons.

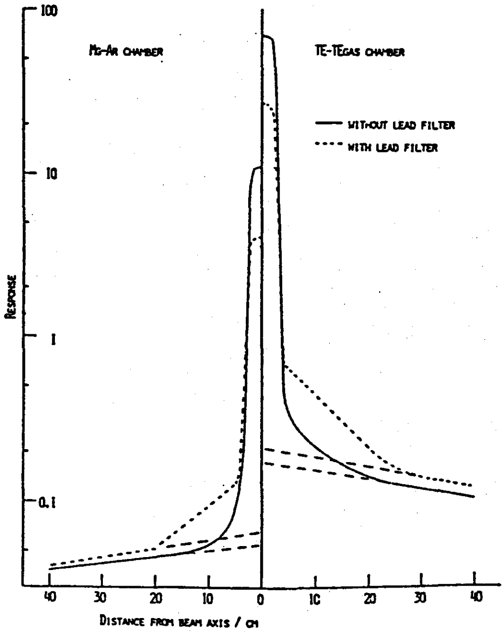

Fig. 5 Profile dose distributions in air with and without lead filter. Right side curves with TE-TE gas chamber and left side ones with Mg-Ar chamber. A=2.8x3.8 cm^2.

Table 1. The values of ku for d(30)Be-neutrons. for various non-hydrogenous chambers

Type of chambers	Volume (ml)	theoretical ku'	ku"	Experimental ku ±sd (kt=0.980)
Mg-Ar	2	0.159	0.045	0.143 ±0.003
graphite-air	1.6	0.307	0.275	0.280 ±0.002
graphite-air	0.1	0.307	0.275	0.306 ±
C+Teflon-air	3.0			0.321 ±0.008
C+Teflon-air	1.3			0.312 ±
C+Teflon-CO2	3.0			0.318 ±0.004
C+Teflon-CO2	1.3			0.286 ±

Submitted to The Third JAPN-CHINA JOINT SYMPOSIUM on Accelerators forNuclear Science and Their Applications,
18-20 November, 1987, Riken, Wako-shi, Saitama 351-01, Japan

HIMAC PROJECT

S. Yamada, K. Endo*, A. Itano, T. Kanai, K. Kawachi, T. Kohno,
Y. Miyazawa**, A. Noda***, H. Ogawa, K. Sato***, Y. Sato,
H. Suzuki, S. Watanabe***, T. Yamada and Y. Hirao

National Institute of Radiological Sciences
4-9-1 Anagawa, Chiba-shi, Chiba 260, Japan

Abstract

HIMAC is a heavy ion synchrotron facility proposed by NIRS in order to introduce the advantages of heavy ion treatment into a hospital environment. The proposed facility is dedicated to the medical use especially to the treatment of the tumor. A main accelerator of HIMAC consists of a couple of separated function type synchrotrons with the maximum magnetic rigidity of 9.7 Tm. The output energy of the synchrotron is as high as 800 MeV/u for light ions with q/A=0.5. Two synchrotron rings are installed in the rooms of different floors and will be operated essentially independent with each other. An average diameter of the rings is about 40 m.

For the medical treatment, four irradiation rooms will be available, two of which are equipped with both of horizontal and vertical treatment lines. Other four experimental rooms will be prepared for the biomedical and related experiments.

Introduction

High energy heavy ions have the therapeutical advantages over the ordinary radiations including protons and neutrons. The superiority of the heavy ion therapy is mainly due to the sharp dose concentration called Bragg's peak in the tumor volume. The advantages of the dose concentration and the resulting high LET characteristics are very well demonstrated through the biomedical experiments and the clinical trials at Lawrence Berkeley Laboratory in United States.

As the further development of the existing radiotherapy with an AVF cyclotron, NIRS has decided to construct HIMAC (Heavy Ion Medical Accelerator in Chiba)1)-3) for clinical treatment of the tumor.

The biomedical accelerators of heavy ions are also proposed by European and American groups. In the European proposal called EULIMA,4) the particle energy of the accelerator is 400 to 600 MeV per nucleon for the heaviest element of Ne. (The exact value of the output energy is not yet determined.) The main accelerator of the EULIMA project is a superconducting separated sector cyclotron equipped with an ordinary type cyclotron as an injector. An ECR source will be used to make very high charge states of light ions.

LIBLA5) is a heavy ion synchrotron facility proposed by LBL. The output energy of the synchrotron varies from 70 to 600 MeV/u for light ions. An injector of the synchrotron is a 200 MHz RFQ linac followed by a short Alvarez type linac. An ion source for the accelerator is a hot cathod PIG source.

These two projects are both in their preliminary design stages.

Table 1.
Requirements for HIMAC facility

Ion species:	from ^{4}He to ^{40}Ar	
Maximum energy:	800 Mev/u	for q/A = 1/2
Minimum energy:	100 MeV/u	for q/A = 1/2
Beam intensity*:	1.2×10^{10} pps	for ^{4}He Ions
	2.0×10^{9}	^{12}C
	3.4×10^{8}	^{20}Ne
	4.5×10^{7}	^{28}Si
	2.7×10^{7}	^{40}Ar
Beam duration:	400 ms	
Repetition rate:	1/2 Hz for each ring	
Beam emittance:	10 π mm・mrad (unnormalized)	
Momentum spread:	< ±0.2 %	
Irradiation facility		
Treatment rooms:	2 (Horizontal beam only)	
	2 (Horizontal & vertical beams)	
Experimental rooms:	4	
Beam characteristics		
Field size:	22 cm (Max. diameter)	
Dose uniformity:	±2 % over entire filed	
Maximum range:	30 cm	
Dose rate:	500 rad/min (5 Gy/min)	
Field broadning:	Wobbler scanning method	

* Extracted beam intensity per ring.

Outline of HIMAC

Requirements

The major requirements for the HIMAC facility are summarized in Table 1. The ion species are ranging from ^{4}He to ^{40}Ar and the output energy of the accelerator is reqiured to vary from 100 to 800 MeV/u. The extracted ion intensities in the table are required to realize the dose rate of as high as 500 rad/min. The rate is determined so that the irradiation of heavy ions will be finished after the duration of a few minutes.

Main Accelerator

A main accelerator of HIMAC consists of a couple of separated function type synchrotrons as shown in Fig.1. The synchrotron rings are installed in the different floors and will be operated independently with each other except that the synchrotron magnets must be excited 180° out of phase.

The two ring structure of the main accelerator is expected to increase drastically the flexibility of the machine operation. The accelerator can provide the horizontal and vertical heavy ion beams simultaneously. In the future extension, two stage acceleration of the

---

* National Institute for High Energy Physics, Oho-machi, Tsukuba-gun, Ibaraki 305

** The Institute of Physical and Chemical Research, Hirosawa, Wako-shi, Saitama 351-01

*** Institute for Nuclear Study, University of Tokyo, Midori-cho, Tanashi-shi, Tokyo 188 heavier ions will be acceptable. It is also possible in the future that one of the synchrotron ring is used as a storage ring, aiming the treatment and diagnostics with radioactive beams and/or a single shot beam of stable isotopes.

Clinical Treatment Rooms

Four treatment rooms are required in total. Two rooms will be equipped with both horizontal and vertical beam lines. These four treatment rooms are required in order to increase efficiency of the beam time because it takes rather long time to set a patient on an exact fixed position.

The accelerated ions must be broadened with a set of Wobbler scanning magnets to the maximum diameter of 22 cm. The uniformity of the dose distribution in the irradiation field must be better than 2% to ensure the effectiveness of the treatment.

Experimental Rooms

Four more irradiation rooms are required, two of which will be prepared for the physics and general purposes, and the biomedical experiments. The other two experimental rooms are for the radioactive beams. A thick Be target will be placed in a secondary beam production room, and the desired ions, for examples ^{19}Ne or ^{10}C, are separated with analyzing magnets from the primary and any other unwanted beams. Two experimental rooms following the production room are for the diagnostics with the radioactive beams and for the general purposes.

Injector System

Figure 2 shows a plan view of an injector system of HIMAC, and the detailed parameters of the system is listed in Table 2.

In the first phase of the project, two ion sources will be prepared: One is a PIG type ion source for light ions, and the other is an ECR type source for heavier ions. Through the low energy beam transport line of about 7 m long, ions are injected into an RFQ linac with an energy of 8 keV/u. The operation frequency of 100 MHz is chosen for the linac so as to give a sufficient focusing strength to these ions. An acceptance of the injector is 0.6π mm.mrad in a normalized value.

RFQ Linac

The RFQ linac covers an energy range from 8 to 800 keV/u with a vane length of 7.3 m. The maximum surface field of the linac is chosen at rather high value of about 200 kV/cm, and about 1.8 times higher than the well known Kilpatrick's limit. This value, however, is lower than that obtained experimentally with an RFQ

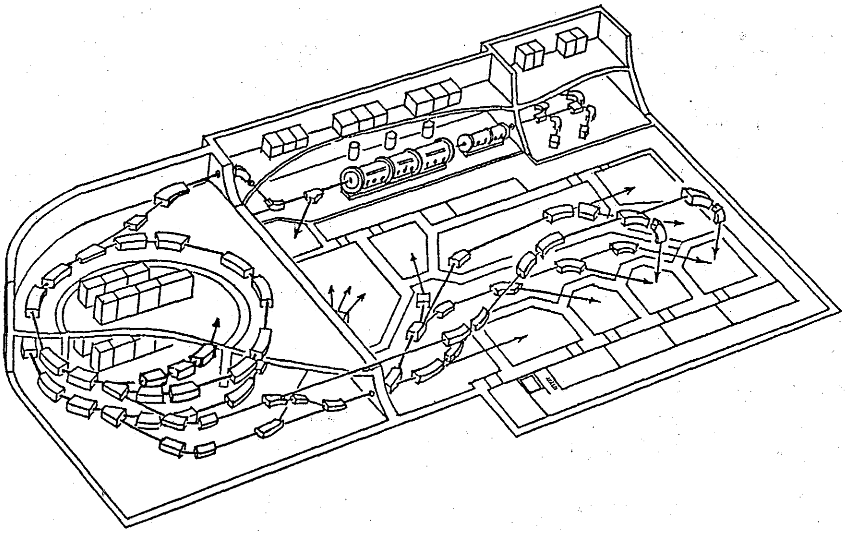

Fig. 1. A bird's eye view of the HIMAC facility.

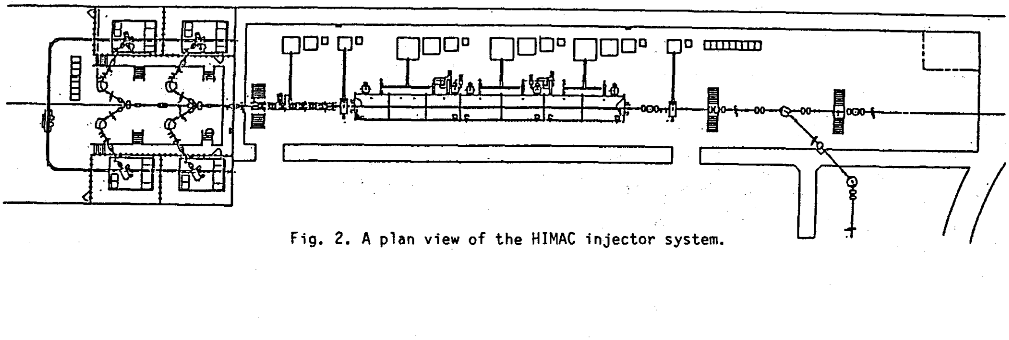

Fig. 2. A plan view of the HIMAC injector system.

cavity having almost the same geometry.6)

The linac has a conventional four vane type structure separated longitudinary into four tanks. The diameter of the linac is about 60 cm. The RFQ linac is essentially the same as that constructed at Institute for Nuclear Study, University of Tokyo.7)

Alvarez Linac

The RFQ linac is followed by three Alvarez type cavities with the same frequency of 100 MHz. The linac tank is separated into three independent rf cavities. Each tank is fed with about 800 kW peak rf power. The maximum surface field is chosen at about 1.3 times higher than the Kilpatrick's limit. The total length of the Alvarez linac is about 25 m, and the diameter of the cavity is about 2 m.

Number of the drift tubes in the linac is about 100 in total. Each drift tube is supported by a horizontal and a vetical stems and is equipped with a quadrupole magnet for beam focusing. Ions are accelerated to 6 MeV/u by the Alvarez linac.

Charge Stripper & Debuncher

Around the output end of the Alvarez linac, an automatic changer of a charge stripper is installed. The orbital electrons of the accelerated ions are stripped out with the carbon foil, and only the fully stripped ions will be injected into the next acceleration stage.

A 100 MHz debuncher cavity will be introduced in the medium energy beam transport line. The debuncher rotates the beam bunch in the longitudinal phase space, and suppresses the momentum spread of the linac beam.

Table 2.
Injector Specification

Ion source	
Type	PIG & ECR
Ion species	^{4}He to ^{40}Ar
q/A	> 1/7
Injector	
Frequency	100 MHz
Repetition rate	3 Hz Max.
Duty factor	0.3 % Max.
Acceptance	0.6 π mm.mrad (normalized)
RFQ linac	
Input/Output energy	8 / 800 keV/u
Vane length	7.3 m
Cavity diameter	0.6 m
Max. surface field	205 kV/cm (1.8 Kilpatrick)
Peak rf power	260 kW (70% Q)
Alvarez linac	
Input/Output energy	0.8 / 6.0 MeV/u
Total length	24 m (3 rf cavities)
Cavity diameter	2.20 / 2.18 / 2.16 m
Average axial field	1.8 / 2.2 / 2.2 MV/m
Shunt impedance	34 - 47 MΩ/m (effective)
Max. surface field	150 kV/cm (1.3 Kilpatrick)
Peak rf power	770 / 820 / 760 kW
Focusing sequence	FFDD (6.8 kG/cm Max.)

Synchrotron

The synchrotron is a separated function type with a FODO focusing structure. The output energy varies from 100 to 800 MeV/u for light ions. The repetition rate of the acceleration is designed to be 0.5 Hz. The required vacuum pressure is in a range of 10^{-8} torr, and not so difficult to realize with an ordinary pumping system.

A layout of the synchrotron ring is shown in Fig.3. A design specification of the synchrotron is given in Table 3.

Magnet System

Numbers of unit cells and the superperiodicities of the ring are 12 and 6, respectively. The betatron wave numbers are chosen at 3.75 for horizontal and 3.25 for vertical direction. Twelve sector type bending magnets have a bending radius of 6.5 m, and the magnetic field changes from 0.11 T at the injection up to 1.5 T at the maximum energy.

Beam Injection

Beams from the linac are injected into the ring through an electrostatic inflector. A multiturn injection scheme is adopted to increase the circulating beam current by ten times. The multiturn injection is achieved during the decaying time of the bump magnets for the duration of 77 s. The horizontal and vertical acceptances of the synchrotron ring are respectively 30 and 3 π mm·mrad in normalized values.

A set of steering magnets and beam position monitors is installed in the ring for the correction of the closed orbit distortion at the injection energy. A set of the sextupole magnets are also prepared for the chromaticity correction.

RF Acceleration

The injected particles are accelerated with two rf cavities placed 180° apart from each other. An rf cavity is composed of a pair of ferrite loaded λ/4 resonators, and generates an acceleration voltage of up to 6 kV at

Table 3.
Synchrotron Specification

General	
Type	Separated function
Output energy	100 - 800 MeV/u (q/A=1/2)
Average diameter	41 m
Magnet system	
Number of unit cells	12 (6 super periods)
Focusing sequence	FODO
Betatron tunes (H/V)	3.75 / 3.25
No. of dipole magnets	12 (sector type, 3.4 m)
Dipole field (Min/Max)	0.11 / 1.5 T
Bending radius	6.5 m
No. of Q magnets	24 (0.4 m each)
Q-field (Min./Max.)	0.51 / 7.0 T/m
Repetition rate	1/2 Hz
Rise/Flat-top time	0.7 / 0.5 s
Acceleration system	
No. of cavities	2
Frequency range	1.0 - 7.5 MHz (harmonic 4)
Acceleration voltage	6 kV per cavity (peak)
RF power input	15 kW per cavity (peak)
Filling factor	0.8
Momentum acceptance	±0.2 %
Vacuum system	
Material of chamber	SUS-316LN (3 mm thick)
Baking tempereture	200 °C
Average pressure	1 x 10^{-8} torr
Pumps	Sputter ion pumps Ti getter pumps Turbo molecular pumps
Extraction system	
Type	Fast & slow (1/3 resonance)
Length of beam spill	400 ms at 600 MeV/u (slow)

the gap. The cavity is designed bakable at a temperature of up to 300 °C.

The rf system must cover a very wide frequency range from 1 to 7.5 MHz, where the harmonic number is chosen at 4. Such a frequency range is excellently realized by an acceleration cavity developed at INS, University of Tokyo.8)

Beam Extraction

After reaching the flat top of the magnet excitation, ions are extracted from the ring through an electrostatic deflector followed by two septum magnets. The bump orbit is formed with the combination of five bump magnets. The slow extraction is performed using a third order resonance excited with sextupole magnets prepared for this purpose. The beam duration depends on the output energy and 400 ms at 600 MeV/u.

A fast extraction channel is prepared at the same long straight section. The bump magnets for the slow extraction scheme are also used for the fast extraction. The bump orbit, however, must be formed to the opposite directions to the slow extraction. The extracted beam will be used by biomedical experiments.

In the future extension, the fast extracted beams will be injected into the lower ring for the further acceleration and/or the beam accumulation.

Beam Delivery System

A beam delivery system is required to switch heavy ion beams from one treatment room to the other one within a very short time of 5 min. The beam switching may be performed only by exciting or deexciting the switching magnet. The bending effects due to the residual field of the switching magnet can be compensated with a small current source prepared for this purpose, or with a pair of steering magnets placed around the switching magnet. The discussions are now underway for the detailed sequence of the beam switching.

Time Schedule

A part of the HIMAC project has been approved by the government and the research and the development program of the machine components has started in cooperation with the industrial companies and with the public laboratries. Based on the achievements of these R&Ds, the construction of the injector system will be begun in this fiscal year.

In a long range schedule of the HIMAC project, the preparatory experiments for the medical treatment are scheduled in 1992 and the clinical trials are expected to start from 1993.

Acknowledgements

The authors would express their sincere gratitude to the physisits and engineers of Sumitomo Heavy Industries, Hitachi, Mitsubishi Electric and Toshiba for valuable discussions in fixing the detailed parameters of HIMAC. The authors also thank Drs. T. Terashima, H. Tsunemoto, E. Tanaka and other persons concerned with the HIMAC project for their continuous encouragement and helpful discussions.

References

1) K. Kawachi, et al, Proc. of 5th Symp. on Accel. Sci. & Technol., KEK, Tsukuba, Japan, 1984, p409.
2) K. Kawachi, Proc. of 5th PTCOG meeting & Int. Workshop on Biomed. Accel., LBL, Berkeley, California, USA, 1986, p73.
3) S. Yamada, et al, Proc. of 6th Symp. on Accel. Sci. & Technol., INS, Tokyo, Japan, 1987, p33.
4) P. Mandrillon, Proc. of 5th PTCOG meeting & Int. Workshop on Biomed. Accel., LBL, Berkeley, California, USA, 1986, p93.
5) R. A. Gough, ibid, p117.
6) T. Nakanishi, et al, Particle Accel., 20 (1987) 183.
7) for an example, N. Ueda, et al, presented in this symposium.
8) K. Sato, et al, Proc. of 6th Symp. on Accel. Sci. & Technol., INS, Tokyo, Japan, 1987, p117.

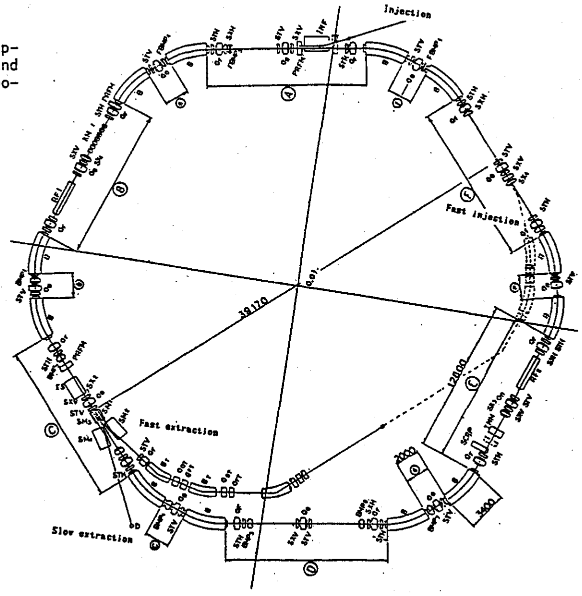

Fig. 3. A layout of the HIMAC Synchrotron.

HIMAC PROJECT AT NIRS

S. Yamada, K. Endo*, A. Itano, T. Kanai, K. Kawachi, T. Kohno,
Y. Miyazawa**, A. Noda***, H. Ogawa, K. Sato***, Y. Sato,
H. Suzuki, S. Watanabe***, T. Yamada and Y. Hirao

National Institute of Radiological Sciences
4-9-1 Anagawa, Chiba-shi, Chiba 260

ABSTRACT

A heavy ion synchrotron complex dedicated to the medical use, HIMAC (Heavy Ion Medical Accelerator in Chiba), has been proposed by NIRS. This paper describes the brief review of the design study of HIMAC. The acceleator complex consists of an injector linac, two heavy ion synchrotron rings and a high energy beam delivery system. Four irradiation rooms are prepared for the medical treatment. Two of the rooms are equipped with both of horizontal and vertical beam courses. Extra four experimental rooms will be available for radiological, biomedical and other related subjects.

A part of the NIRS proposal has been approved by the government and the construction of the injector system will be begun in this fiscal year. The preparatory experiments for the cancer treatment are scheduled in 1992 and the clinical trial is expected to start in 1993.

INTRODUCTION

The radiological effects of heavy ions on organic cells are well suited for medical treatment of the cancer. The formation of the Bragg peak in a human body is one of the most remarkable properties of heavy ions. In the very sharp peak, heavy ions loss most of their kinetic energies resulting the high LET characteristics localized both in transverse and longitudinal directions. The degree of the dose localization is far superior to those of the neutrons and photons. The oxygen enhancement ratio (OER), which is defined as a ratio of doses required to kill the hypoxic and aerated cells, is close to unity in the vicinity of the Bragg peak. The low value of the OER is very much desired to realize homogeneous effects on a tumor which tends to be hypoxic in the central region. The superiority of heavy ion therapy is well demonstrated through radiological experiments and clinical trials at Lawrence Berkeley Laboratory, USA. As a further expansion of the long experience on proton and neutron radiotherapies, NIRS has decided to construct a heavy ion synchrotron facility dedicated to the medical use.[1)]

In the proposed therapy, an output energy should be higher than 800 MeV/u for Si ions in order to realize a residual range of 30 cm in a human body. The high output energy of the accelerator is also very effective to produce the radioactive beams of high quality for the treatment and/or the diagnostics. The area of the heavy ion irradiation must be enlarged to cover the whole area to be treated. The maximum diameter of the irradiation field is chosen to be 22 cm.

The major requirements for the HIMAC facility are summarized in Table 1, and the main parameters of the accelerator complex are listed in Table 2. A layout of the HIMAC facility is shown in Fig.1.

ION SOURCE

Two types of ion sources are prepared for the accelerator: a PIG and an ECR sources. The PIG source will be used mainly for light ions, whereas the ECR source is expected to improve drastically heavy ion capabilities of HIMAC. The ion sources are required to produce heavy ions ranging from He to Ar. For typical ions, the source intensities are listed in Table 3 together with the intensities at each stage of the acceleration. Both types of the ion sources will be installed on a high voltage station of about 50 kV, and the remote control of the source parameters is possible from the earth potential. The output beam energy is 8 keV/u.

The PIG source is of a hot cathode type and the magnetic field of 7 kG is chosen. The magnet gap and the maximum extraction voltage are 20 cm and 35 kV, respectively. A test stand of the PIG source has been constructed and beam tests are now in progress. The pulse operation of the ion source, including the gas feeding system, is expected to be very effective for increasing the beam intensity and the source liftime and is the major subject of the tests.

A plasma chamber of the ECR source consists of two stages, both of which are fed by 10 GHz microwave power with a sigle source of 2.5 kW. Three independent coils with return yokes generate axial magnetic field, whereas the radially sextupole field is produced by $SmCo_5$ permanent magnet installed in the vacuum chamber. The bore diameter of the multipole magnet is 10 cm, and the extraction voltage is about 20 kV. In this summer, the R&D of the ECR source has been started in cooperation with the accelerator people of INS, University of Tokyo. The first beam test of the source is scheduled at the end of this fiscal year.

INJECTOR LINAC

The injector system of HIMAC is composed of an RFQ and Alvarez linacs. The operation frequency of the injector is chosen to be 100 MHz in order to ensure the sufficient focusing strength. The output energies of the linacs are respectively 0.8 and 6 MeV/u. The injector is designed to accelerate heavy ions with a charge to mass

Table 1
Requirements for HIMAC facility

Ion species:	from ^{4}He to ^{40}Ar	
Maximum energy:	800 Mev/u	for q/A = 1/2
Minimum energy:	100 MeV/u	for q/A = 1/2
Intensity per ring*:	1.2×10^{10} pps	for ^{4}He Ions
	2.0×10^{9}	^{12}C
	3.4×10^{8}	^{20}Ne
	4.5×10^{7}	^{28}Si
	2.7×10^{7}	^{40}Ar
Beam duration:	400 ms	
Repetition rate:	1/2 Hz for each ring	
Beam emittance:	10 π mm·mrad (unnormalized value)	
Momentum spread:	< ± 0.2%	
Irradiation facility		
Treatment rooms:	2 (Horizontal beam only)	
	2 (Horizontal & Vertical beams)	
Experimental rooms:	4	
Beam characteristics		
Field size:	22 cm diameter	
Dose uniformity:	±2% over entire field	
Maximum range:	30 cm	
Dose rate:	500 rad/min (5 Gy/min)	
Field broadning:	Wobbler scanning method	

* Extracted beam intensity

---

* National Institute for High Energy Physics, Oho-machi, Tsukuba-gun, Ibaraki 305

** The Institute of Physical and Chemical Research, Hirosawa, Wako-shi, Saitama 351-01

*** Insitute for Nuclear Study, University of Tokyo, Midori-cho, Tanashi-shi, Tokyo 188 ratio of larger than 1/7. The maximum repetition rate and the rf duty factor are 3 Hz and 0.3%, respectively.

The RFQ linac is of four vane type. The length of the vanes and the cavity diameter are about 7 and 0.6 m, respectively. The entire cavity, including the vanes themselves, is divided into four sections. The mechanical setting of the vanes will be performed in a section independently from the other sections. Through the setting procedure, an error of the capacitance distribution due to the vane misalignment is longitudinally smoothed out, resulting the relatively small deviation of the intervane voltage. The peak rf power of about 300 kW is fed to the cavity through a single loop coupler. The maximum surface field on the vane top is about 200 kV/cm (1.8 Kilpatrick), which is well below the experimentally confirmed value at this frequency.[2] The transverse acceptance of the linac is 0.6 π mm·mrad in a normalized value. A fast bunching method[2] is adopted in the beam dynamics design and a transmission efficiency is calculated to be about 90%. The RFQ linac is essentially a copy of TALL[3] developed at INS, University of Tokyo.

Table 2
HIMAC parameters

Ion source	
Type	PIG & ECR
Ion species	from ^{4}He to ^{40}Ar
q/A	≥ 1/7
Injector	
Frequency	100 MHz
Repetition rate	3 Hz Max.
Duty factor	0.3% Max.
Acceptance	0.6 π mm·mrad (normalized)
RFQ linac	
Input/Output energy	8 / 800 keV/u
Vane length	7.3 m
Cavity diameter	0.6 m
Surface field	205 kV/cm (1.8 Kilpatrick)
Peak rf power	260 kW (70% Q)
Alvarez linac	
Input/Output energy	0.8 / 6.0 MeV/u
Total length	24 m (3 rf cavities)
Cavity diameter	2.20/2.18/2.16 m
Average field	1.8/2.2/2.2 MV/m
Shunt impedance	34 - 47 MΩ/m (effective)
Surface field	150 kV/cm (1.3 Kilpatric)
Peak rf power	770/820/760 kW
Focusing sequence	FFDD (6.8 kG/cm Max.)
Synchrotron (for one ring)	
Output energy	100 - 800 MeV/u (q/A = 1/2)
Average diameter	41 m (12 cells, 6 s-periods)
Focusing sequence	FODO
Betatron tunes (H/V)	3.75 / 3.25
No. of dipole magnet	12 (3.4 m each)
Dipole field	0.11 (Min.) / 1.5 (Max.) T
No. of Q magnets	24 (0.4 m each)
Quadrupole field	0.51 (Min.) / 7.0 (Max.) T/m
Long straight sect.	12 (5.0 m each)
Repetetion rate	1/2 Hz
Rise/flat-top time	0.7 / 0.5 s
Acceleration system	
No. of cavities	2
Frequency range	1.0 - 7.5 MHz (harmonic 4)
Acceleration voltage	6 kV per cavity (peak)
RF power input	15 kW per cavity (peak)
Vacuum system	
Material of chamber	SUS-316LN (3 mm thick)
Baking tempereture	200 °C
Average pressure	1 x 10^{-8} torr
Pumps	Sputter ion pumps Ti getter pumps Turbo molecular pumps
Extraction system	
Type	Fast & slow (1/3 resonance)
Length of spill	up to 400 ms (slow)

Table 3
Beam intensity schedule for typical ions

Ion species	C^{6+}	Ne^{10+}	Si^{14+}
Intensity on target (pps)	1.8×10^8	3.1×10^7	4.0×10^6
Treatment delivery transmission		0.1	
Beam transport transmission		0.9	
Extracted intensity (pps)	2.0×10^9	3.4×10^8	4.5×10^7
Synchrotron repetion rate (Hz)		0.5	
Extraction efficiency		0.8	
Acceleration efficiency		0.9	
RF capture efficiency		0.8	
Circulating ion intensity (ppp)	6.9×10^9	1.2×10^9	1.6×10^8
Injection efficiency		0.5	
Injection interval (us)		76.8	
Injected ion intensity (pps)	1.8×10^{14}	3.1×10^{13}	4.1×10^{12}
Injected ion current (euA)	170	49	9.1
Beam transport transmission		0.75	
Stripper efficiency	0.93 (2+→6+)	0.67 (3+→10+)	0.52 (4+→14+)
Alvarez linac transmission		0.9	
RFQ linac transmission		0.8	
Beam transport transmission		0.7	
Source electrical current (euA)	160	58	13
Ions from source	C^{2+}	Ne^{3+}	Si^{4+}

A drift tube of the Alvarez type linac is equipped with a pulsed quadrupole magnet. A FFDD type focusing sequence of quadrupole lenses is adopted to suppress a required field gradient. A transverse acceptance of the linac is 5.8 π mm·mrad with the highest field gradient of 6.8 kG/cm and large enough to accept the output beam from the RFQ. An effective shunt impedance of the linac cells ranges from 34 to 47 MΩ/m (80% of calculated value) and the peak rf power is estimated to be about 2.4 MW in total. A diameter and a length of the linac are respectively about 2 and 24 m. The linac is separated into three cavities to each of which an rf power of about 1 MW is fed through a loop coupler. The average axial fields of the cavities are 1.8, 2.2 and 2.2 MV/m, respectively. After the Alvarez linac, the heavy ions are charge stripped with a 100 μg/cm^2 thick carbon foil.

SYNCHROTRON

The HIMAC synchrotron consists of two rings, which are installed in the different floors and operated essentially independent of each other. The two ring structure of the synchrotron is expected to make the operation mode much more flexible. The synchrotron can provide the horizontal and vertical heavy ion beams simultaneously for the different treatment rooms. The treatment with multiple beams is also acceptable. In the future extension, two stage acceleration of the heavier ions will be possible. It is also possible in the future that one of the synchrotron ring is used as a storage ring, aiming the treatment and diagnostics with radio active beams and/or a single shot beam.

The synchrotron is a separated function type with a standard FODO type focusing sequence. The numbers of unit cells and superperiods are 12 and 6, respectively. A diameter of the synchrotron is about 41 m. The maximum magnetic regidity of the synchrotron magnets is 9.75 Tm. A multiturn beam injection scheme is adopted to increase the beam current by ten times. The horizontal and vertical acceptances of the synchrotron ring are respectively 30 and 3 π mm·mrad in normalized values. A set of steering magnets and beam position monitors is installed in the ring for the correction of the closed orbit distortion at the injection energy. A set of sextupole magnets is also prepared for the chromaticity correction.

The output energy of the synchrotron must be variable in a wide range from 100 to 800 MeV/u for Si ions. Two extraction modes are prepared: a fast and a slow extraction modes. The extraction septum magnets for those modes are installed in the same long straight section. The slowly extracted beam is directed to the outside of the ring, whereas the pulsed beam is extracted to the inside. The slow extraction scheme will use a third order resonance, and the beam spill time will be longer than 400 ms at 600 MeV/u.

A current source for the bending magnets consists of four sets of 12 phase rectifiers followed by a filter circuit. High power thyristor blocks are adopted in the rectifiers and controlled digitally by a computer. A "feed forward loop" with the computer will realize the precise tracking of the current pattern. Two similar current sources are prepared for focusing and defocusing quadrupole magnets. In a proposed current waveform, a flat top and a rising time are about 0.5 and 0.7 s, respectively. The maximum value of the time derivative of the bending field is about 2 T/s.

An rf system of the synchrotron must have a wide frequency range from 1.0 to 7.5 MHz, where a harmonic number is chosen to be 4. An rf station consists of a pair of ferrite loaded $\lambda/4$ cavities, and can generate a voltage of up to 6 kV. The input power for the cavity is about 15 kW. A couple of the rf stations are installed in a ring. The stations are operated with a feed back loop in order to lock the rf frequency with the circulating beam bunches. The signal of the beam position monitor is also fed back to the frequency control circuit. A feed forward technique of the beam position signals developed at BEVALAC4) is considered to be very effective in the acceleration of heavy ions, and may be adopted by the system.

An averaged vacuum pressure of an order of 10^{-8} torr is enough to accelerate fully stripped ions with a negligible amount of the beam loss. A combination of a sputter ion pump, a titanium getter pump and a turbo molecular pump may be the best choice to realize such a pressure. The vacuum chamber of the synchrotron ring is bakable up to 200 °C. A metal gasket will be used as a standard vacuum seal. The chamber is made of 3 mm thick SUS-316LN in order to suppress the unwanted effects of the eddy current due to the varying magnetic fields.

BEAM DELIVERY SYSTEM

A beam delivery system of HIMAC is required to provide heavy ion beams into four different treatment rooms in a very short time of about 5 min. The beam switching is performed only by exciting or deexciting a switching magnet. The high reproducibility of the magnetic field in the switching magnet may be obtained with the specially programmed sequence of the magnet excitation. The residual field, on the other hand, can be compensated with a small current source prepared for this purpose. The position error of only 2.5 mm will be allowed at the target position.

A requirement of the simultaneous irradiation of heavy ion beams makes the beam delivery system very complicated and relatively large. This system is designed to accept an attempt of the medical diagnostics with radioactive beams.

ACKNOWLEDGEMENTS

The authors have cooperated with many accelerator people of public laboratories and industrial companies in fixing the detailed parameters of HIMAC. The authors would express their sincere gratitude to these physicists and engineers. The authors also thank Drs. T. Terashima, H. Tsunemoto and other persons concerned in the HIMAC project for their continuous encouragement and helpful discussions.

REFERENCES

1) K. Kawachi, et al, Proc. of 5th Symp. on Accel. Sci. & Technol., Tsukuba, Japan, 1984, p409.
2) T. Nakanishi, et al, Particle Accel., 20 (1987) 183.
3) N. Ueda, et al, Proc. of 5th Symp. on Accel. Sci. & Technol., Tsukuba, Japan, 1984, p89.
4) M. Clinnick, et al, IEEE Trans. on Nucl. Sci., Vol. NS-22, No.3 (1975) 1261.

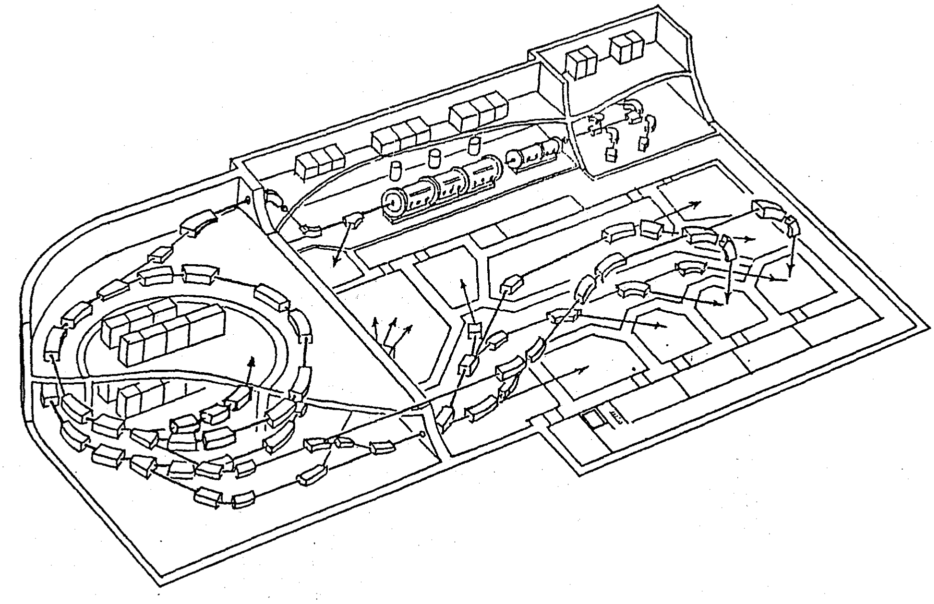

Fig.1 A bird's eye view of the NIRS heavy ion facility HIMAC.

〔原著〕

高ＬＥＴ放射線治療におけるＴＤＦ
—とくに速中性子線治療を中心にして

放射線医学総合研究所臨床研究部
中村　譲，古川　重夫

TDF for the Clinical Use in High LET Radiation Therapy
- Especially Fast Neutron Beam Therapy

Yuzuru KUTSUTANI-NAKAMURA, Shigeo FURUKAWA
Division of Clinical Research,
National Institute of Radiological Sciences

In the clinical application of high LET radiation for radiotherapy it is necessary to establish a criterion as a basis on which assess the biological effect of the widely varied fractionated regimes including mixed and boost use with low LET radiation of photons. These assessements are based on a scale of the biological iso-effect of normal tissues for dose measured both for high and low LET radiation. The generalized NSD (GNSD) and TDF (GTDF) for normal tissues of skin, lung and spinal cord were introduced. RBE formula estimated by the GTDF function is compared with experimental data published.

Key Words: TDF, Generalized TDF, Generalized NSD, Fast neutron therapy, High LET radiation

1. はじめに

放射線治療の際の治療効果を生物効果量として表示する方法はいくつかあるが，多くの治療医に利用されている方法に Orton-Ellis により提唱されたＴＤＦ（time, dose and fractionation factor）がある。[1] ＴＤＦはEllis により提唱されたＮＳＤ（nominal standard dose）から派生したもので，[2][3] 放射線は photon，正常組織は皮膚が対象である。

速中性子線治療の場合のＴＤＦについては久津谷－中村によりＸ線等価ＴＤＦ，生物学等価ＴＤＦが提案され，[4][5] 臨床に利用されている。

近年皮膚以外の組織のＮＳＤおよびＴＤＦが提案されている。

〒260 千葉市穴川４－９－１

しかし速中性子線および高LET放射線の多分割照射に関する報告は photon に比べると少なく，photon と同様に TDF を提案することは困難をともなう。

ここでは速中性子線治療を主体とした高LET放射線治療のTDFについて皮膚以外の組織も含めた計算法およびその利用法について述べる。

2. 方 法

1) Orton-Ellis のTDF

Ellis のNSDは(1)式のように表され，正常組織の耐容線量を与える時の線量－照射回数－照射期間の関係を示している。

$$D = NSD\ N^{0.24}\ T^{0.11} \cdots\cdots\cdots\cdots (1)$$

ここで，Dは総線量（cGy），Nは分割回数，Tは照射日数（日）を表し，NSDの単位は ret である。

Orton-Ellis のTDFは(2)式で表される。

$$TDF = n\,d^{1.538}\ t^{-0.169}\ 10^{-3} \cdots\cdots (2)$$

ここで，dは1回線量（cGy），tは照射間隔（T／N）（日），nは照射回数である。

照射回数Nとnとの違いはNは耐容線量となる時の照射回数を示し，nは耐容線量となる照射回数に達していない時の照射回数である。Ellis-Orton のNSDおよびTDFは photon の場合で正常組織は皮膚を対象にしている。Photon 以外の線質の異なった放射線，すなわち速中性子線，高LET放射線を含む放射線に対しても適用でき，しかも皮膚を含めた他の正常組織のNSDおよびTDF計算法について考える。

2) TDF一般式の導き方— Generalized NSD およびTDFの提案

Ellis のNSDにNとTのべき乗の値を種々の組織に対し，また種々の線質の放射線に対しても適用できるようにαとβで表し，そのNSDを Generalized NSDとしてGNSDで表す。

$$D = GNSD\ N^{\alpha}\ T^{\beta} \cdots\cdots\cdots\cdots (3)$$

ここで，αとβは線質および組織に対して変わる定数である。

GNSDをN, d, t で表すと(4)式で表される。

$$\begin{aligned} GNSD &= D\ N^{-\alpha}\ T^{-\beta} = Nd \cdot N^{-\alpha} \cdot (Nt)^{-\beta} \\ &= N^{1-(\alpha+\beta)}\ d\,t^{-\beta} \\ &= N^{A}\ d\ t^{-\beta} \cdots\cdots\cdots\cdots\cdots\cdots (4) \end{aligned}$$

ただし，$A = 1 - (\alpha + \beta) \cdots\cdots\cdots\cdots (5)$

Aは(5)式で表され，αおよびβと同様，放射線の線質および組織によって変わる定数である。

次に，(3)式により表されるGNSDから求められるTDFを Generalized TDFとしてGTDFで表すと(6)式のように表される。[4)] [5)]

$$GTDF = K\,n\,d^{1/A}\ t^{-\beta/A} \cdots\cdots\cdots\cdots (6)$$

ここで，Kは線質および組織によって変わる定数であるが，Kについての考え方は中村（1978）によって報告されているが耐容線量となる照射スケジュール，すなわち(3)式で示される照射回数N，照射期間Tおよび総線量Dの時，(6)式においてnがNになるのでGTDFは耐容線量となるので，その値を“100”に規格化するための比例定数である。

耐容線量となるTDFをGTDFtol とすると(6)と(4)式から(7)式で表される。

$$\begin{aligned} GTDF\,tol &= K\,N\,d^{1/A}\ t^{-\beta/A} \\ &= K \cdot GNSD^{1/A} = 100 \cdots\cdots (7) \end{aligned}$$

(7)式から

$$K = 100 / GNSD^{1/A} = 100\ GNSD^{-1/A} \cdots\cdots\cdots\cdots (8)$$

(6)式のKに代えてGNSDを用いて表すとGTDFは(9)式で表される。

$$GTDF = 100\ GNSD^{-1/A}\ n\ d^{1/A}\ t^{-\beta/A} \cdots\cdots\cdots\cdots (9)$$

3) 高LET放射線と低LET放射線との併用照射のTDF

TDFは加法則が行えるので[1)] (10)式のように表される。

$$\mathrm{GTDF\,total} = \sum_{i} (\mathrm{GTDFjk})\,i \cdots\cdots\cdots (10)$$

ただし，

$$(\mathrm{GTDFjk})\,i = 100\,\mathrm{GNSDjk}^{-1/\mathrm{Ajk}}\ \mathrm{di}^{1/\mathrm{Ajk}}\ \mathrm{ti}^{-\beta\mathrm{jk}/\mathrm{Ajk}} \cdots\cdots\cdots\cdots (11)$$

(GTDFjk)iは放射線jを用い，組織kに対し，照射スケジュールiのGTDFであり，GTDF totalは各照射スケジュールのGTDFを積算したものである。

4）生物効果比（RBE）の一般式の導き方

線質の異なった放射線を治療に用いる際には生物効果比（RBE)を正確に把握した上で実施されなければならない。RBEは同一組織において同じ効果を示す線量比で表される。(6)式から照射回数，照射間隔が同じで線質が異なった場合同じ効果を示す線量との間には(12)式で示す関係があるので，photonおよび高LET放射線の引数をそれぞれ1および2と書くとRBEは(13)式または(14)式で表される。

$$\mathrm{GTDF} = K_1\,n\,d_1^{1/A_1}\ t^{-\beta_1/A_1} \cdots\cdots\cdots (12)$$

$$= K_2\,n\,d_2^{1/A_2}\ t^{-\beta_2/A_2}$$

$$\mathrm{RBE} = d_1/d_2$$

$$= (K_2/K_1)^{A_2}\ d_1^{1-A_2/A_1}\ t^{\beta_1 A_2/A_1-\beta_2} \cdots\cdots\cdots (13)$$

または

$$= (K_2/K_1)^{A_1}\ d_2^{A_1/A_2-1}\ t^{-\beta_2 A_1/A_2+\beta_1} \cdots\cdots\cdots (14)$$

(13)式はphotonの1回線量 d_1 で表した場合，(14)式は速中性子線または高LET放射線の1回線量 d_2 で表した場合の関係式である。

(8)式を用いると(13)および(14)式はそれぞれ(15)および(16)式で表される。

$$\mathrm{RBE} = \mathrm{RBEs}\cdot \mathrm{GNSD}_1^{A_2/A_1-1}\cdot d_1^{1-A_2/A_1}\ t^{\beta_1 A_2/A_1-\beta_2} \cdots\cdots\cdots\cdots (15)$$

$$= \mathrm{RBEs}\cdot \mathrm{GNSD}_2^{1-A_1/A_2}\cdot d_2^{A_1/A_2-1}\ t^{-\beta_2 A_1/A_2+\beta_1} \cdots\cdots\cdots\cdots (16)$$

ただし，$\mathrm{RBEs} = \mathrm{GNSD}_1/\mathrm{GNSD}_2 \cdots\cdots\cdots\cdots (17)$

ここで，RBEsは1回照射のRBEであるが，多分割照射のデータによると多分割照射から外挿される1回照射のGNSDは1回照射の場合の線量と異なるので多分割照射のデータから外挿されたGNSDにより求められるRBEであり，1回照射のRBEと異なっている。

5）GNSDおよびGTDFに適する各組織のパラメータの求め方

速中性子線の皮膚のαおよびβはField（1972）によるとそれぞれ0.04および0.11であり，中村（1978)は速中性子線のGNSDnおよびGTDFnをそれぞれ(18)および(19)式で表した。

$$\mathrm{GNSD}_{\mathrm{n,skin}} = D\,N^{-0.04}\ T^{-0.11} \cdots\cdots\cdots (18)$$

$$\mathrm{GTDF}_{\mathrm{n,skin}} = 2.90\times 10^{-2}\ \mathrm{nd}^{1.18}\ t^{-0.13} \cdots\cdots\cdots (19)$$

一般の正常組織のGNSDおよびGTDFの一般式は組織としては皮膚，肺，脊髄を取りあげ各パラメータは文献[7)~20)]から求めた。

3. 結果・考察

皮膚，肺および脊髄のGNSDならびにGTDFに適するphotonおよび速中性子線のα，βおよびGNSDの値をTable 1に，K，1／Aおよびβ／AをTable 2にそれぞれ示す。[7)~20)]

組織によって，また線質によって値は異なっている。皮膚のphotonのαの値はEllis-Ortonの値の0.24と異なり，0.26となっている。Orton-EllisのTDFの(2)式とTable 1との比較からGTDFは1回線量dが大きくなれば幾分値は大きくなり，照射間隔tが大きくなると幾分小さくなるが，両者に大きな値の差はない。速中性子線のGTDFはKの値が0.029が0.033と異なっている。

Table 1. Parameters of the generalized NSD formula for normal tissues of skin, lung and spinal cord.

Tissue	Photon			Neutron		
	α	β	GNSD	α	β	GNSD
Skin	0.26	0.11	1,640	0.04	0.11	910
Lung	0.34	0.07	970	0	0.07	620
Spinal cord	0.37	0.03	1,400	0.03	0.03	800

Table 2. Parameters of the generalized TDF formula for normal tissues of skin, lung and spinal cord.

Tissue	Photon			Neutron		
	K	1/A	β/A	K	1/A	β/A
Skin	$7.9\mathrm{X}10^{-4}$	1.59	0.17	$3.3\mathrm{X}10^{-2}$	1.18	0.13
Lung	$8.7\mathrm{X}10^{-4}$	1.69	0.12	$9.9\mathrm{X}10^{-2}$	1.08	0.08
Spinal cord	$5.7\mathrm{X}10^{-4}$	1.67	0.05	$8.2\mathrm{X}10^{-2}$	1.06	0.03

肺および脊髄の値についてみてみると皮膚に比べ，photon では，αはより大きく脊髄が最も大きく，βはより小さく，脊髄が最も小さい。速中性子線では，photon に比べ，βの値は同じであるがαの値が異なり，皮膚，脊髄，肺の順に小さくなり，とくに肺の値は0になっている。

実際の照射スケジュールにあてはめてみてみると，Photon の場合，1回線量200 cGy，週5回照射で30回照射した標準の照射スケジュールの場合の皮膚，肺および脊髄の GTDF はそれぞれ，100，200 および 116 となり，本報で提案した肺，脊髄は幾分値が大きくなり，耐容線量はより低くなっていることが分かる。

速中性子線の場合は1回線量100 cGy，週3回照射で15回照射した時，皮膚ではGTDFは100になるが，肺，脊髄ではそれぞれ199，160となり，photon 同様異なっている。一方肺のGTDFを100とした場合，1回線量 95 cGy，週3回照射では 8 回照射となり，脊髄の場合は1回線量94 cGy，週3回照射で10回照射となるが，皮膚ではそれぞれ50，62となり，耐容線量に達していない。

次に線質の異なる放射線を用いる場合のRBEについて，本報で提案したパラメータを用い，皮膚，肺および脊髄の計算式を求めてみる。パラメータを(16)式に代入するとそれぞれ(20)～(22)式が求め

られる。d_h は高LET放射線の1回線量である。

①皮膚：

$$RBE_{skin} = 10.03 d_h^{-0.26} t^{0.03} \cdots\cdots(20)$$

②肺：

$$RBE_{lung} = 16.42 d_h^{-0.37} t^{0.03} \cdots\cdots(21)$$

③脊髄：

$$RBE_{cord} = 19.64 d_h^{-0.36} t^{0.01} \cdots\cdots(22)$$

Fig. 1に実線で示す。1回線量が大きくなるとRBEは減少し，照射間隔が大きくなるとRBEはわずか増加するが値への影響は少ない。1回線量が小さい所ではRBEは大きく，線量が大きくなると減少する。傾斜は脊髄，肺はほぼ等しく，皮膚は幾分小さい。低線量でのRBEは脊髄，皮膚，肺の順となっているが，400 cGyより高くなると皮膚は脊髄より高くなる。照射間隔を一定とした時RBEと1回線量との関係を両対数グラフ上で表わすと直線になっている。これらの3組織の報告されている文献9) 10) 17)~19)のRBEをFig. 1に点線で示すと実線と比較的良く一致している。

次に同じ線質でエネルギーが変わった場合のGTDFについて考えてみるとGNSDの式で，α，β，GNSDの3つのパラメータの内3つ共変わるものと考えることが一般的であるが，GNSDのみ変わり，α，βは変わらないとしている報告がある。20) 21)

Cohenはp(66)Be速中性子線のGTDF，すなわち(19)式においてKの値を2.4×10^{-2}を用い，他のパラメータは同じ値を用いている。21) また組織の耐容線量のレベルが変わった場合3つのパラメータの内GNSDが変わるとする方が一般的である。EllisのNSDの式を求める基になったCohenのデータにおいて皮膚の紅班と耐容

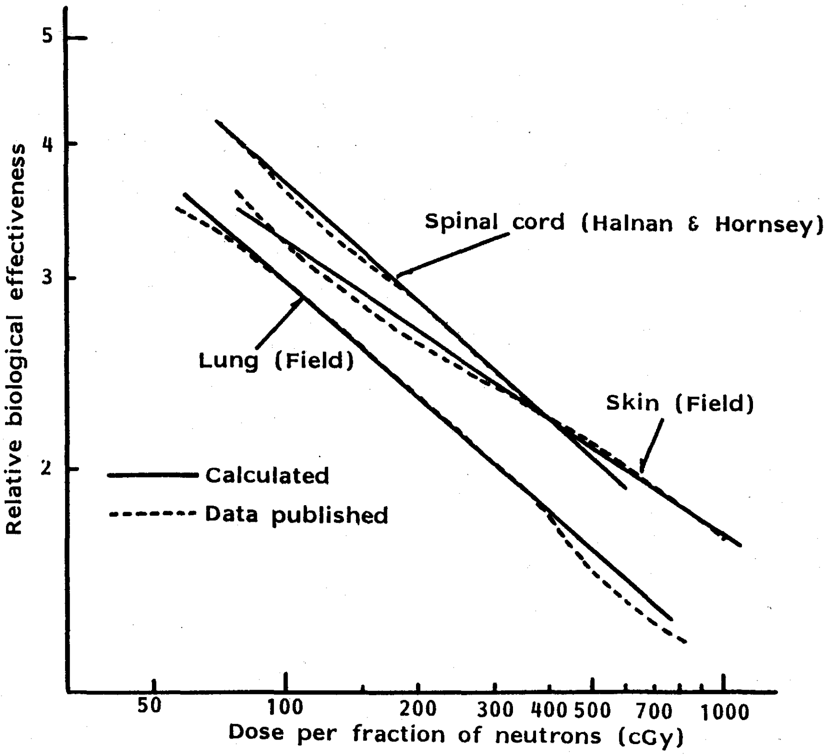

Fig. 1 Comparison of RBE calculated and published for normal tissues of skin, lung and spinal cord as a function of neutron dose per fraction.

線量とでは線量レベルが異なるが，α，βは変わらないとしている。2)この場合，GTDFの計算式においてGNSD，すなわちKに関してのみ変わると考えることができる。

そこで，速中性子線を除く高LET放射線の効果が速中性子線に準じ，GNSDのみ変わるとするとK，すなわち耐容線量GNSDを変えることによりGTDFを推測することができるが，やはり生物，臨床データを基に求めることが必要であると考えている。

最後に高LET放射線治療の際にはGTDFを正確に求め臨床トライアルを実施する必要があるが，速中性子線の分割照射の効果はGNSDの式からみて分かる通り少なく，実際の治療においては正常組織の耐容線量を正確に把握し，GNSDを求めれば，1回線量，分割回数を変えてもあまり影響されず，photonの場合より治療スケジュールが立て易いものと考えられる。問題はとくに放射線に高感受性の組織，臓器が照射野内に含まれる場合や，高LET放射線では至適線量の幅が狭いので照射する線量を精度よく照射しなければならないことなどがあげられ，実際治療の際は慎重でなければならない。

文　献

1) Orton, C.G., Ellis, F.: A simplification in use of the NSD concept in practical radiotherapy. Brit. J. Radiol., 46: 529–537, 1973.
2) Ellis, F.: The relationship of biological effect to dose-time-fractionation factors in radiotherapy. Current Topics in Rad. Research, 4: 357–397, 1968.
3) Ellis, F.: Dose, time and fractionation: A clinical hypothesis. Clin. Radiol., 20: 1–7, 1969.
4) 久津谷譲，梅垣洋一郎：生物学的等価線量の考え方と計算法．癌の臨床別冊「癌・放射線療法」，p79-92, 1973.
5) 中村　譲：速中性子線治療における生物学等価TDFによる治療計画．日本医放会誌，38：950-960, 1978.
6) Fowler, J.F.: Experimental animal results relating to time-dose relationships in radiotherapy and the "ret" concept. Brit. J. Radiol. 44: 81–90, 1971.
7) Field, S.B.: The Ellis formulae for X rays and fast neutrons. Brit. J. Radiol., 45: 315–317, 1972.
8) Cohen, L., Creditor, M.: Iso-effect tables for tolerance of irradiated normal human tissues. Int. J. Radiat. Oncol. Biol. Phys., 9: 233–241, 1983.
9) Hornsey, S., Kutsutani, Y., Field, S.B.: Damage to mouse lung with fractionated neutrons and X-rays. Radiology, 116: 171–174, 1975.
10) Field, S.B., Hornsey, S., Kutsutani, Y.: Effects of fractionated irradiation on mouse lung and a phenomenon of slow repair. Brit. J. Radiol., 49: 700–707, 1976.
11) Cohen, L., Creditor, M.: Iso-effect tables for radiation tolerance of the human spinal cord. Int. J. Radiat. Oncol. Biol. Phys., 7: 961–966, 1981.
12) Hornsey, S., Morris, C.C., Myers, R.: The relationship between fractionation and total dose for X ray induced brain damage. Int. J. Radiat. Oncol. Biol. Phys., 7: 393–396, 1981.
13) Pezner, R.D., Archambeau, J.O.: Brain tolerance unit: A method to estimate risk of radiation brain injury for various dose schedules. Int. J. Radiat. Oncol. Biol. Phys., 7: 397–402, 1981.
14) Wara, W.M., Phillips, T.L., Sheline, G.E. et al.: Radiation tolerance of the spinal cord. Cancer, 35: 1558–1562, 1975.
15) Wara, W.M., Phillips, T.L., Margolis, L.W. et al.: Radiation pneumonitis: A new approach to the derivation of time-dose factors. Cancer, 32: 547–552, 1973.
16) Wigg, D.R., Koschel, K., Hodgson, G.S.: Tolerance of muture human central nervous system to photon irradiation. Brit. J. Radiol., 54: 787–798, 1981.
17) White, A., Hornsey, S.: Time dependent repair of radiation damage in the rat spinal cord after X-rays and neutrons. Europ. J. Cancer, 16: 857–962, 1979.
18) Halnan, K.E., Hornsey, S.: RBE values for neutron therapy. A simple method for converting acceptable photon dose to limiting neutron dose. Int. J. Radiat. Oncol. Biol. Phys., 7: 601–604, 1981.
19) Field, S.B., Hornsey, S.: RBE values for cyclotron neutrons for effects in normal tissues and tumours as a function of dose and fractionation. Europ. J.

Cancer, 7: 161–169, 1971.

20) Hornsey, S., Morris, C.C., Mayers, R. et al.: Relative biological effectiveness for damage to the central nervous system by neutrons. Int. J. Radiat. Oncol. Biol. Phys., 7: 185–189, 1981.

21) Cohen, L., Hendrickson, F., Mansell, J. et al.: Late reactions and complications in patients treated with high energy neutron p (66MeV) Be. Int. J. Radiat. Oncol. Biol. Phys., 7: 179–184, 1981.

資料

放医研医用重粒子加速器施設における放射化ビームラインの設計

放射線医学総合研究所物理研究部 佐 藤 幸 夫

A Design of the Radioactive Beam Line in the NIRS Medical Accelerator

YUKIO SATO

Division of Physics, National Institute of Radiological Sciences, 9-1, Anagawa-4-chome, Chiba-shi 260, Japan

(Received 20 February 1987)

Research Code NO: 200

Key Words: Radioactive beam, Wedge degrader, Super-conducting coil, Shielding of the neutrons

A design of radioactive beam line and the analysis of expected beam quality have been made. In the heavy ion cancer therapy, radioactive beam (positron emitter) can be used to verify the range of the charged particles in tissue, because the radioactive nuclei which are produced by the peripheral fragmentation of relativistic heavy ions, have a similar characteristics with the primary particles. For example, about 1 % of ^{20}Ne will be converted into ^{19}Ne (half life 17.4 S) in a 5cm thickness of beryllium target. ^{19}Ne are magnetically selected and purified from other fragments, then transported to the experimental area. To increase precision of the range measurement, the momentum spread of the ^{19}Ne beam will be reduced to ±0.2 % by a wedge degrader. Around 50 % of the primary particles pass through the target, then are deflected by a super-conducting coil and wasted at a beam dump. Other unuseful particles are stopped at slits. The shielding of the neutrons produced at the target and slits are also discussed.

1. 序

放射化粒子は一般的に、加速された粒子の原子核反応において生成される。最近、短寿命放射化ビームは原子核物理学だけでなく医学にもその応用範囲が拡がってきている〔1〕。特に、放射線がん治療の分野においてその利用が注目されている。重粒子線のブラッグピークを用いるがん治療では腫瘍部に対する高精度なブラッグピーク位置制御を必要とする。重粒子線は1点に大線量を集中させることができるという大きな長所を持つが、位置のズレがあると腫瘍部に対する線量不足を導いたり、近くの正常組織への大線量誤照射による損傷を与えてしまうからである。したがって、重粒子線治療ではブラッグピークを腫瘍部に一致させるために、腫瘍の正確な位置及び範囲の診断技術、並びに腫瘍領域への正確な照準照射を行う治療技術の確立が必要である。いままでは、主にＸ線ＣＴによる位置診断と水中でのブラッグ曲線値からの照射部位の推定の組合わせによる治療が行なわれてきたが、期待される程の信頼性が得られていないのが実情である。つまり組織の差による阻止能の違いから照射部位までの飛程の正確な計算ができないからである。特に大きな骨や空気層がある場合には、飛程の評価が難しく、位置精度が悪い。これを改善し、より良い精度を得るために、高エネルギー放射化ビームと高感度ポジトロンカメラを組み合わせて照射点を確認する新しい位置制御方法がＬＢＬで提案され、テストされている〔2〕。放医研医用重粒子加速器施設においても、^{19}Ne, ^{15}O, ^{11}C 等のポジトロン放出核種を放射化ビームとして治療・診断に用いることが計画されている。第一表にこれらの放射核種の半減期を示す。

Table. 1 Radioactive Nuclei

^{11}C	20.34 min
^{13}N	9.96 min
^{15}O	123 sec
^{18}F	109.7 min
^{19}Ne	17.4 sec

診断・治療応用の手順の1例を簡単に説明すると次のようになる。例えば、^{20}Neが治療用ビームの時は、^{19}Neを診断情報に用いることができる。高エネルギー重粒子による核破砕で生じたポジトロン放出核はその生成量が比較的多く、またその速度及び方向が母核のそれとほとんど変わらないという特長を持つ。よって、ビーム輸送系を検討する際の2次粒子は、ビームとして性質が良く、診断用ビームとして用いることが可能である。ポジトロンは体内では1mm 以内でエネルギーを失い、浮遊エレクトロンと結合して消滅する際にエレクトロンの静止エネルギーに相当する511 KeVの光子を2本互いに反対方向に放出する。したがってこの光子の飛行時間を同時計測して、その位置を求めることができる。^{19}Ne の体内停止位置が2次元ポジトロンカメラで写し出された後、^{19}Ne の入射エネルギーを吸収体により調節して（エネルギー調節は加速器側で行うことが理想である)、写し出された像の中心座標が腫瘍の中心に来るようにする。^{19}Ne と ^{20}Ne は同じ原子番号で荷電状態は同じ10価であるので、治療に最適な ^{20}Ne のエネルギー E_{20} は調整後の ^{19}Ne のエネルギーから容易に計算される。近似的には $E_{20}=19/20\times E_{19}$ である。ここで注意しなければならないことは、ブラッグピークと飛程は少々異

なるということである。治療ではブラッグピークを腫瘍に一致させる心要があるが、ポジトロンカメラは飛程を計測する。そこで、診断・治療応用の前にこの差を知り、補正してやる必要がある。Chatterjee 等の実験〔2〕によれば、ブラックピークの深さは、常に飛程より2～3mm短い。このような方法によりＰＥＢＡ（Posiron-emitting beam analyzer）と呼ばれるポジトロンカメラを用いた診断で位置精度1mmがＬＢＬが実現されている。この値は治療用診断精度として満足できるものである。さらに、^{19}Ne の半減期は短い（17sec)ので患者に与える線量を1 rad 以下に抑えた診断が可能となっている〔3〕。患者の体の表面（ビームの入口）から腫瘍部までの距離の水相当厚は、使用する放射性核種の荷電数とかエネルギーには依らないので、治療用粒子の種類が何であろうと、常に半減期の短い ^{19}Ne を診断用に使用することも可能である（但し、腫瘍部位が適当な位置にある場合)。しかし、これは加速器側で、異なる粒子及びエネルギーに対する加速条件の切り換え時間が十分短いことが必要条件となる。将来の加速器の改良項目として重要であろう。

現在、ＬＢＬにおいて 10^9～10^{10}個/パルス（0.25Hz）の ^{20}Ne が1次ビームとして供給され、10^7～10^8個/パルスの ^{19}Ne が生成されている。実験の経験によれば、ビーム強度があと100 倍増加すれば、ビームの性質の良い部分を選んで利用できるので、非常に良い結果が得られることが分っている〔4〕。また、放射化ビームの最も有効な利用の一つはがんの直接治療である。これは治療中に照射点の情報を直接入手できるメリットがあるが、生成効率から考えて、診断用の100倍のビーム強度を必要とする。つまり放射化ビームの有効利用のためには、1次ビーム強度が大きいことで重要である。その他の医学利用としては、重粒子を直接体内に打ち込み、体内を通過する重粒子が体内組織の原子核と反応して生成した放射性核種をポジトロンカメラで診断する自放射化法（Autoactivation）や生成した放射性核種の体内移動を測定して、各種臓器の生理的機能を調べること等のトレーサーとして応用できる〔5〕。以上のような放射化ビームの医学利用の要請に応える目的で行われた本研究は、1）放射化ビーム生成法、2）放射化ビーム輸送系の設計例、の2つから構成されており、最後に設計例に対対する考察より、1）放射化ビームの性質、2）輸送系設計のポイントをまとめる。

2. 放射化ビーム

1）放射化ビーム生成法

加速器はＰＩＧ型イオン源とＥＣＲ型イオン源、ＲＦＱ及びアルバレリニアックからなる入射系とシンクロトロンによる主加速器から構成されている。第1図〔6〕にその全体図を示す。この施設には $15\times35\mathrm{m}^2$ 程度の面積の放射化ビーム利用室が用意されている。

放射化ビームは通常、高エネルギー重粒子の周辺原子核反応により、核子をいくつか失った破砕核の2次粒子の一部〔7〕として生成される。その様子を第2図に示す。入射重粒子が高エネルギーの場合、1次ビームと比較してあまり大きくないエミッタンスを持つ2次ビームを生成できることが知られている。必要とする破砕核が生じるターゲットの中の確率をＰとすると、断面積 σ は、入射核の質量数を Ai，ターゲットの質量数を At とした場合 Bradt-Peters の式として、

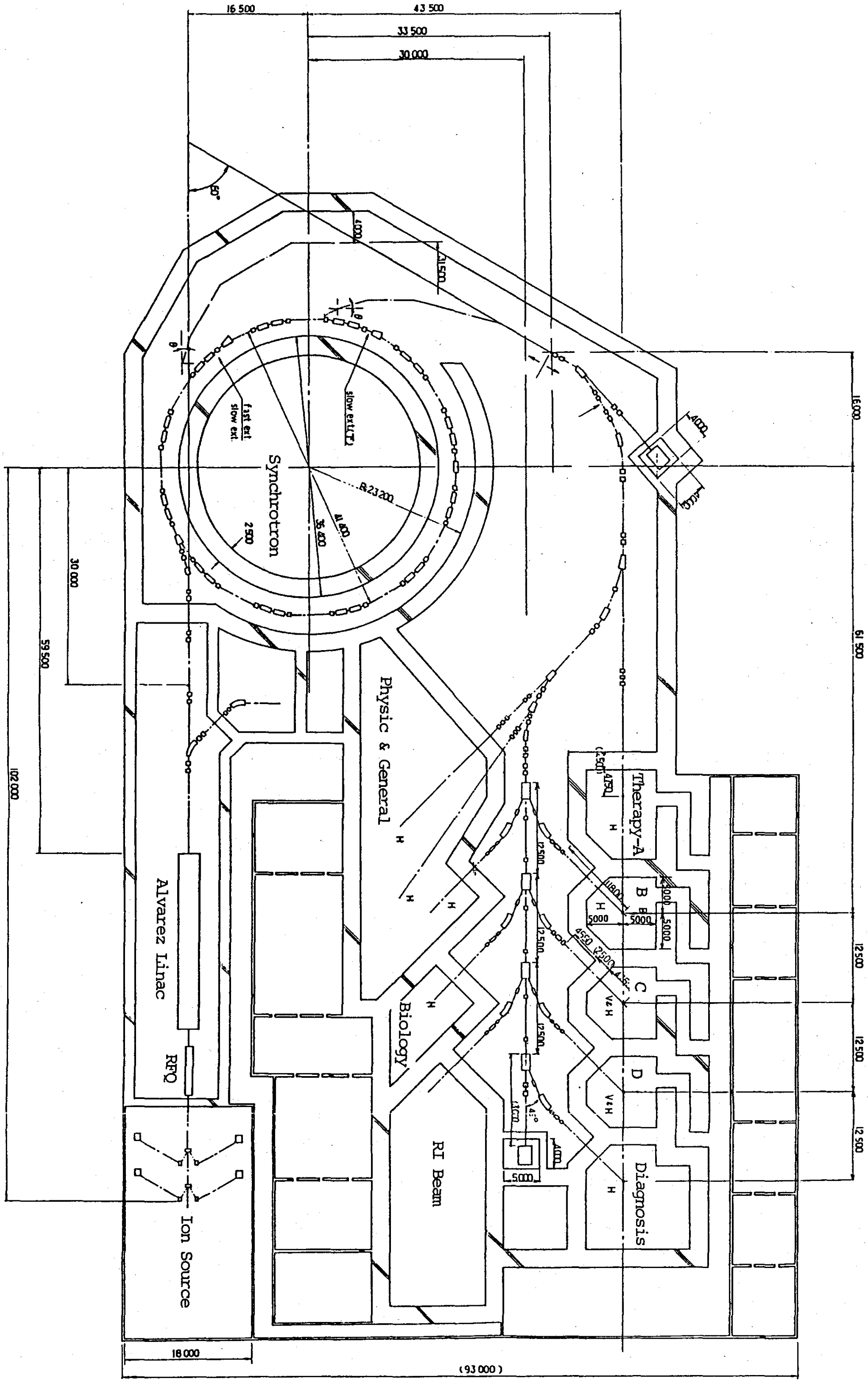

Fig. 1 Medical Heavy Ion Accelerator Facility

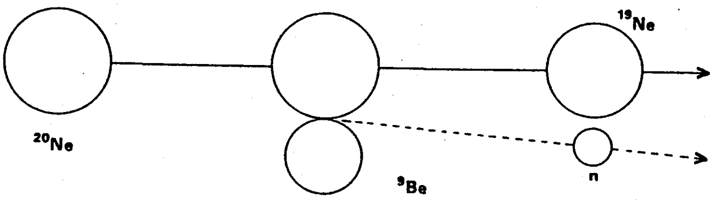

Fig.2 Peripheral Fragmentation

$$\sigma = P \cdot \pi Ro^2 (Ai^{1/3} + At^{1/3} - b)^2 \quad \cdots\cdots (1)$$

と表せる。Ro = 1.45 × 10^{-13}cm、 b = 1.7 である。

高エネルギー領域における周辺核破砕の断面積は詳しいデータが少ないが、Tobias 等がBeターゲットを用いて ^{14}Nから ^{11}Cの生成する確率として、P = 0.03〔8〕を得ている。ポジトロン放出核は、全核反応中の周辺核反応で生成されるので、質量数（Ai）が大きくなれば、Pは減少すると考えられる。そこで ^{19}Ne 生成確率としてP = 0.02 を想定し、Ai = 20, At = 9 とすると σ = 14mb 程度になる。衝突確率Qは単位面積あたりのターゲットの原子数をNとすると σ が一定（厚さの関数でない）として、

$$Q = N \cdot \sigma \quad \cdots\cdots (2)$$

と表せ、2次粒子生成率を表す。例えば、5 cm厚のBeターゲットに対しては、N = 0.7・10^{24}であるので、σ = 14mb とするとQ = 1％となる。又、LBLでの経験〔9〕からも5 cm 程度以上の厚さのターゲットを用いれば1次ビームに対する 10^{-2} のオーダーの2次ビーム生成率が得られることが分かっている。全核砕断面積は約800mbであり、全衝突確率は56％となる。つまり5 cm厚のBeターゲット中において、入射粒子（^{20}Ne）の半分が何らかの核反応を起こし、約1％が必要な短寿命放射化粒子となる。又、残り半分の粒子が入射核と同じ状態で通過する。

400 ～ 500 MeV/u 以上のエネルギー領域では、核反応過程における2次ビームの横方向の拡がりは普通の加速器のビーム輸送系で考慮するビームの拡がりで十分受け入れられるものである。このことは、2次ビームラインの設計方針が今までの 100 MeV/u 以下の領域（リングサイクロトロン等）を考えてきたものとは異なることを意味している。一般的には、2次ビームラインの設計が容易になり、上記の55％の不用粒子と44％の1次粒子の捨て方及び中性子に対する遮蔽が一番の問題になると言える。2次ビームの性質を決める最も重要な要素は、核反応を起こさせるターゲット中でのエネルギー損失にある。この過程における、エネルギーの拡がりと放出角の拡がりが、後に述べるビームライン設計のパラメータとなる。放出角の拡がり $\Delta\theta$ はターゲット中での多重散乱（Coulomb Scattering）による拡がり $\Delta\theta_1$ と核反応過程（Fermi Motion）における拡がり $\Delta\theta_2$ の和で表される。高エネルギー領域での $\Delta\theta_1$ は非常に小さいが、500 MeV/u の ^{20}Ne の入射ビームを2 cm 厚のAlターゲットに当てた場合の散乱角（θ/e） 4.5 mrad〔10〕から外挿して5 cm

厚に対しては8 mrad 程度であり、無視できない。この材質をBe とすると$\triangle\theta_1$として2～3 mrad 程度と推定される。Alonso のデータ〔11〕によれば、500 MeV/u の^{56}F 粒子の1次ビーム入射（Be ターゲット）に対し、2次ビームの$\triangle\theta_2$は2 mrad と推定できる。ここでは、この値を採用して、$\triangle\theta$=3mrad（$\triangle\theta_1$）+2mrad（$\triangle\theta_2$）＝5mrad とする。一方エネルギーの拡がり△Eはターゲット中を通過する時の1次ビームと2次ビームエネルギー損失の差$\triangle E_1$とエネルギー損失の統計的なふらつき（Straggling）による拡がり$\triangle E_2$の和で表される。$\triangle E_1$は、ターゲット厚をd、密度ρ、1次ビームと2次ビームの阻止能の差を△S、1次ビームの阻止能をSとして、

$$\triangle E_1 = d\rho \cdot \triangle S \quad \cdots\cdots(3)$$

と表せる。

また、$\triangle E_2$は通過イオンの原子番号をZ とした場合に、原子番号の小さい材質のターゲットに対して近似的に

$$\triangle E_2 = 1.8z\sqrt{d\rho} \quad \cdots\cdots(4)$$

と表せる〔12〕。

これを通過粒子：^{19}Ne, ターゲット：Be, ターゲット厚：5 cmとすると、$\triangle E_1$ = 9.2 MeV/u 、$\triangle E_2$ = 5.3 MeV/u となり△Eは約14.5 MeV/u 程度と評価できる。ターゲット通過後のエネルギーE_oは1次入射エネルギーをE_iとして、

$$E_o = E_i - S \cdot d \quad \cdots\cdots(5)$$

と表せる。S =20MeV/u/cm であることからE_i= 500MeV/uとするとE_o= 400MeV/uとなるので$\triangle E / E_o$= 3.6％となり、運動量幅にしては±0.9％となる。人体中での2次粒子ビームの飛程曲線を鋭くし、診断の精度を上げるためには、運動量の拡がりは小さい程良いのでウエッジデグレーダを用いてこの拡がりを補正する必要がある〔11〕。エネルギーの拡がりの分布は、後にビーム輸送系を検討する際の重要なパラメータの1つである。ターゲット中における1次ビームと2次ビームのdE/dx が異なることと、ターゲット中のあらゆる点における核反応の確率が一定であることを考え合わせると分布の山がフラットに近いことが推定される〔11〕が、実測データでは、ガウス分布に近いようである〔13〕〔14〕。もちろん、この拡がりはターゲットの厚さ及びその中でのエネルギー損失に依存する。以上の事からターゲット中での dE/dx を小さくし、2次ビームの多重散乱を少なくするためには、ターゲットとして原子番号の小さい材質を使うべきであることが分かる。そこで放射化も小さい Be を使うことにする。LBLでのテストによれば、厚さ15 g/cm^2 の Be ターゲットを用いて

^{12}Cから^{11}Cを生成する際に400 MeV/u の1次ビームの約1.8％が2次ビームに変換されている。この時の2次ビームのサイズはBevalac のビームラインのアクセプタンスを十分満足する程小さい。鉛のターゲットを使用した場合、その生成量は1/4に低下し、多重散乱は2倍になることがAlonso等の実験で確かめられている〔15〕。しかし、この^{11}Cのビームの性質は、平均エネルギー350MeV/uにて$\triangle\theta=12$mrad、$\triangle P/P=\pm 2$％とあまり良くなく、輸送効率は30％であると報告されている。これは収率を上げるためにターゲットの厚みが大きい（8cm）からである。放医研のビームライン設計方針としてはターゲットを少しうすくして、2次粒子生成効率の低下した分をビームの性質の向上による輸送効率改良で補う方法を採用すべきである。これにより無駄な放射化や輸送系建設のコスト上昇を押さえることができる。

2）ビーム輸送設計例

放医研における放射化ビームラインの設計においては、1）混じりの無い単一の同位体を小さいエネルギー幅及び小さいビームスポットで精製すること、及び2）1次ビームをうまく捨てて、ビームラインの保守・管理を容易にすることの2つが基本的な考え方である。本設計例では、使用可能な放射化粒子の中で最も分離が難しく、半減期が短いことから使用頻度が最も高いと思われる^{19}Ne について、決められた面積に収まるように検討する。上記の条件を満足する概念設計の例が図3に示されている。基本的には運動量の分散を持つ系を対称に接続して、全体としてはアクロマティックな系とする。途中の集束点で運動量スペクトルを得て、スリットで必要な2次ビームだけを選択するようにする。ウエッジデグレーダで運動量の拡がりを補正した後さらに2ケ所のスリットを用いて、望みのビームサイズに調整できるようにする。1次ビームはマグネティックチャネルで偏向され、ビームダンプ室へと導かれる。1次ビームの性質はターゲット通過時の散乱による影響や運動量幅の増加が小さいので、ビーム輸送上の問題はない。1次ビームの偏向に対して、電界による方法は無理である。なぜなら400 MeV/u の1次粒子を偏向するために必要な磁束密度1Tに相当する電界は2000KV/cmであり、形状、真空度、電極材質にも依るが、およそ現実的に可能な数値の10倍に達するからである。2次ビームは2本のコースに分け、1本を診断実験に、残りの1本を放射性核種の発生断面積測定や寿命測定等の基礎実験に利用できるようにする。尚、重イオン核反応で生成される種々の粒子は広い質量分布を持つており、分離して捨てることができない。大部分は、S_1、S_2で失なわれるので、局所的にS_1、S_2に対する特別の遮蔽が必要である。実用的にはS_1、S_2を鉛で、さらに周囲を1～2m厚のコンクリートで遮蔽することが良いと思われる。又、ターゲット前方へは少なくとも核反応粒子数（入射粒子の約半分）以上の中性子が放出されるので、ここへコンクリート厚2m程度の遮蔽が必要である。S_2前方へも同様の中性子用遮蔽が必要である。各電磁石はエネルギー800MeV/uの粒子の実験に対応できるようにするため、偏向電磁石は偏向角22.5°、曲率半径6m、ギャップ6cm、最大磁束密度1.6Tに、又Q電磁石は磁束密度勾配10T/m、磁極長40～80cm、ボア半径6cm の仕様とする。ただし最初のQ電磁石（DQ_1）は、ここでの運動量幅±1％ビームの分散が9mmもあり、

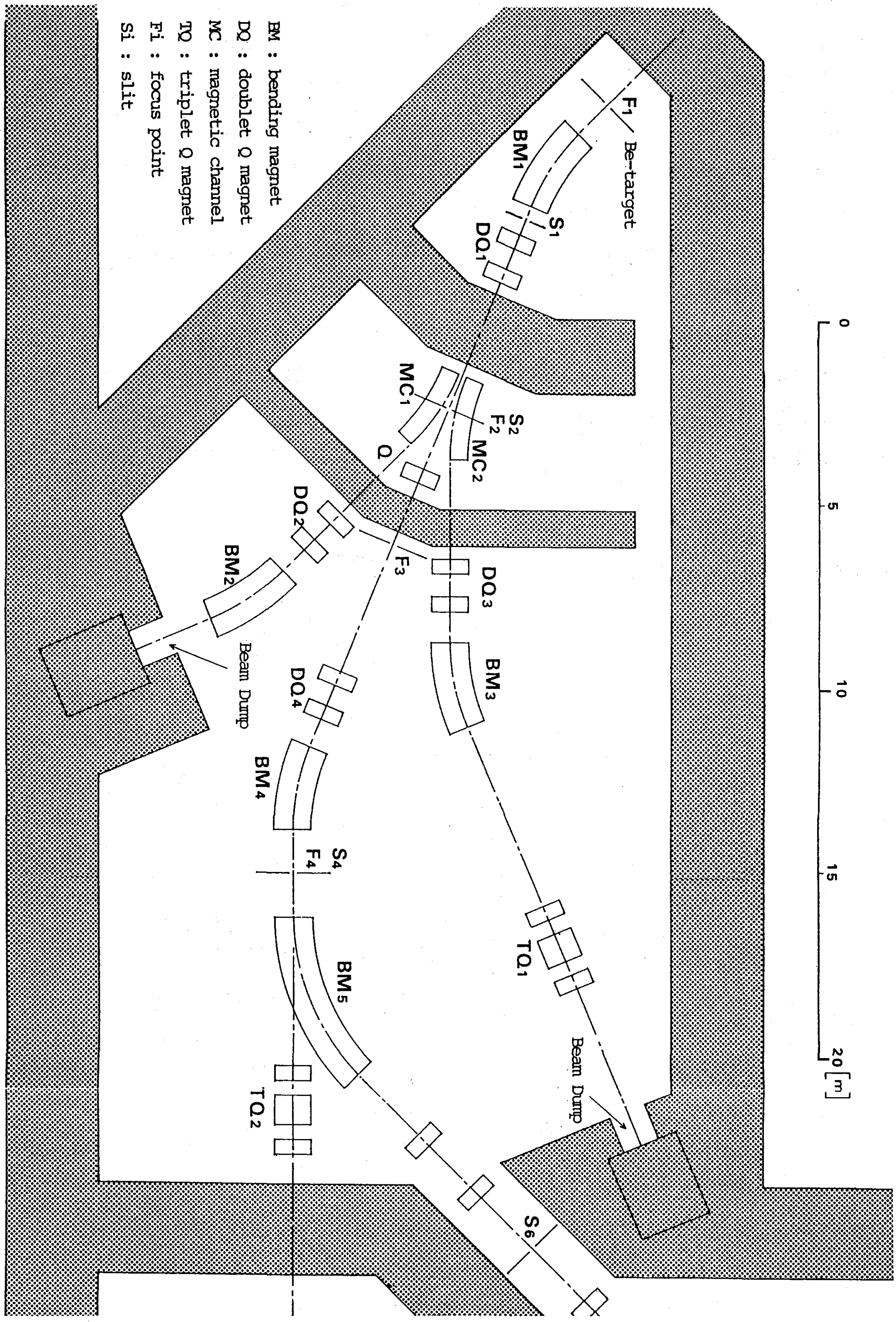

Fig.3 A Design of Radioactive Beam Line

運動量差10％（^{11}Cと^{12}Cのリジディティーの差）ビームに対しては分散が9cmに達するので、^{12}Cを通過させてビームダンプに捨てるためにボア半径を10cm程度に設計する必要がある。マグネティックチャネルの設計については、設置場所での1次ビームの分散が10cm（^{19}Ne と ^{20}Ne の差）程度であることからこの間の有効スペースは5～6cm は取れるので十分製作可能と思われるが、スペースが非常に小さいので超電導型のマグネティックチャネルを設計する必要があるだろう。さらにこのマグネティックチャンネルを2～3分割して独立に水平方向に駆動できるようにし、^{12}C等のような軌道の異なる粒子の軌道修正にも対応できるようにする。又、同じ設計のマグネティックチャネルを2台設置し、1台は中性子の少ない同位体残り1台は中性子の多い同位体の実験に使用する。そして通常は励磁を逆にして、漏れ磁束の補正を行う。この超電導マグネティックチャネルの開発は、将来ターゲットを上流側において全ての照射室に2次ビームを導く際に、ビーム輸送系での放射化を最小限に押さえるために是非とも必要である。以上の系のビームエンベロープと△P/P＝1％運動量分散を図4に示す。計算の条件として、1次ビームのターゲットにおけるスポットサイズを10mm φ（α＝O、η＝η'＝O）、エミッタンス増加を2.5倍とした。

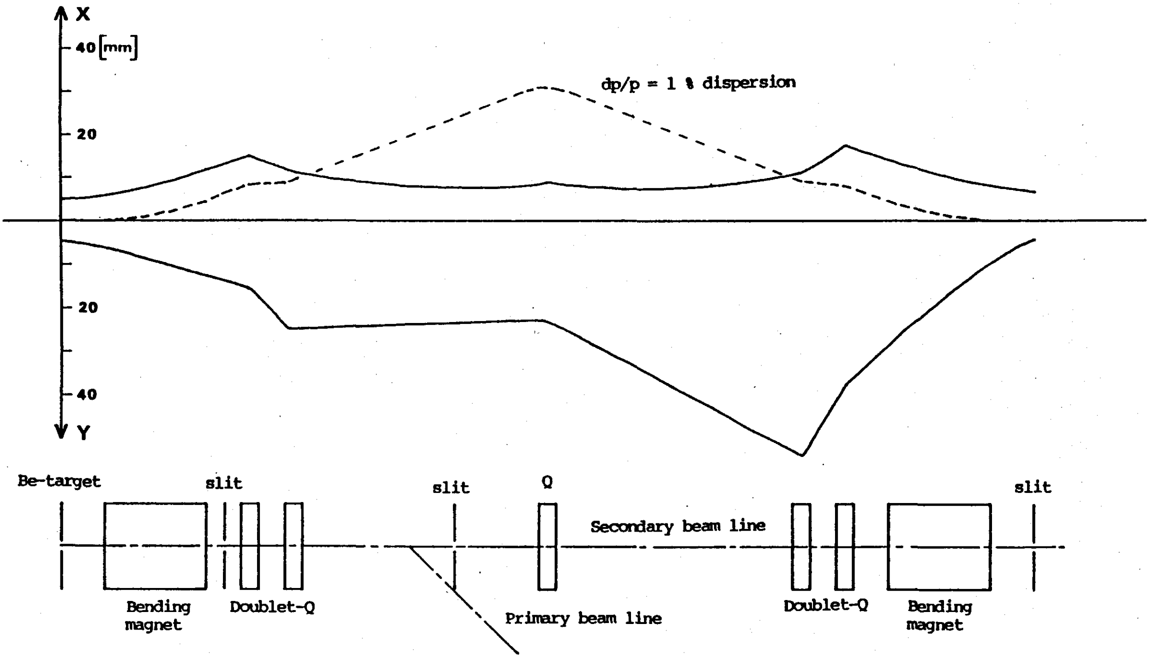

Fig. 4　Beam envelope and dispersion

3）設計例に対する考察

2次ビームにおける散乱等によるある程度の角度拡がりは避けられないが、この拡がりによるエミッタンスの悪化を最小限にするために、ターゲットはアクロマティックなビーム集束点（ビームサイズを一番小さくできる点）に置かれるべきである。この点をF_1とする。^{20}Ne のエネルギーは2次ビームで必要なエネルギー400 MeV/u とターゲット中でのエネルギー損失から推定して500 MeV/u

が予定されており、エミッタンスは7πmm・mradと想定する。本装置に対する仕様条件として、取り出しビームの性質はエミッタンスがX、Y共に7πmm・mrad、△P/Pが±0.2％である。また、このエネルギー領域でのターゲット中の角度の拡がり増加分は5mrad 程度と想定される。もし、ターゲットがビームスポットサイズ10mmφのビームウエイストにおかれているとすると、ここでの角度の拡がりの最大値は±1.4mrad（ε/X）であるので、合計値は±6.4mradとなりエミッタンスの増加は、4.6倍である。ビームウエストのスポットサイズが5mmφにできれば、エミッタンスの増加は小さくなり、2.8倍程度に押えることができる。図5に、この様子を示す。実際にビームスポットサイズを5mmφ以下にすることは可能である。この程度のエミッタンス増加であれば2次ビームラインは1次ビームラインと同様の設計でもスリットを適所に用いることによりビーム輸送は可能であるが、ビーム輸送効率の向上とLBLにおける不安定核の実験の経験〔16〕より2次ビームラインのアクセプタンスが大きい方が実験しやすいので、2次ビームラインのダクト径は1次ビームラインのそれより大きめに設計し100mmφとする。前節でも述べたようにターゲット通過後のエネルギーの拡がりは±1.8％、運動量の拡がりにして±0.9％であったので、1次ビームが本来持っている運動量の拡がり±0.2％を加えて合計±1.1％と評価できる。この値はビーム輸送上、問題がある数値ではないが、医学利用のためにはできるだけ小さくする必要がある。

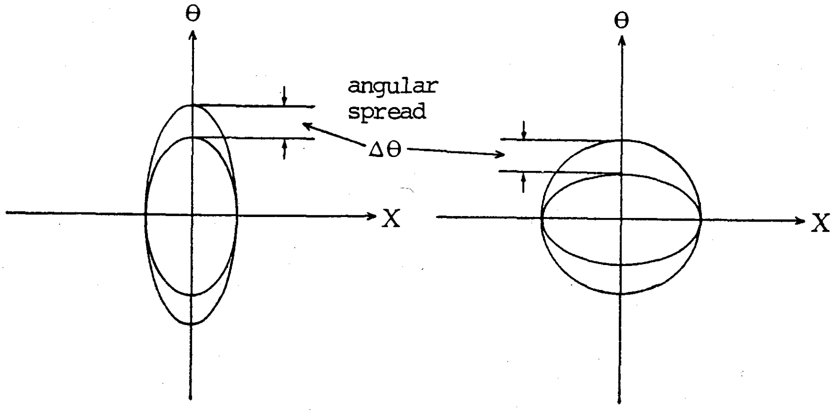

Fig. 5 Emittance Growth at Target

ここでBe ターゲット中の熱損失について検討しておく。予定されている最大仕様値の^{20}Ne のビーム強度は1.6×10^{8} P/secである。である。熱損失P〔W〕はビーム強度をI〔A〕、エネルギー損失をE〔eV〕とすると

$$P = I \times E\ [\mathrm{W}] \quad \cdots\cdots (6)$$

と表せる。

$I = 2.6 \times 10^{-10}$ A、$E = 100$〔MeV/u〕× 20〔u〕= 2×10^{9}〔eV〕よりP = 0.5 Wとなり、この条件では水冷却は特に必要ないが、温度上昇を防ぐために間接的に冷却した方が良い。また将来ビーム

強度100倍までを考慮すると、P＝50Wとなり、水冷却が必要となる。

2次ビームの分離精製のためには、F_2での分散を大きく取ることが望ましい。したがって、分散を消す方向に働くQ電磁石はラインの途中に使用すべきではない。分散を生む偏向電磁石に、集束作用を持たせたエッジ集束型の電磁石が望ましいが、この型の電磁石は入射ビームの性質の変化に対して調節機能に乏しい。解決策として、Q電磁石を偏向電磁石にできるだけ近接して取り付け、エッジ集束電磁石の機能を持たせて分散を大きくすることが考えられる。又、偏向電磁石内でのビームサイズを小さくし、Magnifying Power を大きくして分散をかせぐために、ターゲットは偏向電磁石に近い所へ置いた方が有利である。リジディテイーの分離能力目標値を1％とすると、F_2での 運動量幅＝0のビームのX方向全幅が16mmであると想定されることから、F_2において1％の運動量当たり20 mm 程度の分散が必要である。この場合、^{20}Ne と5％の差がある^{19}Ne に対しては、かなり良い精製ができる〔17〕。偏向電磁石は高エネルギービーム輸送系に用いられている電磁石と同じものを用いて、偏向角は22.5°とする。以下に分離の過程を説明する。F_2 にスリット（S_2）を置くことにより、同じ値の p/A を持つ粒子族が選択される。^{20}Ne と ^{19}Ne の F_2での分離は10 cm（^{12}C と ^{11}C の差は20cm）もあるので、F_2の前のダクトは横拡がりのチエンバー型式とし、^{20}Ne ビームがダクトにあたらないように設計する。次に S_2 を通過した一族は、ウエッジデグレーダを通ることにより、そのエネルギーの拡がりが補正される。デグレーダ材質としては加工性に優れ、散乱の少ないポリエチレンを使用する。ここでデグレーダ通過による運動量幅補正を推定してみる。400 MeV/u の^{19}Neのポリエチレン中の阻止能は核子当たり14.8 MeV・cm^2/g である。密度が0.9g/cm^3 であるので1 cm 当たり13.3 MeV/u のエネルギーを失うことが分かる。ウエッジデグレーダは17.6 MeV/u（△P/Pで±1.1％に相当する）のエネルギーの補正をすれば良いので、三角形のデグレーダの幾何学的条件として、厚さの差（底辺）＝17.6/13.3 = 1.3 cmであれば良い。一方F_2で1％の運動量で20mmの分散があるので、運動量の拡がり±1.1％の粒子はスリットの中心のまわりに±22mmで拡がっている。よって、図6のような角度17°程度（$\tan^{-1}$13/44)ウエッジデグレーダを設置すればこの運動量の拡がりが補正できることになる。しかし、これは粒子の全てが軸上にあると仮定した場合であって、実際は横方向に拡がりを持っているので、補正値には限界があり、X、Y、Z方向の6次元位相空間で、この補正を評価する必要がある。Z（縦）方向は運動量の位相空間であり、直接運動量の拡がりに対応している。ビーム輸送光学上は、このウエッジデグレーダによる補正は縦方向のエミッタンスを横方向(X)のエミッタンスに変換することを意味している。（一般にエミミタンスは横方向エミッタンスを指す）。F_2で運動量幅＝0と仮定した時のX方向ビームサイズが16mmと推定されるので、F_2での±1.1％運動幅のビームのX方向全幅は60（44＋16）mmである。よって、この変換でビームサイズが約3.75倍（60/16）になり、X方向エミッタンスが、3.75倍になったことが分かる。6次元位相空間における体積は不変であるから、運動量幅が1/3.75 すなわ±0.29％まで減少できることが分かる。ウエッジデグレーダ通過前、通過後の運動量の拡がりを、△Pi/Pi, △Po/Po〔％〕とし、通過後の運動量幅＝0及び1％のビームに対するX方向ビーム全幅

及び分散をX、d〔mm〕とすると運動量の拡がりの関係は次のように表せる。

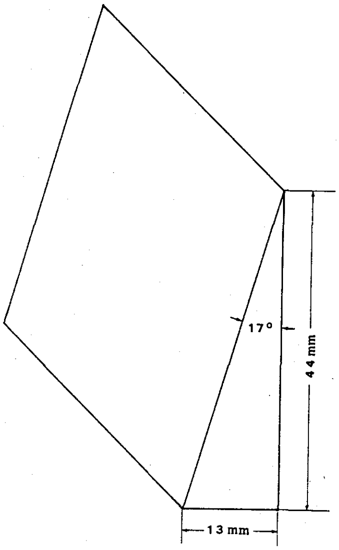

Fig. 6 Wedge Degrader

$$\frac{\triangle Po}{Po}=\frac{X}{X+\dfrac{\triangle Pi}{Pi}d}\ \frac{\triangle Pi}{Pi}\ \cdots\cdots\cdots\cdots\cdots\cdots\cdots\cdots\cdots\cdots(7)$$

この式から、運動量を小さくするには系の分散を大きくし、デグレーダ直前でのビームサイズを小さくすれば良いことが分かる。そこでスリットでビームを絞ることが効果的と言える。実際にはデグレダ直前のS_2のスリット幅を全ビームサイズの1／2の30mm程度にしても、運動量の拡がりがガウス分布であると想定されることによりビームの大部分はこの中に入ると思われるので、ビーム損失を最小にして、かつここでのX方向エミッタンス増加を2倍程度に押さえて、ビームを輸送できる。この場合、スリット直後（ウエッジデグレーダ直前）の運動量の拡がりは、

±1.1%×(30—16)/44=±0.32%になっているので、(7)式を用いると、ウエッジデグレーダ通過後の運動量の拡がりは±0.17%まで減少できることになる。しかし、実際の試験テストにより調整すべきである。以上の様子を7図に表す。図中、β(d/X)=2.5の点線は、本設計例を表しており、スリットを用いることが有効であることを示している。又、分散を1.6倍にして$\beta=4$とすれば、全ビームを±0.2%に押えることができることが分かる。

デグレーダの熱損失は非常に小さく、将来のビーム強度100倍増を考慮しても0.1W以下であるが、空冷による冷却程度は微小部分の損傷を防ぐために必要であろう。放射線によるダメージはデグレーダがS_2直後に設置されることから長期的には問題になる。また、平均6.5mm厚のポリエチレン中での散乱を1mrad程度と想定するとエミッタンス増加は、X方向で2倍程度、Y方向で3倍程度と推定される。このようにして、F_4において^{19}Neを集めた後は下流のビームラインでは分散は消されているので、コリメータの併用でF_5に十分小さいスポットビームを得ることができ、高品質ビームと

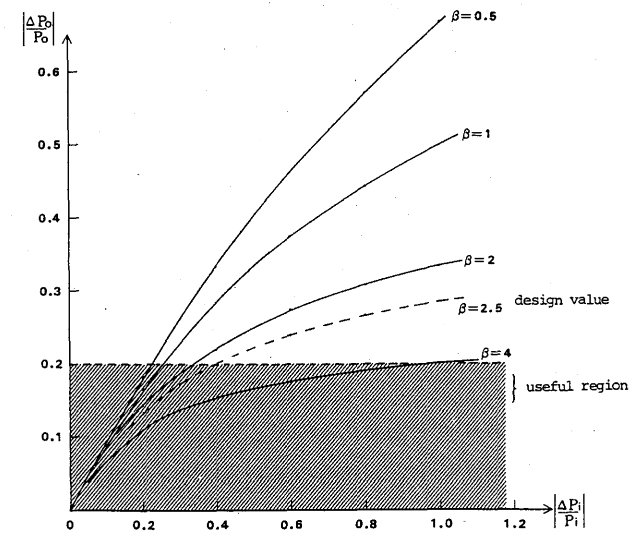

Fig. 7. Momentum spread reduction by a wedge degrader

$\Delta P_i / P_i$: momentum spread before a wedge degrader

$\Delta P_o / P_o$: momentum spread after a wedge degrader

β : ratio of the beam size, X, to the dispersion per percent, d, (d/X)

して医学に利用できる。前にも述べたようにブラッグピークと飛程の差はエネルギーの拡がりだけでなくビームサイズにも依存するので、医学利用としてはこの種のテストも行う必要がある。F_4においては、重イオン核反応で多種の不安定核が生成されることから ^{17}F 等のように、q 値も近く q/A 値が ^{19}Neに非常に近い粒子が分離されず混じる可能性がある。^{17}F と ^{19}Ne はq /A値が0.3％しか違いはない。ポリエチレン中における400 MeV/uの ^{19}Ne, ^{17}F の阻止能は各々8.3 MeV/u/cm, 10.8 MeV/u/cmであり、その差は2.5 MeV/u/cm しかない。平均厚6.5 mmのウエッジデグレーダ通過後の限止能の差は1.6 MeV/uであり△/ Eで0.4％、△±P / Pで±0.1％であり、とても分離できない。そこでウエツジデグレーダの直後に3.5 cm厚以上のポリエチレン平行板デグレーダを設置し、合計の阻止能の差を△P / Pで±0.6％以上とすれば、S_4 スリットにより分離可能であろう。そしてこの平行板デグレーダーとウエッジデグレーダを独立に交換できるように設計し S_4 スリットとの組合わせにより、高精度な分析を行って、単一粒子を最小のエネルギー幅、及びスポットサイズにして F_5 に集め、医学利用及び不安定核の研究等の基礎研究も利用できるようにする。ただしこの場合のビーム強度は、スリットをしぼった分だけ低下することは避けられない。^{19}Neのような不安定核の核物理研究はLBL等で最近始まったばかりであり、不安定核半径が必ずしも $A^{1/3}$ に比例しないこと等が見い出されている。例えば、^{11}Li が特別大きい核半径を持つことが発見されており、核の性質について新しい考え方が求められている〔18〕。核破砕断面積や寿命等の基本量測定は放射化粒子の医学利用のために欠かせない。

3. 結　　論

設計側に対する考察から以下の結論が導かれる。

1） 2次粒子の性質と生成量

(イ) ターゲット材質はBeが適当である。

(ロ) エミッタンス増加を最小限に押さえるために、ターゲットは可能な限り小さいビームスポットの点に置く。

(ハ) 5cm厚のBeターゲットを用いることにより10^{-2}オーダーの2次粒子の収率が期待できる。

(ニ) 運動量幅の低減のためウエッジデグレーダを使うことが効果があり、スリットの併用により運動量の拡がりは±0.2％程度まで押えることができる。

(ホ) ターゲット、デグレーダでのエミッタンス増加は各々2,3倍程度であるが、スリットの併用でビーム損失及びエミッタンス増加を押さえて大部分のビームを輸送することが可能である。

(ヘ) 平行板デグレーダにより2次粒子中に混じわっていると思われる^{17}Fを^{19}Neから分離して、高いpurityを得ることが可能である。

2） ビーム輸送系設計

(イ) 5cm厚のBeターゲット中において、1次粒子の半分は核反応を起こさずそのまま通過するので、この1次ビームを分離し捨てるために、超電導マグネティックチャネルの開発が必要である。

(ロ) 2次ビーム輸送系のアクセプタンスを大きく造る。

(ハ) 1次粒子の約半分が核反応を起こし、大部分がスリットで失われるので、このスリットへの遮蔽及び中性子への遮蔽を考慮する。

又、「高品質放射化ビームの生成」及びその「医学利用及び応用の拡大」には「1次ビーム強度の増加」及び「飛程の調整機能」が必要である。これは、放医研施設における改良課題として、①イオン源におけるビーム強度の改良及びエミッタンスの低減化、②シンクロトロンの入射回数の増大によるビーム強度の改良の2つ、及び③飛程調整用としてシンクロトロンの取り出しエネルギーの連続可変及びそれに伴う高エネルギービーム輸送系パラメータの連続可変を治療側から容易に操作できる制御技術の確立が非常に重要であることを示している。将来、本ビームラインにおける基礎実験の後はターゲットを上流側において、垂直ビームライン及び水平ビームラインでの放射化ビームの診断・治療利用も可能である。

本研究に対して適切な助言をいただローレンスバークレー研究所のJ. Alonso博士、G. Krebs博士他Bevalacのメンバーの方々に厚く御礼を申し上げます。

又、本研究のために、LBLへの留学金を援助していただいた持田記念財団、及びこの研究の指導をしていただいた、放医研物理研究部の河内清光博士に感謝します。

4. 参考文献

1） Proceedings of the Workshop on Prospects for Research with Radioactive Beams from Heavy Ion Accelerators, (1984) LBL-18187.

2） A. Chatterjee, W. Saunders, et al. : Physical Measurements with High-Energy Radioactive Beams. Res. 92(1982) 230-244.

3） J. Llacer, A. Chatterjee, et al. : An Imaging Instrument for Positron Emitting Heavy Ion Beam Injection, IEEE Trans. Nucl. Sci. Vol. Vol. NS−26 №1 (1979) 634−647.

4） A. Chatterjee, Private Communication.

5） C. A. Tobias, E. V. Benton, et al. : Particle Radiography and Autoactivation. Rad. Oncol Bio. Phys. Vol. 3 (197) 35−44.

6） 三菱電機　放医研重粒子線がん治療装置　基本設計報告62年

7） D. L. Olson, B. L. Berman, et al. : Electromagnetic Dissociation of Relativistic ^{18}O Nuclei. Phys. Rev. C. Vol−24, №24 (1981) 1529−1539.

8） C. A. Tobias, A. Chatterjee, et al. : Radioactive Fragmentation of N^{7+} Ion Beam Observed in a Beryllium Target. Phys. Lett. Vol. 37A. №2 (1971) 119−120

9） J. Alonso and G. Krebs, Relativistic Radioactive Heavy Ion Beams at the Bevalac. LBL−17829, 153−158.

10） 三菱電機　放医研医用重粒子加速器概念設計研究報告　61年、　p 196.

11） J. Alonso, Source of Radioactive Ions, LBL−18958 (1985).

12） 岸田則夫、河本　進、理研リングサイクロトロンの生物・医療照射系の設計、理研報告　58 (1982) 77−91.

13） D. E. Greiner, P. J. Lindstrom, et al. : Momentum Distributions of Isotopes Produced by Fragmentation of Relativistic ^{12}C and ^{16}O Projectiles, Phys. Rev. Lett. Vol−35, №3 (1975) 152−155.

14） Y. P. Viyogi, T. J. M. Symons, et al. : Fragmentation of ^{40}Ar at 213MeV/Nucleon, Phys. Rev. Lett. Vol−42, №1 (1979) 33−36.

15） J. Alonso, A. Chatterjee, et al. : High Purity Radioactive Beams at the Bevalac, IEEE Trans. Nucl. Sci. Vol. NS−26, №3, (1979) 3003−3005

16） 谷畑勇夫、Private Communication.

17） G. Krebs, Private Communicaion, Resuls from Bevalac Experiment.

18） 谷畑勇夫、不安定核ビームの生成とその利用、全核破砕断面積の測定と核半径、日本物理学会誌　41巻　第11号、(1986) 905−908.

日本医学物理学会　第４回研究発表会シンポジウム

医学における三次元画像の利用

3次元画像処理の粒子線治療への応用

●放射線医学総合研究所　臨床研究部
遠藤真広

1. はじめに

荷電重粒子線は，非常にシャープな線量分布を形成できるため，従来，放射線治療が困難であった眼球内など重要臓器近傍の腫瘍の治療に用いることができる。しかし，その特色を十分に生かすためには，３次元的な治療計画とそれを利用した精密な治療の実行が不可欠である。このための３次元治療計画システムには，従来の単なる線量計算だけではなく，３次元画像処理技術を用いた，より多くの機能が必要である。ここでは，重粒子線治療の場合に即して，３次元治療計画システムの概要を述べることにする。

2. coplanar と non-coplanar

３次元治療計画システムを設計する際に，考慮すべき第一の問題は，ビームの入射方向を coplanar に限るか，それとも一般的な non-coplanar にまで拡大するかということである。ここで，coplanarとは入射ビームの方向がX線 CTのスライス面と平行な場合であり，non-coplanarとは平行ではない場合である。coplanar ビームを対象とした治療計画システムは，粒子線治療の場合，２次元システムの手法を応用でき，対象とするCTスライスの枚数が複数になるという量的な拡大はあっても，質的な変化は少ない。

それに対して，non-coplanarビームを対象とする場合は，２次元システムと質的に全く異なる問題となり，３次元画像処理の手法を利用する必要が生じる。non-coplanarビームは頭頸部領域などで有効と考えられていたのであるが，治療計画システムが存在しないため，従来は積極的に利用されていなかった。しかし，最近，コンピュータの性能向上と３次元画像処理技術の発展を背景として，non-coplanarビームを対象とするシステムの研究が盛んになった。ここでも，そのようなシステムについて考えることにする。

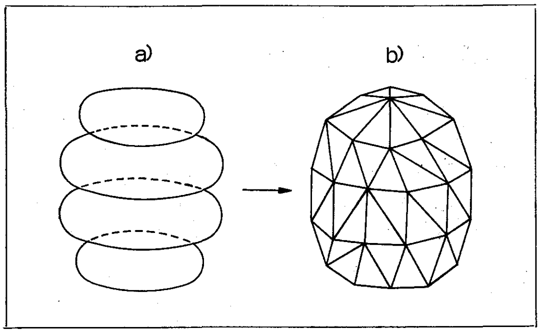

**図１　ターゲットの３次元的表現
(Chriastiansen の方法)**

non-coplanarビームを対象とする場合の最大の問題の一つは，ターゲットを３次元的に表現せねばならないことである。ターゲットの輪郭は治療計画医により，ＣＴ画像上に入力される。３次元治療計画ではこれを複数枚のＣＴ画像に対して行う必要があり，結果として**図1a**に示すような平行輪郭線群が得られる。ターゲットの３次元的な表現は，**図1b**に示すように，これに Chriastiansen の方法[1]により三角形のタイルをはり，多面体に変換することにより得られる。

3. ３次元治療計画システムの機能

３次元治療計画システムの機能としては，単なる線量計算とその表示だけではなく，以下に示すものが必要である。

(1)数十枚のＣＴ画像上へ，ターゲット及び重要臓器の輪郭を対話式に入力する。

(2)(1)で入力された輪郭群をもとにターゲットと重要臓器を3次元的に表現し，視点を色々変えて，最適な照射方向を決める。(計算機内シミュレーション)

(3)(2)で決められた照射方向に対し，コリメータ，補償フィルタを設計し，ビームパラメータを計算する。

(4)線量分布を計算し表示する。

(5)線量分布の適否を判定する。

(6)治療時の位置決めの補助となる画像（デジタル再構成シミュレーション写真）を出力する。

などである。以下，これらのいくつかについて例を用いて説明したい。

図2はターゲット及び重要臓器(左右の眼球及び脳幹)の輪郭を入力したCT画像の例である。一般に3次元治療計画では，このような画像が何十枚も得られる。

図3a, bは，平行輪郭線群からターゲットと重要臓器を3次元的に表現し，その重なり具合を視点を変えて観察するコンピュータ内シミュレーションの様子を示している。**図3a**は前後方向(coplanar)から，**図3b**は前上方，頭頂より30°の方向 (non-coplanar) から観察したものである。1の輪郭はターゲット，2の輪郭は脳幹，3と4はそれぞれ左右の眼状を示す。

コンピュータ内シミュレーションでは，これらの重要臓器とターゲットができるだけ分離される照射方向を選ぶ必要がある。**図3a, b**のいずれの方向についても脳幹(2)はターゲットの後側にあり，重粒子線治療の場合，ビームは照射されない。また，左眼(3)はターゲットから外れているため照射されない。問題は右眼(4)であるが，図よりnon-coplanar(**図b**)の方が，やや分離が良いといえる。

図2　ターゲット及び重要臓器（脳幹及び左右眼球）を入力したCT画像の例

コンピュータ内シミュレーションにより，ビームの照射方向が決まればそれを用いて線量分布を計算できる。光子治療に対する3次元線量分布計算は散乱が大きいため，その見積りに手間がかかり確定的なものがないのが現状である。重粒子線治療の場合は，散乱が非常に少ないためペンシルビームの近似が良く成り立ち，3次元線量分布が比較的容易に計算できる。ここでは，計算法についてはふれず表示法についてのみ述べる。

3次元線量分布表示の基本は，coplanar, non-coplanarとも，CT横断面との重畳表示と考えられる。これは，従来の2次元システムの表示と同一であり直観的に理解しやすく，また引き続く横断面を次々と表示することにより線量分布の立体的イメージを比較的つかみやす

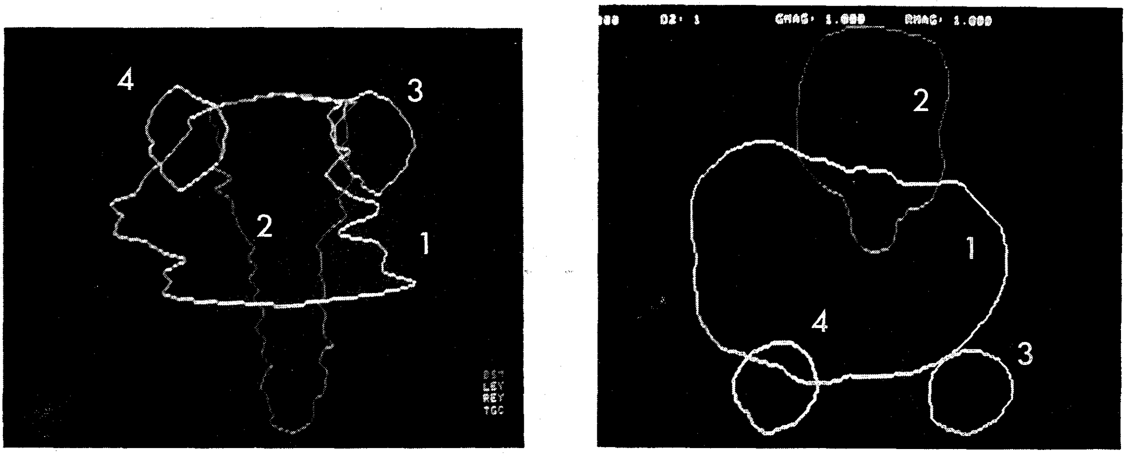

a) 前後方向 (coplanar)　　b) 前上方，頭頂より30° (non-coplanar)

図3　コンピュータ内シミュレーションの一例（1：ターゲット，2：脳幹，3：左眼球，4：右眼球）

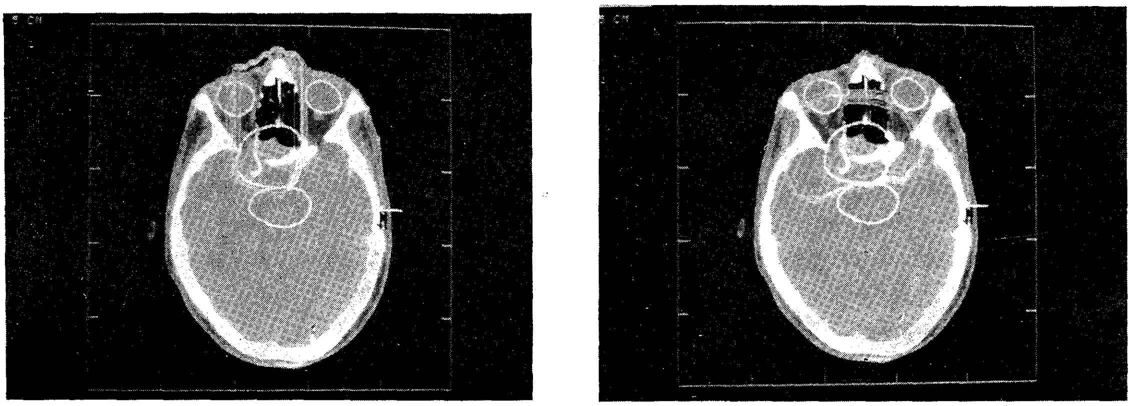

a）coplanar　　b）non-coplanar

図 4　線量分布の表示

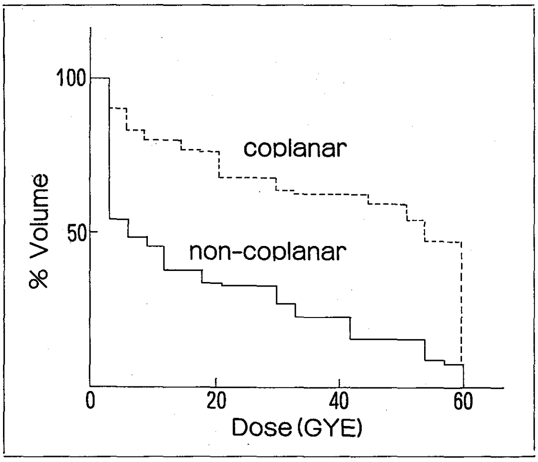

図 5　dose-volumeヒストグラム（右眼球）

い。他に冠状断面や矢状断面上での線量分布の表示，線量分布そのものの立体表示も考えられるが，著者はこれらは補助的なものと考える。

図4a, bはCT横断面と線量分布を重畳表示した例を示している。図4aは，図3aに対応する前方coplanar照射の線量分布であり，図4bは図3bに対応する頭頂より30°前方のnon-coplanar照射のものである。

3次元線量分布，特にnon-coplanar照射を含む線量分布の評価は，図4a, bに示すような線量分布図だけからは困難なことが多い。これを，定量的な観点から補完するため使われるようになったのが，dose-volumeヒストグラム2)3)（小西のdoseスペクトラム4)と同じもの）である。

図5はその例として，図3a, bの照射方向に対する右眼球のdose-volumeヒストグラムを示している。dose-vo-

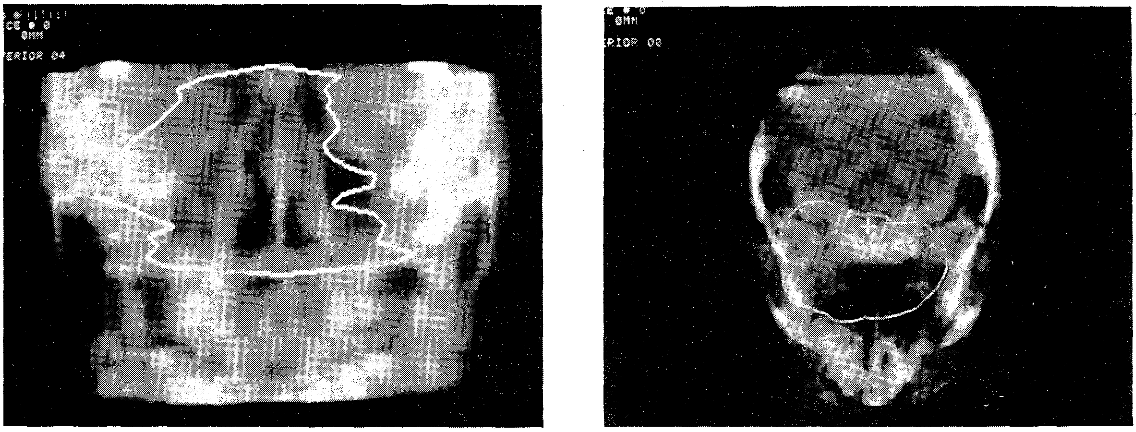

a）coplanar　　b）non-coplanar

図 6　デジタル再構成シミュレーション写真

lumeヒストグラム（積分形）とは，図に示すように，ある線量以上の照射を受ける臓器体積の百分率を線量に対してプロットしたものをいう。このような図を用いて，ある特定臓器に対する線量が定量的に評価できるため，治療計画を選択する指針として使える。例えば，**図5**については，non-coplanar照射の方が，すべての線量域で臓器体積の百分率がcoplanar照射にくらべて小さく，優れていると言いうる。これは図3のコンピュータ内シミュレーションでの結論とも一致している。

照射方向が決まり線量分布が得られれば，治療計画は一応，終了したといえる。2次元システムでは，通常，シミュレータを用いて計画通りに患者の照準を行いシミュレーション写真を撮影し，これを治療の際の位置決めに用いる。3次元治療計画システムでは，この過程を省略することを目的として，デジタル再構成シミュレーション写真の作成を行う。これは3次元CTデータを照射方向に加算し画像化したものである。**図6a, b**はその例であり，**図6a**は**図3a**に対応するcoplanarの場合，**図6b**は**図3b**に対応するnon-coplanarの場合である。図はX線像とターゲット輪郭を重畳表示し，位置決めに役立つようにしてある。

4. おわりに

以上，3次元治療計画システムの概略を重粒子線治療の場合に即して紹介した。このようなシステムの研究はまだ始まったばかりであり，ここで紹介したシステムもプロトタイプ的なものである。今後，実用化に向けていくつかの改良がなされていくものと考える。なお，本研究は厚生省がん研究助成金赤沼班（61-26）の援助を受けた。ここに感謝する。

＜参考文献＞

1) Chriastiansen HN, Sederberg TW : Comput. Graph. 12 : 187-192, 1978.
2) Chen GTY, Austin-Seymour M, Castro JR et al.: In Proc. Eight Int. Conf. on Uses of Computers in Radiation Therapy. IEEE ISBN 0-8186-0559-6, 1984, pp. 264-268.
3) Chin LM, Kijewski PK, Svensson GK et al. : Int J. Radiat. Oncol. Biol. Phys. 7 : 61-70, 1981.
4) 小西圭介：日本医放会誌　31 : 810-824, 1971.

RADIATION RESEARCH **113,** 334–345 (1988)

Radiosensitivity of Late Recurrences following Radiotherapy of Murine Fibrosarcomas

KOICHI ANDO,* SACHIKO KOIKE,* MIKIO SHIKITA,† ISAMU HAYATA,‡
HIROSHI OTSU,§ AND SHINICHIRO SATOH*

**Division of Clinical Research, †Division of Pharmaceutical Sciences, ‡Division of Radiation Hazard, and §Division of Physiology and Pathology, National Institute of Radiological Sciences, 9-1, 4-chome, Anagawa, Chiba-shi, Chiba, Japan 260*

ANDO, K., KOIKE, S., SHIKITA, M., HAYATA, I., OTSU, H., AND SATOH, S. Radiosensitivity of Late Recurrences following Radiotherapy of Murine Fibrosarcomas. *Radiat. Res.* **113,** 334–345 (1988).

Radiosensitivity of late recurrent tumors which emerged after radiotherapy was investigated. Tumors observed were fibrosarcomas. Recurrences emerged in the irradiated area approximately 200 days after a 50% tumor control dose of radiation of ^{60}Co γ rays or mixed irradiation with fast neutrons and γ rays. The recurrent and radiation-induced tumors were differentiated by karyotype analysis. Once transplanted into fresh mice, the recurrent tumors grew more slowly than the original tumor. Tumorigenicity of the late recurrences was lower than that of the original tumor. Radiosensitivity of the late recurrences, which was examined using methods to assess control, tumor growth delay, and colony forming assays, was significantly higher than that of the original tumor. D_0 values of hypoxic tumor cells were significantly smaller in two of the three recurrences compared to the original tumor. Oxic cells, when irradiated *in vitro,* also showed smaller D_0 values for the recurrent tumors than the original tumor. Hypoxic cell fractions were between 0 and 14% in the late recurrences and 10% in the original tumor. These results are consistent with the hypothesis that radiotherapy causes mutation of tumor cells which results in increased radiosensitivity of surviving tumor cells.

INTRODUCTION

Cultured mammalian cells regrowing after a large radiation dose are more sensitive to ionizing radiations than the original cells (*1*). This increased radiosensitivity is hereditary and is associated with various changes in biological characteristics. These cells formed smaller colonies than the original cells. The mean colony size decreased with increasing radiation dose. The doubling time of the regrowing cells was longer than that of the original cells. Chromosome number changed from representing a mainly diploid population to having characteristics of highly polyploid populations along with a broadened distribution with respect to chromosome number.

In an animal tumor study, the TCD_{50} (the radiation dose necessary to yield a local control in one-half of the irradiated tumors) of a tumor which recurred late after a large radiation dose (TCD_{95}) was reported to be smaller than the TCD_{50} of the original tumor (*2*). We have also observed that a murine fibrosarcoma which recurred after a mixed neutron and γ-ray radiotherapy was also more sensitive to γ radiations (*3*). These observations have confirmed that mammalian cells irradiated heavily become

0033-7587/88 $3.00

more sensitive to subsequent irradiation than the original cells. It is likely that a large radiation dose caused a mutation in the original surviving cells, resulting in the increased radiosensitivity observed.

In this report, we have further studied, along with radiosensitivity, the size of hypoxic cell fractions and the oxygen enhancement ratio (OER) of tumors which recurred late after large radiation doses in a series of neutron RBE experiments. The late recurrences most likely arise from a single tumor cell.

MATERIALS AND METHODS

Animals and Tumors

The original tumor was the 17th generation isotransplant of a fibrosarcoma which arose spontaneously in a C3Hf/Kam female mouse at the Department of Experimental Radiotherapy, M. D. Anderson Hospital and Tumor Institute at Houston, Texas (*4*). Animals were 8- to 12-week-old C3H/HeMsNrsf male mice. The NFSa tumor is weakly immunogenic in its syngeneic host (*4*). Mice received an intramuscular injection of 10^6 tumor cells to the right hind legs. The procedure used to prepare single cell suspensions by trypsin has been described elsewhere (*5*). Viability of tumor cells usually exceeded 95% under phase-contrast microscopy. Cell clumps were less than 1% of the total number of cells counted.

Late recurrences were obtained following radiotherapy of the NFSa fibrosarcomas in the legs. Three tumors were examined: the R1137 tumor emerged 198 days after a single γ-ray dose of 90 Gy; the R1260 tumor emerged 200 days after a mixed-beam scheme of two fractions of neutrons (8 Gy each) and three fractions of γ rays (22 Gy each); and the R1268 tumor recurred 180 days after a mixed-beam scheme of two fractions of neutrons (6 Gy each) and three fractions of γ rays (22 Gy each). When the recurrences reached approximately 15 mm in diameter, tumors were removed and cut into halves with scissors. One half of the tumor was put into a 10% formaldehyde solution and processed for histological examination. The other half was further minced with scissors and transplanted subcutaneously to new mice. The transplantation was repeated once more to expand cell yield, and the second generations thus obtained were stocked frozen under liquid nitrogen. Histological examination indicated that all of the tumors were fibrosarcomas. Third generations of isotransplants were used to determine radiosensitivity of the recurrences.

Irradiations

Fast neutrons and ^{60}Co γ rays were used to obtain recurrent tumors. Fast neutrons were obtained by bombarding a thick beryllium target with 30 MeV deuterons produced by the NIRS cyclotron. Dose rate was 0.73 Gy/min. A ^{60}Co therapeutic machine provided γ rays at a dose rate of 0.96 Gy/min at a focus surface distance (FSD) of 47 cm. The beam build-up was obtained by placing a 5- or 8-mm-thick lucite plate on the surface of the tumor for γ and fast-neutron irradiations, respectively. A mixed-beam regimen employed two neutrons and three γ rays in daily fractions (*3*).

A ^{137}Cs γ-ray unit was used to examine radiosensitivity of the recurrent tumors. The dose rate was approximately 0.75 Gy/min at an FSD of 36 cm.

Legs with tumors were placed in a 20 × 3-cm field. Mice were anesthetized with an ip injection of 50 mg/kg sodium pentobarbital prior to irradiation and taped on an acrylic plate. For cell survival experiments, tumor-bearing animals received whole-body irradiation without anesthesia. Irradiations were performed when animals were breathing air or 15 min after they were sacrificed to induce artificial hypoxia of the tumor.

Radiation sensitivity of oxygenated cells was studied by irradiating cells *in vitro*. One million cells were suspended in 100 ml Hanks' solution supplemented with 10% calf serum. The solution was poured into a tissue culture flask (Falcon 3028, 175 cm^2) and flushed with 3 liters/min of 99.9% oxygen during irradiation. Oxygen flushing itself did not affect the colony forming efficiency of cells. Irradiation was performed by the ^{137}Cs-ray unit at room temperature.

Assays

(i) Tumor growth (TG) time assay. Leg tumors were irradiated when they reached an average diameter of 7.0 ± 0.5 mm. Each dose group consisted of 8 mice, and a total of 200 mice were used. Three diameters

of each tumor, *a*, *b*, and *c*, were measured with a caliper three times a week. Tumor volume was calculated by the formula π *abc*/6. Days for a tumor to reach five times the initial tumor volume were determined on the tumor regrowth curve, and the time required for half the tumors to reach five times the initial volume was calculated by probit analysis (*6*).

(ii) TCD_{50} (50% tumor control dose) assay. Tumors were irradiated as mentioned above. Irradiated legs were palpated for recurrences once a week for 120 days, and the tumor control rate was scored. Each dose group consisted of 8 to 10 mice, and a total of 176 mice were used. TCD_{50} was calculated by probit analysis.

(iii) Lung colony assay. Leg tumors were excised immediately after irradiation and single cell suspensions were prepared. Two to four tumors were used for each dose group. The cell suspensions containing an appropriate number of tumor cells and 10^6 heavily irradiated tumor cells in 0.5 ml were injected into the tail vein of the recipient mice which received a pretreatment with 150 mg/kg cyclophosphamide 24 h prior to injection. Heavily irradiated tumor cells and cyclophosphamide were used to increase lung colony forming efficiency (*7, 8*). Five mice per group and a total of 305 mice were used. The times between iv injection of tumor cells and lung removal were 10 to 13 days for the original NFSa tumor and 14 to 18 days for all recurrent tumors. The number of tumor nodules on the surface of each lobe was counted macroscopically. The lung colony forming efficiency was 3 to 8% for the original NFSa tumor cells and 1 to 4% for recurrent tumor cells. Survival curves of oxygenated tumor cells following *in vitro* irradiation was also determined by lung colony assay.

(iv) TD_{50} (50% tumor cell dose) assay. Single cell suspensions were prepared immediately after irradiation. Each suspension was serially diluted and injected subcutaneously into the inguinal and axillary regions of each animal. Seven dilutions were made for each assay, and a total of 112 mice were used. Injected sites were palpated for tumor takes once a week for 60 days. TD_{50} (the number of tumor cells to form a tumor in 50% of challenged sites) was calculated by probit analysis.

Histological Examination

The histology section of each tumor was obtained by the routine procedure and was stained by H and E.

Chromosome Analysis

The tumor cells were suspended in RPMI 1640 with 10% fetal calf serum and incubated overnight with colcemid (0.01 μg/ml) at 37°C. They were then treated with 0.075 *M* KCl hypotonic solution for 25 min at 37°C and fixed with a fixative solution (glacial acetic acid:methanol, 1:3). Air-dried slides were prepared according to our routine method (*9*), and they were stained with the Q-banding technique (*10*). At least seven cells per tumor were photographed. Rearranged chromosomes were compared by means of these photographs. Chromosome pair numbers followed the mouse standard karyotype recommended by the Committee on Standard Genetic Nomenclature System for mouse chromosomes (*11*).

Chromosome analysis was done by one of the authors (I.H.).

Statistical Analysis

Probit analysis was conducted to obtain TG, TD_{50}, and TCD_{50} values. For survival curves, experimental data were fitted to the multitarget–single-hit model by weighted least-squares estimation (*12*), and the D_0 (the radiation dose to reduce the surviving fraction by a factor of $1/e$ in the exponential portion of the survival curve) and the extrapolation number, *n*, were determined along with 95% confidence limits. The radioresistant (hypoxic) fraction was determined by comparing surviving fractions from the terminal portion of the survival curve of controls to those obtained under artificial hypoxia. Student's *t* test was employed to evaluate significant difference.

RESULTS

Chromosomes of the three recurrent tumors, i.e., R1137, R1260, and R1268, were analyzed and compared with those of the NFSa tumors (Fig. 1). The rearranged chro-

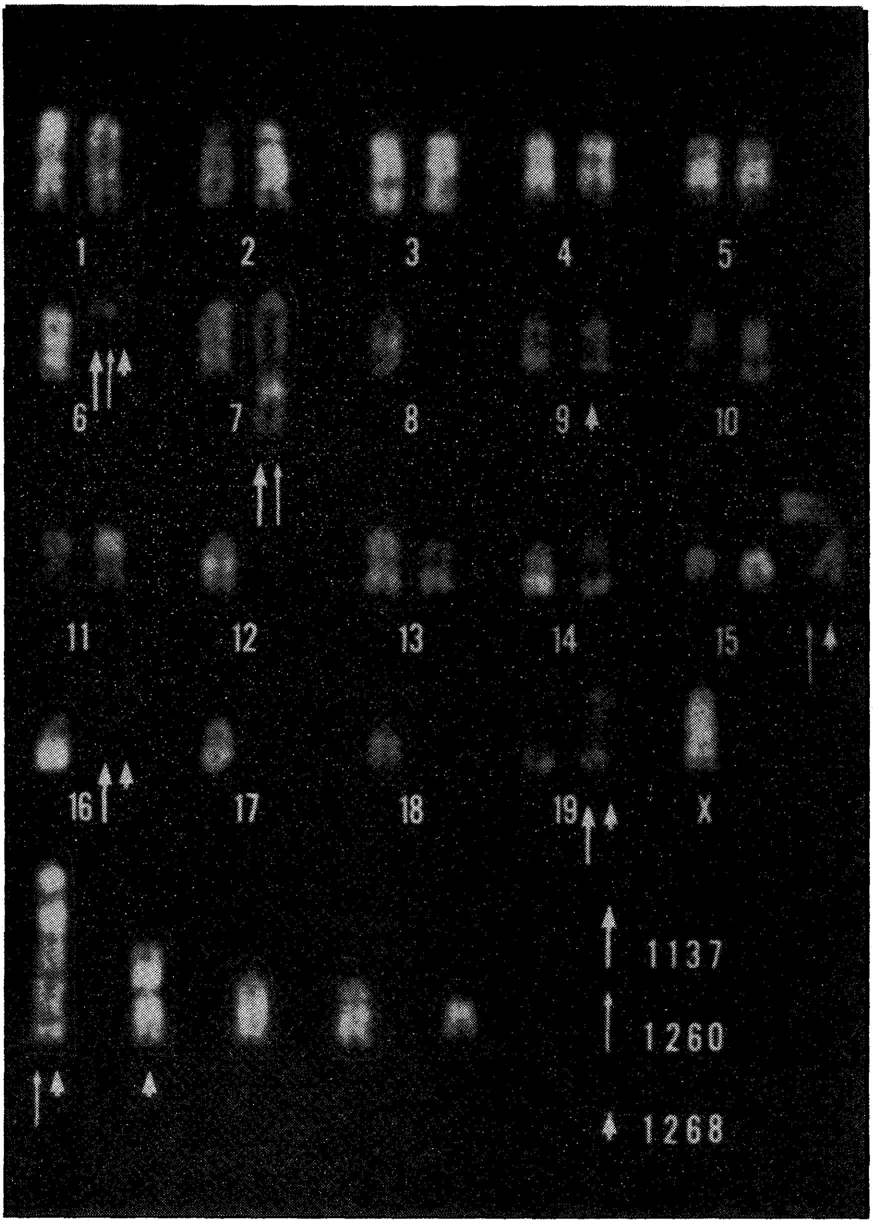

FIG. 1. Chromosomes of the NFSa tumor. Arrows indicate rearranged chromosomes that were also found in the late recurrent tumors.

mosomes, numbers 6, 7, 16, and 19, were found in both the R1137 and the NFSa tumors. The other two tumors also possessed several rearranged chromosomes which were identical to those of the NFSa tumor; i.e., the rearranged chromosomes, 6, 7, and 15, and the largest marker chromosome (bottom of Fig. 1) in the R1260 tumor, and the rearranged chromosomes, 6, 9, 15, 16, and 19, and the metacentric marker chromosome (bottom of Fig. 1) in the R1268 tumor. These observations that at least

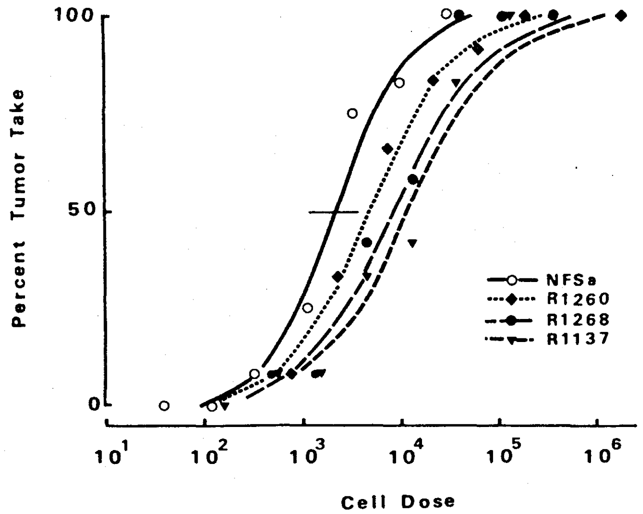

FIG. 2. Tumorigenicity of the NFSa and the late recurrent tumors. Each point consisted of 12 transplanted sites. The horizontal bar indicates a 95% confidence limit.

four rearranged chromosomes of the NFSa tumor were also found in three late recurrent tumors indicated that the R1137, R1260, and R1268 tumors originated from the NFSa tumor and were not induced by radiation.

The TD_{50} values of the three recurrent tumors were marginally larger than that of the original NFSa tumor cells (Fig. 2). These values were 2.15 (1.18–3.92) $\times 10^3$ for the NFSa, 3.74 (1.31–9.13) $\times 10^3$ for the R1260, 8.14 (3.92–41.8) $\times 10^3$ for the R1268, and 10.94 (5.50–31.84) $\times 10^3$ cells for the R1137 tumor.

The growth times of the late recurrences were examined after transplanting a fixed number (10^5) cells into the hind legs of untreated mice. As shown in Fig. 3, times of occurrence for all recurrent tumors were significantly ($P < 0.05$) longer than that for the original NFSa tumor; e.g., the times for tumors to reach 1000 mm^3 after transplantation were 14.7 (14.4–14.9), 19.3 (18.8–19.8), 21.8 (21.4–22.2), and 34.0 (32.6–35.5) days for the NFSa, R1137, R1268, and R1260 tumors, respectively. Moreover, volume doubling times for tumors to grow from 1000 to 2000 mm^3 were 3.9 (3.4–4.3), 5.0 (3.9–6.1), 5.9 (4.6–7.2), and 6.1 (5.4–6.8) days for the NFSa, R1260, R1137, and R1268 tumors, respectively. Statistical significance ($P < 0.05$) was obtained between the original and all recurrent tumors.

The radiosensitivity of the three late recurrent tumors was investigated. First, the R1137, R1260, and R1268 tumors were locally irradiated with graded doses of γ rays when they reached 7 mm in diameter and the TG time was investigated. All three recurrent tumors showed longer TG time than the original NFSa tumor (Fig. 4).

Second, tumor control probabilities of the recurrences were investigated and compared with that of the original tumor. Third generation isotransplants in the legs were irradiated with graded γ-ray doses when they reached 7 mm in diameter. As shown in Fig. 5, higher tumor control rates were obtained for all three recurrent tumors than for the original NFSa tumor. The slope of the dose–response curves was much

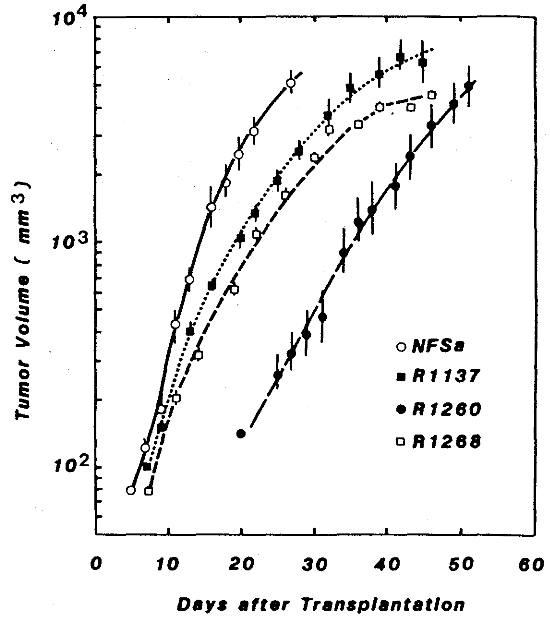

FIG. 3. Growth curves of the NFSa and the late recurrent tumors. Third generations of 10^5 cells were transplanted into unirradiated legs. Each point consisted of 10 tumors. Symbols and bars indicate means and 95% confidence limits.

shallower for the recurrences than for the original tumor. TCD_{50} values are listed in Table I.

Third, the radiation dose–cell survival relationship was determined (Fig. 6, Table I). The original tumor irradiated in animals under air-breathing conditions showed radiosensitive and radioresistant fractions (Fig. 6A). The breaking point of the two fractions was at a radiation dose of ~10 Gy or a survival level of $\sim 10^{-2}$. The D_0 of the radioresistant fraction was 4.42 Gy and was similar to that of artificially hypoxic cells (i.e., 4.13 Gy). The radioresistant fraction was 10% in the NFSa tumor.

On the other hand, the three recurrences showed a variety of survival curves. The R1137 tumor irradiated in animals breathing air showed a single-component survival curve (Fig. 6B). The D_0, i.e., 1.77 Gy, was significantly ($P < 0.05$) smaller than that of the same tumor also irradiated under the condition of artificially induced hypoxia, i.e., 3.20 Gy. The D_0 of the artificially hypoxic R1137 tumor cells was significantly smaller than that of the NFSa tumor.

A single-component curve was also found when the R1260 tumors were irradiated in air-breathing animals (Fig. 6C). Unlike the R1137 tumor, the D_0 of the tumor cells irradiated in air-breathing animals, i.e., 2.32 Gy, was similar to that of the cells irradiated under artificially induced hypoxia (2.54 Gy). Thus the single-component survival curve of the R1260 tumor irradiated in air-breathing animals may represent a naturally occurring or acutely hypoxic cell fraction. However, a difference between these survival curves was observed in the extrapolation numbers which were 1.4 and 6.7 for the tumor cells irradiated under air-breathing and artificially hypoxic conditions, respectively. This indicated that the size of the radioresistant cell fraction was

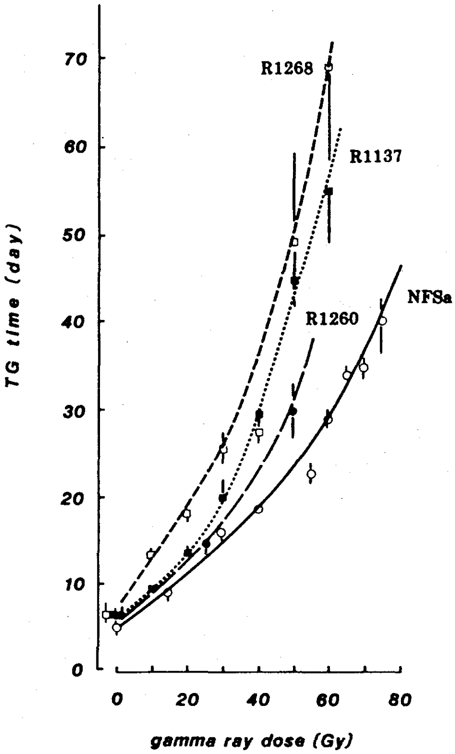

FIG. 4. Tumor growth delay time as a function of γ-ray dose. Tumors transplanted in the unirradiated legs received graded γ-ray doses when they reached an average diameter of 7 mm. Mice were anesthetized with sodium pentobarbital. Symbols and bars are means and 95% confidence limits based on 8 to 10 tumors.

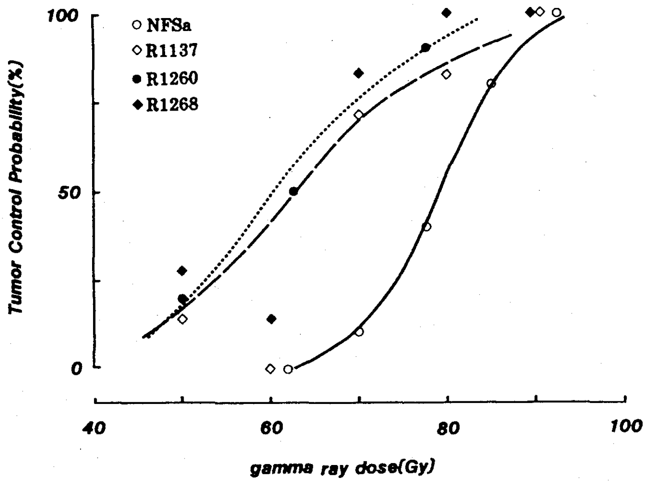

FIG. 5. Tumor control probabilities after single γ-ray doses. Mice were anesthetized with sodium pentobarbital before irradiation. Each point consisted of 8 to 10 tumors.

TABLE I

In Vivo Radiosensitivity of the Original and the Recurrent Tumors

	Original NFSa	*R1260*	*R1137*	*R1268*
A. Survival parameters				
I. Artificial hypoxia[a]				
D_0	4.13[d,e]	2.54*	3.20*	3.96
	(3.51–4.75)	(2.08–3.00)	(2.90–3.50)	(3.36–4.57)
n	1.78	6.71	1.04	2.77
	(0.46–3.10)	(0.21–13.2)	(0.72–1.37)	(2.15–3.39)
II. Air breathing[b]				
1. Radiosensitive fraction				
D_0	2.17	—	1.77	1.52
	(1.84–4.75)		(1.54–2.00)	(1.10–1.94)
n	1.69	—	1.35	2.69
	(0.80–3.38)		(0.40–2.30)	(1.94–3.43)
2. Radioresistant (hypoxic) fraction				
D_0	4.42	2.32*	—	4.05
	(3.12–5.72)	(2.21–2.44)		(3.12–4.97)
n	0.15	1.40	—	0.14
	(0.00–0.35)	(1.00–1.80)		
B. Size of radioresistant (hypoxic) fraction (%)	10	13.7	0	5
C. TCD_{50}[c]	78.9	58.8*	63.2*	62.6*
	(74.9–84.8)	(42.5–66.3)	(54.1–72.2)	(54.0–71.1)

[a] Tumor-bearing mice were whole-body irradiated 15 min after being sacrificed.

[b,c] Tumor-bearing mice were either anesthetized (c) or not anesthetized (b) with sodium pentobarbital during irradiation.

[d,e] Gy, means, and 95% confidence limit.

* $P < 0.05$.

13% in the R1260 tumor and was larger than in the original tumor (statistically not significant). The D_0 values of both naturally and artificially hypoxic R1260 tumor cells were significantly ($P < 0.05$) smaller than those in the original tumor.

The survival curve of the R1268 tumor was very similar to that of the original tumor (Fig. 6D). Irradiation under air-breathing conditions resulted in a biphasic survival curve with a break point at a radiation dose of $\sim$7 Gy or a survival level of $\sim 3 \times 10^{-2}$. The D_0 of the radioresistant cell fraction was 4.05 Gy which was similar to that of artificially hypoxic cells (i.e., 3.96 Gy). The D_0 values of the radiosensitive and the radioresistant cells in the R1268 tumor were slightly smaller than those in the original NFSa tumors (the difference was not statistically significant). The radioresistant cell fraction of 5.1% was smaller than that of the original tumor.

Extrapolation numbers of the recurrent tumor cells ranged from 1.04 to 6.71 (Table I). The R1260 and R1268 tumors showed larger extrapolation numbers than that

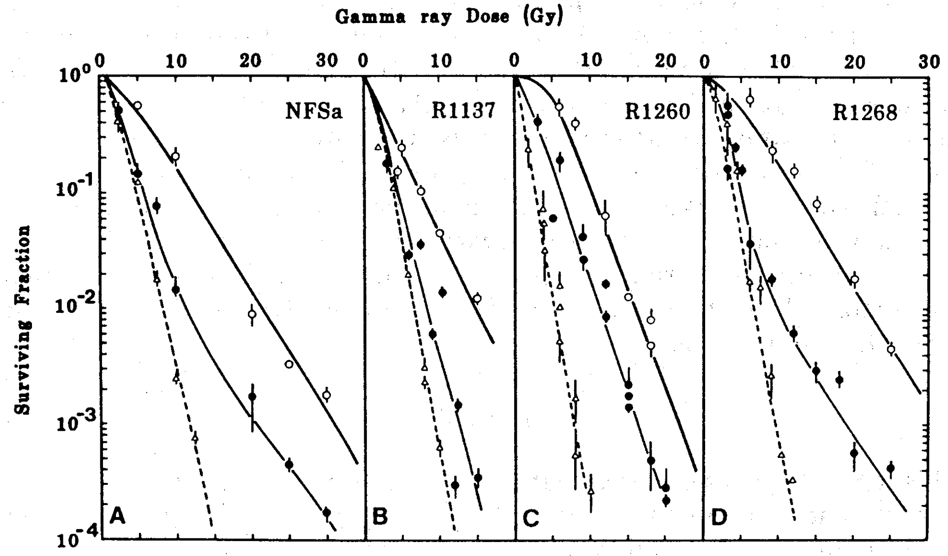

FIG. 6. Clonogenic cell survivals of the NFSa and the late recurrent tumors. For *in vivo* experiments (○,●), tumor-bearing animals were whole-body irradiated without anesthesia. Open symbols represent radiosensitivity of acutely hypoxic cells, while closed symbols are for air-breathing mice. For *in vitro* experiments (▽), cells were exposed to oxygen during irradiation. Symbols and bars are means and SE.

of the original tumor while the R1137 tumor exhibited a smaller extrapolation number. Differences between these extrapolation numbers, however, were not statistically significant.

Cells irradiated *in vitro* under oxygenated conditions also showed different radiosensitivity between the recurrent and original tumors (Fig. 6, Table II). The NFSa tumor cells showed the largest D_0 value and was sequentially followed by the R1268,

TABLE II

In Vitro Radiosensitivity of the Original and the Recurrent Tumors[a]

	Original NFSa	*R1260*	*R1137*	*R1268*
A. Survival parameters				
D_0	1.52[b,c] (1.32–1.71)	1.12* (1.03–1.20)	1.21 (1.06–1.36)	1.28 (1.14–1.42)
n	2.44 (0.72–4.16)	1.73 (1.02–2.44)	4.36 (1.70–7.02)	3.21 (1.10–5.32)
B. Oxygen enhancement ratio[d]	2.72	2.27	2.64	3.09

[a] Cells were exposed with 99.9% oxygen during irradiation.

[b,c] Means and 95% confidence limit.

[d] Ratio of D_0 values between artificially hypoxic tumor and oxygenated cells.

* $P < 0.05$.

R1137, and R1260 tumors. A significant difference ($P < 0.05$) was observed between the D_0 of the NFSa tumor and that of the R1260 tumor. Extrapolation numbers of the three recurrent tumors ranged from 1.73 to 4.36. The R1137 and R1268 tumor cells showed larger extrapolation numbers than the NFSa tumor cells while the R1260 tumor cells possessed a smaller one (statistically not significant).

The OER of the recurrent tumors was different from that of the original tumor (Table II). The OER was determined under *in vitro* conditions by comparing D_0 values of the artificially made hypoxic cells with the oxygenated cells. The R1137 tumor cells showed OER values similar to the original tumor cells. A smaller OER than the NFSa tumor cells was found for the R1260 tumor cells while a larger OER was found for the R1268 tumor cells.

DISCUSSION

This report has demonstrated that, when assayed by TCD_{50}, three late recurrent tumors were more radiosensitive than the original tumor. A similar observation has been reported by Kaneta and Muta (*13*) using the Yoshida sarcoma, i.e., that radiosensitivity increased after repeated irradiations *in vivo.* Increased radiosensitivity of a late recurrent adenocarcinoma, when examined by TCD_{50} assay, has also been reported by Suit (*2*). On the other hand, radiosensitivity of early recurrences which appeared less than 50 days after TCD_{50} doses is unchanged (*14*). It appears to be only late recurrences that acquire an increased radiosensitivity.

Irradiation under *in vitro* conditions demonstrated that the recurrent tumor cells possessed smaller D_0 values than the original tumor cells. The D_0 values of the artificially hypoxic cells irradiated *in vivo* were smaller for the recurrent tumors than the original tumor without significant changes in extrapolation numbers. Decreased D_0 values in the recurrent tumors may be attributed to a heritable damage induced by irradiations. Sinclair (*1*) reported that irradiated Chinese hamster cells showed smaller D_0 values than did unirradiated controls and that the small D_0 value has been maintained for more than 10 months *in vitro.* However, the D_0 and extrapolation number of the R1268 tumor were similar to those of the original tumor, although the TCD_{50} of this tumor was significantly smaller than that of the NFSa tumors. This may be due to low tumorigenicity (i.e., large TD_{50} value) of the R1268 tumor, which suggests that the R1268 tumor could be more immunogenic than the original tumor.

The question we addressed is whether the surviving fractions (SF) at tumor cure doses are identical for the original and recurrent tumors. We have extrapolated the terminal portions of the respective survival curves down to TCD_{50} values and calculated the surviving fractions. SF (TCD_{50}) thus calculated were 3.8×10^{-7}, 9×10^{-9}, 2.8×10^{-9}, and 6.7×10^{-10} for the R1268, NFSa, R1137, and R1260 tumors, respectively. Since a 7-mm NFSa tumor contains approximately 10^8 tumor cells (*15*), only one cell should have survived and recurred after a TCD_{50} radiation dose. It is interesting to note that, among the four tumors, the highest value of SF (TCD_{50}) was found for the R1268 tumor, which possessed the lowest tumorigenicity (Fig. 2). On the other hand, SF (TCD_{50}) of the R1137 and R1260 tumors were suspiciously low. Since D_0 values increase when irradiated tumors are kept *in situ* to repair potentially lethal radiation damage (*16*), higher SF (TCD_{50}) than the present values could be obtained by employing a delayed assay as compared to an immediate assay. The original NFSa tumors possess a marginal capacity to repair potentially lethal radiation damage (*15*).

D_0 values of the radiosensitive fraction were larger than those of the *in vitro* oxygenated cells but smaller than those of the artificially hypoxic cells. This intermediate radiosensitivity between hypoxic and oxygenated cells was prominently observed in the R1137 tumor which did not show a detectable radioresistant fraction. This does not exclude the possibility that a very small hypoxic fraction could be contained in the R1137 tumor. This type of tumor with intermediate radiosensitivity has been reported by Wallen *et al.* (*17*); namely, intracerebrally growing rat 9L tumors showed a single-component survival curve with intermediate radiosensitivity between acutely hypoxic and fully oxygenated cells. The intermediate radiosensitivity may originate from partially hypoxic cells (*18*). Alternatively, cell-to-cell contact may also increase D_0 values of oxygenated cells (*19*).

ACKNOWLEDGMENTS

We thank Drs. Muneyasu Urano, William Dewey, and Sara Rockwell for their helpful discussions and editing of the manuscript. This investigation was supported in part by a Grant-in-Aid for Cancer Research (62010016) from the Japanese Ministry of Education, Science and Culture.

RECEIVED: February 20, 1987; REVISED: August 6, 1987

REFERENCES

1. W. K. SINCLAIR, X-ray induced heritable damage (small colony formation) in cultured mammlian cells. *Radiat. Res.* **21,** 584–611 (1964).

2. H. D. SUIT, Response to x-irradiation of a tumor recurring after a TCD_{95} radiation dose. *Nature (London)* **211,** 996–997 (1966).

3. K. ANDO, S. KOIKE, H. IKEHIRA, I. HAYATA, M. SHIKITA, and M. YASUKAWA, Increased radiosensitivity of a recurrent murine fibrosarcoma following radiotherapy. *Jpn. J. Cancer Res. (GANN)* **76,** 99–103 (1985).

4. K. ANDO, N. HUNTER, and L. J. PETERS, Immunologically nonspecific enhancement of artificial lung metastases in tumor-bearing mice. *Cancer Immunol. Immunother.* **6,** 151–156 (1979).

5. K. ANDO, S. KOIKE, N. FUKUDA, and C. KANEHIRA, Independent effect of a mixed-beam regimen of fast neutrons and gamma rays on a murine fibrosarcoma. *Radiat. Res.* **98,** 96–106 (1984).

6. M. URANO and S. KOIKE, Comparison of the effects of neutron and/or photon irradiation on spontaneous squamous-cell carcinoma in mice. *Radiology* **134,** 219–225 (1980).

7. D. J. GRDINA, I. BASIC, K. A. MASON, and H. R. WITHERS, Radiation response of clonogenic cell populations separated from a fibrosarcoma. *Radiat. Res.* **63,** 483–493 (1975).

8. L. J. PETERS and K. A. MASON, Enhancement of artificial lung metastases by cyclophosphamide: Pharmacological and mechanistic considerations. In *Cancer Invasion and Metastases: Biologic Mechanisms and Therapy* (S. B. Day *et al.*, Eds.). Raven Press, New York, 1977.

9. I. HAYATA, M. SAKURAI, S. KAKATI, and A. A. SANDBERG, Chromosomes and causation of human cancer and leukemia, including five unusual Ph 1 translocations. *Cancer* **36,** 1177–1191 (1975).

10. T. CASPERSSON, L. ZECH, and C. JOHANSSON, Differential binding of alkilating fluorochromes in human chromosomes. *Exp. Cell Res.* **60,** 315–319 (1970).

11. Committee on Standard Genetic Nomenclature for Mice, Standard karyotype of the mouse, *Mus musculus. J. Hered.* **63,** 69–72 (1972).

12. T. NAKAGAWA and Y. OYANAGI, Program system SALS for nonlinear least squares fitting in experimental sciences. In *Recent Developments in Statistical Inference and Data Analysis* (K. Matsushita, Ed.). North Holland, Amsterdam, 1980.

13. K. KANETA and N. MUTA, Radiosensitivity of the preirradiated Yoshida sarcoma, *Nature (London)* **185,** 858–859 (1960).

14. K. MASUDA, Response of recurrent mouse mammary carcinoma to retreatment with a single or fractionated gamma-irradiation. *Nippon Acta Radiol.* **38,** 577–582 (1978).

15. K. ANDO and S. KOIKE, The relationship between lung colony and *in situ* assays. *Int. J. Radiat. Oncol. Biol. Phys.* **11,** 1945–1502 (1985).

16. M. URANO, N. NESUMI, K. ANDO, S. KOIKE, and N. OHNUMA, Repair of potentially lethal radiation damage in acute and chronically hypoxic tumor cells in vivo. *Radiology* **118,** 447–451 (1976).

17. C. A. WALLEN, S. M. MICHAELSON, and K. T. WHEELER, Evidence for an unconventional radiosensitivity of rat 9L subcutaneous tumors. *Radiat. Res.* **84,** 529–541 (1980).

18. A. REYNAUD-BOUGNOUX, F. LESPINASSE, E. P. MALAISE, and M. GUICHARD, Partial hypoxia as a cause of radioresistance in a human tumor xenograft: Its influence illustrated by the sensitizing effect of misonidazole and hyperbaric oxygen. *Int. J. Radiat. Oncol. Biol. Phys.* **12,** 1283–1286 (1986).

19. R. E. DURAND and R. M. SUTHERLAND, Effects of intercellular contact on repair of radiation damage. *Exp. Cell. Res.* **71,** 75–80 (1972).

J. RADIAT. RES., 28, 268–273 (1987)

Short Communication

In Vitro Neoplastic Transformation by Neutron Beams
– Relative Biological Effectiveness and Dose Fractionation –

MIEKO YASUKAWA[1], TOYOZO TERASIMA, TAKESHI FURUSE[1],
HIROSHI OHARA[1] and HIROSHI OHTSU[1]

[1]Division of Physiology and Pathology, National Institute of Radiological Sciences,
Anagawa-4, Chiba, 260, Japan

(Received September 14, 1987)
(Revised version, accepted November 12, 1987)

RBE/Transformation/Neutrons/ 10T½ cells/Van de Graaff/Cyclotron Repair

In vitro cell transformation assay has proved to be a powerful means of quantitating the neoplastic action of sparsely ionizing radiation and analyzing the relevant damage-repair and expression processes[1-3]. With respect to particulate radiations, however, transformation data are rather limited. The oncogenic potential of neutrons has been studied most extensively, due to the ready availability of neutron sources as compared with sources of other radiations. Findings of this kind are undoubtedly needed to provide a basis for high LET radiotherapy and for radiation protection standards.

Borek et al.[4] have reported that low doses of 430 KeV neutrons induced neoplastic transformation of cultured golden hamster embryo cells with a relative biological effectiveness (RBE) of ca. 8. Subsequent studies with mouse 10T½ cells have shown that (1) RBE values for transformation were larger for neutrons of low energy than high energy, and tended to be larger at low doses than high doses[5, 6], and (2) with fission-spectrum nuetrons, transformation was significantly enhanced either at a low dose rate or by multiple fractions as compared to single equivalent total doses at a high dose rate[7, 8]. In this communication, we shall report the RBE of two neutron beams available in the National Institute of Radiological Sciences (NIRS) for transformation of 10T½ cells.

10T½ (clone 8) cells between the 7th and 9th passages were grown in Eagle's basal medium supplemented with 10% heat-inactivated fetal calf serum, which was selected because of is contact-inhibition property. In order to alleviate serum batch-dependent fluctuation of transformation[9], every growth medium was supplemented with 10^{-8} M triiodothyronine and 6 ng/ml insulin (final concentrations). Transformation and survival assay procedures were described in detail previously[10]. In the present experiments, cultures seeded with 6.2×10^4 cells per 25 cm^2 plastic culture flask were grown for 11 days. At the time of medium renewal on the 6th day, flasks were filled with the growth medium and then kept undisturbed until the start of the experiment when irradiation was carried out. Immediately after irradiation of these 11-day-old plateau phase cultures, the cells were dispersed with 0.1% trypsin, then replated into assay dishes for development of transformed foci. A total of 150 assay dishes were normally used in each experiment. Scoring of type II and III transformed foci[11)] was done after cultivation for 8 weeks. The transformation frequency was given as the ratio of the parametric mean of the Poisson distribution of transformed foci induced by a given dose to the number of cells surviving the same radiation dose. For survival assay the same dispersed cells as used for transformation assay were seeded into 100-mm dishes.

Neutrons with a mean energy of 2 MeV were produced by bombarding a Be target with 2.5 MeV deuterons from a Van de Graaff generator. The dose rate was ca. 7 cGy min^{-1} with a 10% gamma dose component. The second experiment was done with cyclotron-produced neutrons delivered at 78 cGy min^{-1} with a mean energy of 13 MeV and a 5% gamma component. The dose was measured at the position of a cell layer in the culture vessel by using the paired ionization chamber[12)] for neutrons of either high or low energy. X-rays were delivered at 50 cGy min^{-1} from the generator operated at 200 KVp and 20 mA with added filtration (HVL: 2 mmCu), as described in the previous report[10)]. In low-energy neutron experiments, flasks, filled with the growth medium since the 6th day, were positioned vertically and cell-side forward to be horizontal beam. In high-energy neutron experiments, flasks maintained under the same growth conditions were set cell-side up and exposed to the vertical beam through a 6 mm lucite plate placed directly on top of the flask. For neutron irradiation, the cells were kept at ambient temperature for 20 to 40 min depending on the experimental design.

Frequencies of transformation induced by 1.5 Gy of neutrons from the Van de Graaff generator and 2 Gy of neutrons from the cyclotron unit are given on a surviving cell basis in Table 1. The values are indicated by a closed circle and a closed square, respectively, in Fig. 1 in relation to the X-ray dose response curve which was reported previously[10)]. The RBE values for transformation were 2.9 with the Van de Graaff radiation and 1.8 with the cyclotron radiation. The finding that low-energy neutrons from the Van de Graaff generator exhibited a higher REB than cyclotron-produced high-energy neutrons is consistent with other data, as shown in Table 2, in which RBE values were calculated at the level of 1 to 2.6 x 10^{-3} transformation frequency. From the table, we see that the RBE of high-energy neutrons is likely to be slightly higher for cell killing (1.8 to 2.0) than for transformation (1.2 to 1.8) at approximately the same dose range (2 – 3 Gy of neutrons; see footnotes 2 and 5), or at least the same for the two

Table 1. Transformation frequency by a single dose of neutrons

Radiation	Dose (Gy)	No. of transformed foci / No. of surviving colonies	Transformation frequency with S.E. per surviving cell
Van de Graaff neutrons	1.5	82.02 / 31,151*	$2.6 \pm 0.3 \times 10^{-3}$
Cyclotron neutrons	2.0	46.50 / 31,026*	$1.5 \pm 0.2 \times 10^{-3}$

* Sum of 3 repeated experiments.

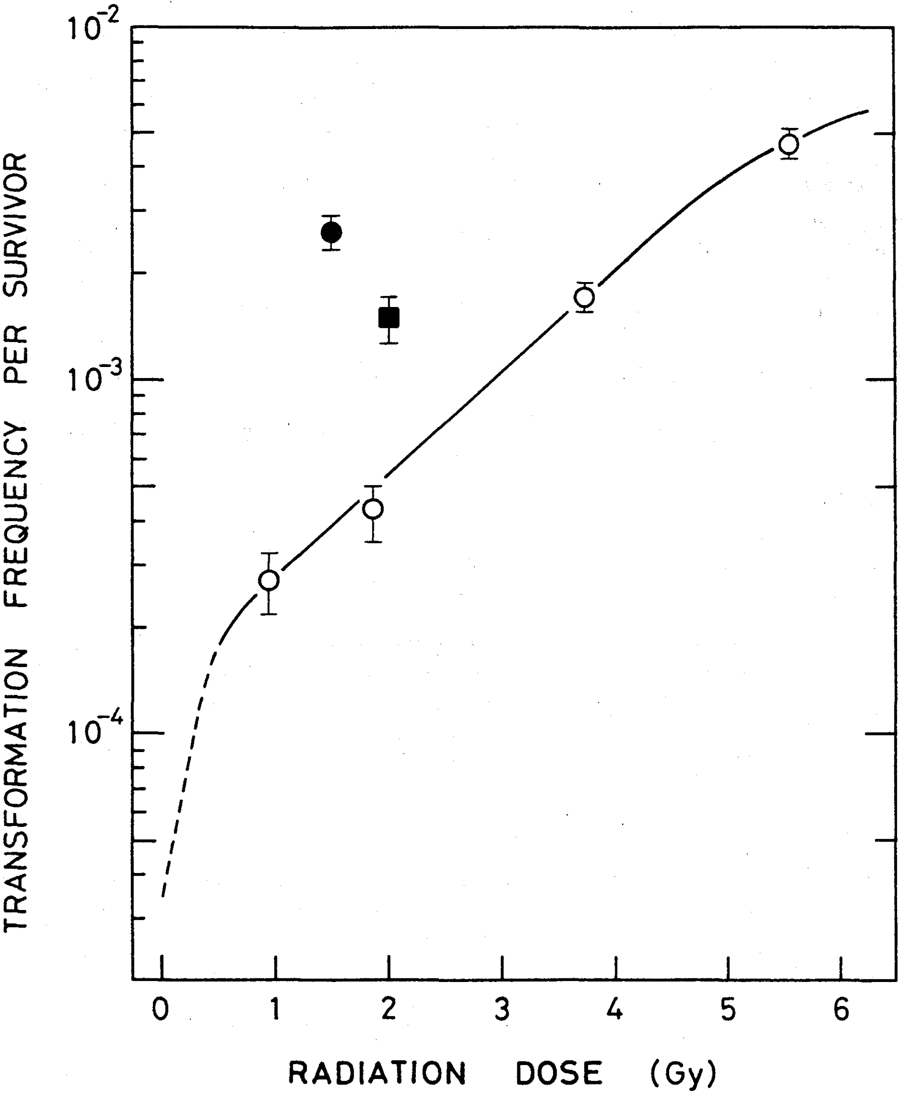

Fig. 1. Transformation frequency of C3H-10T½ cells induced by nautron beams in relation to the X-ray dose-transformation curve. The closed circle and closed square with S.E. represent neutrons from the Van de Graaff generator and the 30 MeV cyclotron, respectively. The solid line shows the transformation response to 200 KeV X-rays reported previously[10].

Table 2. Comparison of RBE values of various neutron beams determined with mouse 10T½ cells

Radiation	Mean energy	RBE Transformation	RBE Cell Killing[5]	Authors
Fission-spectrum neutrons	0.85 MeV	2.6[1]	2.3	Han & Elkind, 1979
Fission-spectrum neutrons	0.5 MeV	2.8[1]	2.3	Balcer-Kubiczek & Harrison, 1983
Cyclotron neutrons	38 MeV	1.2[2]	1.8	
Fission-spectrum neutrons	0.85 MeV	2.7[3]		Hill et al., 1985
Cyclotron neutrons	13 MeV		1.8 – 2.0	Ohara, 1985
Van de Graaff neutrons	2 MeV	2.9[4]		Present report
Cyclotrons neutrons	13 MeV	1.8[2]		Present report

1. Determined at the level of 2×10^{-3} transformation frequency.
2. Determined at the level of 1.5×10^{-3} transformation frequency.
3. Determined at the level of 1.0×10^{-3} transformation frequency.
4. Determined at the level of 2.6×10^{-3} transformation frequency.
5. Determined at the level of 20% survival.

endpoints. Thus, the use of cyclotron neutrons may be preferable in radiotherapy practice.

Two-dose fractionation experiments were intended to see how subtransformation damage caused by neutrons evolves after irradiation. This was carried out by administering two 1 Gy doses of cyclotron-produced neutrons and two 0.75 Gy doses of Van de Graaff neutrons to the plateau-phase cells at a 3-hours interval. Table 3 shows the results. The observed values were slightly affected by a different batch of serum from the one used in the single dose experiments in Table 1, and, therefore, the results seems to be rather inconsistent, additionally because of a limited scale of the experiment shown in Table 3. It appears that subtransformation damage caused by low-energy neutrons resulted in a 50% increase of the transformation frequency in 3 hours, whereas about 30% of transformation damage caused by high-energy neutrons was removed during the same interval. In accordance with the sparing effect found with cyclotron-produced neutrons when 10T½ cell survival was studied with a multifractional design by Ohara[13)], subtransformation damage caused by 13 MeV neutrons appears to be reparable.

Hill et al. first demonstrated that fission-spectrum neutrons at reduced dose rates[7)] and in fractions enhance neoplastic transformation. Our result with Van de Graaff neutrons seems to

Table 3. Two-dose fractionation experiment on transformation by neutron beams

Radiation	Dose (Gy)	Transformation frequency with S.E. per surviving cell (x 10^{-3})	
		Interval between exposures	
		0 hr	3 hr
Van de Graaff neutrons	0.75 + 0.75	1.5 ± 0.4	2.3 ± 0.6
Cyclotron neutrons	1 + 1	2.1 ± 0.5	1.5 ± 0.4

be consistent with theirs. To explain these results, we may suppose that two types of repair reaction occur essentially in series; one acts to modify initial, subeffective damage toward transformation, and the second involves a removal of resultant transformation damage which leads to transformation through a fixation process. On this basis, the above results may be interpreted by assuming that subeffective damage induced by low-energy neutrons is amenable to modification but is not susceptible to subsequent removal, whereas damage caused by high-energy neutrons is equally susceptible to the above two processes. Cellular repair of low-energy neutron damage in such a way as above may be called "error-prone repair" as proposed by Elkind et al.[14).

We thank Dr. M. Seki, Director of the Division of Physiology and Pathology, Mr. Z. Murakoshi of the Division of Technical Services and the staff of the Section of Cyclotron for their kind cooperation. One of the authors (T.T.) especially thanks Dr. T. Maruyama of the Division of Physics for his helpful comments.

REFERENCES

1. Hall, E.J. and Miller, R.C. (1981) The how and why of in vitro oncogenic transformation. Radiat. Res. **87:** 208-223.
2. Terasima, T., Ohtsu, H., Yasukawa, M., Okada, Y. and Watanabe, I. (1984) In vitro neoplastic transformation by radiation. Carcinogenesis (NIRS symposium series 14; in Japanese), pp 39-57. NIRS, Chiba.
3. Borek, C. (1985) The induction and control of radiogenic transformation in vitro: Cellular and molecular mechanisms. Pharmac. Ther. **27:** 99-142.
4. Borek, C., Hall, E.J. and Rossi, H.H. (1978) Malignant transformation in cultured hamster embryo cells produced by X-rays, 430-KeV monoenergetic neutrons and heavy ions. Cancer Res. **38:** 2997-3005.
5. Han, A. and Elkind, M.M. (1979) Transformation of mouse C3H/10T½ cells by single and fractionated doses of X-rays and fission-spectrum neutrons. Cancer Res. **39:** 123-130.
6. Balcer-Kubiczek, E.K. and Harrison, G.H. (1983) Oncogenic transformation of C3H-10T½ cells by X-rays, fast-fission neutrons, and cyclotron-produced neutrons. Int. J. Radiat. Biol. **44:** 377-386.
7. Hill, C.K., Bounaguro, F.M., Myers, C.P., Han, A. and Elkind, M.M. (1982) Fission-spectrum neutrons at reduced dose rates enhance neoplastic transformation. Nature **298:** 67-69.
8. Hill, C.K., Carnes, B.A., Han, A. and Elkind, M.M. (1985) Neoplastic transformation is enhanced by

multiple low doses of fission-spectrum neutrons. Radiat. Res. **102:** 404-410.

9. Terasima, T., Yasukawa, M. and Kimura, M. (1981) Radiation-induced transformation of 10T½ mouse cells in the plateau phase: post-irradation changes and serum dependence. Gann **72**: 762-768.
10. Terasima, T., Yasukawa, M. and Kimura, M. (1985) Neoplastic transformation of plateau-phase mouse 10T½ cells following single and fractionated doses of X-rays. Radiat. Res. **102:** 367-377.
11. Reznikoff, C.A., Bertram, J.S., Brankow, D.W. and Heidelberger, C. (1973) Quantitative and qualtitative studies of chemical transformation of cloned C3H mouse embryo cells sensitive to postconfluence inhibition of cell division. Cancer Res. **33:** 3239-3249.
12. Hiraoka, T., Kawashima, K., Hoshino, K. and Matsuzawa, H. (1977) Dosimetry of fast neutron beams at the NIRS cyclotron. Nippon Acta Radiologica **33:** 369-376.
13. Ohara, H. (1985) Biological studies on 30 MeV neutrons and 70 MeV protons produced by NIRS cyclotron. Medical Application of Particle Accelerator (Edited by H. Tsunemoto and Y. Tateno) pp. 77-86. NIRS, Chiba.
14. Elkind, M.M., Han, A. and Hill, C.K. (1984) Error-free and error-prone repair in radiation-induced neoplastic cell transformation. Radiation Carcinogenesis: Epidemiology and Biological Significance (Edited by J.D. Boice, Jr. and J.F. Fraumeni, Jr.), pp. 303-318. Raven Press, New York.

Fast Neutron Therapy at NIRS

Hiroshi TSUNEMOTO
Yoshiro AOKI
Tatsuo ISHIKAWA
Shinroku MORITA
Tatsuo ARAI

All:
National Institute of Radiological Sciences
Chiba-shi, Japan

Norihiko TAKADA
Chiba Cancer Center Hospital
Chiba-shi, Japan

Haruo ITO
Chiba University
Chiba-shi, Japan

Shinetsu KAMATA
Cancer Institute Hospital
Tokyo, Japan

Introduction

There were 1171 patients, suffering from locally advanced or radioresistant cancers, were treated with 30 MeV (d–Be) neutrons from November 1975 to March 1984. 921 of them had the tumours previously untreated.

The sites involving over 100 patients, were head and neck (196), esophagus (115) and female gynecologicl organs (164).

Determination of the indication has been the main theme for clinical trials in order to confirm the effect of high LET radiations. Progress of the studies is discussed.

Method of studies

The clinical trials were performed with a fixed perpendicular neutron beam, which was produced by bombarding a thick Bellylium target with 30 MeV deuterons. Dose distributions of the fast neutron beam for 10 x 10 cm field at SSD 175 cm measured in a tissue equivalent phantom were found to be almost the same as those of Tele-cobalt γ-rays for 10 x 10 cm field at SSD 80 cm.

The doses for the individual cases were prescribed by use of a concept of biologically equivalent TDF (time dose and fractionation) (1). In the cases treating with a radical purpose, the doses equivalent to TDF 100–110 were delivered to the target volume; neutron only, mixed schedule or fast neutron boost were selected according to the indication.

The doses used in preoperative irradiation were equivalent to TDF 60 and the surgery was performed within 3 weeks after the irradiation.

Postoperative irradiation with fast neutrons was performed with the doses equivalent to TDF 80 and was used in the treatment of carcinoma of the esophagus.

To evaluate the results of the treatment, scores consisting of five steps were used, by which the normal tissue response and the tumour response were recorded..

Results

a) Head and neck cancers

Analysis of the results of the treatment was performed for 150 patients, who were suffering from advanced head and neck cancers and have not been treated previously.

Complete regression of the tumour was seen in 56 cases of all (37%) who were treated by radiation only, and the other 31 have had a local control of the tumour after salvage surgery (Table 1).

Complications due to fast neutron therapy has developed in 10 patients, in which trismus was one of the marked late effects.

The patients suffering from carcinoma of the larynx were treated with fast neutron boost after a 40 Gy of x-rays.

The results show that, when fast neutrons were used, the tumours arising from supraglottis of the larynx have been controlled in higher rate (84.6%:11/13) compared with those who received x-ray treatment (25%:25/100), whereas the results were almost even in the cases of glottic and subglottic cancers (Table 2)

Progress in Radio-Oncology III, Editor K.H.Karcher, Proceedings of the Third Meeting on Progress in Radio-Oncology, Vienna, 1985, ICRO 1987.

Table 1
Result of fast neutron therapy for advanced head and neck cancer (NIRS) (Analysed at November 1984)

			CR	SR	Complication
FOM	T3–T4	8	1	–	1
Palate	T3	2	2	–	1
Gum	T3–T4	10	1	4	1
Tongue	T2–T4	17	2	1	2
Mucosa	T3–T4	2	–	1	–
Oropharynx	T3–T4	3	1	–	2
Nasopharynx	T2–T4	5	2	–	–
Larynx	T1–T4	49	30	11	–
Hypopharynx	T2–T3	9	3	5	1
Max. Sinus		17	–	6	2
Parotid G1					
– Primary		4	1	3	–
– Post op		11	(11)	–	–
Others		11	4	–	–
		150	56 (37%)	31 (26.6%)	10 (6.6%)
			87 (58%)		

Table 2
*Local control rates of carcinoma of the larynx treated with neutron boost**

	T1	T2	T3	T4
Glottic	3/5 (48/57)	5/8 (8/19)	0/2 (3/27)	0/1 (0/1)
Supra-glottic	2/2 (4/8)	3/3 (12/34)	4/6 (7/31)	2/2 (2/27)
Sub-glottic		1/1 (0/5)	0/1 (0/5)	

( ): Treated by x-rays 1964–1971
*: Cancer Research Institute Hospital

Salvage surgery was necessary to manage carcinoma of the hypopharynx, because local control of the tumour was observed in only 3 cases after the fast neutron therapy.

There were 3 patients suffering from carcinoma of the parotid gland. Among them, one was controlled by radiation only and the other three received salvage surgery, one of whom had not active tumour cells in the surgical specimens.

In 17 cases involved by advanced carcinoma of the maxillary sinus, 4 patients were suffering from osteosarcoma and received salvage surgery after fast neutron only, and 3 of them resulted in local control. An additional effect of fast neutron beam could not be expected to manage advanced tongue cancer, where interstitial irradiation and salvage surgery has been used for a radical modality.

b) Lung cancer

Fast neutron beam was applied to 79 patients who were suffering from lung cancer. Among them, 30 patients were T-1 and T-2 and 49 patients were T-3. The results show that local control rates were 20/30 (66.6%) and 21/49 (42.8%) for T-1-2 and T-3 tumours respectively and that 14 cases developed the complications of moderate through severe reactions (Table 3). The doses equivalent to TDF 100-120 were required to manage tumours under acceptable complication rates.

Table 3
Local control and complication in the treatment of fast neutrons for lung cancer (30 MeV,d-Be) NIRS

	Local Control T1 T2	T3	Complication Moderate Severe
<100	2/3	3/9	1/12
100–120	12/20	14/32	9/52
>120	6/7	4/8	4/15
	20/30	21/49	14/79

Cumulative survival rates evaluated at five years were 52% for stage I and 0% for stage II and 24% for stage III. For Pancoast tumour of the lung, cumulative (five year) survival rate was 23%, and mean survival time observed in the patients expired was 11.6 months for fast neutron therapy, whereas the time was shortened to 4.2 months for the cases that received photon beam irradiation.

c) Carcinoma of the esophagus

The results were evaluated in 115 patients with unresectable tumour of the esophagus, 34 of whom were treated with fast neutron beam and the other 81 were treated by photon beams. As shown in Table 4, complete regression of the tumour was observed in 15 of 34 patients (44.1%) who received fast neutron therapy, and was 24 of 81 patients (29.6%) in the photon beam therapy group. When responses of tumour to radiations evaluataed according to x-ray findings, effect of fast neutrons was found to be better for tumorous and serrated type cancers compared with the photon beam treatment.

Table 4
Local control rates of esophageal cancer treated with either fast neutrons or photons. – TDF 90 –

Modalities	No of cases	CR (%)
F–N	34	15 (44.1%)
Mixed Schedule	20	7 (35.0%)
Boost Therapy	14	8 (57.1%)
Photon	81	24 (26.9%)

CR : complete regression

Surgical specimens obtained from the cases that received preoperative irradiation with fast neutrons show that the effects of neutrons were marked in the well differentiated type of cancers.

d) Carcinoma of the uterine cervix

Carcinoma of the uterine cervix, stage III-b and IV-a was treated with mixed schedule and additional intracavitary treatment.

The results show that, although an improvement of local control rates has been obtained in the studies based on a histological classification, there were not significant differences between the survival rates of the patients who received either fast neutron or photon beam therapy.

However, when fast neutron beam was used in the cases with the recurrent tumour in the pelvis, the survival rates have been improved in the cases that received fast neutron therapy, where 5 year survival rate was 26.7%. For the patients treated with photon beams, 5 year survival rate was found to be under 10%.

This fact suggests that intracavitary irradiation has markedly contributed to manage the tumours arising from cervix of the uterus even when an additional effect of mixed schedule would be expected.

Table 5
Local control rates of carcinoma of the uterine cervix treated with either fast neutrons or x-rays, evaluated according to tumour volume and histology

Tumour Volume	Histology*	Local Control (%)	
		Neutrons	X-Rays
Large (150 ml)	L	73 (11/15)	53 (9/17)
	R	55 (6/11)	50 (5/10)
	S	73 (11/15)	66 (6/9)
Medium (100 ml)	L	82 (18/22)	61 (14/23)
	R	56 (5/9)	55 (6/11)
	S	94 (17/18)	79 (19/24)

*L = Large cell type (WHO)
R = Radioresistant type (National Cancer Center)
S = Radiosensitive type (National Cancer Center)

e) Malignant melanoma

There were 54 patients suffering from malignant melanoma, 39 of whom had a disease arising from the skin and the other 15 were with melanoma of the head and neck region. When the residual tumours were found in the course of fast neutron therapy, salvage surgery and cryosurgery were applied to complete the treatment. The results were analysed for the patients involved by malignant melanoma and previously untreated. There were 21 of skin melanoma and 12 of head and neck melanoma.

Of 21 patients with skin melanoma, 4 were stage I-a, 15 were stage I-b and the other 2 were classified stage II and stage III. Five year survival rate of them was 47%. As shown in Table 6, complete regression (CR) was achieved in 2 cases, who were treated with fast neutron only, and the other 17 had local control after a combination therapy of fast neutrons and surgery (N + S). The results suggest that fast neutron irradiation has contributed not only to improve local control rate of melanoma but also to reduce the surgical margin, where an en bloc dissection was required and the margin was decided 5 cm from the tumour. Hence, the policy was modified to use fast neutrons for preoperative irradiation. The preliminary results show that 7 patients, excluding a patient who expired by cardiac disease, were surviving from 22 months to 47 months without local recurrence or remote metastasis.

Table 6
Result of fast neutron therapy for the patients with malignant melanoma of the skin

Site		No Case	Result		
			CR(RT)	CR(N + S)	MT
ALM	Sole	12	2	8	2
	Hand	4	–	4	–
NM	Nose	2	–	2	–
	Ear lobe	1	–	1	–
	Neck	1	–	1	–
LMM	Nose	1	–	1	–
Total		21	2	17	2

ALM: Acral lentiginous melanoma
NM: Nodular melanoma
LMM: Lentigo maligna melanoma

Melanomas arising from head and neck were far advanced and were treated with fast neutron irradiation and surgery. Two of 12 patients have survived over 5 years. One of them was surviving without disease in 8 years and 9 months and the other expired by dissemination 7 years after treatment.
Reactions of skin and mucosa were severe in 8 cases (24%).

f) Osteosarcoma

The patients suffering from osteosarcoma have been treated with a policy for preservation of the function of the leg.

In the beginning of the study, the aim was placed on estimation of the effect of fast neutrons on normal tissue and osteosarcoma and the doses equivalent to TDF 120 were irradiated to the target volume. However, the efforts have not been rewarded by the fact that the late effect of the skin was more severe than expected. Necrosis of the irradiated tumour tissues were common in the histological specimens.

The second series of the trials was opened in 1979 with the doses equivalent to TDF 100 and was closed in 1981.

In this trial, an unirradiated area was made in one side of the leg in order to reduce the late reaction of the soft tissue.

In the third series, initiated in 1982, preservation of the leg was decided for the main purpose of the study and the doses were reduced again to equivalent to TDF 80 for making easy reconstruction of the leg, where the bone involved was replaced by an artificial material.

There were 54 patients suffering from osteosarcoma treated with fast neutron therapy between 1975 and 1984. Cumulative five year survival rate evaluated for 47 cases, excluding 7 patients who received palliative treatment only, was 67%, which was markedly contrasted with the rate of 19% for 18 patients who received photon beam irradiation.

The treatment for preservation of the leg was applied to 29 patients, 5 of whom received amputation due to marked soft tissue damage. There were no local recurrences and the patients, excluding 4 who expired, were surviving 5-96 months.

In the third series, 15 patients where involved and 13 were surviving without disease.

Necrosis of the skin and soft tissue developed in 4 of 8 patients (50%) who

Table 7
Skin reaction developed after radiation therapy (n:43)

	Early skin reaction				Late skin reaction		
	Reddening	Desquamation dry	moist	Ulceration	Atrophy	Pigmentation	Necrosis
^{60}Co Linac X-ray (18 cases)	18/18	18/18	7/18 (39%)	1/18 (5%)	8/8	8/8	4/8 (50%)
Fast neutron (25 cases)	25/25	25/25	9/25 (36%)	0/25	6/12 (75%)	9/12 (75%)	2/12 (17%)

received 90-130 Gy of photon beams and was seen in 2 of 12 patients (17%) treated with fast neutrons (Table 7).

Prior to surgery, chemotherapy was prescribed for the patients, through the regional arteries. When the disease was advanced, general administration of the drugs was performed in addition to the local infusion.

Adjuvant chemotherapy was continued during 18-24 months after surgical procedures.

Table 8

Results of radiation therapy for carcinoma of the urinary bladder evaluated with reduction of tumour volume (cystogram)

Reduction of volume	Fast neutrons	Photons
>50%	3	1
<50%	1	3
No change	2	4
Not evaluated	11	12
	17	20

g) Carcinoma of the urinary bladder

Preoperative irradiation with fast neutrons was designed to 17 patients who were suffering from carcinoma of the urinary bladder, stage c. The effects were evaluated with reduction of the tumour volume using cystogram and with histological finding. As to the tumour volume, the reduction over 50% was observed in 3 of 6 cases (50%) who received fast neutrons, and in 1 of 7 cases (12.5%) with photon beams. In this evaluation, cystograms were of value for estimation of the tumour volume (Table 8).

Discussion and conclusion

Clinical experiences suggest that the tumours have been controlled in higher rates by use of fast neutron beam, compared with photon beam irradiation, but the effects of fast neutrons and photons were found to be almost even in the sites where brachytherapy was common for management of cancers.

As to the indications, carcinoma of the salivary gland and esophagus, Pancost's tumour of the lung, osteosarcoma were selected for fast neutron therapy.

Fast neutron boost was applied to carcinoma of the larynx and glioblastoma multiforme and has contributed to improve local control of the tumour. For glioblastoma multiforme, 22 patients have received fast neutron boost, and 16% of whom have survived for five years. On the other hand, the data of the Brain Tumour Registry in Japan shows that, when photon beam irradiation was performed for 114 patients with glioblastoma multiforme, five year survival rate was 9.8%.

Preoperative irradiation with fast neutrons is of value in the teratment of carcinoma of the esophagus and urinary bladder, osteosarcoma, soft tissue sarcoma and malignant melanoma. The preliminary results of the treatment were promising and will be evaluated by the following clinical trials.

前立腺癌の放射線療法

千葉大学医学部泌尿器科学教室（主任：島崎　淳教授）
秋元　晋　布施　秀樹　島崎　淳
放射線医学総合研究所（所長：寺島東洋三）
森田新六　恒元　博

RADIOTHERAPY OF PROSTATIC CARCINOMA

Susumu Akimoto, Hideki Fuse and Jun Shimazaki
Department of Urology, School of Medicine, Chiba University
(Director: Prof J. Shimazaki)
Shinroku Morita and Hiroshi Tsunemoto
National Institute of Radiological Sciences
(Chief: T. Terashima)

During the period from 1976 to 1985, 28 cases with adenocarcinoma of the prostate localized in the pelvis (Stage A_2; 3, Stage B_1; 4, Stage B_2; 1, Stage C, Nx; 13, C, pN_0; 5, C, pN_1 (D_1) 2) underwent curative external radiotherapy. 21patients were treated by 100～131 TDF of fast neutron combined with or without Lineac X-ray and 7 cases were treated by 6,000～7,000rad of Lineac X-ray. The radiation fields were prostate in 13, small pelvis and prostate in 13, and small pelvis in 2.

16 patients were well controlled by radiation therapy, but 12 patients relapsed and were followed by endocrine therapy. The types of relapse were local growth in 3, distant metastases in 7, both in 1 and unknown in 1. These relapses occurred in the cases of large prostate cancer, small radiation field in Nx patients or low radiation dose.

The three-year disease-free survival rates of Stage A_2, B, C were 100%, 53%, 52%, respectively, and the five-year overall survival rates were 100%, 100%, 59%, respectively. Since 64% of the patients who were added with endocrine therapy were controlled for more than 2 years, endocrine therapy seems to be effective in the case of failure after radiotherapy. Severe complication which needed surgical treatment was in 1 case of sacral decubitus.

It was concluded that external radiotherapy was a good modality for prostate cancer localized in the pelvis.

要旨：千葉大学医学部泌尿器科において，1976年から1985年までの間に，放射線療法にて治療を開始した未治療前立腺癌のうち，骨盤内に限局する病期（Stage A_2 3，Stage B 5，Stage C,Nx 13，Staging Operation 施行 C,pN_0 5，D_1,pN_1，2）のものの予後を検討した．速中性子線単独あるいはリニアック X 線との併用が21，リニアック X 線単独 7 であり，照射線量は，速中性子線では TDF 100～131，リニアック X 線では6,000～7,000rad をおこなった．照射野は原発巣のみ13，小骨盤と原発巣13，小骨盤のみ 2 である．放射線療法で制癌中のものは16で，再発し内分泌療法を追加したものは12であった．後者の再発様式は，局所の制御不充分 3，遠隔転移＋局所の制御不充分 1，遠隔転移のみ 7，転医により不明 1 である．制癌し得なかった原因は，大きな原発巣，照射野設定不良，低線量に帰せられた．3 年非再発率は，Stage A_2 100%，Stage B 53%，Stage C 52%であり，5 年生存率は Stage A_2 100%，Stage B 100%，Stage C 59%であった．内分泌療法追加により64%が有効であることより，放射線療法後に再発した場合にも内分泌療法が有効であった．放射線障害で，外科的処置が必要であったのは，仙骨部褥瘡の 1 例のみであった．

以上より，骨盤内に限局せる前立腺癌に対する放射線療法の有効性を確認した．

緒　言

欧米においては，Stage C以下の前立腺癌に対する根治的治療法としての放射線療法は，有用性が認められ，約20年前より広く行なわれているが[1]，本邦においては，普及が遅れて実施されつつある[2]．千葉大学においては，未治療前立腺癌に対し，速中性子線を用いた放射線療法が優れた制癌効果をみることを，すでに発表した[3]．今回，放射線療法の第1適応である骨盤内限局癌に対する効果を，その後の症例を加えて検討した．

症例および治療方法

対象症例：1976年から1985年までに千葉大学医学部泌尿器科を受診した骨盤内に限局した未治療の前立腺癌28例（内訳は，Stage A_2 3, Staging Operation未施行のStage B_1 4, Stage B_2 1, Stage C（C,Nx）13, Staging Operationを施行し，pN_0のもの5（C, pN_0），pN_1のもの2（C,pN_1（D_1））の症例を対象とした．本論文では，C,Nx，C,pN_0およびC,pN_1（D_1）の3つを一括してStage Cとした．年齢は48歳から85歳までで，40歳台1例，50歳台1例，60歳台11例，70歳台13例，80歳台2例，平均70.0歳であった．病理組織分化度はGleason score分類[4]，及び前立腺癌取扱い規約の組織学的分類法[5]によった．なお，Stage Cの予後を比較するために，歴史的対照として，1961年から1985年までの期間に初回治療として内分泌療法を行った46例を用いた．

治療方法：速中性子線は，放射線医学総合研究所の30MeV（d → Be）サイクロトロン装置を用い，一部の症例はリニアックX線との混合照射を併用した．照射野が小骨盤の場合は，腸管の障害を少なくする目的で，リニアックX線との混合照射を，照射野が原発巣のみのときには，速中性子線単独を原則とした．Staging Operationを実施した場合pN_0およびpN_1までを放射線療法の適応として，最初の3例は小骨盤及び原発巣，次の4例は原発巣のみの照射とした．放射線医学総合研究所のサイクロトロンが稼動していない期間に，放射線療法を開始した例に対し，リニアックX線単独照射をした．照射方法は，速中性子線は前後2門，リニアックX線単独は対向4門で行った．線量は，中性子線とX線との算術加算では，線量を十分に表現できないため，time dose and fractionation（TDF）とした[6]．TDF 115は，リニアックX線，200rad×35回，7週間の線量に相当する．生存率，非再発率の算定は，Kaplan-Meier法により，有意差の検定は，generalized Wilcoxon testによった．

結　果

A）治療成績：対象症例28例の経過を表1に示した．観察期間は最短8カ月，最長114カ月，平均48カ月である．16（速中性子線21中11，リニアックX線7中5）は，放射線治療のみで制癌されており，12（速中性子線21中10，リニアックX線7中2）が再発し，内分泌療法（去勢，直後よりジエチルスチルベステロール2燐酸250～500mg/日約1カ月投与後，ヘキセステロール30mg/日又はエチニールエステラジオール1.5mg/日内服したもの10，去勢後酢酸クロルマジノン100mg/日内服したもの1，転医により去勢＋薬剤不明のもの1）を施行した．

再発様式は，局所の制御不充分3，遠隔転移＋局所の制御不充分1，遠隔転移のみ7，転医により不明1である．局所の制御不充分例は，いずれもStage Cで，1例を除き前立腺の大半を占める大きな腫瘍であった．そのうち2例は速中子線照射例であるが，TDF 100，101と低線量であった．遠隔転移例は，骨シンチにて骨転移が認められたもの4，頸部リンパ節転移1，酸性ホスファターゼ高値であるが，骨シンチにて骨集積像の認められないもの3であった．遠隔転移例のStage分布はB_1 2例，C 6例であり，初期のStaging Operation未施行にも拘らず照射野が前立腺部のみのものが3例あり，他の5例中3例はTDF 100，100，101と低線量であった．したがって制癌出来なかった原因として，大きな原発巣，照射野設定不良，または低線量に帰せられた．

内分泌療法追加12例で，追加直後の1例を除いた11例中，同療法で2年以上制癌されたものは7（64％）であった．他の4例は内分泌療法が無効であったが，いずれもStage Cであり，病理組織分化度にてGleason score 8が3，Gleason score 3が1であった．この内分泌療法の反応性の悪かったものは内分泌療法において，高危険群と考えられるものであった[7]．

表2は，Gleason scoreのStage別分布および前立腺癌取扱い規約の組織学的分類における分化度のStage別分布であるが，Stageが進むにつれ，前者の増点と後者の低分化傾向が認められた．これも，一般に認められていることである[8]．表3は，Gleason scoreと追加療法の有無との関係であるが，内分泌療法追加のものは，Gleason score 2～4では，33％，5～7では43％，8～10では46％とGleason scoreの増点にともない内分泌療法追加の比率が増加した．前立腺癌取扱い規約の組織学的分類における分化度との場合も，

表 1

放射線照射後再発をみない例

	年令	Stage	Gleason score	分化度1)	線　種	照射野	線量2)	照射開始より（月）
1.	71	B_2	3－3	中	速中性子線	小骨盤	100TDF	114 †（老衰）
2.	79	C	5－3	低	速中性子線	前立腺	100TDF	34 †（脳卒中）
3.	58	A_2	1－2	高	速中性子線	小骨盤→前立腺	102TDF	73
4.	66	B_1	5－4	低	速中性子線	小骨盤→前立腺	106TDF	73
5.	69	A_2	2－3	高	速中性子線	小骨盤→前立腺	100TDF	70
6.	70	C	3－2	高	速中性子線	小骨盤→前立腺	108TDF	81
7.	64	C	3－5	中	速中性子線	小骨盤→前立腺	124TDF	72
8.	75	C	3－5	中	速中性子線	前立腺	100TDF	44
9.	68	A_2	1－2	高	リニアックX線	前立腺	6000rad	29
10.	74	C,pNo	3－5	高	リニアックX線	小骨盤→前立腺	7000rad	25
11.	67	C,pNo	3－2	高	リニアックX線	小骨盤→前立腺	7000rad	24
12.	69	C,pNo	3－3	中	速中性子線	小骨盤→前立腺	105TDF	22 †（老衰）
13.	74	B_1	2－3	高	速中性子線	前立腺	110TDF	24
14.	70	D_1	2－3	高	リニアックX線	前立腺	6600rad	18
15.	77	C,pNo	5－3	低	リニアックX線	前立腺	6600rad	17
16.	64	D_1	3－2	中	速中性子線	前立腺	102TDF	8

放射線照射後内分泌療法追加例

▨ 内分泌療法追加開始からの期間

	年令	Stage	Gleason score	分化度	線　種	照射野	線量	照射開始より（月）
1.	80	C	3－5	中	速中性子線	前立腺	100TDF	6 13 †（癌死）
2.	85	C	2－1	高	速中性子線	前立腺	100TDF	60 80 †（癌死）
3.	74	C	3－4	中	速中性子線	前立腺	100TDF	9 42 †（癌死）
4.	76	C	3－3	高	速中性子線	前立腺	100TDF	3 77
5.	65	C	3－4	中	速中性子線	小骨盤→前立腺	100TDF	20 70
6.	73	B_1	3－3	中	速中性子線	小骨盤→前立腺	100TDF	27 68
7.	78	C	5－3	低	速中性子線	小骨盤→前立腺	101TDF	18 65 †（肺炎）
8.	64	C	3－5	中	速中性子線	小骨盤	101TDF	15 64
9.	66	B_1	2－3	高	速中性子線	小骨盤→前立腺	131TDF	17 52
10.	71	C	5－3	低	リニアックX線	前立腺	7000rad	9 36 †（癌死）
11.	48	C	5－3	低	速中性子線	小骨盤→前立腺	118TDF	2 29 †（癌死）
12.	65	C,pNo	3－3	高	リニアックX線	前立腺	6000rad	10 11

1）前立腺癌取扱い規約の組織学的分類法
2）TDF : time dose and fractionation

ほぼ同様の傾向をみた．

Stage Cにおいて，高分化型は低分化型よりも有意に良い治療成績を示した（図1）．放射線治療開始から再発までの期間を求め，非再発期間を算定した（図2）．Stage A_2 B，Cで再発したものは，おのおの0，2，10であり，3年非再発率は，Stage A_2 100%，Stage B 53%，Stage C 52%であった．Stage CにおいてはGleason scoreの増点と前立腺癌取扱い規約の組織学的分類における分化度の低分化傾向にともない，3年非再発率は低下した．すなわち，Gleason score 2～4が1例のみのため，Gleason score 2～7とGleason score 8～10に分けると，それぞれ54%，48%であり，又，高分化型71%，中分化型44%，低分化型30%であった．

表 2

Gleason score と Stage

Gleason score	2～4	5～7	8～10	計
Stage A_2	2	1		3
B		4	1	5
C (D_1を含む)	1	9	10	20
計	3	14	11	28

前立腺癌取扱い規約組織学的分類と Stage

分化度	高分化型	中分化型	低分化型	計
Stage A_2	3			3
B	2	2	1	5
C (D_1を含む)	7	8	5	20
計	12	10	6	28

表 3　Gleason score と追加療法の有無

Gleason score	2～4	5～7	8～10	計
放射線療法単独	2	8 (2)	6 (1)	16 (3)
内分泌療法追加群	1 (1)	6 (1)	5 (4)	12 (6)
計	3 (1)	14 (3)	11 (5)	28 (9)

( ) 死亡例

Stage A_2, B, C の実測 5 年生存率はそれぞれ100%, 100%, 59%であった（図は示さず）. Stage C を放射線照射単独例（A 群）, 内分泌療法追加例（B 群）に分け, 1961年から1985年までの期間に初回治療として去勢およびジエチルスチルベステロール 2 燐酸250～500 mg/日以降ヘキセストロール30mg/日あるいはエチニールエストラジオール1.5mg/日又は酢酸クロルマジノン100mg/日を内服した46例（C 群）と比較すると, 生存曲線が A 群は B, C 群と比し良い傾向をみたが, 統計的な有意差はなかった（図 3 ）.

B）死因：全28例のうち, 死亡は 9 例である. このうち癌死は 5 例（56%）で, Stage A_2, B では癌死はなく, 全て Stage C であった. 他病死は, 老衰 2 例, 肺炎 1 例, 脳卒中 1 例であった.

C）放射線障害：膀胱刺激症状, 皮膚糜爛などの早期放射線障害は, 治療の継続を妨げるものはなく, 晩期放射線障害は, 尿失禁 3（2 は TUR 後の障害, 1 は原因不明）, 仙骨部褥瘡 2, 陰茎屈曲 2, 血便 2, 尿道狭窄 1, 持続する下痢 1, 計11例に認められたが, 外科的処置が必要であったものは, 仙骨部褥瘡の 1 例のみであった.

図 1　放射線療法 Stage C 組織分化度別予後

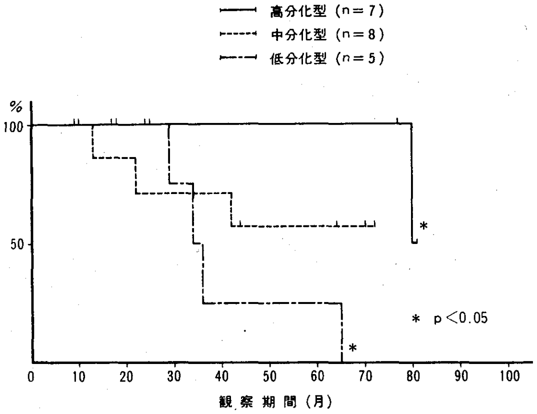

図 2　非再発期間

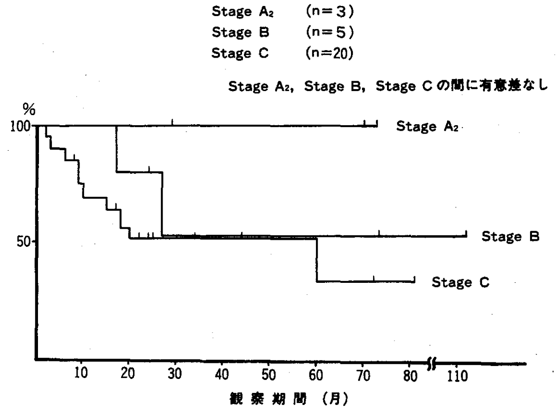

図 3　Stage C の生存曲線

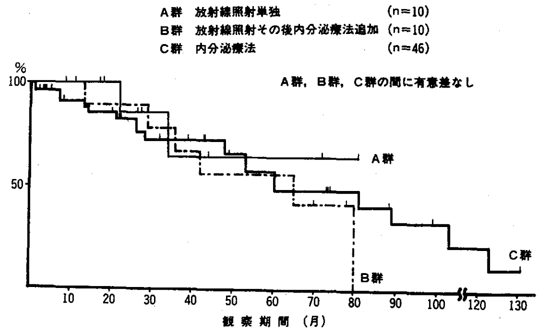

考　案

骨盤内限局前立腺癌の治療法として, 根治的前立腺全摘除術が行なわれているが, 同施行例においては 0 ～ 5 %の術後死亡と10～60%の尿失禁の合併症の危険

があり9)，合併症の多い高齢者の癌である本疾患に対する実施は，未だ問題が多く，本邦においては一般的な治療法に至っていない．一方，放射線療法は，手術療法にみる合併症がないうえに，制癌効果が強く，ほぼ手術療法と同じ生存率のため欧米では広く普及してきた10)．

局所の制御不充分なものについて自験例は14％であったが，これはCuppsらの報告11)14％と同じである．Aristizabalら12)はStage Cの局所の再発率を3施設で比較しており，Stage Cでは，局所の再発はそれぞれ25％，13％，12％であったという．自験例の局所制御不充分例は，いずれもStage Cであり，同Stageの20％であった．照射方法の改善が必要なことであろう．高橋ら13)は，あらかじめエストロゲンなどにより原発巣を縮小してのち照射することを主張しており，これも一つの方法と考えられる．

非再発期間は，前立腺癌の制御についての放射線療法の有効性をそのまま反映するために重要である．Stage，Gradeと放射線療法後再発するまでの期間は良く相関するという報告もあるが，自験例でも同様の傾向をみた．

骨盤リンパ節転移は，Stage A_2の23％，Stage B_1の15～20％，Stage B_2の35％，Stage Cの50％にみられるとされ14)，当教室ではStage Cで71％の陽性率をみた15)．Stage Cにおいて，前立腺部のみの照射と全骨盤＋前立腺照射を比較した場合，5年生存率，3年非再発率とも後者の成績がよかったという16)．自験例においても，Staging Operation未施行のStage Cで，照射野が前立腺部のみである初期例7例5例が再発しており，Staging Operation未施行にてリンパ節転移の有無が不明な場合には，骨盤部に照射野を広げる必要性は当然であろう．しかし，Smithら17)は，N(＋)の骨盤内照射をした72％は5年以内に再発（局所，全身）をし，5年で再発のない生存例は，わずか17％であったとしており，N(＋)の予後は不良である．N(＋)に対して，照射野を傍大動脈リンパ節を含む領域まで拡大しても，生存にはほとんど影響をおよぼさないという18)．以上のことから，N(＋)例には，放射線療法のみでは，根治できないといえる．しかし，本報告の2例はいずれもpN_1であり，観察期間は8カ月，18カ月と短いが，再発をみていない．

放射線療法にて再発しても，その64％が内分泌療法にて2年以上制癌し得たので，一般に約80％の前立腺癌が内分泌療法に反応するとされている7)ことを考えると，放射線療法を先行させ，無効例に対しての内分泌療法の治療効果は期待出来るといえる．

放射線療法による5年生存率をStage Cのそれで比較すると，Harisiadisら19)58％，高橋ら13)，59％，Aristizabalら12)60％，Bagshaw10)60％，Rosenら20)61％と約60％が多く，自験例でも59％であった．しかしKurupら21)74％，Ploysongsangら16)81％と更に良好な成績も近年みられているので，照射方法の改善が必要なことである．多くの報告は，Staging Operation未施行例であり，約半数のN（＋）が含まれているので，C，pN_0の放射線療法の治療成績は，更に向上すると考えられ，適応の選択が必要であろう．

放射線療法の治療成績は，内分泌療法の本邦報告例における5年生存率である高安ら22)51％，竹内ら23)45％，丸岡ら24)50％と比較すると，幾分良好であり，これは照射による局所の制癌効果が，内分泌療法とくらべ，同程度以上に強力であることを示している．アメリカでは，ここ10年間でStage Cにおける放射線療法の割合が著増しており，根治的前立腺摘出術は減少している25)．後者の良好な治療成績の報告26)27)もあるが，本邦においても，Stage C以下の前立腺癌における放射線療法は，今後一層一般的なものになるであろう．

速中性子線は，低酸素細胞に与える効果が強く，腫瘍細胞の致死障害からの回復を遅らせることが特徴である．Laramoreら28)によれば，局所の制御や生存率について，速中性子線とリニアックX線との混合照射術は，リニアックX線単独照射例よりも良好な成績であったという．今回の報告ではリニアックX線のみの施行例は，観察期間が短かく，症例数も少ないため速中性子線施行例との治療成績の比較検討が出来なかった．しかし，両方法とも現時点では同様の制癌効果をみた．

速中性子線は，脂肪組織に，X線よりも14％多く吸収されるとされ，皮膚及び皮下組織の放射線損傷が懸念されたが，外科的処置を必要としたものは1例のみであった．

結　語

1976年から1985年までに，千葉大学医学部泌尿器科を受診した骨盤内限局の未治療前立腺癌28例に対して，速中性子線又はリニアックX線による放射線療法を施行し，以下の結論を得た．

1. 放射線療法で制癌中16例，再発し内分泌療法を追加したもの12例であり，制癌し得なかった原因は，大きな原発巣，照射野設定不良，低線量に帰せられた．

2．Stage A_2，B_1，Cの3年非再発率はそれぞれ100%，53%，52%，5年生存率は100%，100%，59%であった．

3．内分泌療法を追加したものの64%が有効であることより，放射線療法後に再発した場合でも内分泌療法は有効なことが示唆された．

4．放射線障害で，外科的処置が必要であったのは仙骨部褥瘡の1例のみであった．

本研究の一部は厚生省がん研究助成金によった．

文　献

1）Bagshaw, M.A., Kaplan, H.S. and Sagerman, R. H.: Linear accelerator supervoltage radiotherapy. VII. Carcinoma of the prostate. Radiotherapy, 85, 121—129, 1965.

2）Tsuya, A., Kawai, T., Fukushima, S., Shida, K., Shimazaki, J., Matsumoto, K. and Seto, T.: Radiotherapy combined with hormone therapy for prostate cancer. Strahlentherapie, 148, 24—34, 1974.

3）丸岡正幸，安藤　研，野積邦義，伊藤晴夫，島崎淳，松嵜　理，森田新六，恒元　博：前立腺癌の速中性子線療法．日泌尿会誌，74，409—417，1983．

4）Gleason, D.F. and The Veterans Administration Cooperative Urological Research Group: Histologic grading and clinical staging of prostatic carcinoma. in Urological Pathology: The Prostate, p. 171—197, Lea & Febiger, Philadelphia, 1977.

5）日本泌尿器科学会，日本病理学会編：前立腺癌取扱い規約，第1版，66—79, 1985.

6）Orton, C.G. and Ellis, F.: A simplification in the use of the NSD concept in practical radiotherapy. Brit. J. Radiol., 46, 529—537, 1973.

7）島崎　淳，伊藤晴夫，宮内大成，布施秀樹，井坂茂夫：前立腺癌の内分泌療法．Oncologia, 10, 82—98, 1984.

8）島崎　淳，布施秀樹，座間秀一：前立腺癌．癌の臨床，31，1195—1201，1985．

9）Nichols, R.T., Barry, J.M. and Hodges, C.V.: The morbidity of radical prostatectomy for multifocal stage I prostatic adenocarcinoma. J. Urol., 117, 83—84, 1977.

10）Bagshaw, M.A.: Potential for radiotherapy alone in prostatic cancer. Cancer, 55, 2079—2085, 1985.

11）Cupps, R.E., Utz, D.C., Fleming, T.R., Carson, C. C., Zincke, H. and Myers, R.P.: Definitive radiation theapy for prostatic carcinoma: Mayo Clinic Experience. J. Urol., 124, 855—859, 1980.

12）Aristizabal, S.A., Steinbronn, D. and Heusinkveid, R.S.: External beam radiotherapy in cancer of the prostate. Radiother. Oncol., 1, 309—315, 1984.

13）高橋　卓，河合恒雄，鷲塚　誠，楠山弘之：前立腺癌Stage Cにおけるエストロジェン先行・放射線治療の試み．臨泌，40，225—229，1986．

14）Donohue, R.E., Fauver, H.E., Whitesel, J.A., Augspurger, R.R. and Pfister, R.R.: Prostatic carcinoma. Influence of tumor grade on results of pelvic lymphadenectomy. Urology, 17, 435—440, 1981.

15）布施秀樹，座間秀一，秋元　晋，島崎　淳，松嵜理，村上信乃，五十嵐辰男：前立腺癌のstaging pelvic lymphadenectomy．泌尿紀要，32，1465—1470，1986．

16）Ploysongsang, S., Scott, R.M., Aron, B.S., Ho, P.Y., Shehata, W.M., Morand, T.M. and Jazy, F.K.: Comparison of whole pelvis versus small-field radiation therapy for carcinoma of prostate. Urology, 27, 10—16, 1986.

17）Smith, J.A., Haynes, T.H. and Middleton, R.G.: Impact of external irradiation on local symptoms and survival free of disease in patients with pelvic lymph node metastasis from adenocarcinoma of the prostate. J. Urol., 131, 705—707, 1984.

18）Sause, W.T., Richards, R.S. and Plenk, H.P.: Prostatic carcinoma: 5-year follow up of patients with surgically staged disease undergoing extended field radiation. J. Urol., 135, 517—519, 1986.

19）Harisiadis, L., Veenema, R.J., Senyszyn, J.J., Puchner, P.J., Tretter, P., Romas, N.A., Chang, C.H., Lattimer, J.K. and Tannenbaum, M.: Carcinoma of the prostate: Treatment with external radiotherapy. Cancer, 41, 2131—2142, 1978.

20）Rosen, E.M., Cassady, J.R., Connolly, J. and Chaffey, J.T.: Radiotherapy for localized prostatic carcinoma. Int. J. Radiat. Oncol. Biol. Phys., 10, 2201—2210, 1984.

21）Kurup, P., Kramer, T.S., Lee, M.S. and Phillips, R.: External beam irradiation of prostate cancer. Cancer, 53, 37—43, 1984.

22）高安久雄，小川秋実，小磯謙吉，小峰志訓，石井泰憲：前立腺癌の治療成績．日泌尿会誌，69，426—435，1978．

23）竹内弘幸，山内昭正：前立腺癌のhormone療法における継続的estrogen投与の意義に関する臨床的研究．日泌尿会誌，69，1552—1561，1978．

24）丸岡正幸，安藤　研，野積邦義，安田耕作，伊藤晴

夫, 島崎　淳, 松嵜　理, 村上信乃：前立腺癌の内分泌療法. 日泌尿会誌, 73, 432—437, 1982.

25) Schmidt, J.D., Mettlin, C.J., Natarajan, N., Peace, B.B., Beart, R.W. Jr., Winchester, D.P. and Murphy, G.P.: Trends in patterns of care for prostatic cancer, 1974—1983: Results of surveys by the American College of Surgeons. J. Urol., 136, 416—421, 1986.

26) 千葉隆一, 石井延久, 常盤峻士, 目時利林也：前立腺癌に対する経恥骨式前立腺全摘出術症例の術後成績とその予後. 日泌尿会誌, 72, 407—415, 1981.

27) Schroeder, F.H. and Belt, E.: Carcinoma of the prostate: A study of 213 patients with stage C tumors treated by total perineal prostatectomy. J. Urol., 114, 257—260, 1975.

28) Laramore, G.E., Krall, J.M., Thomas, F.J., Griffin, T.W., Maor, M.H. and Hendrickson, F. R.: Fast neutron radiotherapy for locally advanced prostate cancer: Results of an RTOG randomized study. Int. J. Radiat. Oncol. Biol. Phys., 11, 1621—1627, 1985.

(1987年２月16日受理)

II. 治療可能比向上のための時間的，空間的線量配分

高 LET 放射線治療の現況

森田新六[*1]　恒元博[*1]　青木芳朗[*1]
久保田進[*1]　中野隆史[*1]　五味弘道[*1]
熊谷和正[*1]　荒居竜雄[*1]　佐藤真一郎[*1]
飯野祐[*2]　熊沢昭良[*2]　小野田昌一[*3]
島崎淳[*4]　高田典彦[*5]　鎌田信悦[*6]
尾形佳郎[*7]　花岡英弥[*8]　笠松達弘[*9]
森俊二[*10]

はじめに

日本の粒子線治療トライアルは，現在放射線医学総合研究所（放医研）で30 MeV速中性子線治療と70 MeV陽子線治療，東京大学医科学研究所（医科研）で14 MeV速中性子線治療，筑波大学粒子線医科学センターで250 MeV陽子線治療が行われている．速中性子線は優れた生物効果（高RBE, Relative Biological Effectivenessや低OER, Oxygen Enhancement Ratio）を，陽子線は優れた線量分布（Bragg peak）を生かした治療である．

本報告では，高 LET 放射線治療の観点から，速中性子線治療について本年2月に行われた放医研の粒子線治療研究委員会・臨床部会で報告されたデータを中心に，放医研の成績を検討し，さらに医科研の成績も加えて，現在の問題点を明らかにしたいと考えた．

1. 症　例

放医研では昭和50年に，医科研では昭和51年に，速中性子線治療を開始した．治療症例数は61年末までに放医研で1,496名，医科研で391名であった．対象は多岐にわたっているので，各疾患毎の症例数は50～150名である．これらはすべて紹介患者である．放医研で速中性子線治療の適応となった疾患毎の頻度は，婦人科癌23%，頭頸部癌16%，肺癌11%，食道癌10%，骨腫瘍7%，軟部組織腫瘍6%，泌尿器癌5%，脳腫瘍5%，皮膚癌（悪性黒色腫を含む）4%の順であり，医科研では頭頸部癌35%，肺癌29%，乳癌7%，食道癌5%，軟部組織肉腫5%，悪性黒色腫5%，骨肉腫2%，婦人科癌2%であった．両施設の頻度の差は，サイクロトロン加速エネルギーの違いによるところが大きい．

このうち，速中性子線とX線の対比を行うクリニカル・トライアルを行ったものは，放医研では進行期子宮頸部扁平上皮癌，喉頭癌，膀胱癌，医科研では肺癌であった．ランドマイズの方法は，厳格な意味でのアメリカ方式とは異なるが，放医研方式を採用している．すなわち，サイクロトロンのマシンタイムに合わせた振り分け法で，サイクロトロンの稼動中で，スケジュール通りの治療が可能な場合は速中性子線治療を，それ以外のサイクロトロン調整期間中はX線治療を行うことと

[*1] 放射線医学総合研究所病院部
[*2] 東京大学医科学研究所放射線科
[*3] 千葉大学医学部第二外科
[*4] 千葉大学医学部泌尿器科
[*5] 千葉県がんセンター整形外科
[*6] 癌研究会病院頭頸科
[*7] 栃木県がんセンター外科
[*8] 慶応大学医学部整形外科
[*9] 国立がんセンター病院婦人科
[*10] 岐阜大学医学部皮膚科

表 1　速中性子線照射の条件

	放医研	医科研
加速エネルギー	30 MeV（d-Be）	14 MeV（d-Be）
ビーム	垂直（臥位） 固定	水平（坐位） 固定
照射門	対向2門	対向2門
50％線量 （10 cm×10 cm）	12 cm	8 cm
線量分布	コバルト60と同様	セシウム137と同様

した．調整期間は夏休み，年末年始，5月ゴールデンウィークと年3回である．

2. 照射スケジュール

放医研と医科研の照射の条件を表1に示した．サイクロトロンの加速エネルギーが放医研30 MeV（d-Be），医科研14 MeV（d-Be），50％線量（10 cm×10 cm）は12 cmと8 cm．ビームは垂直固定1門（臥位）と水平固定1門（坐位），線量分布はCo-60あるいはCs-137のそれと類似している．マシンタイムは週3回（火，水，金）と週2回（月，金）である．照射スケジュールは，① 速中性子線単独照射，② ミックス照射（中性子線週2回，X線週3回），③ ブースト照射（X線30～40 Gy照射後に速中性子線を追加）であり，それぞれの1週照射線量，合計の目標線量を表2に示した．このようなスケジュールにおいて，速中性子線のX線に対するRBEは3.0と計算している．総照射線量は，照射野が広い場合はTDF* 80～90（50～55 Gyに相当），小さな照射野の場合はTDF 110～120（60～70 Gy）を目標にしている．* TDF＝Time Dose Fractionation（生物学的等価TDF法）[1]

これら照射スケジュールの各疾患毎の比率を検討すると，中性子線単独照射では根治照射例が意外と少なく，術前照射のトライアルを行った例が多かった．食道癌，膀胱癌，骨肉腫，悪性黒色腫などが含まれる．中性子線とX線のミックス照射は比較的照射範囲が広い疾患に，晩発障害を軽減する意味合で用いられた．子宮頸癌の進行期例でランドマイズ・クリニカル・トライアルが行われた．医科研の肺癌のトライアルも，速中性子線は週2回医科研で，X線は週3回紹介病院で行うという変則スケジュールで治療されている．ブースト照射は比較的広い照射野でX線照射を開始し，腫瘍を小さくしてから，狭い範囲で速中性子線を追加照射する場合と，あるいはX線照射したが縮小が少なく，腫瘍が残存しそうなので，速中性子線を追加照射した場合がある．しかしブースト照射の頻度が多かったのはマシンタイムの影響も強く，中性子線単独では線量が不足なので，X線照射が追加された，という例が多かった事情もある．これには脳腫瘍，頭頸部腫瘍，肺癌，子宮頸癌などが含まれた．このうち喉頭癌は癌研との間でランドマイズ・クリニカル・トライアルを行った．

表 2　照射スケジュール

	放医研	医科研
マシンタイム	週3回 （火・水・金）	週2回 （月・金）
速中性子線・単独	270 cGy/3回/週 6～7週 （TDF 100～120）	240 cGy/2回/週 7週 （TDF 101）
ミックス照射	速中性子線： 144 cGy/2回/週 X線： 510 cGy/3回/週 5週（TDF 85）	速中性子線： 160 cGy/2回/週 X線： 540 cGy/3回/週 6週（TDF 104）
ブースト照射，X線の30～40 Gy照射後	270～300 cGy/ 3回/週 2～3週 （合計 TDF 120）	240 cGy/2回/週 3週 （合計 TDF 102）

3. 治療成績

1）速中性子線単独照射の成績

手術不適な早期肺野型肺腺癌例[2]，小さな再発子宮頸癌例[3]，大きな腫瘤の前立腺癌例[4]など，個々の例では期待通りの局所制御効果を得て，速中性子線照射の有用性を強く印象づけられている．これらの印象を裏づけるために，以下のトライアルが各関連施設の協力で遂行された．

(1) 食道癌

千葉大医2外との共同研究として速中性子線の術前照射が行われ，切除標本の病理組織学的解析

で効果が検討された．線量はTDF 50～60が原発巣に照射される．中性子線またはX線単独照射の場合と，これにブレオマイシンと免疫療法を併用した場合の結果を表3にまとめた．食道癌取扱い規約の判定規準による無効，乃至やや有効（Ef 1）は，中性子線27.3%，コバルトγ線35.9%，有効（Ef 2・Ef 3）は72.7%と64.1%，ことに著効Ef 3は27.3%と16.5%であった．とくに補助療法を加えた場合のEf 3の比率が多くなっており，速中性子線の原発巣に対する効果のγ線より優れていることの証明であった．この局所効果が遠隔成績に結びつくかどうかは，食道癌切除例の術前合併療法からみた5年生存率で検討している．合併療法なしの群：21.2%（126例），γ線照射群：22.7%（172例），中性子線照射群：18.5%（42例）で有意差はなかった．これはリンパ節転移や脈管内侵襲といった他因子が，原発巣に対する局所効果の改善を修飾してしまうためと考えている．

表 3　術前合併療法別にみた食道癌原発巣に対する組織学的効果
（千大医2外・小野田）

術前照射法		組織学的効果		
		Ef 1	Ef 2	Ef 3
照射単独	速中性子線 15例	6 （40%）	7 （47%）	2 （13%）
	X線　39例	21 （54%）	13 （33%）	5 （13%）
照　射 ＋BLM 免疫療法	速中性子線 18例	3 （17%）	8 （44%）	7 （39%）
	X線　64例	16 （25%）	36 （56%）	12 （19%）

(2) 膀胱癌

浸潤性膀胱癌の術前照射を千葉大医泌尿器科との共同研究で行った．速中性子線群とX線群を放医研方式で振り分けてランドマイズした．TDF 60（速中性子線 910 cGy/7回/15日，X線 3,000 cGy/10回/15日）を膀胱全体に照射し，終了後1～2週間で，膀胱全摘術を施行し，術後化学療法を加えた．昭和56年2月から61年12月までに中性子線群20例，X線群29例で，① 病理組織学的照射効果（大星・下里分類のGrade Ⅱb, Ⅲ）の比較で，中性子線群30%，X線群24%，② 術前と術後のT分類のdown stageの割合の比較で，中性子線群32%，X線群31%，③ N＋，M＋は除いたT2またはT3症例の照射方法別遠隔成績でも，5年累積生存率が中性子線群82%（13例），X線群76%（15例）有意差なし，という結果であった．

(3) 骨肉腫

千葉県がんセンター整形外科との共同研究を行っている．骨肉腫のように肺転移を生じやすい疾患では，局所治療のほかに全身治療が重要になってくる．また患肢を切断せずに温存できれば，患者・家族にとって非常な幸いである．したがって，これらのことを含んだ集学的治療が治療方針として適当になる5)．速中性子線がこれら集学的治療の中で占める役割はなにか，これを明らかにすることが本トライアルの目的の一つであった．初期にはTDF 120まで照射していた線量が，術後の皮膚修復のさまたげとなり，しかもTDF 70～80の線量で，患肢温存のための切除手術のsurgical marginの安全性を確保できることが判明している5)．局所再発率は5.9%（3/51）であり，再発例はいずれも照射範囲の設定不良などによるもので，照射野外の再発であったことは，中性子線の局所制御での有効性を示している結果といえる．骨肉腫の集学的治療の結果としての累積生存曲線を図1に示す．中性子線群の5年生存率は67%（48例）で，とくに患肢温存群は85%（20例）であった．X線群はhistorical controlだが19%（39例）であった．

(4) 軟部組織肉腫

慶応大医整形外科との共同研究を行った．昭和54年から61年までの39例（脂肪肉腫16例，滑膜肉腫6例，横紋筋肉腫4例など）を手術的にmarginal resectionしたあと，局所再発防止の目的で速中性子線（22例）とX線（17例）を照射し，対比した．線量はTDF 80を目標とした．局所再発率は中性子線群23%（5/22），X線群23%（4/17）で差がなく，5年累積生存率も77%（中性子線群）と81%（X線群）と有意差がなかった．

2）ミックス照射の成績

(1) 子宮頸部扁平上皮癌

放医研のみでランドマイズ・クリニカル・トラ

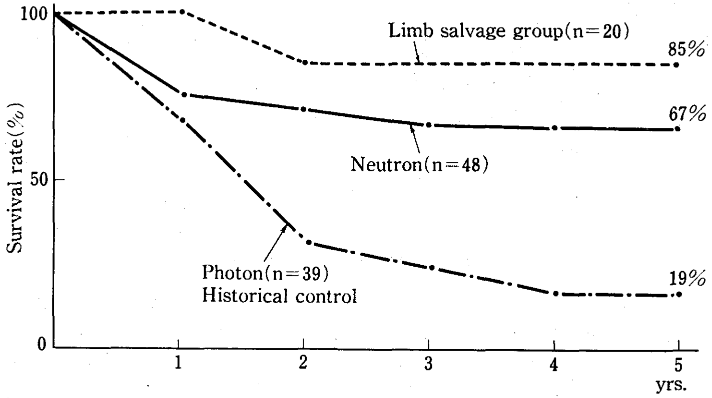

図 1　速中性子線治療を行った骨肉腫患者の累積生存曲線
（千葉県がんセンター・高田）

イアルを行うには，症例数の多い過去の実績のある子宮頸癌が最適と考えられた．進行期 3 b，4 a の症例が，前述の放医研方式の振り分け法で，中性子線群とX線群に分けられた．照射線量は，外照射で全骨盤に 50 Gy 相当，ラルス腔内照射でA点 10 Gy/ 2 回を基準とした．治療結果として，① 粗 5 年生存率：中性子線群 43%（18/42)，X線群52%（27/52）有意差なし，② 局所障害発生率も，中等度以上の障害で38%（中性子線群）と42%（X線群）で有意差なし，③ 病理組織学的検討でも局所制御率で，大細胞癌で中性子線群78%（29/37)，X線群 58%（23/40）と多少の差が認められたが，全体的には有意差がなかった．これらのことより，子宮頸部扁平上皮癌の中性子線とX線のミックス照射は，臨床的に有意でないと結論された[6,7]．

(2) 術後子宮頸部腺癌

国立がんセンター婦人科との共同研究でトライアルが行われた．従来，予後が悪いと考えられていたT2N1症例の 6 例中 3 例が生存中で，局所制御率も7/10（3 年経過）と比較的良好な，期待のもてる結果が得られている．

(3) 肺　癌

東大医科研サイクロトロンの速中性子線治療結果を示す．ランドマイズ・トライアルを行いにくかったので，次善のものとして，積極的な協力を得ている病院で，同時期にリニアックX線で治療された例を対照とした．症例数は中性子線群62例（1 期：12，2 期：6，3 期：21，4 期：23)，X線群 134 例（1 期：12，2 期：41，3 期：38，4 期：43）であった．両群の粗生存曲線を病期別に比較したのが図 2 である．有意差は 2 期の 1 年生存で P <0.05が示されているが，1 期，2 期では十分期待が持てるとの印象をうけた．3 期は転移死が多いのでこのような結果になったと思われるが，原発巣を制御することが生存率の向上につながるので，そのための努力は必要である．この点パンコスト型肺癌は腫瘍の発生部位が十分線量の照射を可能にするので，中性子線の効力を十分に生かせる利点がある．5 年累積生存率の23%（22例）は優れた成績と考える[8]．

3）ブースト照射の成績

(1) 喉頭癌

癌研頭頸科との共同研究が昭和54年より開始されている．初期のトライアルで喉頭癌31例と下咽頭癌 8 例が検討され，喉頭癌は NO 症例に限定してコントロール・スタディに移行することができたが，下咽頭癌は原発病巣の制御が 2/8 であったが，頸部リンパ節転移の多いことで，総合的に治癒率を改善することが難かしいと判断されて，このトライアルは中止された[9]．昭和57年に開始された NO 症例のトライアルは，X線 30〜40 Gy 照射後に根治照射か手術かを決定し，さらに封筒法で中性子線ブーストかX線続行かを決定した．その結果は表 4 に示した．原発巣の制御率において，中性子線群とX線群の有意差はなかった．したがって，現時点では喉頭癌は中性子線照射の適応でないとされた．

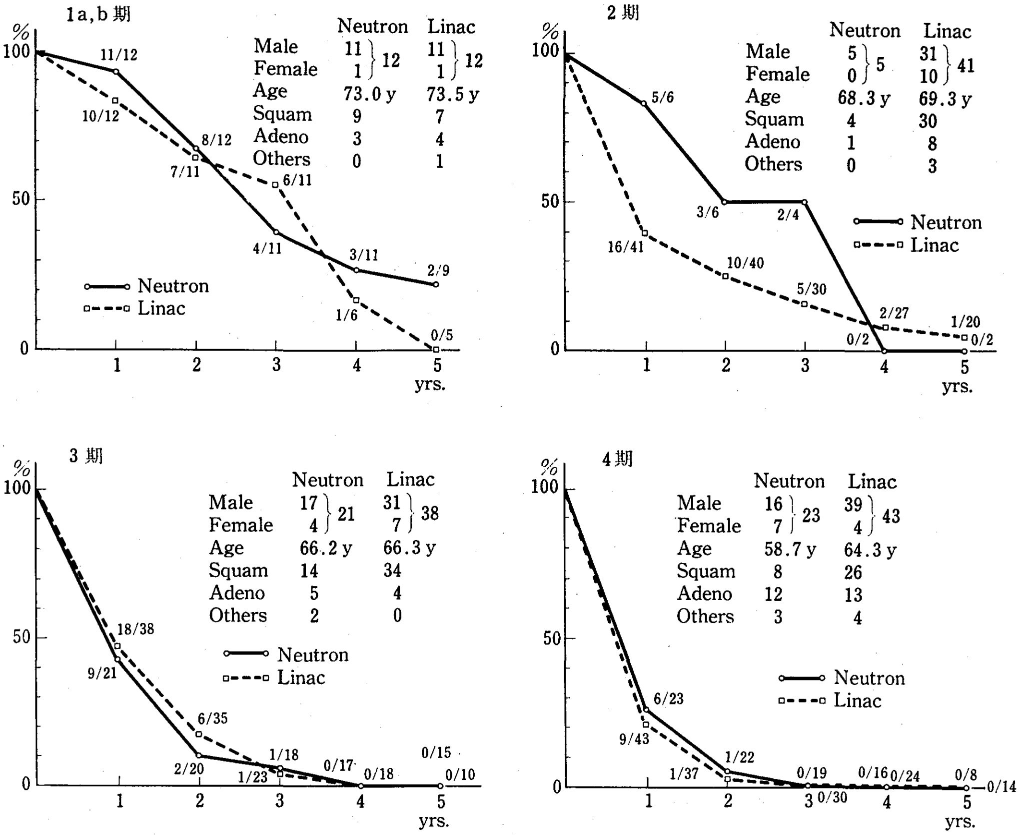

図 2　肺癌の期別放射線治療成績粗生存率曲線
（東大・医科研飯野・熊沢）

(2) 脳腫瘍

Glioblastoma multiforme も主としてブースト治療されている．X線照射の照射野の設定はX線CT スキャンを参考にして，腫瘍境界より 2 cm はなした．中性子線のブースト照射の際はなるべく小さな照射野を設定して，全脳照射は行っていない．線量はX線で 40 Gy 照射した後，中性子線を TDF 90～94 まで追加した．全国統計の治療成績を上廻る生存曲線が得られている（図 3）10)．さらに線量分布をよくして，多くの線量を照射できれば，期待十分な治療法と考える．

(3) 膵　癌

慶応大医外科との共同研究で行われたこの疾患は，もっとも速中性子線治療の効果が期待されたものの一つであった．昭和55年より 9 例治療された結果を表 5 に示した．ミックス照射が主体で，線量は TDF 61～113（平均 88）で，進行期症例の治癒切除例に局所再発なしの例がみられたが，副作用の面で十二指腸・空腸よりの出血がきびしく，癌の遺残がないにもかかわらず，これが原因で死亡した例があった．正確な線量分布を形成することが決め手であり，今後に改善の余地を残した結果であった．

表 4　喉頭癌に対する速中性子線ブースト治療原発巣制御率（1982～1985）

T分類	リニアック X線	X線＋中性子線ブースト	（X線＋）手術
T1	23/28	6/7	1/1
T2	7/11	3/7	5/5
T3	0/1	0/1	22/22
T4	0/1	0/1	7/8

（癌研頭頸科・鎌田）

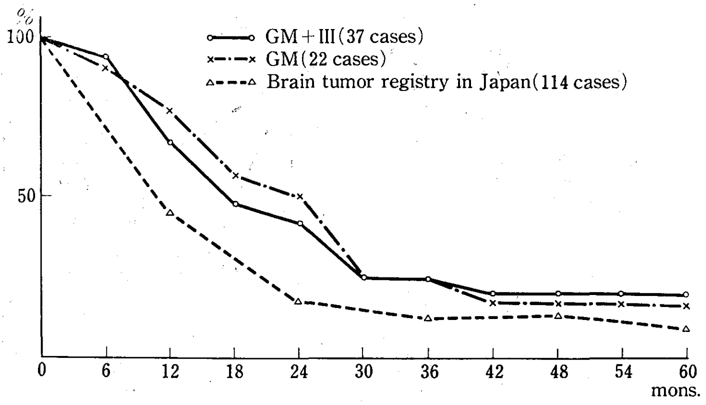

図 3　悪性神経膠腫の速中性子線治療相対生存曲線（放医研・青木）

表 5　膵癌の速中性子線治療（慶応大医外科・尾形）

	手術術式	例数	生　存	癌　死	他因死
膵頭部	治癒切除	2	1（2年）		1（3年）*
	非治癒切除	2		2（10ヵ月 16ヵ月）	
	非　切　除	1		1（9ヵ月）	
膵体部	治癒切除	0			
	非治癒切除	1		1（9ヵ月）	
	非　切　除	3		3（12ヵ月 2.3ヵ月 9.5ヵ月）	

＊空腸よりの出血→輸血→肝不全で死亡

4. 考　察

速中性子線治療の評価を Cohen[11] が述べている．1983年までに世界中で9,000例以上が治療されている．ほとんどが non-randomized であり，各国での治療方針や方法はまちまちであるが，概していえることは，① 副作用は強いが，局所制御能はX線より良好，② 頭頸部の扁平上皮癌では明らかに生存率がよい．③ ミックス照射治療では差が出そうもない，④ 耳下腺，膵，胃，大腸などの腺癌は高LET放射線に反応する，⑤ 骨肉腫，軟部組織肉腫，悪性黒色腫といった抵抗性癌も局所制御率がX線に比べて高い，⑥ 脳腫瘍は治療可能比が小さくてむずかしい，ということであった．しかし頭頸部の扁平上皮癌の成績がよいというのも，ハマースミス病院のトライアルと頸部リンパ節の成績を除けば利点がないという見方[12]もあり，最近の Duncan の報告[13]もそれを裏づけた．

今回の報告の成績に，若干のデータを追加して，日本での成績をまとめたのが表6である．これからもわかるように，X線照射との間にランドマイズ・トライアルを行った子宮頸癌，膀胱癌，喉頭癌では，局所制御効果に多少よい傾向はみえても，生存率の上では有意差が認められていない．食道癌でも同様であった．これは症例数の少ないことと，進行期症例の他の因子の関与が大きすぎることによると考えられる．個々の症例をみると，副作用をあまり考えずにすむ部位に，十分線量を照射し得た場合は，差のある結果に結びついてくる事実があるので，線量分布をよくして，十分線量を照射することが，中性子線の生物効果

表 6　速中性子線治療の評価（1987，放医研）

疾患部位	速中性子線照射			局所効果		遠隔成績		備　考	文　献
	目的	方　法	線　量 TDF	組織的	臨床的	生存率	副作用		
脳	術後	ブースト	90～94			○		限局照射	青　木10)
喉　頭	根治	ブースト	120		△			ランドマイゼイション	
下咽頭	根治	ブースト	120		△				
食　道	術前	単　独	50～60	○		△			
	根治	ミックス ブースト	90≦		○				石　川15)
肺	根治	ミックス ブースト	100～120			○		早期症例	
	根治	ブースト	120			◎		パンコスト型症例	沢　田8)
膵	術後	ミックス ブースト	80～110		△		×	十二指腸出血	
子宮頸部	根治	ミックス	85	△	○	△	△	ランドマイゼイション	
	術後	ミックス	85～90		○	○		腺癌症例	荒　居6)
	姑息	単　独	88		○			再発症例	荒　居6)
膀　胱	術前	単　独	60	○	△	○	△	ランドマイゼイション	
前立腺	根治	単　独	100			△	×	尿道狭窄	伊　藤4)
軟部組織	術後	単　独	80		△	△		境界切除術例	
骨	術前	単　独	80～120	◎		◎	△—×	化学療法との併用 TDF 120では強い障害	高　田5)
悪性黒色腫	術前	単　独	100～130	○		○	△	早期症例	森16)

X線照射群との比較　◎ 極めて良好，○ 良好な傾向，△ 差なし，× 悪い，空白評価なし

を顕著にする方法だと考えられる．骨肉腫の優れた成績は，患肢温存手術，積極的化学療法を含めた集学的治療の成果であるが，骨に対するRBEが5.0に近い14)速中性子線の局所制御効果が大きな力になっていることは確かである．他の腫瘍についてのRBEは2.0～4.0の間と推定されているので，この効果の大きさがわかる．

照射方法別では，中性子線の割合の少ないミックス照射よりはブースト照射，さらにそれよりは中性子線単独照射で良好な局所制御効果を得ている印象があるので，現在の装置的ハンディキャップを克服して，線量分布の改善に努め，中性子線の結果を最大限に発揮するようにするためのトライアルを今後も続けなければならない．速中性子線治療を一般化して普及させるには，もっと使いやすい照射装置が望ましい．この点で，現在欧米に設置された回転照射可能な速中性子線照射装置での治療成果が待たれるところである．

さらにその先は，中性子線の生物効果と陽子線の線量分布の特徴を兼ね備える重粒子線治療であるが，この治療法は現在アメリカのバークレイ研究所で臨床トライアルが行われており，日本でも8年後の臨床トライアル開始に向けて，放医研で医用シンクロトロンの建設の準備中である．

文　献

1) 久津谷譲，梅垣洋一郎：生物学的等価線量の考え方と計算法．癌の臨床別冊，癌・放射線療

法，79-92，1978，篠原出版．

2) 森田新六，恒元　博，荒居竜雄，石川達雄：肺癌の速中性子線治療．特別研究「粒子加速器の医学利用に関する調査研究」最終報告書（NIRS-R-10），12-18，1984.

3) 荒居竜雄，森田新六，五味弘道，恒元　博，中野隆史，笠松達弘，近江和夫：子宮頸部扁平上皮癌の速中性子線治療，特別研究最終報告書(NIRS-R-10)，24-30，1984.

4) 伊藤晴夫，井坂茂夫，布施秀樹，島崎　淳：泌尿器系癌の速中性子線治療，特別研究最終報告書（NIRS-R-10)，31-36，1984.

5) 高田典彦，保高英二，梅田　透：骨・軟部組織肉腫に対する速中性子線照射の役割とその治療成績，第16回放医研シンポジウム報文集，粒子加速器の医学利用，現況と将来への展望（NIRS-M-56)，122-129，1985.

6) 荒居竜雄，森田新六，中野隆史，五味弘道，恒元　博，笠松達弘，近江和夫：子宮頸癌の速中性子線治療，産婦人科の実際，**35**: 47-53, 1986.

7) 森田新六，荒居竜雄，恒元　博，笠松達弘，近江和夫，福久健二郎：速中性子線照射した子宮頸癌症例の組織型分類と局所制御の関連性．癌の臨床，**30**: 1280-1284，1984.

8) 沢田勤也，福間誠吾，関　保雄，田中文隆，石田逸郎，松村公人，中野政雄，飯田孔陽，佐藤滋宏，梅垣洋一郎，恒元　博，森田新六：Pancoast 型肺癌に対する速中性子線治療について．癌の臨床，**29**: 111-114，1983.

9) 鎌田信悦：頭頸部癌に対する速中性子線ブースト治療クリニカルトライアルの問題点，第16回放医研シンポジウム報文集（NIRS-M-56)，104-113，1985.

10) 青木芳朗，森田新六，荒居竜雄，栗栖　明，恒元　博：Glioblastoma multiforme（Astrocytoma grade Ⅳ）に対する速中性子線療法．癌の臨床，**28**: 181-185，1982.

11) Cohen, L., Hendrickson, F.R., Kurup, P.D., Mansell, J.A., Awschalom, M., Rosenberg, I. and Ten Haken, R.K.: Clinical evaluation of neutron beam therapy, current results and prospects, 1983, *Cancer,* **55**: 10-17, 1985.

12) Parker, R. G.: Particle radiation therapy, *Cancer,* **55**: 2240-2245, 1985.

13) Duncan, W., Arnott, S.J., Jack, W.J.L., Kerr, G.R. and Williams, J.R.: Fast neutron therapy for squamous cell carcinoma in the head and neck region: Results of a randmized trial, *Int. J. Radiation Oncology Biol. Phys.*, **13**: 171-178, 1987.

14) Tatezaki, S.: Systematic multi-modal treatment of osteosarcoma, with special reference to the role of fast neutron radiotherapy, *J. Jap. Orthop. Ass.*, **53**: 831-846, 1979.

15) 石川達雄：食道がんの速中性子線治療成績，第16回放医研シンポジウム報文集（NIRS-M-56)，114-121，1985.

16) 森　俊二，石原和之，広根考衛，恒元　博：悪性黒色腫の速中性子線治療．第16回放医研シンポジウム報文集（NIRS-M-56)，140-149，1985.

Present Status of High LET Radiation Therapy—Fast neutron radioterapy in Japan: S. Morita, H. Tsunemoto, Y. Aoki, S. Kubota, T. Nakano, H. Gomi, K. Kumagaya, T. Arai, S. Sato*[1], Y. Iino, A. Kumazawa*[2], S. Onoda, A. Shimazaki*[3], N. Takada*[4], S. Kamata*[5], Y. Ogata*[6], H. Hanaoka*[7], T. Kasamatsu*[8] & S. Mori*[9] (*1 National Insitute of Radiological Sciences (NIRS), *2 Institute of Medical Science, Tokyo Univ. (IMS), *3 Chiba Univ. Hospital, *4 Chiba Cancer Center Hospital, *5 Cancer Institute Hospital, *6 Tochigi Cancer Center Hospital, *7 Keio Univ. Hospital, *8 National Cancer Center Hospital, *9 Gifu Univ. Hospital)

More than 1,900 patients of advanced and inoperable malignant tumor were treated with fast neutron radiotherapy using 30 MeV (d-Be) and 14 MeV (d-Be) beams at NIRS and IMS between 1975 and 1986. Protocols were largely nonrandomized. Some results have been obtained: 1) results with mixed beam studies for advanced squamous cell carcinoma of the utrine cervix have been equivocal compared with the photon controls. 2) some trends of local control have been observed in the trial of esophagial cancer, early cases of adenocarcinoma of the lung and malignant melanoma. 3) significant better results were observed in the pancoast type lung cancer and osteo sarcoma which was treated by the systemic multi-modal treatment. It is concluded that neutrons are efficacious for certain specific tumor types owing to some biological effects, however the problem of inferior dose distribution was the weakness of neutron therrapy at present.

Key words: High LET radiotherapy, Fast neutrons

Jap. J. Cancer Clin., **33**(13): 1647～1654, 1987.

Appl. Radiat. Isot. Vol. 38, No. 6, pp. 437–445, 1987
Int. J. Radiat. Appl. Instrum. Part A
Printed in Great Britain. All rights reserved

0883-2889/87 $3.00 + 0.00

[^{13}N]Ammonia in Organic Solvents; a Potent Synthetic Precursor for ^{13}N-labeling

TOSHIYOSHI TOMINAGA,[1]* KAZUTOSHI SUZUKI,[2] OSAMU INOUE,[2] TOSHIAKI IRIE,[2] TOSHIO YAMASAKI[2] and MASAAKI HIROBE[1]

[1]Faculty of Pharmaceutical Sciences, University of Tokyo, 7-3-1 Hongo, Bunkyo-ku, Tokyo, 113, Japan and [2]Division of Clinical Research, National Institute of Radiological Sciences, 9-1 Anagawa-4-chome, Chiba-shi (CHIBA), 260, Japan

(*Received* 12 *August* 1986; *in revised form* 1 *December* 1986)

$^{13}NH_3$ in an organic solvent was prepared and its utility as a labeling precursor was studied. [^{13}N]adenine ([^{13}N]ADN), [^{13}N]nicotinamide ([^{13}N]NAM), [^{13}N]*p*-nitrophenyl carbamate ([^{13}N]NPC), and [^{13}N]L-glutamine ([^{13}N]Gln) were labeled utilizing this precursor. [^{13}N]ADN and [^{13}N]NAM were labeled in much better yields than from an aqueous solution of $^{13}NH_3$. [^{13}N]NPC and [^{13}N]Gln, which could not be labeled in an aqueous solution, were labeled in high radiochemical yields. Thus, the advantages of this precursor are the improvement of the labeling yield and the feasibility of labeling compounds unstable in aqueous conditions.

Introduction

As previously reported, we have developed the synthesis of ^{13}N-labeled compounds ([^{13}N]adenosine and [^{13}N]nicotinamide) by ammonolysis in an aqueous solution (Irie *et al.*, 1985). Since $^{13}NH_3$ is supplied in the form of a dilute aqueous solution, the labeling reactions using $^{13}NH_3$ as a precursor have generally been carried out in water (Irie *et al.*, 1985; Tominaga *et al.*, 1985; Finn *et al.*, 1980). However, the yield of ammonolysis is known to be better when the reaction is carried out in an organic solvent such as ether or methanol. Ammonolysis in a non-aqueous medium also enables the labeling of compounds unstable in water, which enlarges the scope of this reaction.

Therefore, we developed $^{13}NH_3$ in an organic solvent in order to gain better yields in [^{13}N]-ammonolysis and evaluated its potential utility as a synthetic precursor. We selected adenine (ADN), nicotinamide (NAM), *p*-nitrophenyl carbamate (NPC), and glutamine (Gln) as target compounds and studied [^{13}N]-ammonolysis in an organic medium.

Materials and Methods

1. *Materials*

6-fluoropurine was synthesized according to the method of Kiburis *et al.* (1971). Nicotinic acid chloride hydrochloride (NAClHCl) was synthesized from nicotinic acid and thionyl chloride (Mayer and Graf, 1928). Tetrahydrofuran (THF) and triethylamine were distilled prior to use. Other chemicals and solvents were of the highest grade commercially available.

2. *Methods*

2.1. *Preparation of* [^{13}*N*]*ammonia*

The aqueous solution of $^{13}NH_3$ was prepared according to the modified method of Suzuki and Tamate (1984); briefly, proton-irradiated water was introduced into a reduction flask containing an aqueous solution of titanium chloride and NaOH, and the radiolabeled ammonia was distilled with water in a stream of helium.

2.2. *Synthesis of* [^{13}*N*]*ADN*

2.2.1. Preparation of $^{13}NH_3HCl$. To 500 μL of $^{13}NH_3$ (5–10 mCi)-containing water, 10 μL of 0.1 N HCl was added, and the mixture was thoroughly evaporated in a microwave oven.

2.2.2. Labeling of [^{13}*N*]*ADN* (*Scheme 1*). The substrate (6-fluoropurine, 6-chloropurine, or 6-methylmercaptopurine), NaOH (0.1–10 μmol in 5 μL of aqueous solution) and carrier ammonia (0–10 μmol in 5 μL of aqueous solution) were added to the methanol solution (400 μL) of $^{13}NH_3HCl$. The mixture was sealed and heated for 10 min in a boiling water bath. The radiochemical yield of [^{13}N]ADN was determined by thin-layer chromatography (TLC, silica gel, ethyl acetate:methanol (2:1)).

---

* All correspondence should be addressed to the National Institute of Radiological Sciences.

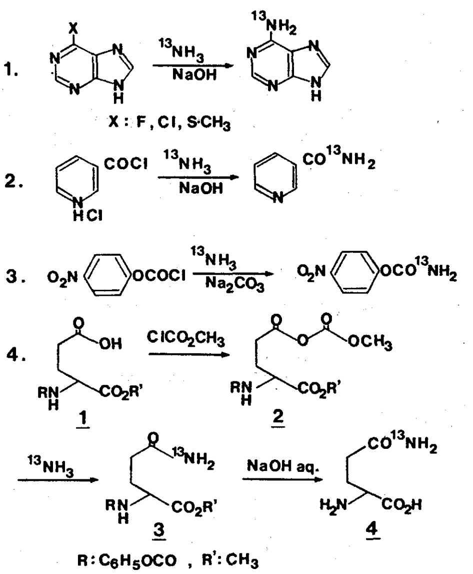

Schemes 1–4

2.3. *Synthesis of* [^{13}N]*NAM*

2.3.1. *Preparation of* $^{13}NH_3HCl$. To 1 mL of $^{13}NH_3$ (10–20 mCi)-containing water, 5 μL of 1 N HCl and about 20 mL of benzene were added, and the mixture was evacuated (about 10 mmHg) using a rotary evaporator in a boiling water bath to remove water as the benzene azeotrope.

2.3.2. *Labeling of* [^{13}N]*NAM* (*Scheme 2*). To $^{13}NH_3HCl$, 200 μL of 20 N NaOH, 2 mL of acetone, carrier ammonia (5–10 μmol in 1N solution, except in non-carrier-added synthesis), and freshly prepared NAClHCl were added. then the mixture was stirred vigorously for 30 s. The labeling yield of [^{13}N]NAM was determined by TLC (silica gel, acetone).

2.3.3. *Isolation of* [^{13}N]*NAM*. After the reaction described above (non-carrier-added state), the upper layer (acetone) of the mixture was loaded on the column of silica gel (10 mmϕ × 40 mm) and eluted with acetone. [^{13}N]NAM was obtained in 4–10 mL of eluent. Removal of the eluent afforded [^{13}N]NAM. The radiochemical purity of the product was determined by TLC (silica gel, acetone) and high performance liquid chromatography (HPLC, adsorbent: Finepak C-18 (JASCO), eluent: acetonitril: 0.04% H_3PO_4 (6:4), 1 mL/min).

2.4. *Synthesis of* [^{13}N]*NPC*

2.4.1. *Preparation of anhydrous organic solution of* $^{13}NH_3$. The anhydrous organic solution of $^{13}NH_3$ was prepared either with a remote-controlled micro-scale distillation apparatus (Fig. 1) or with a manually-controlled device made up of normal laboratory glasswares. The former duly afforded better recovery of $^{13}NH_3$. The distillation apparatus was controlled as follows. The irradiated water was introduced in a reduction flask containing Devarda's alloy (200 mg) and NaOH (400 mg); the flask was heated to about 400°C and the radiolabeled ammonia was distilled. Only the distilled fractions containing much radioactivity (detected by RS2) were dehydrated by passage through a drying column containing about 10 g of ascarite (8–20 mesh) heated by a stream of hot air (200°C). Other fractions containing less radioactivity (and much water) were introduced to the waste vessel. $^{13}NH_3$ trapped in the drying column was expelled by a stream of helium (100 mL/min) after the distillation. The process of this apparatus corresponding to the outputs from beam current and radioactivity detectors is shown in Fig. 2. The dried $^{13}NH_3$ was trapped in the cooled (about −10°C) organic solution (1–2 mL) of the reagents (*p*-nitrophenyl chloroformate and base). The amount of each reagent and the solvent used are shown in Table 3. The water content of the dried distillate was measured as follows: molecular sieves were put in the place of the trapping solvent, and the increase in the weight of the molecular sieves was measured after the distillation.

2.4.2. *Labeling of* [^{13}N]*NPC* (*Scheme 3*). After the distillation, carrier NH_3 (5–10 μmol in THF, except in non-carrier-added synthesis) was added and the mixture was stirred vigorously for 2 min. The radiochemical yield of [^{13}N]NPC was determined by TLC (silica gel, ethyl acetate: hexane (5:4)).

2.4.3. *Isolation of* [^{13}N]*NPC*. Diethyl ether (20 mL) was added to the filtrate of the reaction mixture (non-carrier-added state) and this solution was washed with 2 N HCl and saturated aq. NaCl solution. Removal of the solvent afforded [^{13}N]NPC in a radiochemical purity of 98%. [^{13}N]NPC was identified by TLC (conditions described above) and HPLC (absorbent: Finepak C-18 (JASCO), eluent: methanol: water (9:1), 0.5 mL/min).

2.5. *Synthesis of* [^{13}N]*Gln*

2.5.1. *Preparation of N-phenyloxycarbonyl-L-glutamic acid-α-methyl ester* (**1**). This compound was synthesized according to a conventional method (Schröder and Klieger, 1964; Scheme 5). In short, *N*-phenyloxycarbonyl-L-glutamic acid (**a**) prepared from L-glutamic acid and phenyloxycarbonyl chloride was dehydrated with dicyclohexyl carbodiimide (DCC) into *N*-phenyloxycarbonyl-L-glutamic anhy-

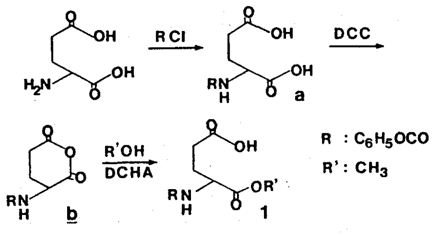

Scheme 5

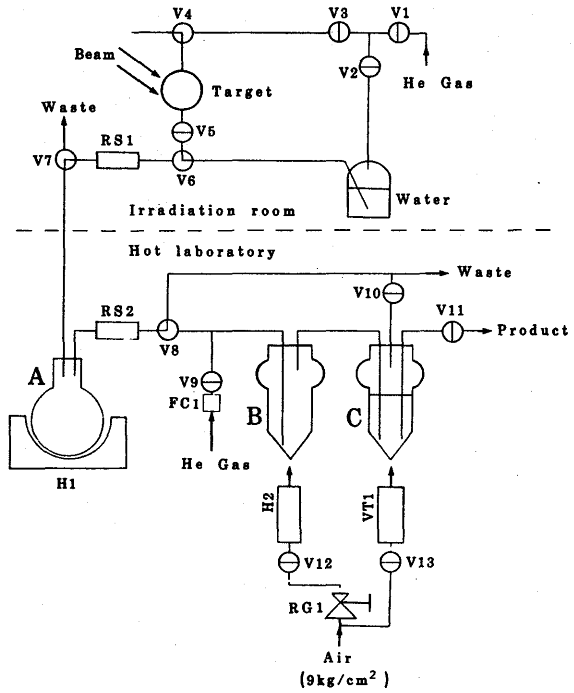

Fig. 1. Schematic diagram of $^{13}NH_3$ distillation apparatus. A: reduction flask (Devarda's alloy and NaOH), B: drying column (ascarite), C: trapping vessel (substrate solution), V1–V13: electric valves, RS1–RS2: radioactivity sensors, VT1: vortex tube for cooling, H1–H2: heaters, RG1: pressure regulator, FC1: flow controller.

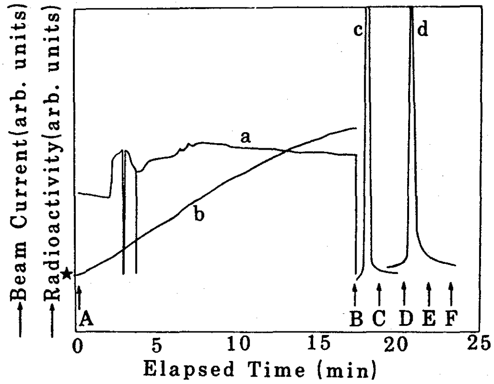

Fig. 2. Procedures using the apparatus, and output from the current and the radioactivity sensors. a: beam current, b: radioactivity produced in the target (calculated), c: radioactivity detected by RS1 (Fig. 1), d: radioactivity detected by RS2 (Fig. 1), ★: zero point of the beam current (a) and radioactivity in the target (b), A: start of the bombardment, B: end of the bombardment, start of the transfer of irradiated water to the reduction flask, C: end of transfer and start of reduction and distillation, D: start of passage of the distillate through the drying column, E: end of the passage and start of expulsion of $^{13}NH_3$ from the drying column by He gas (100 mL/min), F: removal of the organic solution of $^{13}NH_3$.

dride (**b**). Then **b** was methanolized in the presence of dicyclohexylamine (DCHA). Neutralization of this DCHA salt afforded **1**, colorless oil; ^{1}H NMR ($CDCl_3$) 10.9 (s, 1H, COOH), 7.1 (m, 5H, C_6H_5), 6.3 (b, 1H, NH), 4.7 (b, 1H, CH), 3.7 (s, 3H, OCH_3), 2.5 (m, 4H, CH_2–CH_2).

2.5.2. Labeling of [^{13}*N*]*Gln* (*Scheme 4*). Methyl chloroformate (5 μL, 60 μmol) and triethylamine (Table 3 shows the amount) were added to THF (3 mL) solution of **1** (120 μmol), and the mixture was stirred for 5 min in an ice bath. The anhydrous $^{13}NH_3$ was distilled into this solution and the reaction mixture was stirred at room temperature for 5 min. The yield of *N*-phenyloxycarbonyl-[^{13}N]L-glutamine-α-methyl ester (**3**) was determined by TLC (silica gel, ethyl acetate). To this reaction mixture, 2 N NaOH (150 μL) and methanol (150 μL) were added and stirred vigorously at 50°C for 5 min. The radiochemical yield of [^{13}N]Gln (**4**) was estimated by TLC ((a) silica gel, ethyl acetate:methanol:acetic acid (20:5:0.2) (R_f of **4**: 0.0), (b) KC18F (Whatman), methanol:5 N ammonia (20:3) (R_f of **4**: 0.8)).

Results

As a substrate for the synthesis of [^{13}N]ADN, 6-fluoropurine was found to be by far the most

Table 1. Labelling efficiency of [^{13}N]ADN

Carrier (μmol)	NaOH (μmol)	Substrate* (μmol)	Yield (%)
0	0.1	20	7
0	1	20	19
0	5	20	14
5	5	20	21
5	10	20	18
5	50	20	5
10	10	20	13
10	10	50	19

* 6-fluoropurine.
Reaction conditions: total volume 400 μL, 100°C, 10 min. Carrier NH_3 and NaOH was each added in 5 μL of aqueous solution, separately.

Table 2. Labelling efficiency of [^{13}N]NAM

Carrier (μmol)	Substrate (μmol)	Yields (%)
0	40	95
0	80	94
0	160	95
5	40	97
5	80	97
5	160	98
10	160	96

Reaction conditions: total volume 2.2 mL, room temperature, 30 s.

reactive. The effects of the amount of NaOH, carrier NH_3, and the substrate (6-fluoropurine) on the labeling yield of [^{13}N]ADN are shown in Table 1. The labeling efficiency was mainly affected by the amount of NaOH. [^{13}N]ADN was synthesized in a higher yield (max. 21%) in methanol than in water (8%). The labeled [^{13}N]ADN was identified by TLC (Fig. 3).

The labeling yield of [^{13}N]NAM is shown in Table 2. The labeling reaction proceeded with a much higher yield (nearly quantitative) than in water (about 25%, Irie *et al.*, 1985) in both a non-carrier-added state and a carrier-added state. The purification of [^{13}N]NAM was undertaken in a short period (total preparation time about 15 min) at a high level of radiochemical purity (over 98%). [^{13}N]NAM was identified by TLC (Fig. 3) and HPLC (Fig. 4).

The recovery of $^{13}NH_3$ by distillation apparatus (Fig. 1) was about 80% based on $^{13}NO_x$ produced in the target (decay corrected). Typically, about 200 mCi of $^{13}NH_3$ in an organic solvent was obtained from a bombardment of a 18 MeV proton beam (15 μA) for 15 min. The total preparation time was about 5 min after the irradiation (Fig. 2). The dried distillate contained practically no water.

Table 3 shows the effects of the base, substrate amount, carrier NH_3, and solvent used, on the yield of [^{13}N]NPC. THF and Na_2CO_3 were best fitted as a solvent and a base, respectively. Under optimal conditions, [^{13}N]NPC was labeled almost quantitatively in a short period. The isolation of the product was performed in a short period (total preparation time was about 10 min after the distillation) in a radiochemical purity of over 97%. [^{13}N]NPC was identified by the TLC (Fig. 3) and HPLC (Fig. 5).

The radiochemical yields of *N*-phenyloxycarbonyl-[^{13}N]L-glutamine-α-methyl ester (**3**) and [^{13}N]Gln (**4**) are shown in Table 4. [^{13}N]Gln was synthesized without isolating **3** in a short period (about 12 min after the distillation). The amount of triethylamine affected the yield of **3**. The radiochemical yield of [^{13}N]Gln could not be determined precisely because of the lack of an appropriate TLC system. However, the efficiency of the deprotection was estimated to be more then 80%. Compounds **3** and [^{13}N]Gln (**4**) were identified with TLC (Fig. 3).

Discussion

1. Preparation of $^{13}NH_3$ in an organic solvent

In this paper, we present two methods of preparing an organic solution of $^{13}NH_3$: one via $^{13}NH_3HCl$, and the other by distillation. In the method via $^{13}NH_3HCl$, a small amount of aqueous base was added to the organic solution of dried $^{13}NH_3HCl$, in order to liberate free $^{13}NH_3$ and quench the acid (such as HF from 6-fluoropurine) generated in the course of the reaction. The content of the intentionally added water was less than 3% in the case of the labeling reaction of [^{13}N]ADN. The labeling of [^{13}N]NAM was performed in a biphasic medium (Schotten–Baumann reaction), in which concentrated NaOH (lower layer) neutralized the HCl salt of the acid chloride and quenched HCl liberated in the course of the reaction, and the ^{13}N-ammonolysis proceeded in the acetone (upper) layer. The advantage of the method via $^{13}NH_3HCl$ is its simplicity of operation and the quantitative recovery of $^{13}NH_3$. This method is applicable to the labeling of compounds stable to aqueous bases.

Distillation of $^{13}NH_3$ seems the only way to prepare a completely anhydrous organic solution of $^{13}NH_3$. This solution serves as a general precursor of ^{13}N-ammonolysis. Especially in the labeling of compounds labile to aqueous bases, this solution should be used as a precursor. In that case, an anhydrous base (such as powder $NaHCO_3$ or triethylamine) should be used to quench the acid generated in the course of the ammonolysis.

2. ^{13}N-ammonolysis in organic medium

(1) [^{13}N]ADN and [^{13}N]NAM. Ammonolysis generally proceeds in better yields in organic solvents than in water, because in water, hydrolysis of a substrate (such as an acid chloride) completes the desired reaction and ammonia is hydrated to be less reactive. As expected, the same tendency was observed in the labeling of [^{13}N]ADN and [^{13}N]NAM, whose labeling yields were low in an aqueous medium (Tables 1 and 2).

6-Fluoropurine was the best substrate for the labeling of [^{13}N]ADN, probably because of the intensive induction effect of fluorine atoms. Lower labeling yield in the presence of excess NaOH can be attributed to hydrolysis of the substrate.

The labeling efficiency of [^{13}N]NAM by Schotten–Baumann reaction was very much higher than that in water. This is attributed to the far greater reactivity

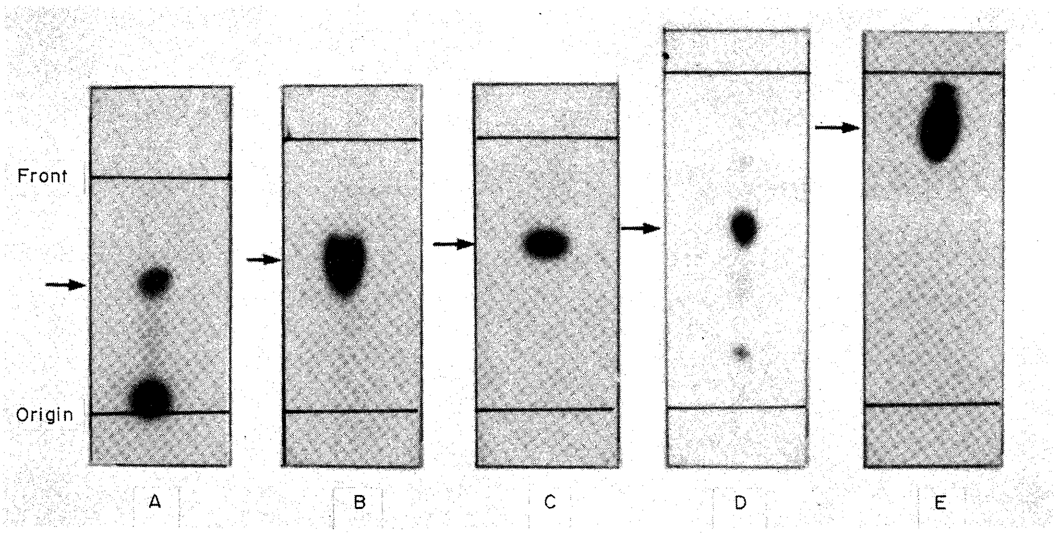

Fig. 3. TLC of ^{13}N-compounds. A: [^{13}N]ADN (reaction mixture), B: [^{13}N]NAM (isolated), C: [^{13}N]NPC (isolated), D: *N*-phenyloxycarbonyl-[^{13}N]L-glutamine-α-methyl ester (**3**, reaction mixture), E: [^{13}N]Gln (reaction mixture). Each target compound (carrier) detected by u.v. or ninhydrin stain is shown with an arrow.

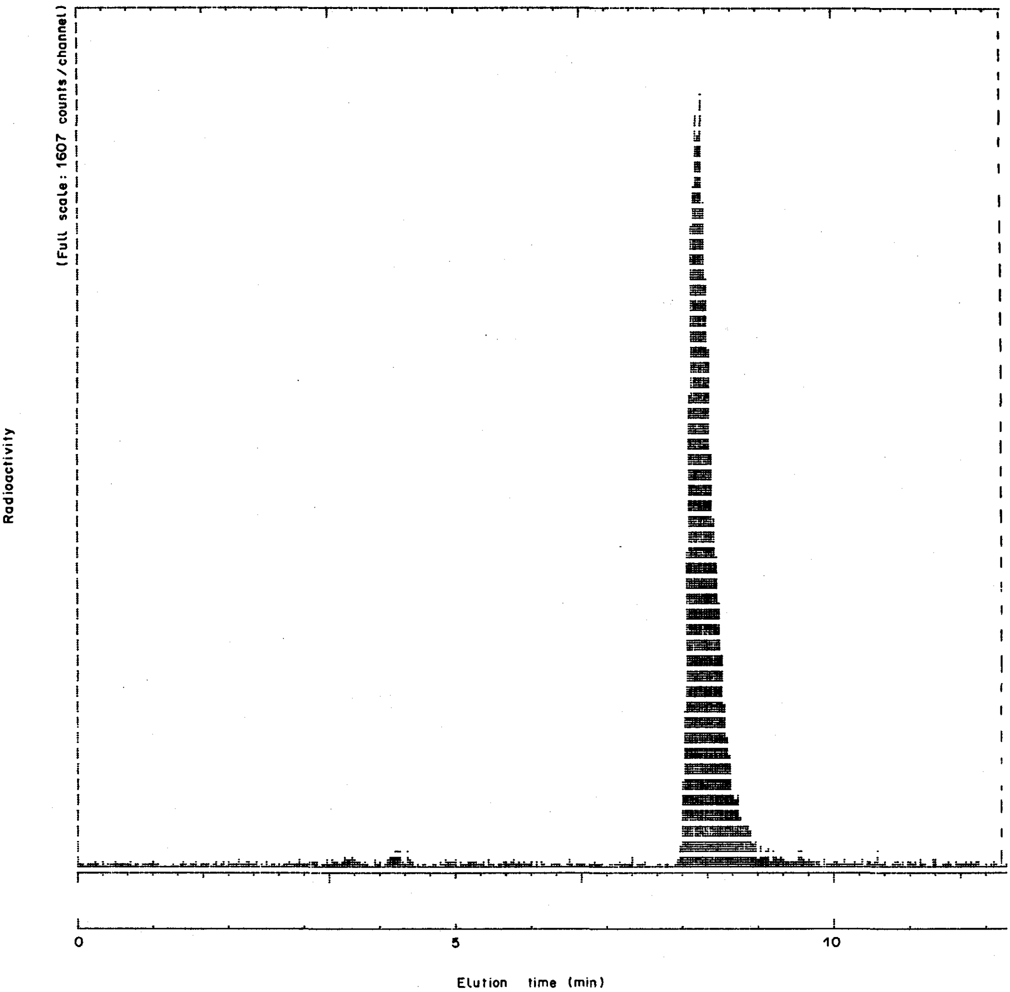

Fig. 4. HPLC of [^{13}N]NAM. Conditions; adsorbent: Finepak C-18 (25 cm, 4.6 mmϕ) (JASCO), eluent: acetonitril:0.04% H_3PO_4 (6:4), 1 mL/min. Retention time, [^{13}N]NAM (8.2 min).

of the acid chloride in an organic solvent such as acetone. The quality of the acid chloride greatly affected the labeling yield, especially in a non-carrier-added state.

Table 3. Labelling efficiency of [^{13}N]NPC

Carrier (μmol)	Base	Substrate (μmol)	Solvent	Yield (%)
0	Na_2CO_3*	100	THF	97
0	$NaHCO_3$*	100	THF	93
0	$(C_2H_5)_3N$†	100	THF	<2
5	Na_2CO_3	100	THF	92
10	Na_2CO_3	100	THF	92
0	Na_2CO_3	50	THF	93
0	Na_2CO_3	25	THF	86
0	Na_2CO_3	100	$(C_2H_5)_2O$	90
0	Na_2CO_3	100	$CHCl_3$	50
0	Na_2CO_3	100	CH_3OH	3

* Excess base was suspended in the reaction mixture.
† 1.5 mmol (200 μL).
Reaction conditions: total volume 2 mL, room temperature, 2 min.

This reaction system permitted simple and rapid separation, in which the upper (acetone) layer was directly chromatographed over silica gel without any pretreatment. When the reaction was carried out in water as described in the previous report (Irie *et al.*, 1985) and the reaction mixture was directly loaded on the column, the water destroyed the column and the separation was unsuccessful. Since most of the nicotinic acid (NA, derived from NAClHCl by hydrolysis) remained in the basic water layer (lower layer), this method also heightened the chemical purity of the product.

ADN and NAM are essential constituents of organisms and play important roles in the form of nucleotides and cofactors. Therefore, ^{13}N-labeling of these compounds is of great significance for visualization of their biodisposition in live animals or human. ^{11}C-labeling of these compounds has already been reported (Ido *et al.*, 1982; Machulla, 1979). The

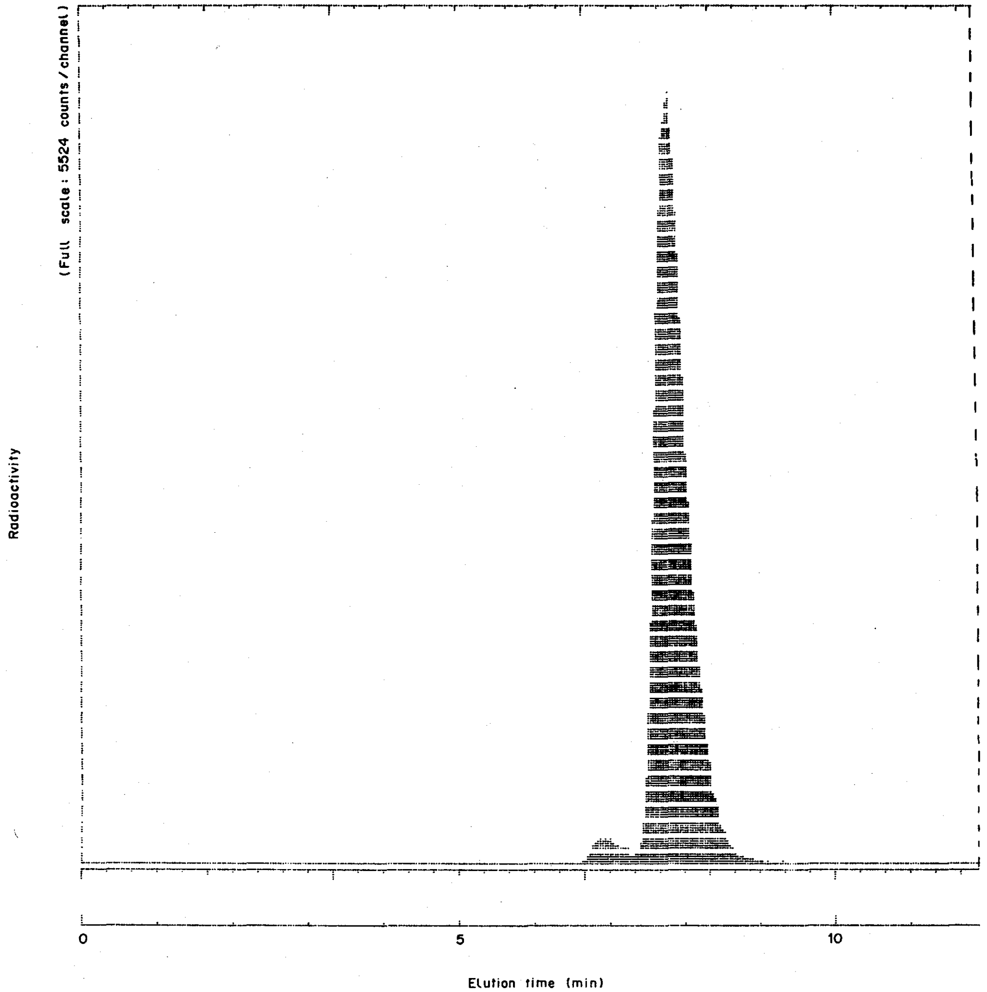

Fig. 5. HPLC of [^{13}N]NPC. Conditions; adsorbent: Finepak C-18 (25 cm, 4.6 mmϕ) (JASCO), eluent: methanol:water (9:1), 0.5 mL/min. Retention time; [^{13}N]NPC (7.8 min).

Table 4. Labelling efficiency of [^{13}N]Gln

Carrier (μmol)	Substrate (**1**) (μmol)	$ClCO_2CH_3$ (μmol)	Et_3N (μmol)	Yield **3** (%)	Yield **4** (%)
0	120	60	36	60	—
0	120	60	72	71	—
0	120	60	144	81	75
0	120	60	288	78	—
5	120	60	144	73	70
10	120	60	144	77	65

* Reaction conditions: total volume 3 mL, ammonolysis 5 min (room temperature), deprotection 5 min (50°C).

combination use of the ^{11}C- and ^{13}N-labeled compounds may greatly contribute to obtaining information about the *in vivo* metabolism of these compounds.

(2) [^{13}*N*]*NPC and* [^{13}*N*]*Gln.* Some compounds easily decompose in aqueous conditions. Such compounds, especially one labile to aqueous bases, cannot be labeled from the aqueous solution of $^{13}NH_3$. $^{13}NH_3$ in an organic solvent is useful also for the labeling of such compounds.

[^{13}N]NPC is a potential metabolic trapping tracer for estimation of choline esterase activity *in vivo* (Inoue *et al.*, 1985). This compound is very easily hydrolyzed even in a weak alkaline solution, as follows:

$$p\text{-}NO_2\text{-}C_6H_4\text{-}OCO^{13}NH_2 \xrightarrow{OH^-} p\text{-}NO_2\text{-}C_6H_4OH + CO_2 + {}^{13}NH_3$$

Therefore, the labeling must be carried out under thoroughly anhydrous conditions.

As a base, anhydrous Na_2CO_3 afforded the best yield, probably because of the strongest basicity (pK_a value of HCO_3^- is 10.2 while that of NH_4^+ is 9.2).

Triethylamine caused unknown side reactions which greatly reduced the labeling yield. In the heterogeneous reaction suspending an insoluble powder base (such as Na_2CO_3), vigorous stirring is essential to gain a good yield, since without it the efficiency of neutralizing HCl becomes low and $^{13}NH_3$ is protonated to be inactive.

The isolated [^{13}N]NPC was radiochemically pure. However, removal of non-radioactive impurities such as unreacted NPCl and *p*-nitrophenol would be necessary before it could be put to clinical use.

$^{13}NH_3$ in an organic solvent also permits the selective labeling of multifunctional compounds such as amino acids by utilizing appropriate protective groups. We selected L-glutamine (Gln) as an example and investigated its selective labeling (^{13}N-amidation) at ω-position. [^{13}N]Gln has been reported to be a useful tracer for the study of amino acid metabolism (Henze *et al.*, 1982). Although the enzymatic labeling of this compound has already been reported (Gelbard *et al.*, 1975), chemical labeling has not yet been explored. This chemical labeling method would be applicable to the labeling of peptides which cannot be labeled with enzymes, as the chemical labeling of [^{11}C]methionine is applied to the synthesis of ^{11}C-enkephalines (Någren *et al.*, 1984).

Protective groups used need to be stable during ammonolysis and easy to remove after the labeling. Such protection is almost impossible in the case of labeling in an aqueous medium. We selected the phenyloxycarbonyl group as an amino-protecting group and the methyl group as a carboxyl-protecting group (Scheme 5). These groups are known to be stable under anhydrous conditions and easily cleaved in an aqueous NaOH solution.

In this labeling, the ω-carboxyl group was activated by the mixed-anhydride method. In its yield (about 80%) and reaction time (5 min), this method is as effective as the acid chloride method. Since acid chlorides are known to cause side reactions in the modification of amino acids, we avoided using this method of activation. The mixed anhydride used (**2**) was unstable and was allowed to react without isolation. Since impurities in THF and triethylamine hindered the formation of **2** and reduced the yield of **3**, we concluded that these reagents must be purified prior to use.

This reaction is considered to be applicable to the labeling of aspargine. We have already labeled [^{13}N]aspargine in a similar way.

Conclusion

In conclusion, the advantages of ^{13}N-ammonolysis in orgainc media are as follows:

(1) the improvement in the yields of ^{13}N-compounds ([^{13}N]ADN, [^{13}N]NAM); and (2) the feasibility of labeling compounds containing functional groups unstable in aqueous solutions ([^{13}N]NPC, [^{13}N]Gln).

Acknowledgement—The authors are grateful to Mr K. Tamate for the isotope production.

References

Finn R. D., Christmann D. R. and Wolf A. P. (1980) A rapid synthesis of nitrogen-13 labelled amphetamine. *J. Labelled Compd. Radiopharm.* **18,** 909.

Gelbard A. S., Clarke L. P., McDonald J. M., Monahan W. G., Tibury R. S., Kuo T. Y. and Laughlin J. S. (1975) Enzymatic synthesis and organ distribution studies with ^{13}N-labelled L-glutamine and L-glutamic acid. *Radiology* **116,** 127.

Henze E., Schelbert H. R., Barrio J. R., Egbert J. E., Hansen H. W., MacDonald N. S. and Phelps M. E. (1982) Evaluation of myocardial metabolism with N-13- and C-11-labelled amino acids and positron computed tomography. *J. Nucl. Med.* **23,** 671.

Ido T., Yamada H., Iwata R. and Kawashima K. (1982) *Proc. 22nd Annual Meeting of the Japanese Society of Nuclear Medicine*, p. 1331.

Inoue O., Irie T., Tominaga T., Hashimoto K. and Yamasaki T. (1985) *Proc. 25th Annual Meeting of the Japanese Society of Nuclear Medicine*, p. 1148.

Irie T., Inoue O., Suzuki K. and Tominaga T. (1985) Labeling of ^{13}N-labeled adenosine and nicotinamide by ammonolysis. *Int. J. Appl. Radiat Isot.* **36,** 345.

Kiburis J. and Lister J. H. (1971) Nucleophilic displacement of the trimethylammonio group as a new route to fluoropurines. *J. Chem. Soc. (C)* **1971,** 3942.

Machulla H. J. and Dutschka K. (1979) ^{11}C-labelled radiopharmaceuticals: synthesis and high pressure liquid chromatography of nicotinic-^{11}C-acid amide. *J. Labelled Compd. Radiopharm.* **16,** 287.

Mayer H. and Graf R. (1928) Über die Einwirkung von Thionylchlorid auf die Pyridin-monocarbonsäuren. *Chem. Ber.* **61,** 2202.

Någren K., Bergson G., Franzén H., Ragnarsson U. and Långström B. (1984) The synthesis of ^{11}C-labelled enkephalines. *J. Labelled Compd. Radiopharm.* **21,** 1205.

Schröder E. and Klieger E. (1964) Darstellung und Reaktionen von N-substituerten L-glutaminsäurederivaten. *Ann. Chem.* **673,** 196.

Suzuki K. and Tamate K. (1984) Automatic production of $^{13}NH_3$ and L-(^{13}N-)glutamate ready for an intravenous injection. *Int. J. Appl. Radiat. Isot.* **35,** 771.

Tominaga T., Inoue O., Irie T., Suzuki K., Yamasaki T. and Hirobe M. (1985) Preparation of ^{13}N-β-phenethylamine. *ibid.* **36,** 555.

Nucl. Med. Biol. Vol. 14, No. 6, pp. 587–592, 1987
Int. J. Radiat. Appl. Instrum. Part B
Printed in Great Britain. All rights reserved

0883-2897/87 \$3.00 + 0.00

Synthesis and Evaluation of $[^{11}C]$Cyanoimipramine

KENJI HASHIMOTO,[1]* OSAMU INOUE,[2] KAZUTOSHI SUZUKI,[2] TOSHIRO YAMASAKI[2] and MASAHARU KOJIMA[1]

[1]Department of Radiopharmaceutical Chemistry, Faculty of Pharmaceutical Sciences, University of Kyushu, 3-1-1 Maidashi, Fukuoka 812, Japan and [2]Division of Clinical Research, National Institute of Radiological Sciences, 9-1 Anagawa-4-chome, Chiba-shi 260, Japan

(*Received* 25 *February* 1987)

$[^{11}C]$Cyanoimipramine has been prepared by methylation of the desmethyl cyanoimipramine with $[^{11}C]$methyl iodide. The chemically and radiochemically pure labelled product was obtained with a high specific activity (>300 mCi/μmol). When ^{11}C (or ^{3}H)-cyanoimipramine was intravenously administered in mice, high accumulations were shown in brain and lung. Thirty minutes after injection of the tracer, differences were found in the radioactivity between the cerebral cortex and the cerebellum. The regional distribution of radioactivity in the rat brain 30 min after i.v. injection of $[^{11}C]$cyanoimipramine was also examined, and the radioactivity was high in receptor rich areas (striatum, cerebral cortex *etc.*) but low in receptor poor area (cerebellum). The *in vivo* stability of $[^{3}H]$cyanoimipramine was quite stable in the mouse brain for at least 30 min. Thirty minutes after injection, the radioactivity in the cerebral cortex of the carrier-added state was reduced as compared with the carrier-free state. Taken together, the *in vivo* specific binding of $[^{3}H]$cyanoimipramine in the cerebral cortex was estimated at about 40–50% of the total radioactivity. Furthermore, the distribution of $[^{3}H]$cyanoimipramine in the mice forced to swim was examined. Significant changes in the distribution of $[^{3}H]$cyanoimipramine were observed in the cerebral cortex.

Introduction

The possibility of *in vivo* studies of neuroreceptors in the living human brain using positron emission tomography (PET) has recently been demonstrated (Wagner *et al.*, 1983; Frost *et al.*, 1985; Farde *et al.*, 1985; Samson *et al.*, 1985; Shinotoh *et al.*, 1985; Persson *et al.*, 1985; Frost *et al.*, 1986; Wagner, 1986). Tricyclic antidepressants like imipramine are widely used in the treatment of depression. Furthermore, high affinity $[^{3}H]$imipramine binding sites have been described in mammalian brain and platelets (Raisman *et al.*, 1979; Paul *et al.*, 1980). These $[^{3}H]$imipramine binding sites are related to the 5-hydroxytryptamine (serotonin) uptake system. Thus, a good correlation exists between the potencies of a variety of drugs to inhibit $[^{3}H]$imipramine binding and $[^{3}H]$5-hydroxytryptamine uptake in rat hypothalamus (Langer *et al.*, 1980) and in human platelets (Paul *et al.*, 1981). Importantly, $[^{3}H]$imipramine binding sites are decreased in number (B_{max}) in platelets of depressed patients (Briley *et al.*, 1980; Langer *et al.*, 1984) and in frontal cortex of suicidal patients (Stanley *et al.*, 1982). The study of these binding sites in the living human brain using PET is of interest due to their possible role in affective disorders such as depression.

The synthesis of $[^{11}C]$imipramine and $[^{11}C]$chloripramine was previously reported (Maziere *et al.*, 1978; Berger *et al.*, 1979), but these ligands are not suitable for *in vivo* receptor studies because of a high component of non-specific binding. Cyanoimipramine. Ro 11-2465 (5-[3-(dimethylamino)-propyl]-10,11-dibenz[b,f]azepine-3-carbonitrile) is a more potent serotonin uptake inhibitor than imipramine and chloripramine (Burkard, 1980; Maitre *et al.*, 1982; Dumbrille-Ross and Tang 1983), and was reported to bind one subclass of imipramine binding sites (Dumbrille-Ross and Tang, 1983). In this study, we synthesized $[^{11}C]$cyanoimipramine ($[^{11}C]$Ro 11-2465) with a high specific activity and evaluated the biodistribution of the tracer in animals.

Materials and Methods

1. *Materials*

Ro 11-2465(cyanoimipramine) and Ro 12-5419(*N*-

---

* Author to whom all correspondence should be sent. Present address: Department of Radiopharmaceutical Chemistry, Faculty of Pharmacy & Pharmaceutical Sciences, University of Fukuyama, 985 Higashimura-cho, Fukuyama 729-02, Japan.

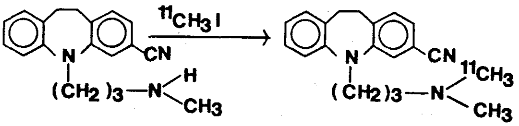

Fig. 1. Synthesis of [^{11}C]cyanoimipramine.

desmethyl cyanoimipramine) were kindly provided by Nippon Roche Ltd, Kamakura, Japan. [^{3}H]-Cyanoimipramine (65.4 Ci/mmol) was obtained from New England Nuclear, Boston, Mass., U.S.A. Other chemicals were purchased from Waco Pure Chemical Industries Ltd, Tokyo, Japan.

2. *Synthesis of* [^{11}C]*cyanoimipramine*

[^{11}C]Methyl iodide was produced as described previously (Suzuki *et al.*, 1985). [^{11}C]Cyanoimipramine was synthesized by the methylation of *N*-desmethyl compound in acetone (500 μL) at 70°C for 5 min, and purified by preparative high performance liquid chromatography (HPLC) (Megapack) SIL, $CHCl_3:MeOH:NH_3 = 700:4:1$). The radioactive peak corresponding to cyanoimipramine was corrected, evaporated to dryness in a rotary evaporator and dissolved in saline.

3. *Determination of radiochemical purity and specific activity of* [^{11}C]*cyanoimipramine solution*

Radiochemical purity of [^{11}C]cyanoimipramine solution was determined by analytical HPLC (Finepack SIL, $CHCl_3:MeOH:NH_3 = 200:8:0.5$). Specific activity was determined by gas chromatography (HP-5890A, Megabore DB-1 (5 m), NP detector).

4. *Biodistribution of* [^{11}C]*cyanoimipramine in mice*

In this study, 10 weeks old male C3H mice (25–30 g) were used, into which 0.2 mL of [^{11}C]cyanoimipramine solution (100 μCi) was intravenously injected. Mice were killed by decapitation at 1, 10, 20 and 30 min after injection of the tracer. Blood, cerebral cortex, cerebellum and lung were removed and were counted in a Packard automated gamma counter, and expressed in the percent dose per gram (% dose/g).

5. *Regional distribution of* [^{11}C]*cyanoimipramine in rat brain*

In this study, 11 weeks old male Wistar strain rats (370–390 g) were intravenously injected with 0.5 mL of [^{11}C]cyanoimipramine solution (2.0 mCi). Rats were killed by decapitation at 30 min after injection of the tracer. Blood, cerebellum, striatum, frontal cortex, posterior cortex, pons-medulla, hippocampus, midbrain and thalamus were removed and the percent dose per gram (% dose/g) was determined as described above.

In the carrier-added experiment, 1 h after i.p. injection of carrier cyanoimipramine (10 mg/kg), 0.5 mL of [^{11}C]cyanoimipramine solution (2.0 mCi) was intravenously injected into the rats, and the percentage dose per gram (% dose/g) was determined as described above.

6. *Stability of* [^{3}H]*cyanoimipramine in mouse brain*

About 10 μCi of [^{3}H]cyanoimipramine (0.15 nmol) was intravenously injected into a mouse. Thirty minutes after injection of the tracer, the mouse was killed by decapitation. The brain was quickly removed and homogenized with 1 mL of saline solution, and 0.2 mL of brain homogenate was sampled as a standard for the determination of extraction efficiency. One milligram of carrier cyanoimipramine and 2 mL chloroform were added to the rest of the brain homogenate and radioactive materials were extracted. Extraction efficiency determined by comparison with a standard was more than 95%. Organic extractable materials were analyzed by thin layer chromatography (TLC: silicagel, $CHCl_3:MeOH = 15:1$ and tetrahydrofuran:hexane:ammonium hydroxide = 7:3:0.1).

7. *Biodistribution of* [^{3}H]*cyanoimipramine in mice*

In this study, 8 weeks old male C3H mice (30–35 g) were intravenously injected with 0.2 mL of [^{3}H]-cyanoimipramine solution (1 μCi). The mice were killed by decapitation at 1, 5, 15, 30 and 60 min after injection of the tracer. Blood, cerebral cortex and cerebellum were removed and weighed, each sample being incinerated by a Packard 306 sample oxidizer, and the percent dose per gram (% dose/g) in each sample was determined by a Beckmann 6800 liquid scintillation counter.

In the carrier-added experiment, 0.2 mL of [^{3}H]cyanoimipramine solution (1 μCi, 1 mg/kg) was intravenously injected into mice, and the percent dose per gram (% dose/g) was determined as described above.

8. *Biodistribution of* [^{3}H]*cyanoimipramine in mice forced to swim*

Mice were forced to swim in a water basin (30 cm dia. × 30 cm height, 20 cm water depth) at 15°C for 5 min. Within 3 min after the mice were removed from the water, 0.2 mL of [^{3}H]cyanoimipramine solution (1 μCi) was intravenously injected. The mice were killed by decapitation at 1, 15, 30 and 60 min after injection of the tracer. The percent dose per gram (% dose/g) was as described above.

Results

Synthesis

[^{11}C]Cyanoimipramine was synthesized by the methylation of *N*-desmethyl cyanoimipramine (Fig. 1) yielding 20–30 mCi of [^{11}C]cyanoimipramine solution. The radiochromatogram of [^{11}C]cyanoimipramine solution is shown in Fig. 2. Radiochemical purity was more than 99%, and specific activity of

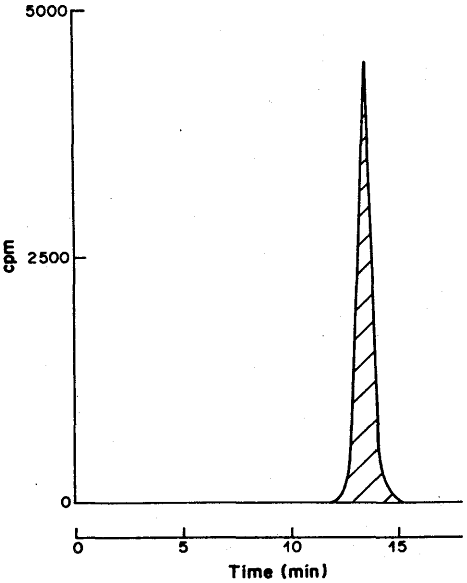

Fig. 2. HPLC of [^{11}C]cyanoimipramine solution: conditions Finepack SIL (JASCO); solvent system $CHCl_3$:MeOH:c.NH_3 = 200:8:0.5 1 mL/min; Retention time of [^{11}C]cyanoimipramine (13.4 min).

[^{11}C]cyanoimipramine solution was determined to be more than 300 mCi/μmol by gas chromatography.

Biodistribution of [^{11}C]cyanoimipramine in mice

When [^{11}C]cyanoimipramine was administered, high accumulations were observed in the brain and lung as shown in Table 1. Thirty minutes after injection of the tracer, there was found to be a difference in radioactivity between the cerebral cortex and the cerebellum.

Regional distribution of [^{11}C]cyanoimipramine in rat brain

Table 2 shows the regional distribution of the radioactivity in brains of rats 30 min after i.v. injection of [^{11}C]cyanoimipramine. The radioactivity was high in the striatum, frontal cortex, posterior cortex, hippocampus, midbrain and thalamus, but low in the cerebellum. The regional distribution of the radioactivity *in vivo* was found to resemble that of the imipramine binding sites of rat brains measured *in vitro* (Burkard, 1980; Fuxe *et al.*, 1983; Savaki *et al.*, 1985). When carrier cyanoimipramine (10 mg/kg) was intraperitoneally given 1 h before injection of [^{11}C]cyanoimipramine, the radioactivity in the different regions of the brain was reduced as compared with the control values.

Table 2. Regional distribution of [^{11}C]cyanoimipramine in rat brain 30 min after i.v. injection

	Percent dose/g	
	Control	Carrier-added*
Blood	0.161 ± 0.08	0.082 ± 0.01
Cerebellum	0.295 ± 0.05	0.214 ± 0.02
Striatum	0.477 ± 0.10	0.288 ± 0.05
Frontal-cortex	0.498 ± 0.10	0.288 ± 0.03
Posterior-cortex	0.509 ± 0.09	0.303 ± 0.04
Pons-medulla	0.314 ± 0.14	0.263 ± 0.04
Hippocampus	0.646 ± 0.31	0.363 ± 0.15
Midbrain	0.452 ± 0.10	0.206 ± 0.06
Thalamus	0.468 ± 0.08	0.274 ± 0.04

Three rats in each group; average ± 1 SD.

*Carrier cyanoimipramine (10 mg/kg) was given intraperitoneally 1 h before i.v. injection of [^{11}C]cyanoimipramine.

Stability of [^{3}H]cyanoimipramine in mouse brain

Thin-layer chromatographic analysis of radioactive materials in the mouse brain was performed, and almost all the radioactivity was due to cyanoimipramine itself.

Biodistribution of [^{3}H]cyanoimipramine in mouse brain

When carrier-free [^{3}H]cyanoimipramine was administered, the tracer passed rapidly into the mouse brain as shown in Fig. 3(a). Fifteen minutes after injection of the tracer, the maximum peak of radioactivity in the cerebral cortex and the cerebellum were observed, but the radioactivity in the blood was at a maximum 1 min after injection. Between 30 and 60 min after injection, there was shown to be a difference in radioactivity between the cerebral cortex and the cerebellum. One hour after injection, the cerebral cortex to cerebellum ratio was about 2.

On the other hand, when the tracer was injected with a large amount of carrier cyanoimipramine (1 mg/kg), the radioactivity in the blood was significantly lower than that in the carrier-free state as shown in Fig. 3(b). One minute after injection of the tracer, the radioactivity in the cerebral cortex and the cerebellum was high compared with the carrier-free state. One hour after injection of the tracer, the radioactivity of the cerebral cortex in the carrier-added state was remarkably reduced as compared to the carrier-free state.

Table 1. Biodistribution of [^{11}C]cyanoimipramine in mice

	Percent dose/g			
	1 min	10 min	20 min	30 min
Blood	4.08 ± 0.30	3.72 ± 0.39	2.27 ± 0.14	2.57 ± 0.33
Cerebral cortex	4.02 ± 0.54	6.70 ± 0.29	5.93 ± 0.31	5.89 ± 0.77
Cerebellum	3.44 ± 0.42	4.89 ± 0.24	3.73 ± 0.41	3.30 ± 0.36
Lung	35.6 ± 5.84	26.1 ± 1.89	17.8 ± 0.78	15.0 ± 0.95

Three mice in each group; average ± 1 SD.

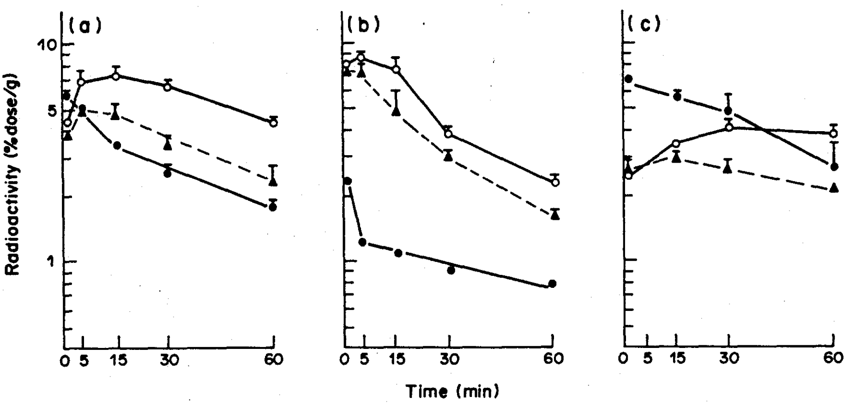

Fig. 3.(a) Biodistribution of carrier-free (0.015 nmol/mouse) [^{3}H]cyanoimipramine in mice after i.v. injection. Radioactivity in cerebral cortex (○——○), cerebellum (▲-----▲) and blood (●——●) were expressed as percentage dose per gram (% dose/g). Values are presented as an average ± SD of three mice in each point. (b) Biodistribution of carrier-added (1 mg/kg) [^{3}H]cyanoimipramine in mice after i.v. injection. Radioactivity in cerebral cortex (○——○), cerebellum (▲-----▲) and blood (●——●) were expressed as percentage dose per gram (% dose/g). Values are presented as an average ± 1 SD of three mice in each point. (c) Biodistribution of carrier-free (0.015 nmol/mouse) in forced-to swim mice after i.v. injection. The tracer was injected into mice within 3 min after having been forced to swim as described in Materials and Methods. Radioactivity in cerebral cortex (○——○), cerebellum (▲-----▲) and blood (●——●) were expressed as percentage dose per gram (% dose/g). Values are presented as an average ± 1 SD of three mice in each point.

Biodistribution of [^{3}*H*]*cyanoimipramine in mice forced to swim*

As shown in Fig. 3(c), the radioactivity of the blood and the cerebral cortex in the mice forced to swim was significantly changed as compared with the control mice. In particular, the radioactivity of the cerebral cortex in the mice forced to swim was increased over a period of 30–60 min after injection, and the radioactivity of the cerebellum in the mice forced to swim was slightly reduced as compared with the control mice.

Discussion

[^{11}C]Cyanoimipramine solution was readily obtained with a high specific activity.

A high accumulation of [^{11}C]cyanoimipramine was observed in the brain and lung. The difference between the radioactivity present in the cerebral cortex and in the cerebellum was shown after a period of 10–30 min after injection of the tracer. The regional distribution in the rat brain was examined using [^{11}C]cyanoimipramine with a high specific activity. As can be seen in Table 2, the distribution of [^{11}C]cyanoimipramine in the brain areas of the carrier-added state was reduced as compared with the control. The *in vivo* stability of [^{3}H]cyanoimipramine 30 min after injection was found to be quite stable in the mouse brain for at least 30 min. The relative difference of radioactivity between the cerebral cortex and the cerebellum may probably be due to specific binding of the tracer. It was clearly unknown whether the high accumulation of [^{11}C]cyanoimipramine in the lung depended on specific binding or amine uptake system.

In order to further determine the degree of specific binding of [^{3}H]cyanoimipramine, we studied a carrier-added experiment. In the carrier-added experiment, 1 min after [^{3}H]cyanoimipramine injection with a large amount of carrier cyanoimipramine the radioactivity in the blood was significantly decreased, but unexpectedly the radioactivity in the cerebral cortex and the cerebellum was significantly increased as compared with the carrier-free state. There is a possibility that the high accumulation of the radioactivity in the brain may be due to the redistribution of [^{3}H]cyanoimipramine from peripheral organs such as platelets. Taken together, the *in vivo* specific binding of [^{3}H]cyanoimipramine in the cerebral cortex (receptor rich area) 1 h after injection was estimated at about 40–50% of the total radioactivity.

The mice (or rats) forced to swim were frequently used as animal models for depression (Porsolt *et al.*, 1977; Willner, 1984). The interesting result of this study was that the dynamic changes of the biodistribution of [^{3}H]cyanoimipramine were observed in the mice forced to swim. The radioactivity of the cerebral cortex (receptor rich area) and the blood was significantly changed as compared with that of the cerebellum (receptor poor area). In addition, we previously reported that the accumulation of [^{14}C]iodoantipyrine, a radiotracer for studying regional blood flow, did not differ between control and forced to swim mice (Inoue *et al.*, 1985). This change in the cerebral cortex did not seem to be due to such changes in physiological functions such as blood flow etc. It was clearly unknown whether these dynamic changes of the biodistribution of [^{3}H]cyanoimipramine in the mice forced to swim depended on the change of specific binding or of non-specific binding in the cerebral cortex. Studies to further determine the relationship between the biodistribution of [^{3}H]cyanoimipramine and animal models of depression are necessary.

Dumbrille-Ross and Tang reported that [^{3}H]cyanoimipramine labels a subpopulation of imipramine binding sites in cortical membranes, and might indicate that cyanoimipramine was selectively labelling only the [^{3}H]imipramine binding sites associated with the serotonin transporter (Dumbrille-Ross and Tang, 1983). As previously reported, the dissociation constant (K_d) of ligands was remarkably increased by increase of the temperature (Dumbrille-Ross and Tang, 1983; Plenge and Mellerup, 1984). The dissociation constant (K_d) of [^{3}H]cyanoimipramine at 37°C is 1.39 nM, and this high affinity constant (K_d) almost equals the K_d values of [^{3}H]Ro 15-1788 (Moehler and Richard, 1981) and [^{3}H]spiperone (Laduron and Leysen, 1977), which are used as radioligands for *in vivo* receptor studies (Goeders and Kuhar, 1985; Inoue *et al.*, 1985; Laduron and Leysen, 1977). Nevertheless, [^{3}H]cyanoimipramine binds with its high non-specific component of distribution.

Because of its high non-specific binding, this labelled antidepressant seems to have some problems for *in vivo* receptor studies, although it might be possible to use for pharmacodynamic studies in the living human brain.

Acknowledgements—The authors wish to thank Dr Y. Kahida for valuable advice, and Mr K. Tamate for his technical assistance. Special thanks are also given to Nippon Roche for the kind officer of Ro 11-2465 and Ro 12-5419.

References

Berger M., Maziere M. and Comar D. (1979) An example of a completely automatic method to synthesize a radiopharmaceutical molecule: ^{11}C-Imipramine. *J. Labelled Compd. Radiophram.* **16,** 97.

Briley M. S., Langer S. Z., Raisman R., Sechter D. and Zarifian E. (1980) Tritiated imipramine binding sites are decreased in platelets of untreated depressed patients. *Science* **209,** 303.

Burkard W. P. (1980) Specific binding sites in rat brain for a new and potent inhibitor of 5-hydroxytryptamine uptake: Roll-2465. *Eur. J. Pharmacol.* **61,** 409.

Dumbrille-Ross A. and Tang S. W. (1983) Binding of ^{3}H-Roll-2465: Possible identification of a subclass of ^{3}H-imipramine binding sites. *Mol. Pharmacol.* **23,** 607.

Farde L., Ehrin E., Eriksson L., Greitz T., Hall H., Hedstrom C., Litton J. and Sedvall G. (1985) Substituted benzamides as ligands for visualization of dopamine receptor binding in the human brain by positron emission tomography. *Proc. Natl. Acad. Sci. USA* **82,** 3863.

Frost J. J., Wagner H. N., Dannals H. T., Ravert H. T., Links J. M., Wilson H. D., Burn D. F., Wong R. W., Mcpherson R. W., Rosenbaum A. E., Kuhar M. J. and Snyder S. H. (1985) Imaging opiate receptors in man by positron emission tomography. *J. Comput. Assist. Tomogr.* **9,** 231.

Frost J. J., Wagner H. N., Dannals R. F., Ravert H. T., Wilson A. A., Links J. M., Rosenbaum A. M., Trifiletti R. R. and Snyder S. H. (1986) Imaging benzodiazepine receptors in man with ^{11}C-suriclone by positron emission tomography. *Eur. J. Pharmacol.* **122,** 381.

Fuxe K., Calza L., Benfenati F., Zini I. and Agnati L. F. (1983) Quantitative autoradiographic localization of ^{3}H-imipramine binding sites in the brain of the rat: Relationship to ascending 5-hydroxytryptamine neuron systems. *Proc. Natl. Acad. Sci. USA* **80,** 3836.

Goeders N. E. and Kuhar M. J. (1985) Benzodiazepine receptor binding *in vivo* with ^{3}H-Ro15-1788. *Life Sci.* **37,** 345.

Inoue O., Akimoto Y., Hashimoto K. and Yamasaki T. (1985) Alterations in biodistribution of ^{3}H-Ro15-1788 in mice by acute stress: Possible changes in *in vivo* binding availability of brain benzodiazepine receptor. *Int. J. Nucl. Med. Biol.* **12,** 369.

Laduron P. M. and Leysen J. E. (1977) Specific *in vivo* binding of neuroleptic drugs in rat brain. *Biochem. Pharmacol.* **26,** 1001.

Langer S. Z., Molet C., Raisman R., Dubocovich M. L. and Briley M. S. (1980) High affinity ^{3}H-imipramine binding in rat hypothalamus is associated with the uptake of 5-HT but not norepinephrine. *Science* **210,** 1133.

Langer S. Z., Raisman R., Sechter D., Gay C., Loo H. and Zarifian E. (1984) ^{3}H-Imipramine and ^{3}H-desipramine binding sites in depression. *Frontiers in Biochemical and Pharmacological Research in Depression* (Eds Usdin E. *et al.*), p. 113. Raven Press, New York.

Maitre L., Baumann P. A., Jaekel J. and Waldmeiner P. C. (1982) 5-HT uptake inhibitors: Psychopharmacological and neurobiochemical criteria of selectivity. *Serotonin in Biological Psychiatry*, p. 229 (Eds Ho B. T. *et al.*), p. 229. Raven Press, New York.

Maziere M., Berger G. and Comar D. (1978) ^{11}C-Chloripramine: synthesis and analysis. *J. Radioanal. Chem.* **45,** 453.

Moehler H. and Richards J. G. (1981) Agonist and antagonist benzodiazepine receptor interaction *in vitro*. *Nature* **294,** 763.

Paul S. M., Rehavi M., Skolnick P. and Goodwin F. K. (1980) Demonstration of specific high-affinity binding sites for ^{3}H-imipramine on human platelets. *Life Sci.* **26,** 953.

Paul S. M., Rehavi M., Ricw K. C., Ittah Y. and Skolnick P. (1981) Dose high affinity ^{3}H-imipramine binding label 5-HT reuptake sites in brain and platelets? *Life Sci.* **28,** 2753.

Persson A., Ehrin E., Eriksson L., Farde L., Hedstrom C., Litton J., Mindus R. and Sedvall G. (1985) Imaging of ^{11}C-labelled Ro15-1788 binding to benzodiazepine receptors in the human brain by positron emission tomography. *J. Psychiat. Res.* **19,** 609.

Plenge P. and Mellerup E. T. (1984) Imipramine binding site: Temperature dependence of the binding of ^{3}H-labelled imipramine and ^{3}H-labelled paroxetine to human platelet membrane. *Biochim. Biophy. Acta* **770,** 22.

Porsolt R. D., Bertin A. and Jalfre M. (1977) Behavioural despair in mice: a primary screening test for antidepressants. *Arch. Intern. Pharmacodyn. Ther.* **229,** 327.

Raisman R., Briley M. S. and Langer S. Z. (1979) Specific tricyclic antidepressant binding sites in rat brain. *Nature* **281,** 148.

Samson P., Hantraye P., Baron J. C., Soussaline F., Comar D. and Maziere M. (1985) Kinetics and displacement of ^{11}C-Ro15-1788, a benzodiazepine antagonist, studied in human brain *in vivo* by positron tomography. *Eur. J. Pharmacol.* **110,** 247.

Savaki H., Malgouris C., Benavides J., Laplace C., Uzan A., Gueremy C. and Le Fur G. (1985) Quantitative autoradiography of ^{3}H-indalpine binding sites in the rat brain: II. Regional distribution. *J. Neurochem.* **45,** 521.

Shinotoh H., Yamasaki T., Inoue O., Itoh T., Hashimoto K., Tateno Y., Ikehira H., Suzuki K. and Kashida Y. (1985) A study of benzodiazepine receptor in human brain using ^{11}C-Ro15-1788 and positron emission tomography. *Jap. J. Nucl. Med.* **22,** 1789.

Stanley M., Virgilio J. and Gershon S. (1982) Tritiated imipramine binding sites are decreased in the frontal cortex of suicides. *Science* **216,** 1337.

Suzuki K., Inoue O., Hashimoto K., Yamasaki T., Kuchiki M. and Tamate K. (1985) Computer-controlled large scale production of high specific activity ^{11}C-Ro15-1788 for PET studies of benzodiazepine receptors. *Int. J. Appl. Radiat. Isot.* **36,** 971.

Wagner H. N., Burn H. D., Dannals R. F., Wong D. F., Langstrom B., Duelfer T., Frost J. J., Ravert H. T., Link J. M., Rosenbloom S. B., Lukas S. E., Kramer A. V. and Kuhar M. J. (1983) Imaging dopamine receptors in the human brain by positron tomography. *Science* **221,** 1264.

Wagner H. N. (1986) Quantitative imaging of neuroreceptors in the living human brain. *Semin. Nucl. Med.* **16,** 51.

Willner P. (1984) The validity of animal models of depression. *Psychopharmacology* **83,** 1.

Biochemical Pharmacology, Vol. 36, No. 21, pp. 3671–3675, 1987.
Printed in Great Britain.

0006-2952/87 \$3.00 + 0.00

[^{13}N]-β-PHENETHYLAMINE ([^{13}N]PEA): A PROTOTYPE TRACER FOR MEASUREMENT OF MAO-B ACTIVITY IN HEART

Toshiyoshi Tominaga,*† Osamu Inoue,‡ Kazutoshi Suzuki,‡ Toshio Yamasaki‡ and Masaaki Hirobe*

*Faculty of Pharmaceutical Sciences, University of Tokyo, Tokyo, 113, Japan; and ‡Division of Clinical Research, National Institute of Radiological Sciences, Chiba-shi (CHIBA) 260, Japan

(*Received* 3 *November* 1986; *accepted* 24 *March* 1987)

Abstract—[^{13}N]β-Phenethylamine ([^{13}N]PEA) was evaluated as a radio tracer for the measurement of mouse heart monoamine oxidase (MAO) activity *in vivo*. After intravenous administration, [^{13}N]PEA was deaminated by MAO-B. $^{13}NH_3$ formed thereby was taken up by amino acids and trapped in the heart. The relation between the radioactivity trapped in the heart and the enzyme activity was examined. The radioactivity in the heart 15 min after administration was reduced in a dose-dependent manner by pretreatment with a specific MAO-B inhibitor, *l*-deprenyl, but not with a specific MAO-A inhibitor, clorgyline. A linear correlation existed between the heart radioactivity level and the heart MAO-B activity (0–45%). [^{13}N]1,1-d$_2$-2-Phenethylamine (C_6H_5-CH_2-CD_2-$^{13}NH_2$, [^{13}N]d$_2$PEA), a modified tracer with less reactivity towards the enzyme, was tested similarly. This tracer possessed a higher sensitivity than [^{13}N]PEA, and a wider range (0–85%) of MAO-B activity correlated linearly with the trapped radioactivity. These results indicate that [^{13}N]PEA derivatives ([^{13}N]PEA and [^{13}N]d$_2$PEA) can be useful radiotracers for noninvasive measurements of MAO-B activity in the human heart.

Monoamine oxidase (EC 1.4.3.4, amine:O_2 oxidoreductase, MAO) plays a major role in the metabolism of both endogenous and exogenous amines. MAO has been subdivided into MAO-A and MAO-B according to substrate and inhibitor specificities. Several studies have been carried out to clarify the function of each form of MAO under physiological as well as under pathological conditions. The positron tracer technique, which uses tracers labeled with positron-emitting nuclides (^{11}C, ^{13}N, ^{18}F, etc.), and positron emission tomography (PET) are useful methods for the noninvasive measurement of the rates of transport, metabolism and excretion of various substances in humans and animals *in vivo*. So is [^{18}F]deoxyglucose which is widely used to study cerebral metabolic rates of glucose [1].

In several studies, positron tracer techniques have been applied in the estimation of MAO activity *in vivo* [2–4]. Recently, we developed [^{11}C]*N*,*N*-dimethylphenylethylamine as a tracer for the measurement of brain MAO-B activity, utilizing the principle of metabolic trapping [5].

Previously, we had reported [6] the synthesis of several [^{13}N]amines as well as their distribution and metabolism after injection in mice. After administration of these [^{13}N]amines, the radioactivity is metabolically trapped in the cardiac muscle. The amines are metabolized by MAO into $^{13}NH_3$, which is then trapped as part of labeled amino acids. The unmetabolized amines are excreted from the organ. Since the radioactivity is trapped in proportion to the amount of $^{13}NH_3$, the heart radioactivity may correlate with the activity of MAO. Based on this assumption, we are designing tracers for the estimation of heart MAO activity *in vivo*.

In this study, we evaluated [^{13}N]β-phenethylamine ([^{13}N]PEA) as a prototype tracer and found that changes in MAO-B activity in mice hearts were selectively detected and that the sensitivity of the tracer towards the enzyme activity was changed by chemical modification.

MATERIALS AND METHODS

Materials. Clorgyline hydrochloride (CLO) and *l*-deprenyl hydrochloride (DPL) were provided by May & Baker Ltd., Dagenham, U.K. and Dr. J. Knoll, Department of Pharmacology, Semmelweis University of Medicine, Budapest, Hungary, respectively. Other chemicals and solvents were of the highest grade commercially available.

Preparation of [^{13}*N*]*PEA and* [^{13}*N*]*d*$_2$*PEA*. [^{13}N]PEA and [^{13}N]d$_2$PEA were synthesized according to a method we published previously [7]. Briefly, [^{13}N]phenylacetamide was synthesized from phenylacetyl chloride and [^{13}N]ammonia; the intermediate amide was reduced by $LiAlH_4$ to yield [^{13}N]PEA and by $LiAlD_4$ to yield [^{13}N]d$_2$PEA. The radiochemical purities and the specific activities of the products were over 90% and about 100 Ci/mmol respectively.

Time course of heart and blood radioactivity levels after i.v. administration of [^{13}*N*]*PEA*. Aqueous solutions of [^{13}N]PEA hydrochloride (prepared in a non-carrier-added state, 0.2 ml, about 30 μCi/mouse,

---

* All correspondence should be addressed to T. Tominaga, Division of Chemical Research, National Institute of Radiological Sciences, 9-1 Anagawa-4-chome, Chiba-shi (CHIBA) 260, Japan.

1.2 μg/kg) were injected into tail veins of male C3H mice (10–12 weeks, about 30 g). After given time intervals, the animals were killed, blood and hearts were removed and weighed, and their radioactivity levels were determined in a well-scintillation counter. The results are expressed in terms of percent dose per g heart or blood respectively. In the study of the effect of MAO inhibition, pargyline hydrochloride (PGL, 100 mg/kg, i.p.) was administered 1 hr before the injection of the tracer.

Effect of specific MAO inhibitors on the amount of radioactivity trapped in the heart after administration of [^{13}*N*]*PEA or* [^{13}*N*]*d*$_2$*PEA*. CLO (MAO-A inhibitor, 0.1 to 10 mg/kg) or DPL (MAO-B inhibitor, 0.01 to 10 mg/kg) was injected into the tail veins of male C3H mice. One hour after this pretreatment, [^{13}N]PEA or [^{13}N]d$_2$PEA was injected intravenously and 15 min later the mice were killed; hearts and blood were removed and weighed, and their radioactivity levels were determined. The results are expressed in terms of percent dose per g heart or blood respectively.

Analysis of the radioactive metabolites after i.v. administration of [^{13}*N*]*PEA*. [^{13}N]PEA was injected into tail veins of control mice or mice pretreated with either CLO (10 mg/kg, i.v.) or DPL (10 mg/kg, i.v.). Three or 15 minutes later, the mice were killed, and the hearts were removed and homogenized in 2 ml of physiological saline. The homogenates were basified with NaOH and extracted with water-saturated ethyl acetate. The extraction efficiency was determined by comparing the radioactivity in the extract and that in the homogenate. The extract of the homogenate from DPL-pretreated mice was analyzed using thin-layer chromatography [TLC, silica gel, chloroform–methanol (2:1)].

In vitro *assay of MAO activity in heart and liver.* MAO activity in mice was determined radiometrically *in vitro* as described previously [8]. The tissue homogenate was incubated with a final concentration of 0.01 mM [^{14}C]PEA (as a substrate for MAO-B) or 0.01 mM [^{14}C]5-HT (as a substrate for MAO-A) at 37° and pH 7.4. The incubation period was 10 min with 5-HT and 5 min and PEA. The amount of product formed was found to be proportional to the incubation time and the amount of enzyme preparation used. For the determination of *in vivo* inhibition of MAO activity, C3H mice were pretreated with various doses of either CLO or DPL 1 hr before they were killed, and the enzyme activity was measured as described above.

RESULTS

Figure 1 shows the time courses of the radioactivity in the heart after the administration of [^{13}N]PEA in control and pargyline-pretreated mice. MAO inhibition hindered the retention of the radioactivity in the heart, though there was little change in the blood radioactivity (see Ref. 6 for the radioactivity in organs other than the heart). The effects of specific MAO inhibitors on the radioactivity trapped in the heart after the injection of [^{13}N]PEA are shown in Fig. 2. The radioactivity levels were decreased markedly and in a dose-dependent manner by the pretreatment with the specific MAO-B inhibitor DPL, whereas the specific MAO-A inhibitor CLO had no significant effect up to a dose of 10 mg/kg.

The extraction efficiency of radioactive material from the heart homogenate after the administration of [^{13}N]PEA was low unless the animal had been pretreated with DPL (Table 1). Over 86% of the radioactivity in extracts from the hearts of DPL-pretreated mice was that of unmetabolized [^{13}N]PEA.

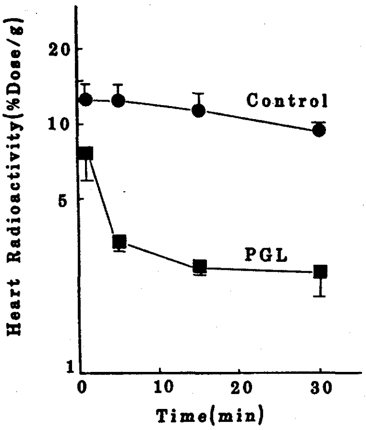

Fig. 1. Time course of heart radioactivity after intravenous administration of [^{13}N]PEA in control mice and PGL-pretreated mice. Radioactivities are expressed as percent dose per gram organ. Values are expressed as averages ±1 SD of three mice for each point.

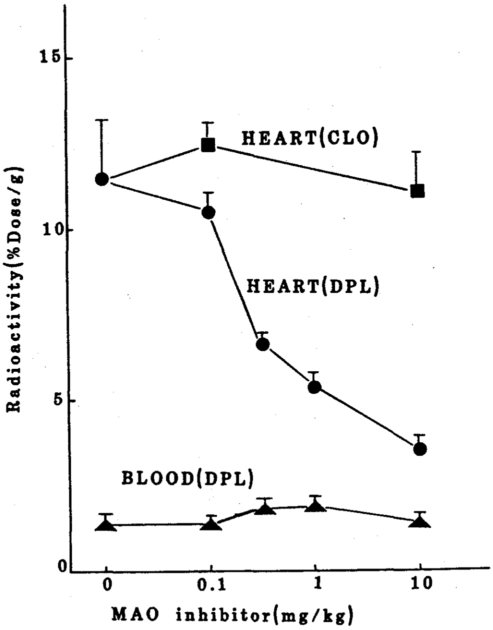

Fig. 2. Effect of specific MAO inhibitors on heart and blood radioactivities 15 min after administration of [^{13}N]PEA. Radioactivities are expressed as percent dose per gram organ. Values are expressed as averages ±1 SD of three mice for each point.

Table 1. Extractable metabolites in the heart after i.v. administration of [^{13}N]PEA

Pretreatment	Time after i.v. (min)	Extraction efficiency* (%)
None	3	5
	15	4
DPL	3	79
	15	60
CLO	3	3
	15	4

* The homogenate of a heart was basified and extracted with water-saturated ethyl acetate as described in the text; each value given is the mean of two mice.

MAO-A and MAO-B activities remaining in the hearts and the livers of mice pretreated with specific MAO inhibitors are summarized in Table 2. CLO as well as DPL keeps its MAO subtype specificity also *in vivo*.

Plots of the radioactivity trapped in the heart (Fig. 2) against the activity of two forms of MAO remaining after the pretreatment with CLO or DPL (Table 2) are shown in Fig. 3. The radioactivity was proportional to the percentage of remaining MAO-B activity in a range between 0 and about 45%, but it did not correlate with the MAO-A activity (CLO pretreatment).

The effect of DPL on the heart radioactivity after the administration of [^{13}N]d$_2$PEA was compared with that after the administration of [^{13}N]PRA (Fig. 4). Substitution of the α-position with deuteriums markedly increased the sensitivity of the tracer to DPL. An appreciable decrease in the radioactivity was observed only at the DPL doses over 0.3 mg/kg

Table 2. Remaining NAO activity in mice hearts and livers after pretreatment with various doses of CLO and DPL respectively

MAO inhibitor (mg/kg)		Heart MAO-A	Heart MAO-B	Liver MAO-A	Liver MAO-B
		Percent of initial enzyme remaining			
CLO					
	0.1	68.1	116.8	110.3	126.1
	10	25.3	87.1	32.0	90.0
DPL					
	0.01	98.6	84.5	74.0	109.3
	0.1	110.8	43.8	91.1	90.0
	0.33	68.9	7.6	66.5	82.2
	1.0	37.9	3.8	45.5	35.7
	10	45.4	3.5	40.0	9.0

Various doses of either CLO or DPL were injected intraveneously into mice 1 hr before decapitation. Remaining activities were assayed as described in the text and expressed as percentages of the control activity. Each value is the mean of three mice, MAO-A activities of the heart and the liver were 0.08 and 0.19 nmol product formed per mg of protein per min respectively. MAO-B activities of the heart and the liver were 1.1 and 3.8 nmol product formed per mg protein per min respectively.

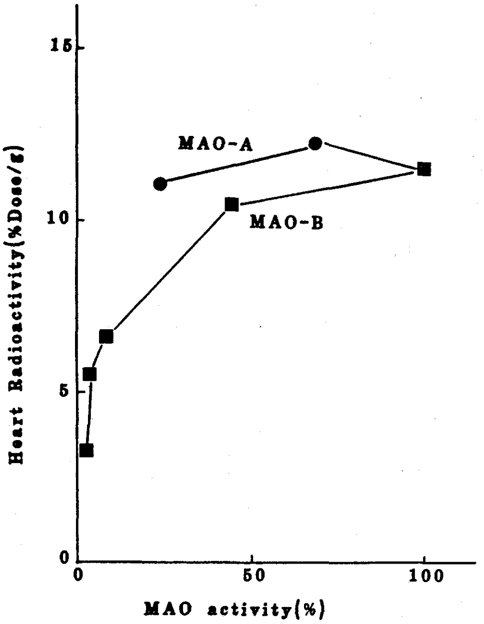

Fig. 3. Relation between MAO activity and heart radioactivity after administration of [^{13}N]PEA. Radioactivities are expressed as percent dose per gram organ. Values are expressed as averages of three mice for each point.

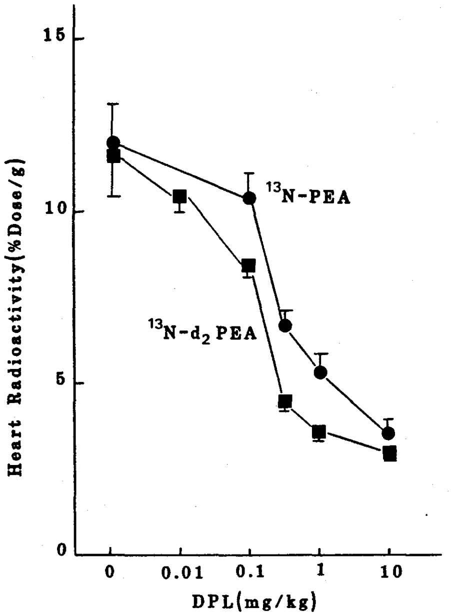

Fig. 4. Effect of DPL on heart radioactivity 15 min after administration of either [^{13}N]PEA or [^{13}N]d$_2$PEA. Radioactivities are expressed as percent dose per gram organ. Values are expressed as averages ±1 SD of three mice for each point.

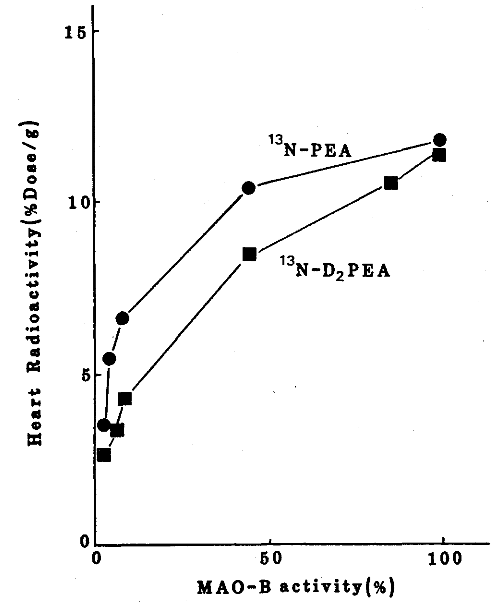

Fig. 5. Relation between MAO-B activity and heart radioactivity after administration of either [^{13}N]PEA or [^{13}N]d$_2$PEA. Radioactivities are expressed as percent dose per gram organ. Values are expressed as averages of three mice for each point.

in the case of [^{13}N]PEA, whereas in the case of [^{13}N]d$_2$PEA, it was observed at doses over 0.1 mg/kg. [^{13}]d$_2$PEA afforded a lower level of trapped radioactivity in the hearts of mice that had been pretreated with equal dose of DPL. Furthermore, a wider range of the MAO-B activity (0–85%) showed a linear correlation with the trapped radioactivity (Fig. 5).

DISCUSSION

Recent advances in positron-tracer techniques have opened up the possibility of using various organic compounds as tracers to study various physiological functions. In the field of cardiac nuclear medicine, ^{11}C-labeled tracers have been used to study fatty acid metabolism [9] and β-receptor functions [10] in the heart. However, there have been few studies using this tracer technique to clarify degradation processes of the transmitting amines, an important aspect in the regulatory system of a heart. Therefore, we have tried to develop a tracer for the estimation of myocardial MAO activity.

Three different methods using the tracer technique for the estimation of MAO activity *in vivo* have been reported. The first one by Gallagher *et al.* [2] is the radiorespirometric method, e.g. the measurement of expired ^{11}CO$_2$ after injection of α[^{11}C]-*n*-octylamine. However, the rate-determining step in the ^{11}CO$_2$ excretion has been reported to occur after the deamination. The second one uses ^{11}C-labeled MAO inhibitors, [^{11}C]deprenyl, [^{11}C]clorgyline, and [^{11}C]pargyline, as tracers [3, 4]. This method has been reported to be useful to assay MAO activity *in vivo*, though the correlation between tracer uptake and MAO activity in organs has not yet been established.

The third method uses a labeled substrate as a tracer, and the radioactivity of a metabolite trapped in the target organ is measured. In our previous report [5], we evaluated [^{11}C]*N,N*-dimethylphenylethylamine ([^{11}C]DMPEA) as a substrate tracer to measure the brain MAO-B activity *in vivo*. After intravenous administration, this tracer rapidly enters the brain and is selectively deaminated by MAO-B into [^{11}C]dimethylamine which is then trapped by the blood–brain barrier (BBB). The unmetabolized tracer is rapidly eliminated from the brain so that the radioactivity trapped in the brain is in proportion to the brain MAO-B activity. The same principle seems to be applicable in the estimation of MAO activity in other organs. However, [^{11}C]DMPEA itself cannot be used for this purpose, because [^{11}C]dimethylamine is trapped only by the BBB in the brain and is eliminated rapidly from other organs such as the heart.

After intravenous injection, [^{13}N]amines liberate ^{13}NH$_3$ upon MAO oxidation. This ^{13}NH$_3$ is converted into labeled amino acids (mainly [^{13}N]glutamine) and retained in the organ according to metabolic turnover (Ref. 6; for the metabolic fate of ^{13}NH$_3$, see Ref. 11). In the mouse heart, the labeled amino acids are trapped for at least 30 min after administration, while unmetabolized amines are rapidly excreted from the organ (Ref. 6, Fig. 1). Since ^{13}NH$_3$-fixing enzymes (mainly glutamine synthetase) exist in large excess to the ^{13}NH$_3$ liberated in the heart and the conversion proceeds very rapidly [11], the rate-determining step of the trapping of the radioactivity should be the MAO oxidation. After elimination of the unmetabolized tracer, all the radioactivity in the heart corresponds to that of the labeled amino acids whose amount correlates with the MAO activity. Therefore, the myocardial MAO activity can be assayed via the radioactivity in the heart.

We selected [^{13}N]PEA as a prototype substrate tracer for the following reasons. (1) PEA is a specific substrate for MAO-B, and the effects of chemical modification such as β-hydroxylation or α-deuteration on the properties have been well studied. (2) [^{13}N]PEA can be rapidly synthesized in a good yield according to the method described in our previous paper [7]. (3) [^{13}N]PEA shows high heart uptake and is therefore suitable for external measurement of the heart radioactivity. We measured the heart radioactivity 15 min after the injection of the tracer, because by that time the metabolism as well as the elimination of unmetabolized tracer were found to be completed (Fig. 1, Table 1).

As shown in Fig. 2, the heart radioactivity 15 min after intraveneous injection of [^{13}N]PEA was reduced in a dose-dependent manner by DPL pretreatment but not by CLO pretreatment. This reduction is accompanied by the hindrance of metabolism of the tracer (Table 1). Although the pretreatment with 0.33 mg/kg of DPL had only a slight effect on the MAO-B activity in the liver (Table 2), the main amine-metabolizing organ, it significantly reduced the radioactivity trapped in the heart. The radioactivity in the blood was low (about 2% dose/g) and remained unchanged by the pretreatment. These facts show that the determining factor for heart radioactivity was the MAO-B activity in the heart and not the metabolism of the tracer in other organs or the unchanged or metabolized tracer in the blood. For detailed studies on human myocardial MAO activity using PET, however, the amount of the unchanged tracer as well as that of the metabolites in the blood would have to be measured in order to achieve accurate quantitation of the enzyme activity.

As shown in Fig. 3, there is a good correlation between the radioactivity trapped in the heart and the activity of heart MAO-B, but not that of MAO-A. This fact clearly indicates that $[^{13}N]$PEA can be used as a prototype tracer for the measurement of human heart MAO-B activity by external detection (PET). However, we observed direct linearity only when the MAO-A activity was in a range of 0–45% of the control activity. Accordingly, a small change in the enzyme activity cannot be detected with this tracer.

Model considerations of metabolic trapping of a labeled tracer [12] revealed that the measurable range (range of an enzyme activity showing linear correlation with the trapped radioactivity) depends primarily on the rate of metabolism of a substrate tracer. The relationship between the upper limit of the measurable range and the rate of the metabolism is expressed in the following equation:

$$UL = C \times K_{el}/K_m$$

where UL is the ratio of the upper limit to the total enzyme activity, C is a constant which depends on the detector such as a positron camera, K_{el} is the rate constant of the elimination of the tracer from the organ, and K_m is the rate constant of the metabolism of the tracer. From this equation, the following are clear. If a tracer is metabolized very easily, an appreciable decrease in the trapped radioactivity appears only when the enzyme activity is reduced severely, whereas a tracer that is metabolized slowly is suitable for detecting a small decrease in activity. Therefore, in order to upgrade the measurable range of the MAO-B activity, a tracer with a lower reactivity than that of $[^{13}N]$PEA but an unchanged specificity towards the enzyme should be used.

According to Yu *et al.* [13], deuterium substitution in the α-position of PEA reduces its reactivity (V_{max}) to half but does not reduce the specificity towards the subtypes of MAO. Taking advantage of this fact, we adopted $[^{13}N]d_2$PEA as a modified tracer. As expected, a smaller decrease in the enzyme activity could be detected using $[^{13}N]d_2$PEA and, consequently, the MAO-B range that shows a linear correlation with the heart radioactivity was extended (Figs. 4 and 5). Thus, one advantage of this method is that the property of the tracer can be adjusted to the respective needs. In a clinical application, the tracer should be modified so as to match the human heart MAO activity.

In conclusion, $[^{13}N]$PEA derivatives ($[^{13}N]$PEA and $[^{13}N]d_2$PEA) were found to be useful radiotracers for the measurement of heart MAO-B activity by external detection. It was also shown that the property of the tracer can be adjusted by chemical modification.

Acknowledgement—The authors are grateful to Mr. K. Tamate for the isotope production.

REFERENCES

1. M. E. Phelps, S. C. Huang, E. J. Hoffmann, C. Slein, L. Sokoloff and D. E. Kuhl, *Ann. Neurol.* **6**, 371 (1979).
2. B. M. Gallagher, J. S. Fowler, R. R. MacGregor and A. P. Wolf, *Biochem. Pharmac.* **26**, 1917 (1977).
3. R. R. MacGregor, C. Halldin, J. S. Fowler, A. P. Wolf, C. D. Arnett, B. Langstrom and D. Alexoff, *Biochem. Pharmac.* **34**, 3207 (1985).
4. K. Ishiwata, T. Ido, K. Yanai, K. Kawashima, Y. Miura, M. Monma, S. Watanuki, T. Takahashi and R. Iwata, *J. nucl. Med.* **26**, 630 (1985).
5. O. Inoue, T. Tominaga, T. Yamasaki and H. Kinemuchi, *J. Neurochem.* **44**, 210 (1985).
6. T. Tominaga, O. Inoue, K. Suzuki, T. Yamasaki and M. Hirobe, *Int. J. nucl. Med. Biol.*, in press.
7. T. Tominaga, O. Inoue, K. Suzuki, T. Yamasaki and M. Hirobe, *Appl. Radiat. Isot.* **37**, 1209 (1986).
8. C. J. Fowler and L. Oreland, *Biochem. Pharmac.* **29**, 2225 (1980).
9. E. Livni, D. R. Elmaleh, S. Levy, G. L. Brownell and W. H. Strauss, *J. nucl. Med.* **23**, 169 (1982).
10. A. Syrota, D. Dormont, J. Berger, M. Maziere, C. Prenant, J. Sastre, J. M. Davy, M. C. Aumant, J. Motte and R. Gourgon, *J. nucl. Med.* **24**, p 20 (1983).
11. H. R. Schelbert, M. E. Phelps, S. Huang, N. S. MacDonald, H. Hansen, C. Selin and D. E. Kuhl, *Circulation* **63**, 1259 (1981).
12. O. Inoue, T. Tominaga, N. Fukuda, K. Suzuki and T. Yamasaki, *Jap. J. nucl. Med.* **21**, 671 (1984).
13. P. H. Yu, S. Barclay, B. David and A. A. Boulton, *Biochem. Pharmac.* **30**, 3089 (1981).

Specific Biodetection of B16 Mouse Melanoma In Vivo by Syngeneic Monoclonal Antibody

Toshiro Yamasaki, M.D., Seiji Wakabayashi, M.D., Osamu Inoue, M.D., Koichi Ando, M.D., Kiyoko Kusakabe, M.D., Yukiko Kawasaki, M.D., Shoji Okamoto, M.D., and Masaru Taniguchi, M.D.

National Institute of Radiological Sciences (TY, OI, KA), Chiba; Departments of Dermatology (SW, SO) and Immunology (MT), School of Medicine, Chiba University, Chiba; Department of Radiology, Tokyo Women's Medical College (KK, YK), Tokyo, Japan

---

The specific detection of tumors in vivo using a radiolabeled syngeneic monoclonal antibody made by fusion of P3U1 (BALB/c myeloma cells) and C57BL/6 spleen cells primed with syngeneic B16 melanoma cells was investigated by color imaging, autoradiography, and biodistribution. The radiolabeled antimelanoma antibody specifically accumulated only in the tumor lesions, whereas no radioactivity was observed in normal tissues or organs. The distribution patterns of the radioactive antibody in the tumor lesions depended on the sizes of the tumor. Almost the entire region of the small metastatic tumor in lymph nodes was labeled, whereas the radioactive antibody was irregularly localized mainly in the center of the medium-sized tumor. However, only the peripheral region of the large primary tumor was labeled. The highest uptake of radioactivity (tumor:blood ratio) was observed in the small lymph node metastatic tumor lesions rather than in the large primary tumor. Furthermore, high resolution color imaging of B16 melanoma was also obtained by using ^{125}I-labeled monoclonal antibody. Tumor location was specifically visible without subtraction or enhancement methods 3–5 days after injection of the radiolabeled antibody. *J Invest Dermatol 89:225–229, 1987*

The development of monoclonal antibody technology enabled us to use specific antitumor antibodies as diagnostic or therapeutic agents for cancer. The use of cytotoxic drugs, toxins, or radioisotopes coupled to monoclonal antitumor antibodies may be ideal to specifically kill tumor cells [1–5]. A prerequisite for passive immunotherapy, however, is that the antibodies are able to reach target tumor cells in vivo without degradation or removal of the antibody activity. In this sense, the murine syngeneic monoclonal antimelanoma antibody (M2590), recently established in our laboratory by the fusion of BALB/c myeloma (P3U1) and C57BL/6 spleen cells primed with syngeneic B16 melanoma cells, has ideal characteristics for application of diagnostic and therapeutic means. The antibody reacts with both human and mouse melanoma antigens on the cell surface [6] and detects the antigens in the tumor tissues, but not in the sera of patients or animals with melanomas [7], and also shows no reactivity to normal tissues and organs [6,8]. Therefore, the monoclonal antibody is expected to give higher tumor uptake with less clearance from the circulation.

The location of animal and human tumors in vivo has been demonstrated by use of radiolabeled monoclonal antibodies [9–14]. Some radiolabeled mouse monoclonal antibodies against human tumor cells have been shown to exhibit high background activity in the imaging of the human tumor that obscures the location of tumor lesions if the subtraction methods were not applied. However, syngeneic monoclonal antimelanoma antibodies without detectable reactivity to normal tissues would provide ideal tools for specific detection of the location of tumors in vivo. Moreover, the use of the monoclonal antibody with interspecies reactivity is ideal for establishing animal models for the diagnosis of human melanomas in vivo.

In this report, we describe the tumor location of the syngeneic monoclonal antimelanoma antibody (M2590). The results show excellent detection of melanomas by external photoscanning with display of radioactivity data as a color-scaled image or autoradiography in the experimental animal model.

MATERIALS AND METHODS

Mice C57BL/6 CrSlc mice, 8–12 weeks old, were purchased from the Shizuoka Experimental Animal Laboratory Co., Ltd., Hamamatsu, Japan.

Tumor Cell Line C57BL/6 derived B16 melanoma cell line [15] was used.

Monoclonal Antibody Mouse syngeneic monoclonal antimelanoma antibody (M2590:IgM) was established by the fusion of BALB/c myeloma (P3U1) with C57BL/6 spleen cells repeatedly immunized with syngeneic B16 melanoma cells [6]. Properties and characteristics of the monoclonal antibody (M2590) have been described elsewhere [6,8]. The antibody reacted with melanoma cells of mouse, human, and hamster origin, but not with normal tissues of C57BL/6 mice so far tested, including eye, skin, and brain, nor with other mouse tumor cells, including neuroectodermal tumors, such as neuroblastomas. The interspecies determinants detected by the M2590 antibody were found to be GM$_3$(NeuAc) gangliosides [16]. Affinity (kD) of M2590 to GM$_3$ ganglioside was 1 μg/ml as enumerated by scatchard analysis.

Manuscript received October 20, 1986; accepted for publication January 8, 1987.

This work was supported in part by grants from the Ministry of Education, Culture and Science, and from the Ministry of Welfare, Japan.

Reprint requests to: Masaru Taniguchi, M.D., Department of Immunology, School of Medicine, Chiba University, 1-8-1 Inohana, Chiba, Japan 280.

Iodination Conjugation of monoclonal antibody with iodine-125 was carried out by the iodogen method of Salacinski and colleagues [17]. The reaction mixture was passed through a Sephadex G-25 column for separation of free radioiodine. Specific activity used in this study was 2–4 μCi/μg protein. Immunoreactivity of the labeled antibody was generally ½ to ⅓ of original antibody activity as tested in cell-binding assay.

Organ Distribution of Isotope-Labeled Immunoglobulin in Tumor-Bearing Mice B16 melanoma-bearing mice received i.v. ^{125}I-labeled monoclonal antibody (M2590) or ^{125}I-labeled control myeloma protein (CBPC-112:IgM) without specific binding activity (50 μCi). Generally, drinking water was supplemented with 0.1% Lugol's iodine throughout the experiments. Five days later, the mice were killed and dissected. Tumors, visceral organs, eye, brain, thyroid, skin, and blood samples were weighed and assayed for radioactivity. Results were expressed as a percentage of injected radioactivity per gram tissue (% dose/g) and as the organ:blood ratio of radioactivity. Finally, the specificity index of organ location was calculated by dividing the specific antibody uptake into the organ by the control myeloma protein uptake according to the following formula:

$$\text{Specificity index} = \frac{(\text{organ:blood ratio})\text{M2590}}{(\text{organ:blood ratio})\text{CBPC-112}}$$

Scintigraphy and Autoradiography B16 melanoma cells (1 × 10^6) were inoculated s.c. into the lower back of C57BL/6 mice. Mice were injected i.v. through the tail vein with 50 μCi of ^{125}I-labeled monoclonal antibody or ^{125}I-labeled myeloma protein (CBPC-112) (sp act 4 μCi/μg). Six days later, the accumulation of radioactive antibodies was investigated by scintigraphy as described elsewhere [9]. In another experiment, the technique of whole-body autoradiography was used to study the distribution of radioactive monoclonal antibodies in sections of the tumor-bearing mice [18]. Seven days after the antibody injection, the mice were sacrificed, freeze-dried, and cut into 40 μm-thick slices with an autocryotome (NA 200F, Nakagawa-Seikado, Tokyo). Sections were air-dried for 24–48 h at 4°C and then exposed to Fuji x-ray film (Fuji Industrial Photo Film Co., Ltd., Tokyo) at room temperature for 2–4 weeks in light-tight boxes.

External Color Imaging Normal and melanoma-bearing mice in groups of 3 were given an i.v. injection of 50 μCi of the ^{125}I-labeled monoclonal antimelanoma antibody (sp act 4 μCi/ug). In this experiment, mice were given Lugol's iodine in drinking water starting 3 days before administration of radioactive agents. To avoid movement artifacts, animals were anesthetized with sodium pentobarbital (50 mg/kg i.p. injection) prior to imaging. The mice were scanned sequentially for 7 days with a scintillation camera (Ohio Nuclear Sigma 410S, Technicare, Solon, Ohio) interfaced to a computer (VIP450 Computer System, Technicare).

Table I. Organ Distribution of Radioiodinated Monoclonal Antibody in Melanoma-Bearing Mice[a]

Organ	Antimelanoma Antibody (M2590) % Dose/g	Antimelanoma Antibody (M2590) Organ/Blood	Control Antibody (CBPC-112) % Dose/g	Specificity Index
Tumor	5.23 ± 0.62	3.35	1.03 ± 0.19	4.4
Blood	1.56 ± 0.65	1.00	1.34 ± 0.28	1.0
Brain	0.30 ± 0.05	0.19	0.30 ± 0.06	0.9
Retina	0.51 ± 0.07	0.33	0.56 ± 0.08	0.8
Thyroid	1.06 ± 0.15	0.68	1.14 ± 0.38	0.8
Heart	0.96 ± 0.18	0.62	0.79 ± 0.23	1.1
Lung	1.61 ± 0.16	1.03	1.46 ± 0.40	0.9
Liver	1.89 ± 0.23	1.21	1.92 ± 0.22	0.8
Spleen	1.40 ± 0.31	0.90	1.01 ± 0.10	1.2
Kidney	1.87 ± 0.50	1.20	1.47 ± 0.48	1.1
Skin	0.95 ± 0.13	0.61	0.80 ± 0.28	1.0

[a] C57BL/6 mice (4 mice) bearing B16 melanoma (20 × 30 mm) were injected with 50 μCi of ^{125}I-labeled antimelanoma (M2590) or with 50 μCi ^{125}I-labeled control myeloma protein (CBPC-112). Results were shown as percent of initial radioactivity per gram of organ (mean ± SD of 4 samples) and as organ/blood ratio. Specificity index = (organ/blood ratio) M2590/(organ/blood ratio) CBPC-112.

Table II. Accumulation of Monoclonal Antibody Depending on Size of Tumor

Tumor Size (mm^2)	^{125}I-Antibody Uptake (tumor/blood ratio)[a]
1 × 2	20.7
20 × 30	3.4
30 × 50	1.2

[a] A C57BL/6 mouse bearing B16 melanoma was injected with 50 μCi of ^{125}I-labeled monoclonal antibody (M2590). The mouse was the same as shown in Fig 2. Another experiment gave similar results. The data of one experiment were shown here. Tumor/blood ratio = (% dose/g) tumor/(% dose/g) blood.

RESULTS

Biodistribution of ^{125}I-Labeled Monoclonal Antibody in Melanoma-Bearing Mice The organ distribution of radioactivity in mice bearing syngeneic B16 melanoma was investigated by i.v. injection with 50 μCi of ^{125}I-labeled syngeneic monoclonal antimelanoma antibody or an equal amount of ^{125}I-labeled control myeloma protein (CBPC-112:IgM) (Table I). Five days after the injection of antibody into mice bearing medium-sized tumor (about 20 × 30 mm), the radioactivity of M2590 antibody, expressed as a percent dose/g tissue, was significantly greater in tumors (5.23%) than in healthy organs (0.30–1.89%). The differences in the radioactivity of tumors and normal tissues are sufficiently high to achieve statistical significance ($p < 0.01$). The control myeloma protein (CBPC-112), however, could not show significant differences between tumors (1.03%) and healthy organs (0.3–1.92%). The specificity index of tumors derived from the organ:blood ratio of the M2590 antibody was 4.4 when compared with the control myeloma protein, indicating preferential uptake of the M2590 antibody into melanoma. The accumulation of radioactive monoclonal antibody (M2590) into the tumor, however, was found to depend on the tumor size (Table II). The highest ratio of uptake of radioactivity (20.7) was observed in the small metastatic tumor lesions (about 1 × 2 mm) in regional lymph nodes, whereas the ratio of uptake detected in the large primary tumor (about 30 × 50 mm) was rather low (1.2–3.4).

Tumor Location With ^{125}I-Labeled Monoclonal Antimelanoma Tumor location by the radiolabeled antimelanoma antibody was attempted with scintigraphy and autoradiography. Mice bearing B16 melanoma in the lower back were given 50 μCi of ^{125}I-labeled antimelanoma or ^{125}I-labeled control myeloma protein (CBPC-112) 6 days previously. Scintigraphy showed significant localization of radioactivity in the region of the melanoma tumor (Fig 1*A*). On the other hand, the radioactivity was not detected in the area corresponding to the tumor when the radioactive control myeloma protein was used (Fig 1*B*). It is thus demonstrated that the accumulation of radioactivity in the tumor entirely depends on the antibody specificity. Nonspecific accumulation of radioactivity was observed in the upper part of mice. This is due to the uptake of radioactive free iodine in the thyroid in this particular experiment.

The same mice as those used in the scanning experiment were sacrificed and examined for tumor location of radioactive monoclonal antimelanoma by autoradiography. As shown in Fig 1*C* and *D*, the radioactivity was localized only in the tumor region. The radioactive antibody was irregularly accumulated in the center of the tumor, however, when the tumor size was about 20 × 30 mm. The radioactivity in the stomach was probably the result of metabolism of radioactive iodine (Fig 1*D*). When the

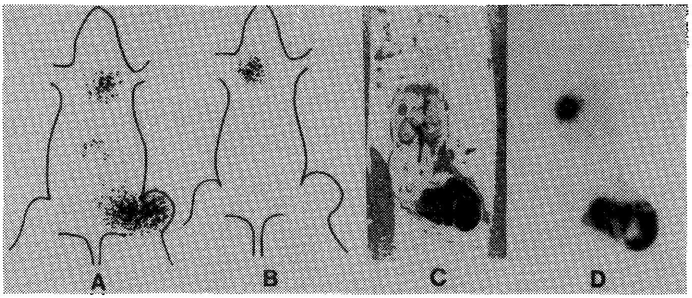

Figure 1. Scintigram and autoradiogram of melanoma-bearing mice. The scintigrams were obtained in C57BL/6 mice bearing B16 melanoma (20 × 30 mm in the right lower or back) 6 days previously injected with (*A*) ^{125}I-labeled monoclonal antimelanoma (M2590), or (*B*) ^{125}I-labeled control myeloma protein (CBPC-112). Note that the accumulation of radioactivity in a round shape at the top of the scintigram in (*A*) and (*B*) is due to the uptake in the thyroid. The accumulation of the antimelanoma antibody was further investigated in hemisection (*C*) of melanoma-bearing mice injected with ^{125}I-antimelanoma (M2590) and corresponding autoradiograph (*D*) showing irregular but central accumulation of the radioactive M2590 antibody in the tumor. Note that the radioactive area (round shape) of the middle left in (*D*) is not due to the melanoma, but to the secretion of free iodine in the stomach. Two other experiments showed similar results.

localization of the radioactive antibody was investigated in large tumor lesions (about 30 × 50 mm), the antibody preferentially accumulated at the peripheral region but not in the center of the tumor (Fig 2*B*). Moreover, 3 metastatic tumor lesions in the regional lymph nodes (Fig 2*B*) were also visible, and almost their entire regions were labeled.

Time Course of Gamma Camera Images in Normal and Tumor-Bearing Mice The feasibility of color imaging with time after injection of ^{125}I-labeled monoclonal antibody (M2590) into normal and melanoma-bearing mice was studied. One hour after injection (Fig 3*A*), the majority of radioactivity was observed in the blood pool without organ-specific uptake of the radioactive antibody in both normal and tumor-bearing mice. In tumor-bearing mice, however, the radioactivity gradually accumulated with time in the tumor area, such as at 24 h (Fig 3*B*), 3 days (Fig 3*C*), and 5 days (Fig 3*D*) after the antibody injection. In contrast, normal animals injected with the same doses of ^{125}I-antimelanoma antibody showed diffuse and nonspecific weak radioactivity. The optimal time for tumor imaging was observed on day 5 after injection of the antibody.

DISCUSSION

This study shows that the radiolabeled mouse monoclonal antimelanoma antibody with interspecies reactivity to various human melanomas could effectively reveal the transplanted solid mouse melanoma grown in syngeneic mice. The conditions of the experimental animal model in the present study reflect those of human patients with melanoma in terms of the treatment of hu-

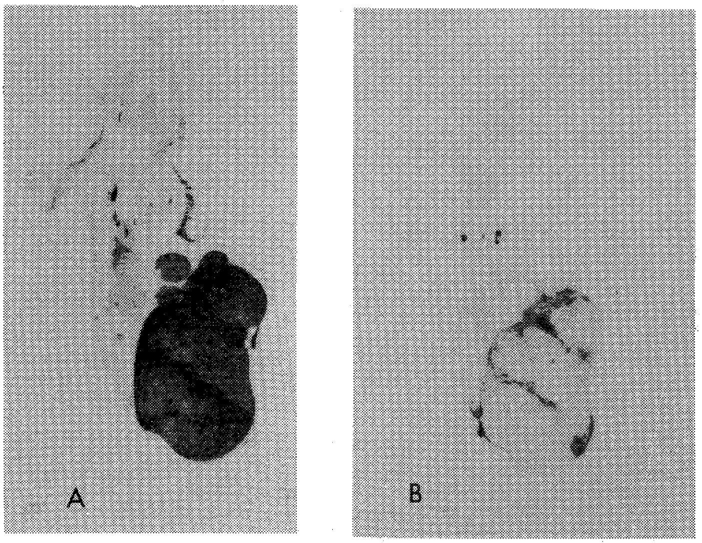

Figure 2. Localization of radioactive monoclonal antimelanoma antibody (M2590) in a mouse bearing large-sized melanoma. A C57BL/6 mouse bearing B16 melanoma (30 × 50 mm) was injected with ^{125}I-labeled monoclonal antimelanoma antibody (M2590) 7 days previously. Section (*A*) of the melanoma-bearing mouse was examined for accumulation of radioactivity by autoradiography (*B*). Note the localization of radioactivity at the peripheral area of the tumor and also in 3 metastatic tumor lesions in the regional lymph nodes. Another experiment gave similar results.

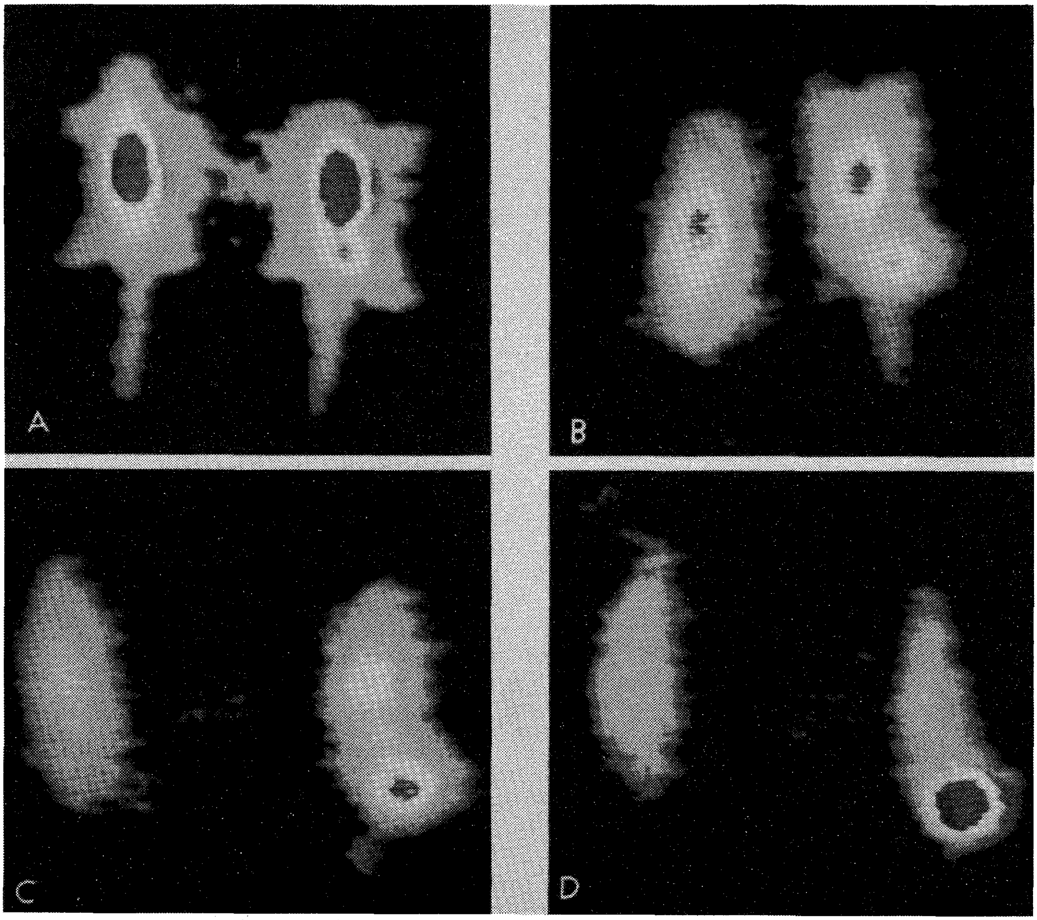

Figure 3. External color imaging with ^{125}I-syngeneic monoclonal antimelanoma (M2590) antibody in C57BL/6 mice with (*right*) or without (*left*) B16 melanoma. The melanoma used in the experiments was approximately 20 × 20 mm. The images were obtained at (*A*) 1 h, (*B*) 24 h, (*C*) 3 days, and (*D*) 5 days after the injection of [^{125}I]M2590. The same mice were used throughout. Three other experiments yielded similar results. The raw data are presented without any background subtraction.

man melanoma with syngeneic monoclonal antitumor antibodies as in vivo diagnostic reagents.

In fact, the present studies demonstrated that the antibody was specifically accumulated in the tumor (Table I; Figs 1,2). The tumor location was easily detected by the external imaging with the syngeneic ^{125}I-labeled monoclonal antibody (Fig 3). The computerized blood pool or normal tissue subtraction technique was not necessary to reveal the location of tumor. Nonspecific accumulation of radiolabeled antibody was not observed by autoradiography and external imaging technique (Figs 2,3).

The distribution patterns of the radiolabeled antibody in the tumor lesions seem to depend on the size of the tumor. The entire tumor regions were strongly and rather homogeneously labeled when they were small lymph node metastatic lesions (about 1 × 2 mm) (Fig 2). This was also reported by Epenetos et al [19] in human cases that were given i.v. injection with radiolabeled tumor-associated monoclonal antibodies, demonstrating that lymph node metastasis showed higher antibody uptake than their corresponding primary tumors. The radiolabeled antibody, however, was irregularly localized in the center of the tumor of medium size (about 20–30 mm) (Fig 1) and in the peripheral regions of the large-sized tumor (about 30 × 50 mm) (Fig 2). Two small nodules adjacent to the large tumor do not label (Fig 2*B*). It is possible these are parts of large tumors. In any event, the localization patterns of radioactive antibodies are quite irregular in tumors.

It is likely that the irregular distribution of radioactive antibody is a reflection of an expression of M2590 determinants on melanoma cells in various differentiation stages. In fact, our recent experiment using two radioactive monoclonal antibodies, [^{125}I]M562 and [^{131}I]M2590, either of which recognizes different melanoma antigen, clearly demonstrated that the distribution patterns of

[^{125}I]M562 and [^{131}I]M2590 are quite distinct in the large tumor; peripheral localization was obtained by M2590, whereas central localization was observed by the M562 antibody. These results cannot be accounted for simply by the vascular architecture in the tumor tissues. Similar findings on the distribution of radioactivity has also been observed by others, such as Moshakis et al [20] on malignant teratoma xenografts and Pimm et al [21] on osteosarcoma xenografts.

Radioimmunoimaging using the monoclonal antibodies reactive against human melanoma has been carried out by Murray et al [22]. They used the antibody recognizing an M_r 97,000 antigen found on over 80% of melanoma cell lines and tissue extracts. Of a total of 100 previously documented metastatic sites, only 50 were visible with imaging. Moreover, uptake of radioactive monoclonal antibodies was variable among metastatic lesions in different organs. However, some metastases were revealed in patients receiving high doses of radioactive antibody. This suggests that the expression of antigen on the surface varies in metastatic lesions in various organs. The background tissues may affect the differentiation of tumor cells so that the expression of tumor antigens is variable. Therefore, these restricted localizations of monoclonal antitumor antibody will be of considerable importance in the application of monoclonal antibodies for specific diagnosis and therapy.

In our previous studies [7], melanoma antigens failed to be detected in the sera of patients with melanoma, whereas the antibody detected the antigens in melanoma tissues from the same patient. The antigenic determinants detected by the M2590 antibody were demonstrated to be composed of GM$_3$ ganglioside [16] and the terminal sialic acid was crucial for the expression of the antigenicity [8]. It is therefore likely that the circulating melanoma antigens lose their interspecies reactive determinants due to the action of sialidases in the tissue [23], suggesting that the M2590 antibody injected into the tumor-bearing host should directly reach the tumor nest without loss of its antibody activity. Thus, the antibody injected seems to become effectively localized in the tumor.

The mouse monoclonal antibody used in this study recognizes the melanoma antigenic determinants widely shared in various mammalian melanomas and reacts with human as well as mouse melanomas [6,8]. It is thus easy to speculate that human monoclonal antibodies recognizing the interspecies reactive melanoma determinants, when they are established, will prove to effectively reveal human melanomas.

REFERENCES

1. Gilliland DG, Steplewski Z, Coller RJ, Mitchell KF, Chang TH, Koprowski H: Antibody directed cytotoxic agents: use of monoclonal antibody to direct the action to toxin A chains to colorectal carcinoma cells. Proc Natl Acad Sci USA 77:4539–4543, 1980
2. Hashimoto Y, Sugawara M, Masuko T, Hojo H: Anti-tumor effect of actinomycin D entrapped in liposomes bearing subunits of tumor-specific monoclonal immunoglobulin M antibody. Cancer Res 43:5328–5334, 1983
3. Krolick KA, Uhr JW, Slavin S, Vitetta ES: In vivo therapy of a murine B cell tumor (BCL1) using antibody-ricin A chain immunotoxins. J Exp Med 155:1797–1809, 1982
4. Mew D, Wat CK, Towers GHN, Levy JG: Photoimmunotherapy: treatment of animal tumors with tumor specific monoclonal antibody-hematoporphyrin conjugates. J Immunol 130:1473–1477, 1983
5. Thorpe PE, Brown ANF, Ross WCJ, Cumber AJ, Detre SI, Edwards DC, Davies AJS, Stirpre F: Cytotoxicity acquired by conjugation of an anti-Thy-1.1 monoclonal antibody and the ribosome-inactivating protein, Gelonin. Eur J Biochem 116:447–454, 1981
6. Wakabayashi S, Saito T, Shinohara N, Okamoto S, Tomioka H, Taniguchi M: Syngeneic monoclonal antibodies against melanoma antigens with species specificity and interspecies cross-reactivity. J Invest Dermatol 83:128–133, 1983
7. Wakabayashi S, Okamoto S, Taniguchi M: Sandwich radioimmunoassay using single monoclonal antibody that detects minute amounts of melanoma antigens from various mammalian species. Gann 75:427–432, 1984
8. Taniguchi M, Wakabayashi S: Shared antigenic determinant expressed on various mammalian melanoma cells. Gamm 75:418–426, 1984
9. Colcher D, Zalutsky M, Kaplan W, Kufe D, Austin F, Schlom J: Radiolocalization of human mammary tumors in athymic mice by a monoclonal antibody. Cancer Res 43:736–742, 1983
10. Mach JP, Chatal JF, Lumbrosa JD, Buchegger F, Forni M, Ritschard J, Berche C, Douillard JY, Carrel S, Herlyn M, Steplewski Z, Koprowski H: Tumor localization in patients by radiolabeled monoclonal antibodies against colon carcinoma. Cancer Res 43: 5593–5600, 1983
11. Haskel CM, Buchegger F, Schreyer M, Carrel S, Mach JP: Monoclonal antibodies to carcinoembrionic antigen: Ionic strength as a factor in the selection of antibodies for immunoscintigraphy. Cancer Res 43:3857–3864, 1983
12. Larson SM: Radiolabeled monoclonal anti-tumor antibodies in diagnosis and therapy. J Nucl Med 26:538–545, 1985
13. Buchegger F, Mach JP, Leonnard P, Carrel S: Selective tumor localization of radiolabeled anti-human melanoma monoclonal antibody fragment demonstrated in the nude mouse model. Cancer 58:655–662, 1986
14. Delanoye B, Bischof-Delaloye A, Buchegger F, von Flidner V, Grob JP, Volant JC, Pettavel J, Mach JP: Detection of colorectal carcinoma by emission-computerized tomography after injection of ^{123}I-labeled Fab or F(ab')$_2$ fragments from monoclonal anti-carcinoembryonic antigen antibodies. J Clin Invest 77:301–311, 1986
15. Hu F, Lesney PF: The isolation and cytology of two pigment cell strains from B16 mouse melanomas. Cancer Res 24:1634–1643, 1964
16. Hiyabayashi Y, Hamaoka A, Matsumoto M, Matsubara T, Tagawa M, Wakabayashi S, Taniguchi M: Syngeneic monoclonal antibody against melanoma antigen with interspecies cross-reactivity recognizes GM$_3$, a prominent ganglioside of B16 melanoma. J Biol Chem 260:13328–13333, 1985
17. Salacinski PRP, Mclean C, Sykes JEC, Clement-Jones VV, Lowry PJ: Iodination of proteins, glycoproteins, and peptides using a solid-phase oxidizing agent, 1,3,4,6-tetrachloro-3,6-diphenyl glycoluril (Iodogen). Anal Biochem 117:136–146, 1981
18. Bergman K, Tjalve H: Three-step autoradiography of organic solvents and plastic monomers to register total radioactivity, nonvolatile metabolites, and non-extractable metabolites. Acta Pharmacol Toxicol (Copenh) 41:22–23, 1977
19. Epenetos AA, Snook D, Durbin H, Johson PM, Taylor-Paradimitriou J: Limitations of radiolabeled monoclonal antibodies for localization of human neoplasms. Cancer Res 46:3183–3191, 1986
20. Moshakis V, Mcilhinney RAJ, Neville AM: Cellular distribution of monoclonal antibody in human tumors after iv administration. Br J Cancer 44:663–669, 1981
21. Pimm MV, Embleton MJ, Perkins AC, Price MR, Robins RA, Robinson GR, Baldman RW: In vivo localization of anti-osteogenic sarcoma 791T monoclonal antibody in osteogenic sarcoma xenografts. Int J Cancer 30:75–85, 1982
22. Murray JL, Rosenblum MG, Sobol RE, Bartholomew RW, Plager CE, Haynie TP, Jahns MF, Glenn HJ, Lamki L, Benjamin RS, Papadopoulos N, Boddie AW, Frincke JM, David GS, Carlo DJ, Hersh EM: Radioimmunoimaging in malignant melanoma with ^{111}In-labeled monoclonal antibody 96.5. Cancer Res 45:2376–2381, 1985
23. Baba T, Ishii M, Aoki K: Elevation of liver neuraminidase activity in the tumor-bearing host. A biochemical approach to the mechanism of cancer invasion and metastasis formation. Gamm 55: 331–339, 1964

A Fast Reconstruction Algorithm for Stationary Positron Emission Tomography Based on a Modified EM Algorithm

EIICHI TANAKA

Abstract—**An efficient iterative reconstruction method for positron emission tomography (PET) is presented. The algorithm is basically an enhanced EM (expectation maximization) algorithm with improved frequency response. High-frequency components of the ratio of measured to calculated projections are extracted and are taken into account for the iterative correction of image density in such a way that the correction is performed with a uniform efficiency over the image plane and with a flat frequency response. As a result, the convergence speed is not so sensitive to the image pattern or matrix size as the standard EM algorithm, and nonuniformity of the spatial resolution is significantly improved. Nonnegativity of the reconstructed image is preserved.**

Simulation studies have been made assuming two PET systems: a scanning PET with ideal sampling and a stationary PET with sparse sampling. In the latter, a "bank array" of detectors is employed to improve the sampling in the object plane. The new algorithm provides satisfactory images by two or three iterations starting from a flat image in either case. The behavior of convergence is monitored by evaluating the root mean square of $C(b)$-1 where $C(b)$ is the correction factor for pixel b in the EM algorithm. The value decreases rapidly and monotonically with iteration number. Although the theory is not accurate enough to assure the stability of convergence, the algorithm is promising to achieve significant saving in computation compared to the standard EM algorithm.

I. INTRODUCTION

IN recent nuclear medicine, an imaging process of positron-emitting radionuclide, positron emission tomography (PET), has become into prominence. This technique is based on the coincidence detection of annihilation photons resulting from positron emission *in vivo*. Most PET devices currently used consist of multiple ring arrays of discrete detectors around a subject. Coincidence counts between detectors are accumulated and arranged into projections for a number of view angles from which radionuclide distribution is reconstructed [1].

The algorithm widely used for image reconstruction from projections is an analytical technique of filtered backprojection. The method is computationally efficient, but it needs a complete set of projection data with sufficiently fine linear and angular sampling [2], [3]. To meet the sampling requirement, the rings of detectors usually undergo some type of scanning motion (e.g., wobbling, rotation, and translation) [4]–[7].

However, the above sampling requirement arises from the filtered backprojection algorithm. If we use a sophisticated algorithm such as an iterative reconstruction method, the sampling requirement is relaxed, and we can obtain a reasonable spatial resolution without mechanical scanning [8].

In the conventional multislice PET, the reconstruction of a three-dimensional object is performed slice by slice using the two-dimensional reconstruction technique. To increase the detection sensitivity, cross-layer coincidence between adjacent detector rings is used to generate a "cross-layer image" midway between the two detector planes in a similar manner. With this method, however, detection sensitivity decreases with increasing axial resolution because the sensitivity is proportional to the square of the slice thickness [9]. To obtain higher sensitivity by using larger slant angle coincidence, the three-dimensional reconstruction technique must be employed, in which analytical methods are not generally applicable [10].

A number of iterative reconstruction algorithms have been reported which are applicable to image reconstruction from incomplete projections [11]. Among them, the EM (expectation maximization) algorithm proposed by Shepp and Vardi [12] and others [13], [14] is relevant to emission computed tomography because the algorithm has several advantages by incorporating the Poisson nature of data. The algorithm keeps nonnegativity of the reconstructed images, and preserves the total image density at every iteration. The convergence is assured by the theory, and the reconstructed image approaches the maximum likelihood estimate with increasing iteration number.

The EM algorithm, however, has some drawbacks, although these are more or less common properties of the other iterative techniques. First, the convergence speed is slow and it takes a long computation time. Second, the correction efficiency of each iteration is not uniform over an image, and the frequency response of the correction is inversely proportional to the spatial frequency as shown later. In addition, the statistical noise tends to increase with the iteration number, and we have to stop the iteration at a certain level of the noise magnitude or at another

Manuscript received October 3, 1986; revised January 5, 1987. This work was supported in part by grants from the Ministry of Health and Welfare and the Ministry of Education of Japan.

The author is with the Division of Physics, National Institute of Radiological Sciences, 9-1, Anagawa-4-chome, Chiba-shi, 260 Japan.

IEEE Log Number 8613509.

0278-0062/87/0600-0098$01.00 © 1987 IEEE

appropriate criteria. As a result, spatial resolution of the reconstructed image is not uniquely defined, but it strongly depends on the image pattern, on the number of iterations, and on the point of interest in the image.

Several techniques to enhance the converging speed of the EM algorithm have been reported [15]-[17]. A simple method is to amplify the correction factor by replacing it by a power of the value before multiplying an old image, but the degree of the amplification is limited by the occurrence of oscillation at a low frequency. A more sophisticated method was reported by Lewitt and Muehllehner [18]. In this method, the amount of correction is amplified by a factor in additive correction form, the factor being determined at each iteration in a range where nonnegativity of images is preserved.

The aim of this paper is to present an efficient iterative algorithm which overcomes the above-mentioned drawbacks and is useful for a stationary PET system. The algorithm is based on the EM algorithm with some modifications for improving the frequency response and spatial nonuniformity of the iterative correction.

II. THEORETICAL CONSIDERATIONS

A. *Frequency Response of the EM Algorithm*

The basic iteration process of the EM algorithm to estimate the new emission density $s'(b)$ of a pixel b from the old value $s(b)$ is expressed by [11]

$$s'(b) = s(b) \sum_d \left[n(d)/m(d)\right] p(b, d) \qquad (1)$$

where

$$m(d) = \sum_{b'} s(b')\, p(b', d) \qquad (2)$$

where d is a coincidence detector tube and $n(d)$ is the number of events detected in the tube d. $p(b, d)$ is the probability that emission in pixel b is detected in detector tube d, and $m(d)$ represents the number of events of tube d estimated from the old image. The term of summation in (1) is the backprojection of $n(d)/m(d)$ into the image plane with a weight $p(b, d)$. Suppose the detector tubes are grouped with view angle θ. Equation (1) is expressed by

$$\begin{aligned} s'(b) &= s(b) \sum_\theta \sum_i \left[n_\theta(i)/m_\theta(i)\right] p_\theta(b, i) \\ &= s(b) \left\langle n(i)/m(i) \right\rangle \qquad (3) \end{aligned}$$

where $\langle\ \rangle$ denotes the backprojection operation hereafter and i is the bin number of the projections. The term $\langle\ \rangle$ in (3) is a correction matrix to be multiplied to an old image.

Equation (3) is rewritten as

$$s'(b) = s(b) \left[1 + \left\langle e(i)/m(i) \right\rangle\right] \qquad (4)$$

where

$$e(i) = n(i) - m(i) \qquad (5)$$

where $e(i)$ is the difference between measured and calculated projections. The amount of correction on pixel b is given by

$$\Delta s(b) = s(b) \left\langle e(i)/m(i) \right\rangle. \qquad (6)$$

For a rough evaluation of the correction efficiency, we assume the $m(i)$ is roughly independent of view angle. Then we have

$$\Delta s(b) = s(b)\, B_m(b) \left\langle e(i) \right\rangle \qquad (7)$$

where

$$B_m(b) = \left\langle 1/m(i) \right\rangle. \qquad (8)$$

The frequency response of the correction is given by

$$R_L(f) = s(b)\, B_m(b)/(\pi f) \qquad (9)$$

where f is the spatial frequency, in the unit pixel^{-1}, along a radial coordinate in a two-dimensional Fourier space. The term $1/(\pi f)$ represents the frequency response of simple backprojection. Equation (9) indicates that the correction efficiency is inversely proportional to the spatial frequency and that the efficiency also depends on each pixel by $s(b)\, B_m(b)$. If we consider a uniform disk phantom having a diameter of D pixels, the mean value of $s(b)$ $B_m(b)$ is nearly equal to $4/(\pi D)$, and (9) becomes

$$R_L(f) = 4/(\pi^2 D f) = 0.405/(Df). \qquad (10)$$

B. *Enhancement of Correction for High-Frequency Components*

To enhance the correction for high-frequency components, we shall consider the following iteration scheme:

$$s'(b) = s(b) \left\langle \frac{n(i)\, \overline{m}(i)}{m(i)\, \overline{n}(i)} \right\rangle \qquad (11)$$

where $\overline{n}(i)$, $\overline{m}(i)$ are the smoothed projection of $n(i)$, $m(i)$, respectively, convolved with a low-pass filter $h(i)$: $\overline{n}(i) = n(i) * h(i)$ and $\overline{m}(i) = m(i) * h(i)$ where the asterisks denote convolution. The term in $\langle\ \rangle$ represents the high-frequency component of $n(i)/m(i)$. Note that the value of the term is nonnegative as long as $h(i) \geq 0$, and the value is nearly equal to unity when $n(i)/m(i)$ has few high-frequency components. The cutoff characteristics are determined by the filter $h(i)$.

Assuming $h(i)$ is normalized by $\Sigma\, h(i) = 1$, we denote the high-frequency component of $n(i)$ by

$$\hat{n}(i) = n(i) - \overline{n}(i) = n(i) * \left[\delta(i) - h(i)\right] \qquad (12)$$

where $\delta(i)$ is a delta function. Then, (11) becomes (see the Appendix)

$$s'(b) = s(b) \left\langle \frac{1 + \hat{m}(i)/\overline{n}(i)}{1 + \hat{m}(i)/\overline{m}(i)} + \frac{\overline{m}(i)}{\overline{n}(i)\, m(i)}\, \hat{e}(i) \right\rangle. \qquad (13)$$

In an early stage of successive iterations where the old image has few high-frequency components, we can put $\hat{m}(i) \ll \overline{m}(i)$ and $\hat{m}(i) \ll \overline{n}(i)$. With increasing iteration number, the high-frequency component $\hat{m}(i)$

appears, but at the same time, $\overline{m}(i)$ approaches $\overline{n}(i)$. Accordingly, (13) is approximated, throughout the iteration process, by

$$s'(b) = s(b)\left[1 + \left\langle \frac{\overline{m}(i)}{\overline{n}(i)\, m(i)}\, \hat{e}(i) \right\rangle\right]. \tag{14}$$

Assuming that $\overline{m}(i)/[\overline{n}(i)\, m(i)]$ is roughly independent of view angle for each pixel, the amount of error correction is given by

$$\Delta s(b) = s(b)\, B(b)\, \langle \hat{e}(i) \rangle \tag{15}$$

where

$$B(b) = \langle \overline{m}(i)/[\overline{n}(i)\, m(i)] \rangle. \tag{16}$$

The term $\langle \hat{e}(i) \rangle$ in (15) represents a filtered backprojection of the error $e(i)$. The frequency response is given by

$$R_H(f) = s(b)\, B(b)\, (\pi f)^{-1}\, [1 - H(f)] \tag{17}$$

where $H(f)$ is the Fourier transform of $h(i)$. The term $s(b)\, B(b)$ represents the pixel dependency of the correction efficiency. This suggests that a uniform correction over an image plane will be obtained by amplifying the correction scheme of (11) by a factor inversely proportional to $s(b)\, B(b)$.

C. Filtered Iterative Reconstruction (FIR) Algorithm

From the analysis described above, an iterative algorithm is derived which is called the filtered iterative reconstruction (FIR) algorithm. It is basically an EM algorithm with high-frequency enhancement. The iteration process is expressed by

$$s'(b) = \begin{cases} s(b)\, C(b)^{\alpha}\, U(b)^{\beta/[s(b)B(b)]} & \text{if } U(b) \le 1 \\ s(b)\, C(b)^{\alpha} + \beta B(b)^{-1}\, [U(b) - 1] & \text{if } U(b) > 1 \end{cases} \tag{18}$$

where

$$C(b) = \langle n(i)/m(i) \rangle$$

and

$$U(b) = \langle n(i)\, \overline{m}(i)/[m(i)\, \overline{n}(i)] \rangle$$

where α and β are constants. $C(b)$ is the correction matrix appearing in the standard EM algorithm [see (3)] and $U(b)$ is the correction matrix for high frequencies [see (11)]. Note that, when $\alpha = 1$ and $\beta = 0$, (18) becomes the standard EM algorithm given by (3). For the high-frequency component, a multiplicative correction mode is used when $U(b) < 1$ so as to satisfy nonnegativity of the image, while an additive correction mode is used when $U(b) > 1$ to avoid overcorrection. The frequency response of the error correction is given by, referring to (10) and (17),

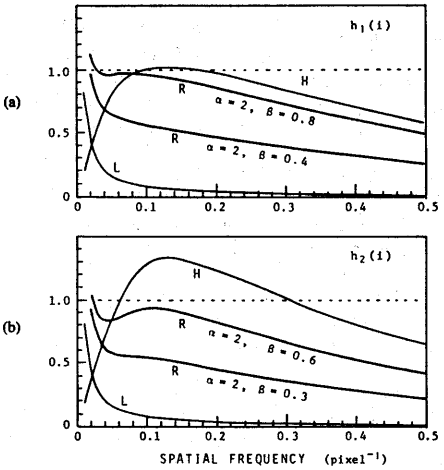

Fig. 1. Frequency response of iterative correction [see (19)]. $D = 50$ pixels. Curve H: response of high-frequency enhancement given by $[s(b)\, B(b)]^{-1}\, R_H(f)$. Curve L: response of the EM algorithm given $R_L(f)$. Curve R: response of the FIR algorithm given by (19). (a) $h_1(i) = a_1/(i^3 + 2i^2 + 3)$, $i = -10 \sim 10$. (b) $h_2(i) = a_2/(i^3 + 4)$, $i = -6 \sim 6$.

$$\begin{aligned} R(f) &= \alpha R_L(f) + \beta [s(b)\, B(b)]^{-1}\, R_H(f) \\ &= \frac{4\alpha}{\pi^2 D f} + \frac{\beta}{\pi f}[1 - H(f)]. \end{aligned} \tag{19}$$

The constants α, β, and the filter $h(i)$ are determined in such a way that $R(f) \le 1$ for the spatial frequencies involved in objects.

First, we shall determine α considering the stability of convergence at low frequencies. Since an object is limited in a certain area of a diameter D, the projections are also in a region of length D. The radial response of the Fourier transform of the object is then expressed by a Fourier series having a fundamental frequency $1/(2D)$. At the fundamental frequency, the value of the first term of (19) is 0.81α. This suggests that the use of $\alpha > 0.81^{-1}$ may cause hunting or oscillation at the frequency. However, if we normalize the total image density at each iteration, the oscillation is prevented because the image is assured to be nonnegative, and accordingly, the total image density reflects the amount of the fundamental frequency component. Since the next lowest frequency of the object is $1/D$, we can use $\alpha = 2$ without spoiling the stability of convergence by normalizing the total density. The following study is then made with $\alpha = 2$.

The filter function $h(i)$ and the value of β are determined empirically to obtain a good response at higher frequencies. Fig. 1 shows examples of the response analysis for two filters defined by

$$h_1(i) = a_1/(i^3 + 2i^2 + 3) \qquad i = -10 \sim 10 \tag{20}$$

$$h_2(i) = a_2/(i^3 + 4) \qquad i\ -6 \sim 6 \tag{20$'$}$$

where a_1 and a_2 are constants for normalization. The diameter of the object is assumed to be 50 pixels. The curves denoted by "R" are the response of the FIR algorithm in a frequency range $(1/D) < f < 0.5$. It is seen that the appropriate value of β is 0.8 for $h_1(i)$ and 0.6 for $h_2(i)$.

III. Implementation of the Filtered Iterative Reconstruction Algorithm to Stationary PET's

In the previous section, we have implicitly assumed that a projection for each view angle is fully sampled. In some applications, however, the full sampling may not be achieved. If the sampling is sparse, the filter $h(i)$ should be broad enough to cover several sampled data in such a way that the high-frequency component is extracted adequately by (11).

An example is the application to a stationary PET using a circular array of discrete detectors. For the stationary PET, a "bank array" of the detectors has been proposed, in which all the detectors are grouped into odd number banks, each bank has a closely packed detector array, and the gap between the banks is equal to half the detector width. With this configuration, the object plane is more adequately sampled by coincidence lines than a uniform circular array [8]. A system consisting of 15 banks of 16 detectors each is considered, and simulation studies have been made. A part of the "$t - \theta$ map" of this system is shown in Fig. 2, in which t represents sampling points (square dots) in the projection at view angle θ. The bin width is a quarter of the detector spacing, and the angular step is $\pi/120$. The pattern shown in Fig. 2 appears repeatedly in the full $t - \theta$ map. The maximum angular error of the projections from the actual coincidence lines is 0.75°, which is negligibly small for the present purpose. Note that about half of the projection bins are empty.

Another problem arising in the case of sparse sampling is the nonuniformity of the sampling density over the image plane. In this case, all the matrices $C(b)$, $U(b)$, and $B(b)$ appearing in (18) must be normalized by the sampling pattern defined by

$$P(b) = \langle 1 \rangle = \sum_d p(b, d) \tag{21}$$

which can be stored in a computer as a lookup table. Furthermore, the correction matrix $U(b)$ for the high-frequency component is smoothed by a nine-point weighted filter (1:2:1 for the X and Y directions) after being normalized by $P(b)$. This smoothing prevents excess enhancement of the high-frequency component of statistical noise.

Furthermore, the original FIR algorithm defined by (18) may be unstable when $s(b) = 0$ because the equations involve divisions by $s(b)$. To overcome this instability, we use the following equations in the practical implementations of the algorithm:

$$s'(b) = \begin{cases} s(b)\, C(b)^{\alpha}\, U(b)^{\beta/[\{s(b)+\rho\}B(b)]} & \text{if } U(b) \leq 1 \\ s(b)\, C(b)^{\alpha} + \dfrac{\beta}{B(b)}\, \dfrac{s(b)}{s(b)+\rho}\, [U(b) - 1] & \text{if } U(b) > 1 \end{cases} \tag{22}$$

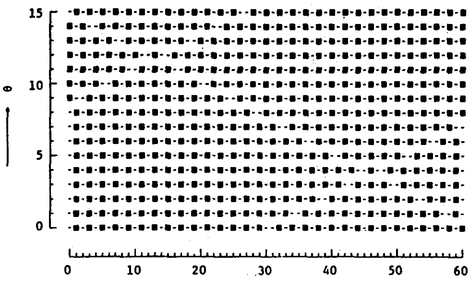

Fig. 2. A part of $t - \theta$ map of the stationary PET having 15 banks of 16 detectors. The projection bin width is a quarter of the detector spacing. The angular step is $\pi/120$.

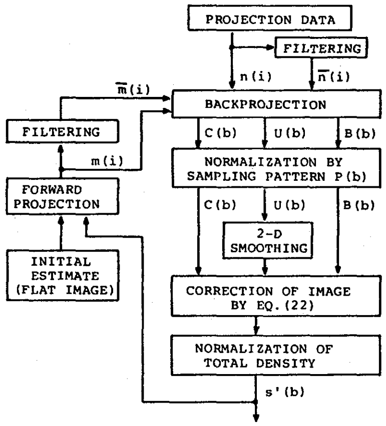

Fig. 3. Flow diagram of implementation of the FIR algorithm.

where

$$C(b) = \langle n(i)/m(i) \rangle$$

and

$$U(b) = \langle n(i)\, \bar{m}(i)/[m(i)\, \bar{n}(i)] \rangle$$

where ρ is a small positive constant. In the calculation of $C(b)$ and $U(b)$, zero divided by zero is defined as zero. The flow diagram of the FIR algorithm is shown in Fig. 3.

IV. Simulation Studies and Their Results

Simulation studies have been performed considering two PET systems: one is a scanning PET having a uniform array of 240 detectors, and the other is the stationary

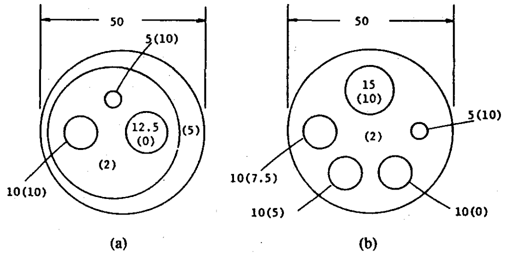

Fig. 4. Mathematical phantoms used in the simulation studies. The values without parentheses are diameters in terms of pixel number and the values in parentheses are relative emission densities.

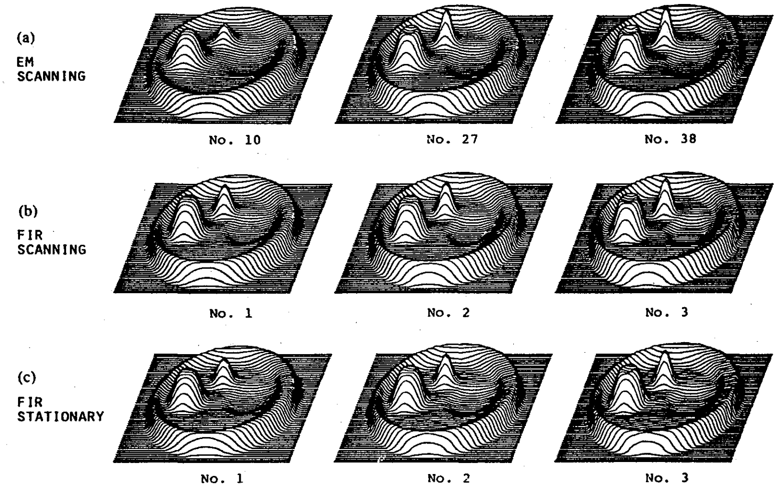

Fig. 5. Images of the phantom shown in Fig. 4(a). The iteration is started from a flat image. The number of iterations is shown under each image. (a) EM algorithm for the scanning PET. (b) FIR algorithm for the scanning PET. (c) FIR algorithm for the stationary PET.

PET having a bank array (16 detectors × 15 banks) described in the previous section. The crystal width is 5 mm, and the center-to-center spacing of the crystals is 6 mm. The imaging matrix is 62 × 62. The pixel size and the bin width of projections are 1.5 mm, a quarter of the crystal spacing. The detection efficiency $p(b, d)$ is calculated as the overlapping area between the pixel and the rectangular strip having a width equal to the projection bin width. The mathematical phantoms used are shown in Fig. 4.

The projection data are generated by two ways. In the first method, a mathematical phantom is digitized in a 62 × 62 matrix, and the phantom is projected with probability $p(b, d)$. The latter step is similar to the forward projection in the reconstruction algorithm, and hence the error associated with the projection step will be cancelled in the reconstruction. This method is suitable for a test of the algorithm. The second method is more realistic. The projections are calculated directly from a precise mathematical phantom by taking into account the detector response. The detector response is assumed to be a Gaussian function having a full width at tenth maximum of 5 mm (detector width) which corresponds to a full width at half maximum of 2.74 mm. Attenuation and scattering of photons are ignored.

Iteration is initiated from a flat image having a little larger diameter than the phantom. The total density is normalized to that of the phantom. The filter used is $h_1(i)$ or $h_2(i)$ defined by (20) or (20′), respectively. The parameters $\alpha = 2$ and $\beta = 0.8$ for $h_1(i)$ or $\beta = 0.6$ for $h_2(i)$ are used in the first iteration, but the β value is halved in the following iterations because the successive use of the initial value often produces overenhancement of the peripheral edge for some phantoms.

Fig. 5 shows the comparison of images obtained with the FIR algorithm and the standard EM algorithm. The

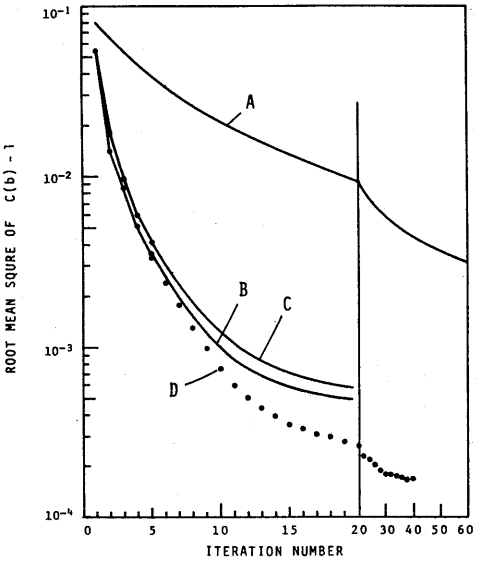

Fig. 6. Plot of root mean square of $C(b) - 1$ as a function of iteration number. *A*: EM algorithm for the scanning PET. *B*: FIR algorithm for the scanning PET. *C*: FIR algorithm for the stationary PET. *D*: FIR algorithm for the stationary PET without smoothing of $U(b)$ matrix.

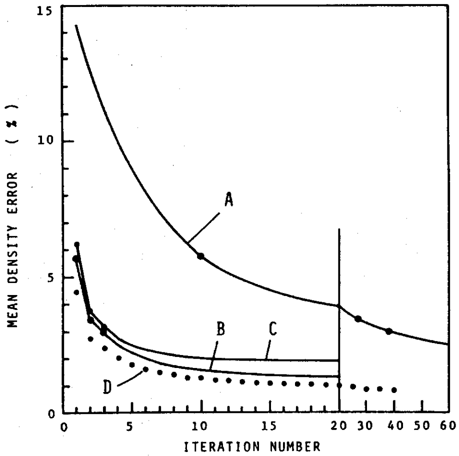

Fig. 7. Plot of mean density error given by (23) as a function of iteration number. *A*: EM algorithm for the scanning PET. *B*: FIR algorithm for the scanning PET. *C*: FIR algorithm for the stationary PET. *D*: FIR algorithm for the stationary PET without smoothing of $U(b)$ matrix.

phantom is the one shown in Fig. 4(a). In this study, the projection data were generated by the first method described above. The filter used is $h_1(i)$. Statistical noise was not incorporated. The FIR images are those after one, two, and three iterations, while the EM images are those having similar "mean density error" as the FIR images. The mean density error will be defined later. Note that the spatial resolution is much more uniform in the FIR images than the equivalent EM images. With the FIR algorithm, the source distribution is roughly reconstructed by the first iteration, and another one or two iterations yield fairly good images.

To check the behavior of convergence, the root mean-square value of $C(b) - 1$ is plotted in Fig. 6 as a function of iteration number for the above data. The value should approach zero in the ideal EM algorithm. The value for the FIR algorithm seems to approach a finite value of about 0.0005. This is due to the smoothing process on $U(b)$. In fact, without the smoothing, the value decreases further as shown by a dotted curve in the figure, but the reconstructed image is sharpened too much and statistical noise, if it exists, is amplified intolerably.

Fig. 7 shows the plot of another parameter showing the mean density error defined by

$$\text{ERROR} = \frac{1}{s_{\max}} \frac{1}{N} \sum_{b} \left| s(b) - s_0(b) \right| \tag{23}$$

where $s_0(b)$ is the image density of the phantom, $s_{\max}$ is the maximum value, and N is the number of pixels involved. The comparison of the EM and FIR images in Fig. 5 is made at the same ERROR values. Note that the convergence of the FIR algorithm is satisfactory despite the fact that heavy enhancement is incorporated.

Fig. 8 shows the FIR images of another phantom [Fig. 4(b)]. In this study, the projection data were generated by the second method described before. The filter used is $h_2(i)$. The images with statistical noise were obtained assuming that the total number of events is 200 000.

V. CONCLUSION AND DISCUSSIONS

A filtered iterative reconstruction (FIR) algorithm has been developed. By incorporating high-frequency enhancement adequately, the frequency response of iterative correction is significantly improved, and acceptable images are obtained by two or three iterations. The correction efficiency is automatically adjusted at each pixel, and accordingly, the convergence speed is not as sensitive to the image pattern or the matrix size as the standard EM algorithm. For the same reason, the nonuniformity of the spatial resolution over an image is significantly improved. The algorithm preserves the nonnegativity of the image, but it needs normalization of total image density after each iteration. The theory of the algorithm is not sufficiently quantitative and no accurate analysis has been made on the stability of convergence or on the performance as a maximum likelihood estimator. Nevertheless, the FIR algorithm shows a good convergence by a suitable choice of the parameters involved.

It has been shown that the FIR algorithm is useful for the stationary PET in which the filtered backprojection method is not useful due to poor linear sampling. The intrinsic detector resolution is reasonably restored in the re-

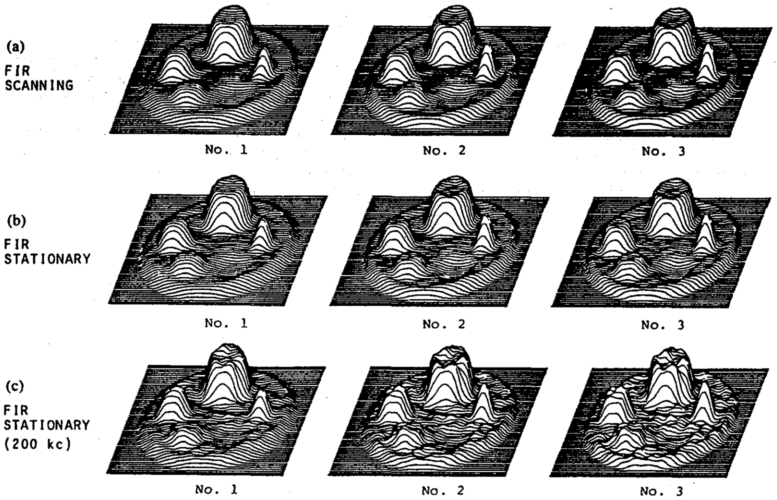

Fig. 8. Images of the phantom shown in Fig. 4(b), obtained with the FIR algorithm. The iteration is started from a flat image. The number of iterations is shown under each image. (a) FIR algorithm for the scanning PET. (b) FIR algorithm for the stationary PET. (c) FIR algorithm for the stationary PET with statistical noise (total counts = 200 000).

constructed images. From these results, we may conclude that the FIR algorithm is promising to achieve significant savings in computation compared to the standard EM algorithm. Further studies will be desirable on the details of performance, on the possible improvements, and on the limitation in applications.

APPENDIX
DERIVATION OF (13)

For the sake of simplicity, we use n, m, and e instead of $n(i)$, $m(i)$, and $e(i)$, respectively. The term in $\langle\ \rangle$ of (11) is then written as

$$\begin{aligned} \frac{n\overline{m}}{m\overline{n}} &= \frac{\overline{m}}{\overline{n}}\left[1 + \frac{\overline{e}}{m} + \frac{\hat{e}}{m}\right] \qquad [\because n = m + \overline{e} + \hat{e}] \\ &= \frac{\overline{m}}{\overline{n}}\left[\frac{m + \overline{n} - \overline{m}}{m}\right] + \frac{\overline{m}\hat{e}}{\overline{n}m} \qquad [\because \overline{e} = \overline{n} - \overline{m}] \\ &= \frac{\overline{m}(\overline{n} + \hat{m})}{\overline{n}(\overline{m} + \hat{m})} + \frac{\overline{m}\hat{e}}{\overline{n}m} \qquad [\because m = \overline{m} + \hat{m}] \\ &= \frac{1 + \hat{m}/\overline{n}}{1 + \hat{m}/\overline{m}} + \frac{\overline{m}}{\overline{n}m}\hat{e}. \qquad \text{(A1)} \end{aligned}$$

Using (A1) in (11), we have (13).

ACKNOWLEDGMENT

The author wishes to thank N. Nohara, T. Tomitani, M. Yamamoto, and H. Murayama of NIRS for their useful discussions.

REFERENCES

[1] G. Muehllehner and J. S. Karp, "Positron emission tomography imaging—Technical considerations," *Sem. Nucl. Med.*, vol. XVI, no. 1, pp. 35-50, 1986.
[2] R. A. Brooks, V. J. Sank, A. J. Talbert, and G. DiChiro, "Sampling requirements and detector motion for positron emission tomography," *IEEE Trans. Nucl. Sci.*, vol. NS-26, pp. 2760-2763, 1979.
[3] K. Kouris, E. S. Garnett, and G. T. Herman, "Sampling properties of stationary and half-rotation rings in positron emission tomography," *J. Comput. Assist. Tomog.*, vol. 5, pp. 744-754, 1981.
[4] C. Bohm, L. Eriksson, M. Bergstrom, T. Litton, R. Sundman, and M. Singh, "A computer assisted ring detector positron camera system for reconstruction tomography of the brain," *IEEE Trans. Nucl. Sci.*, vol. NS-25, pp. 624-637, 1978.
[5] E. Tanaka, N. Nohara, M. Yamamoto, T. Tomitani, and H. Murayama, "Positology—The search for suitable detector arrangements for a positron ECT with continuous rotation," *IEEE Trans. Nucl. Sci.*, vol. NS-26, pp. 2728-2731, 1979.
[6] N. Nohara, E. Tanaka, T. Tomitani, M. Yamamoto *et al.*, "POSITOLOGICA: A positron ECT device with a continuously rotating detector ring," *IEEE Trans. Nucl. Sci.*, vol. NS-27, pp. 1128-1136, 1980.
[7] Z. H. Cho, K. S. Hong, J. B. Ra, and S. Y. Lee, "A new sampling scheme for the ring positron camera: Dichotomic ring sampling," *IEEE Trans. Nucl. Sci.*, vol. NS-28, pp. 94-98, 1981.
[8] E. Tanaka, N. Nohara, T. Tomitani, M. Yamamoto, and H. Murayama, "Stationary positron emission tomography and its image reconstruction," *IEEE Trans. Med. Imaging*, vol. MI-5, pp. 199-206, 1986.
[9] E. Tanaka, N. Nohara, T. Tomitani, and M. Endo, "Analytical study of the performance of a multilayer positron computed tomography scanner," *J. Comput. Assist. Tomog.*, vol. 6, pp. 350-364, 1982.
[10] M. E. Daube-Witherspoon and G. Muehllehner, "An iterative image space reconstruction algorithm suitable for volume ECT," *IEEE Trans. Med. Imaging*, vol. MI-5, pp. 61-66, 1986.
[11] G. T. Herman, Ed., *Image Reconstruction from Projections, Implementation, and Applications*. New York: Springer-Verlag, 1979.
[12] L. A. Shepp and Y. Vardi, "Maximum likelihood reconstruction for emission tomography," *IEEE Trans. Med. Imaging*, vol. MI-1, pp. 113-122, 1982.

[13] K. Lange and R. Carson, "EM reconstruction algorithms for emission and transmission tomography," *J. Comput. Assist. Tomog.*, vol. 8, pp. 306-316, 1984.
[14] Y. Vardi, L. A. Shepp, and L. Kaufman, "A statistical model for positron emission tomography," *J. Amer. Statist. Ass.*, vol. 80, pp. 8-37, 1985.
[15] F. Vermeulen, "An improved stochastic reconstruction technique for tomographic imaging," in *Proc. 2nd Int. Symp. Fundamentals Tech. Progr. Med.*, Liege, Belgium, Apr. 1983.
[16] E. Tanaka, N. Nohara, T. Tomitani, and M. Yamamoto, "Utilization of nonnegativity constraints in reconstruction of emission tomograms," in *Proc. 9th Conf. Inform. Processing Med. Imaging*, S. L. Bacharach, Ed. The Netherlands: Martinus Nijhoff, 1985.
[17] S. Vishampayan, J. Stamos, R. Mayans, K. Koral, N. Clinthorne, and W. L. Rogers, "Maximum likelihood image reconstruction for SPECT," *J. Nucl. Med.*, vol. 26, p. 20, 1985.
[18] R. M. Lewitt and G. Muehllehner, "Accelerated iterative reconstruction for positron emission tomography based on the EM algorithm for maximum likelihood estimation," *IEEE Trans. Med. Imaging*, vol. MI-5, pp. 16-22, 1986.

RADIOISOTOPES, **36**, 221-226 (1987)

全身用ポジトロンCT装置POSITOLOGICA Ⅱの計数率特性と数え落としの補正

遠藤真広，野原功全*，飯沼　武，篠遠　仁，田中栄一*，吉田勝哉**，
氷見寿治**，加賀谷秋彦**，大串　明***，井上愼一***
放射線医学総合研究所臨床研究部，*同研究所物理研究部
260 千葉市穴川4-9-1
**千葉大学医学部第3内科学教室
280 千葉市亥鼻1-8-1
***㈱日立メディコ研究開発センター
277 柏市新十余二2-1

1987年1月30日　受理

いくつかのファントムを用い，多層型全身用ポジトロンCT装置POSITOLOGICA Ⅱの計数率特性を調べ，その補正法を検討した。非常に高い放射能では計測システムは飽和し，全同時計数率の最大値は660 kcpsであった。しかし，それ以下の放射能では，計数損失と単一光子計数率の間に，被写体の形状や構成によらない一定の関係が見出され，この関係を用いて計数損失を補正できることを示した。

Key Words: positron emission tomography, count rate characteristics, count loss correction

1. はじめに

ポジトロンCT（PCT）法は，人体の生理的過程を映像化し，また生理パラメータを定量的に求める方法として期待され，すでに多くの研究に利用されている。しかしながら，PCT装置を定性的なイメージング装置としてだけではなく，人体内放射能分布の定量的な計測装置として利用するためには，注意深くその特性を測定し，理想的な特性からのずれを補正することが前提となる。

理想的な特性からのPCT値のずれは，散乱などいくつかの原因が組み合わさって生じるものであるが，高い計数率における同時計数事象の数え落としもその原因の一つとして数えられる。一般に，PCT装置における真の同時計数の数え落としは，単に真の同時計数率だけではなく，単一光子計数率や偶発同時計数率にも関係し，その補正を行うためには十分な注意が必要である[1]。ここでは，放射線医学総合研究所に設置されている全身用PCT装置POSITOLOGICA Ⅱの計数率特性を調べ，数え落としの実用的な補正法を考案したので，それらについて報告したい。

2. 方　法

2·1 PCT装置

実験に用いた装置は全身用PCT装置POSITOLOGICA Ⅱである[2]。本装置は3段の検出器リングよりなり，各リングは40個の4連結検出器[3]により構成される（1リングあたりのBGO結晶数は40×4＝160個）。Fig. 1に本装置の回路系のブロックダイヤグラムを示

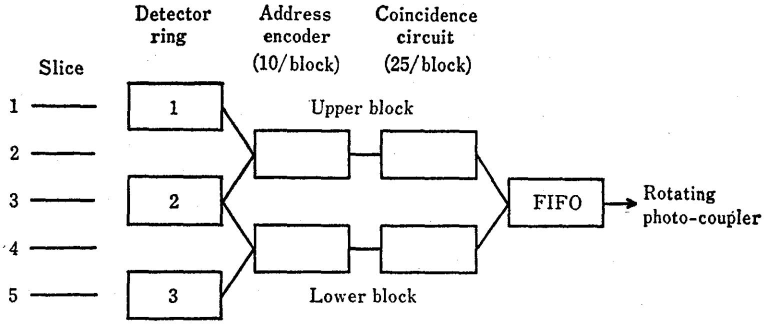

Fig. 1　Schematic diagram of data acquisition system for POSITOLOGICA Ⅱ.

す。

40個の4連結検出器は4個ずつ10組にグループ分けされる。アドレスエンコーダ系は上下2つのブロックよりなり，各ブロックは検出器のグループに対応する10個のアドレスエンコーダにより構成される。アドレスエンコーダには2つの隣り合うリングの検出器の出力信号が入り，時間信号とそれを発生している検出器のアドレス信号が出力される。

アドレスエンコーダからの信号は同じブロックの対向する5個のアドレスエンコーダからの信号と同時計数され，検出器対のアドレス信号がFIFO (first-in first-out)，回転フォトカプラーを経てバッファメモリーに送られる。同時計数回路の数はブロック当たり25個である。隣り合うリング間の同時計数により2つの層間スライスが得られ，同一リング内の同時計数により決められる3つの層内スライスと合わせて，5スライスの計測が行われる。第3スライスのデータは上下2つのブロックで同時に処理されるが，FIFOの入口で上ブロックのデータのみが選択される。このため，1，2，3スライスは上ブロックにより，4，5スライスは下ブロックにより処理される。

本装置では偶発同時計数を補正するため，on time window の計測だけではなく，off time window の計測も行う[4]。On time window で計測されるデータは真の同時計数と偶発同時計数の和であり，off time のデータは偶発同時計数だけであるので，本システムでは（真の同時計数)＋2×(偶発同時計数）を扱うことになる。これらはすべてバッファメモリーまで送られるから，収集の過程でおたがいに競合し数え落としの原因となる。

2・2 ファントムおよび測定法

計数率特性を調べるため，適当なファントムに高放射能の ^{13}N-アンモニア（半減期9.96分）を注入し，減衰のさいの計数率の変化を測定した。実験に用いたファントムは次の3種類である。

(1) 内径20 cm，長さ22 cm，板厚3 mmのプラスチック製円筒ファントムの内側に^{13}N-アンモニア水溶液を満たしたもの。

(2) 内径5 cm で他は(1)と同じもの。

(3) 京都科学標本㈱製の胸部ファントム（Fig. 2にその断面を示す）の左心室部（容量135 ml）に^{13}N-アンモニア水溶液を満たしたもの。

用いた^{13}N-アンモニアの放射能はいずれの場合も1.85 GBq(50 mCi) 以上であった。

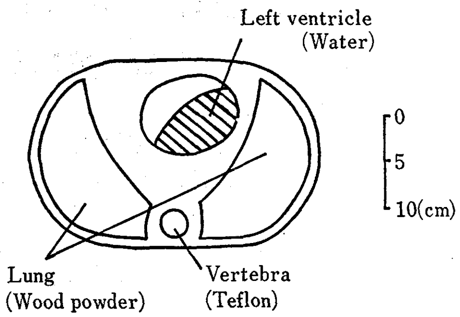

Fig. 2 Cross sectional view of chest phantom. Left ventricle space (hatched region) was filled with ^{13}N ammonia water solution.

これらのファントムを POSITOLOGICA Ⅱ の視野中央に置き，80-90分の間，真の同時計数率，偶発同時計数率および単一光子計数率の計測を適当な時間間隔で繰り返した（各ファントムの計測点数は18-19)。それぞれの同時計数率は，計算機に収集された計数をスライスごとに加算し，収集時間で除すことにより求めた。各測定における真の同時計数の5スライスの和が10^6カウント前後になるよう，計数率が低くなるほど収集時間を増大させた。

単一光子計数は，Fig. 1のアドレスエンコーダの途中から信号を取り出し，それを1/100にスケールダウンした後，Fig. 1の同時計数データの収集回路とは別系統でリングごとに収集する。単一光子計数率は，これを収集時間で除すことにより求めた。

以下，とくに断わらない限り，各スライスごとの真の同時計数率と偶発同時計数率の測定値を n_t, n_r と書き，これらを5スライス加算してシステム全体の値として求めたものをそれぞれ N_t, N_r と書くことにする。単一光子計数率に関してはブロック当たりの計数率を N_s と書く。本報ではとくに断わらない限り，N_s として上ブロックの値（1，2リングの和）を用いる。

数え落としを補正する係数は，千田らの方法[5]に準じて各スライスごとに求めた。すなわち，各スライスごとの真の同時計数率の測定値を n_t とし，半減期から計算される放射能の相対値をQとする。数え落としのため，Qが増大すると n_t/Q は減少する。Qを横軸，n_t/Q を縦軸とする座標上に測定点をプロットし，$Q=0$ の外挿点 $(n_t/Q)_{Q=0}$ を求める。この値は，数え落としがまったくないときの n_t とQの比を表していると考えられるから，数え落としの補正係数(真の値/測定値）f は，

$$f=\frac{(n_t/Q)_{Q=0}}{n_t/Q} \qquad (1)$$

で与えられる。

3. 結　果

3·1 同時計数率の変化

Fig. 3は，ファントム(1)および(2)に対して，真の同時計数率の計測値（5スライスの和）N_t と偶発同時計数率（5スライスの和）がファントム中の放射能の減衰に伴い，どのように変化するかを示したものである。横軸は実験開始後の時間（分）を表し，2つのファントムの偶発同時計数が一致するように時間の原点を合わせてある。図より N_t 曲線の位置がファントムにより異なることがわかる。また，本システムで扱う同時計数事象の総和（on time と off time の和）の計数率 N_t+2N_r の変化も同じ図に示してある。図より，N_t+2N_r の値は，いずれのファントムも高放射能側で飽和し一定値660 kcps となることがわかる。この図では，ファントム(3)の曲線は示していないが，N_t 曲線の位置はファントム(1)と(2)の中間であり，N_t+2N_r が高放射能側で660 kcps となることは他と同じである。

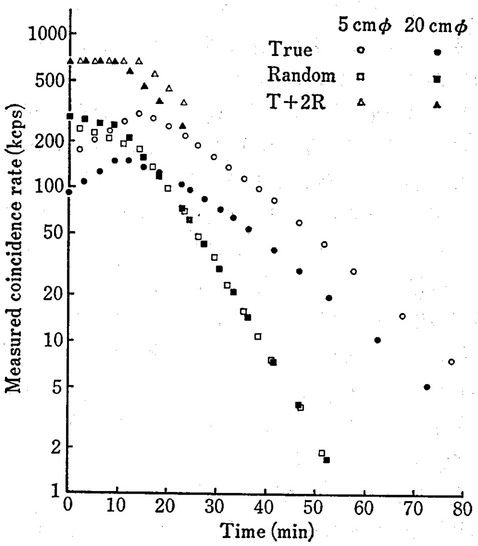

Fig. 3 Measured coincidence rates of phantoms. Open symbols show data from the 5 cm diameter cylinder (○, true rate N_t; □, random rate N_r; △, rate of total coincident event N_t+2N_r), while closed symbols show data from the 20 cm diameter cylinder.

3·2 数え落としの補正係数

Fig. 4は式(1)より求めた第3スライスの数え落としの補正係数 f と N_t の関係を示したものである。なお f の計算は Fig. 3で N_t+2N_r が飽和しない範囲で行った。図に示すように f と N_t の関係はファントムごとに大きく変化し，この関係を用いて臨床例に対する数え落としを補正することは困難なことがわかる。

Fig. 5は Fig. 4と同じ第3スライスの補正係数 f と単一光子計数率の上ブロックの計測値（1，2リングの和）N_s との関係を示したものである。この図の場合，Fig. 4とは異なり f-N_s 関係のファントムによる差は少ないことがわかる。

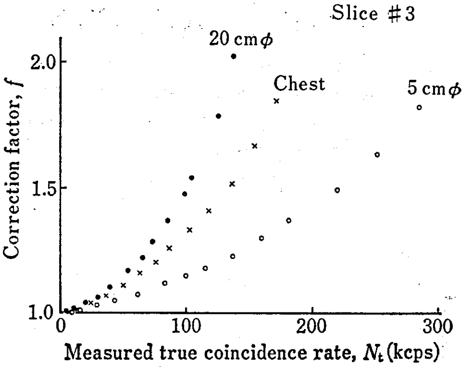

Fig. 4 Correction factor for count loss vs. measured true coincidence rate N_t (slice #3). The relationship depends severely on phantom configurations.

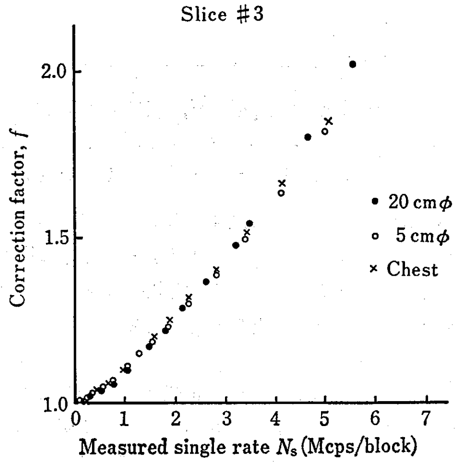

Fig. 5 Correction factor for count loss vs. measured single rate per block N_s (slice #3). The relationship is almost independent of phantom configurations.

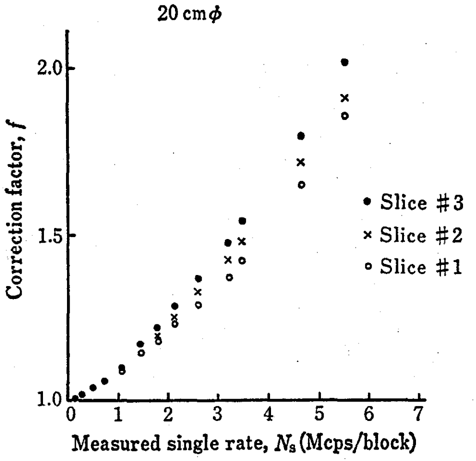

Fig. 6 Correction factor for count loss vs. measured single rate per block (20 cm diameter cylinder). The relationship depends slightly on slices.

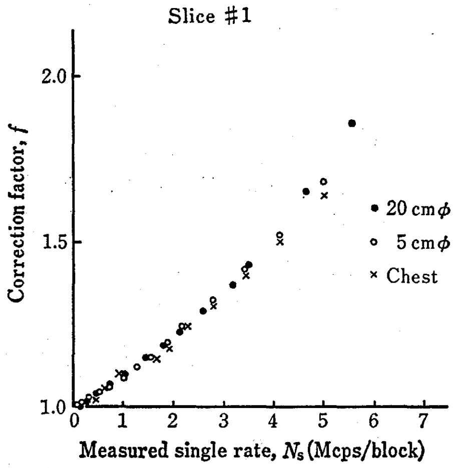

Fig. 7 Correction factor for count loss vs. measured single rate per block (slice #1).

Fig. 6は上ブロックに属する3つのスライスそれぞれに対してファントム(1)の補正係数fとN_sの関係を示したものである。図よりf-N_s関係はスライスごとに異なり，スライスごとの補正が必要であることがわかる。

Fig. 7は第1スライスの補正係数fとN_sの関係を示したものである。本図においても，補正係数のファントムによる差は少ないことがわかる。Fig. 5-7をまとめると，fとN_sの関係はスライスごとに相当に異なるが，ファントムによる差は少ないことがいえる。

4. 考察

4・1 PCT 装置の計数率特性

PCT 装置における真の同時計数の数え落としは，一般に，①単一光子計数の数え落とし，②同時計数事象の数え落とし，および，③②にさいしての偶発同時計数との競合に由来し，そのいずれが支配的かは装置の設計や被写体の特性にも関係し，必ずしも単純な形にまとめることはできない[1],[6]-[8]。本報の結果もFig. 3にみられるように，この一般的な事実を反映していると考えられる。

Fig. 3の高放射能側ではN_t+2N_rはいずれのファントムに対しても660 kcpsで一定値となる。これは上の②の同時計数事象の数え落としによるものである。計測される同時計数事象が一定値をとるのは，Fig. 2の回転フォトカプラーの誤動作を防ぐため，FIFOの読み出し周波数を660 kcpsに設定していることの結果である。

Fig. 3に示したごとく，N_rの曲線が重なるように時間の原点を選んだ場合，N_t曲線の位置はファントムにより大きく異なる。数え落としの影響の少ない低放射能側で，同一のN_r (N_r=1 kcps)に対するN_tの比 (N_t曲線の高さの比) を求めてみると，5 cmφ/20 cmφ=2.1となる。これは主として，ファントム径が小さくなるほど (真の同時計数率)/(単一光子計数率) の比が大きくなるためである。Tanakaらの計算式[9]に従い単一光子計数率（したがって偶発同時計数率）が等しいときのN_tの比を求めると5 cmφ/20 cmφ=2.37となり実験値とほぼ一致する。

単一光子計数率が等しい場合にN_tが等しくないこと，言い換えれば，(真の同時計数率)/(単一光子計数率) の値がファントム径により異なることは，PCT装置の数え落としの補正を行う場合，重大な問題を引き起こす。すなわち，N_tが等しい場合でも，被写体が異なれば，単一光子計数率や同時計数事象の総和の計数率N_t+2N_rは等しくならない。数え落としの割合は，すでに述べたように単一光子計数率やN_t+2N_rに従って変化すると考えられるから，N_tを使って異なる被写体の数え落としを補正することは困難である。これを端的に示したのがFig. 4であり，図ではN_tと数え落としの補正係数fの関係はファントムにより大きく変化している。

そこで，被写体依存性の少ない数え落としの補正をいかに行うかが実用上，重要な問題となる。POSITO LOGICA II の場合，Fig. 5およびFig. 7から考え

て，FIFOが飽和しない範囲では，ブロック当たりの単一光子計数率N_sによる数え落としの補正が可能のように思われる。次節ではこの点について考察したい。

4･2　数え落としの補正

最近のPCT装置は，感度と空間分解能の向上を図るための多段の検出器リングを用い，また各リングの検出器数を非常に多くしている。このような装置では，同時計数回路の数を削減するため，POSITOLOGICA Ⅱのように，検出器群をいくつかのグループに分け，グループごとの同時計数と，グループ内検出器アドレスの決定を組み合わせている。アドレスエンコーダでの検出器アドレスの決定には無視できない時間がかかり，数え落としの原因となる。

また，POSITOLOGICA Ⅱの4連結検出器のように，検出器自身に位置演算の機能を持たせた場合，位置演算に要する時間も数え落としの原因になると考えられる。

以上の2つはいずれも単一光子の数え落としに寄与する。付録はこれらの原因が数え落としにどのように効くかを計算したものである。付録に示したように設計値から計算したdead time τの値は35 nsである。一方，実測値に対する曲線あてはめにより求めた値は，3つのファントムに対して(1) 52.1，(2) 49.3，(3) 51.3 nsであった。

計算値の方が実測値よりやや小さいが，これは検出器や回路が設計どおりに働いていないためと考えられる。Fig. 5，7に示すように，N_sとfの関係にファントム依存性がほとんどないことも考え合わせると，本装置における同時計数の数え落としは，FIFOの飽和が起こらない範囲では，検出器およびアドレスエンコーダにおける単一光子の数え落としに起因しているものといえる。

したがって，そのような計数範囲ではN_sを使って数え落としの補正が可能である。本装置ではfをN_sのつぎのような3次関数で近似し，

$$f=1+a_1N_s+a_2N_s^2+a_3N_s^3 \qquad (2)$$

a_1, a_2, a_3を20 cmϕファントムのデータを使ってスライスごとに決め，臨床データの補正に使用している。N_sとしては1，2，3スライスに関しては上ブロック（1，2リングの和），4，5スライスに関しては下ブロック（2，3リングの和）を用いる。また，スライスごとの補正はFig. 6に示すように，かなりのスライス依存性があることから必要である。

FIFOの飽和が起こっている場合は，本装置においては情報の一部が失われるため，本報で述べたような単純な方法による補正は困難であり，今後の検討課題としたい。

謝　辞

稿を終えるにあたり，常にご指導いただいた放射線医学総合研究所臨床研究部長舘野之男博士に深く感謝いたします。本研究は放射線医学総合研究所の特別研究「重粒子線等の医学利用」（班長恒元　博病院部長）の一部として行われた。同特別研究関係者のご協力に感謝いたします。とくにラジオアイソトープを生産していただいた同研究所技術部サイクロトロン管理課鈴木和年，玉手和彦両氏に感謝いたします。

付　録

数え落としのないブロックあたりの単一光子計数率をN_s^0とする。4連結検出器，アドレスエンコーダとも飽和型の数え落とし特性を示すとし，それぞれのdead timeをτ_1, τ_2とする。一様な放射線場に対して単一光子計数率の計測値（これは同時計数回路に入る率であり，途中で別経路を通る本文中のN_sとは異なる）は近似的に，

$$N_s'=\frac{N_s^0}{1+\tau N_s^0} \qquad (\mathrm{A1})$$

ここで，

$$\tau=\frac{\tau 1}{l1}+\frac{\tau 2}{l1/l2} \qquad (\mathrm{A2})$$

また，$l1(=40\times2=80)$はブロック当たりの4連結検出器の数，$l2(=8)$はアドレスコーダあたりの4連結検出器の数である。これに装置の設計パラメータ$\tau 1=800$ ns[3)]，$\tau 2=250$ nsを代入すると，$\tau=10+25=35$ nsとなる。

単一光子の数え落としに基づく同時計数の数え落としは，その2乗に比例するから，数え落としの補正係数fは，

$$f=\left(\frac{N_s^0}{N_s'}\right)^2=(1+N_s^0\tau)^2 \qquad (\mathrm{A3})$$

fとN_s^0の関係を本文で述べた方法で求め，そのデータに対して曲線あてはめを行うならば，ファントム(1)，(2)，(3)に対してそれぞれ52.1，49.3，51.3 nsとなる。

文　献

1） Hoffman, E.J., Phelps, M.E. and Huang, S.C.:

J. Nucl. Med., **24**, 245-257 (1983)

2) Takami, K., Ueda, K., Tanaka, E. et al.: *IEEE Trans. Nucl. Sci.*, **30**, 734-738 (1983)

3) Murayama, H., Nohara, N., Tanaka, E. and Hayashi, T.: *Nucl. Instrum. Methods*, **192**, 501-511 (1982)

4) Derenzo, S.E., Budinger, T.F. and Huesman, R.H.: *IEEE Trans. Nucl. Sci.*, **28**, 81-89 (1981)

5) 千田道雄, 米倉義晴, 向井孝夫, 他：核医学, **22**, 1133 (1985)

6) Mazoyer, B.M., Rools, M.S. and Huesman, R.H.: *Phys. Med. Biol.*, **30**, 385-399 (1985)

7) Stearns, C.W., Chesler, D.A., Kirsh, J.E. and Brownell, G.L.: *IEEE Trans. Nucl. Sci.*, **32**, 898-901 (1985)

8) Kanno, I., Miura, S., Yamamoto, S. et al.: *J. Comput. Assist. Tomogr.*, **9**, 931-939 (1985)

9) Tanaka, E., Nohara, N., Tomitani, T. et al.: *ibid.*, **6**, 350-364 (1982)

Abstract

Count Rate Characteristics and Count Loss Correction of POSITOLOGICA II: A Whole Body Positron Emission Tomograph

Masahiro ENDO, Norimasa NOHARA*, Takeshi A. IINUMA, Hitoshi SHINOTO,
Eiichi TANAKA*, Katsuya YOSHIDA**, Toshiharu HIMI**,
Akihiko KAGAYA**, Akira OGUSHI*** and Shinichi INOUE***
Division of Clinical Research and *Division of Physics, National Institute of Radiological Sciences
9-1, Anagawa 4-chome, Chiba-shi 260
**Department of 3rd Internal Medicine, Chiba University School of Medicine
8-1, Inohana 1-chome, Chiba-shi 280
***Research and Development Center, Hitachi Medical Corp.
2-1, Shintoyofuta, Kashiwa-shi 277

This paper describes evaluation and correction of count rate characteristics of POSITOLOGICA II, a multi-slice whole body positron emission tomography system. The present study was performed using three phantoms; ① a 5 cm inner diameter, water-filled lucite cylinder, ② a 20 cm inner diameter, water-filled lucite cylinder and ③ a chest phantom. After injection of high activity (about 1.85 GBq (50 mCi)) of ^{13}N *ammonia into each phantom, rates of true coincidence, random coincidence and single photon detections were measured during decay of the isotope through more than two orders of magnitude of activity. At very high levels of activity, count rate characteristics of the system were saturated and limited to 660 kcps of total coincidence rate, which was the sum of rates in on-time and off-time windows, by the FIFO (first-in first-out) output frequency. Below those levels of activity the relationship between count loss and true coincidence rate was not unique but depended on the phantom configurations, suggesting that count loss correction using the above relationship was inadequate for quantitative study. However, the relationship between count loss and single rate was almost independent of the phantom configurations. Thus in conclusion count loss could be corrected using single rate for POSITOLOGICA II. A practical method of count loss correction was also proposed.*

(Received January 30, 1987)

《原　著》

ECTにおける種々の逐次型画像再構成法の比較

村山　秀雄*　　田中　栄一*　　野原　功全*　　富谷　武浩*
山本　幹男*

要旨　ECTにおける6つの逐次型画像再構成法をアルゴリズムの比較によって分析すると同時に，計算機によるシミュレーション実験により逐次近似画像を作成してこれらの方法の特性および収束性を分析した．期待値最大化アルゴリズム(EM)法は加算式同時逐次近似(ASIRT)法および最急降下式最小自乗逐次近似(GRADY)法にアルゴリズムが類似しており，EM法はASIRT法よりも収束性が良好であった．像空間逐次近似アルゴリズム(ISRA)法は乗算式同時逐次近似(MSIRT)法を簡素化したアルゴリズムであるが収束速度は劣化した．共役傾斜最小自乗逐次近似(CONGR)法は高周波成分の補正を増強する効果があるため，上述の6つの方法の中では最も収束性が良好であった．また，逐次近似画像の収束性を示すための4つの適合関数について相互比較を行い，各適合関数の特色や相互の関連性を分析した．

I. はじめに

ポジトロンECT(PET)やシングルフォトンECT(SPECT)などの放射型CT(ECT)の画像再構成法として，多くは通常のX線CTで用いられる重畳積分法[1]もしくはフーリエ変換法[2]などの解析的手法が利用されてきた．しかるに，ECTでは投影データが元来負でない整数値であることや，検出器の3次元的配列により同時に3次元の投影データを収集して感度を向上できる等の特徴がある．近年，このようなECTの特徴を生かす試みとして，新しい逐次型画像再構成法の研究が急速に進められつつある[3~14]．

Sheppらが提案した期待値最大化アルゴリズム(Expectation Maximization Algorithm, EM)法[3]は収束性が数学的に証明されており[4]，逐次近似画像の総和が自動的に測定投影データの総和に等しくなることや，原理的にいずれの画素値も負値にならないことが保証されているなどの利点があるため，ECTへの実用化が大いに期待されている[5~12]．しかし，PET装置の多層化および高解像力化に伴い，逐次型画像再構成の計算に必要な計算機の記憶容量は急激に増加する傾向にある．記憶容量の効率的利用をはかるために，Daube-Witherspoonらは像空間逐次近似アルゴリズム(Image Space Reconstruction Algorithm, ISRA)法[13]を提案した．この方法は測定投影データの逆投影画像を基準にして，これと推定投影データの逆投影画像との比較から画像の補正を行う点に特徴がある．

一般にCTの画像再構成のために開発された逐次型画像再構成法は2つに大別できる．1つは各投影方向ごとに推定画像から作成した投影データを実測投影データと比べて，画像の補正をそのたびに行う(ray-by-ray)方式であり，各種のART法がその例である[15]．ここではこの方式を単一逐次型と名づける．

もう1つの方式は，各画素ごとに全投影データに対する実測値との誤差を調べて補正値を求め，全画素の補正を同時に行う(point-by-point)方式である．このような方式をここでは連立逐次型と名づける．EM法やISRA法はこの連立逐次型に属しており，そのほかにも，加算式同時逐次近似

---

* 放射線医学総合研究所物理研究部
受付：62年1月13日
最終稿受付：62年1月13日
別刷請求先：千葉市穴川4-9-1（〶260）
放射線医学総合研究所物理研究部
村山秀雄

(Additive Simultaneous Iterative Reconstruction Technique, ASIRT) 法[16]や乗算式同時逐次近似(Multiplicative Simultaneous Iterative Reconstruction Technique, MSIRT) 法[16]，および最急降下式最小自乗逐次近似 (Gradient Method, GRADY) 法[17]や共役傾斜式最小自乗逐次近似 (Conjugate Gradient Method, CONGR) 法[18,19]などがある．連立逐次型は単一逐次型の画像再構成法に比べると，雑音を含む投影データに対して収束性の良い安定した逐次近似画像の得られる点に特色があるため，ECT に適している[18]．

本論文では，上にあげた6つの連立逐次型画像再構成法について分析する．特に EM 法および ISRA 法と他の方法との相違点や類似点を系統的に比較し，それらの特徴を明らかにする．また，計算機を用いたシミュレーション実験によって，これらの方法の収束性や逐次近似画像の特徴を分析する．さらに逐次近似画像がどれだけ真の画像に近い像であるか，またはどれだけ収束値に近づいたかを示す尺度(ここでは適合関数と名づける)を4つとりあげる．同一のシミュレーション実験に対するこれらの適合関数を求めて収束性の分析を行うと同時に，それらの比較によって各適合関数の特徴や，相互の関連性を示す．

II. 逐次型画像再構成法

1. アルゴリズムの比較

簡単のためにここでは一平面内の画像および投影データの組を考える．Fig. 1 のように対象とする領域は円形内とした．この領域は J 個の画素で構成されているものとし，その各画素に1から J までの通し番号をつける．j 番目 ($j=1, \ldots, J$) の画素における画素値は x_j で表す．

投影データの組に対してはその投影方向に関する区別をせずに，1から I までの通し番号をつける．i 番目 ($i=1, \ldots, I$) の測定投影データは y_i とする．以下の議論においては投影データ y_i が統計雑音を含まないものと仮定する．

j 番目の画素内に分布する線源が i 番目の投影データとして検出される確率を a_{ij} で表す．ただし，すべての画素 j に対して a_{ij} が次式を満たすと仮定する．

$$\sum_{i=1}^{I} a_{ij}=1 \qquad (j=1, \ldots, J) \qquad (1)$$

すなわち，a_{ij} は i に関する規格化が行えるものとする．

逐次型画像再構成法を用いて得られた n 回目の逐次近似画像を $x_j^{(n)}$ と表せば，この画像を元にして作成される推定投影データ $z_i^{(n)}$ は次式で与えられる．

$$z_i^{(n)}=\sum_{j=1}^{J} a_{ij}x_j^{(n)} \qquad (i=1, \ldots, I) \qquad (2)$$

各逐次型画像再構成法のアルゴリズムは，(n+1) 回目の逐次近似画像 $x_j^{(n+1)}$ を与える式によって表せる．以下に6つの連立逐次型のアルゴリズムを列記する．

1) EM 法[3]

$$x_j^{(n+1)}=x_j^{(n)}\cdot\left\{\sum_{i=1}^{I}(y_i a_{ij}/z_i^{(n)})\right\} \qquad (3)$$

2) ISRA 法[13]

$$x_j^{(n+1)}=x_j^{(n)}\cdot\left\{\left(\sum_{i=1}^{I} y_i a_{ij}\right)\Big/\left(\sum_{i=1}^{I} z_i^{(n)}a_{ij}\right)\right\} \qquad (4)$$

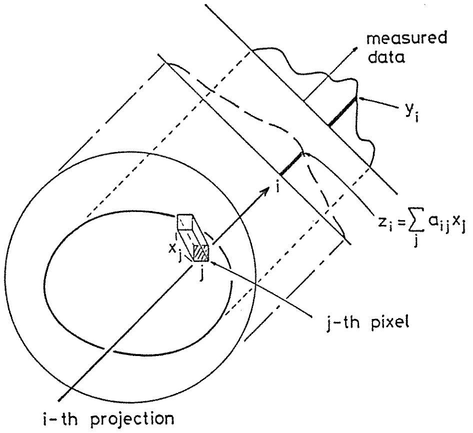

Fig. 1 Scheme of the reconstruction domain and projection data. The j-th pixel has a value of x_j. The i-th projection has a measured value of y_i and an estimated value of z_i. The a_{ij} denotes the probability that an event emitted from pixel j is assigned to projection i.

3) ASIRT 法[16)]

$$x_j^{(n+1)}=x_j^{(n)}+\sum_{i=1}^{I}\left\{(y_i-z_i^{(n)})a_{ij}\Big/\sum_{j=1}^{J}a_{ij}\right\} \quad (5)$$

4) MSIRT 法[16)]

$$x_j^{(n+1)}=x_j^{(n)}\cdot\left\{\sum_{i=1}^{I}\left(y_i a_{ij}\Big/\sum_{j=1}^{J}a_{ij}\right)\right\}$$

$$\Big/\left\{\sum_{i=1}^{I}\left(z_i^{(n)}a_{ij}\Big/\sum_{j=1}^{J}a_{ij}\right)\right\} \quad (6)$$

5) GRADY 法[17,19)]

$$x_j^{(n+1)}=x_j^{(n)}+\beta^{(n)}$$

$$\cdot\left\{\sum_{i=1}^{I}(y_i-z_i^{(n)})a_{ij}\Big/\sum_{i=1}^{I}a_{ij}^2\right\} \quad (7)$$

ただし，$\beta^{(n)}$ は偏差自乗関数

$$N^2(x_j^{(n+1)})=\sum_{i=1}^{I}(y_i-z_i^{(n+1)})^2$$

が極小値をとるように選ばれる．

6) CONGR 法[18,19)]

$$x_j^{(n+1)}=x_j^{(n)}+\beta^{(n)}\cdot\varDelta x_j^{(n)}$$

$$\varDelta x_j^{(n)}=\sum_{i=1}^{I}(y_i-z_i^{(n)})a_{ij}\Big/\left(\sum_{i=1}^{I}a_{ij}^2\right)$$

$$-\gamma^{(n)}\varDelta x_j^{(n-1)} \quad (8)$$

ただし，$\gamma^{(0)}=0$. $\gamma^{(n)}\ (n\neq 0)$ は $\varDelta x_j^{(n-1)}$ と $\varDelta x_j^{(n)}$ が互いにa_{ij}を要素とする行列に関して直交するような共役関係をとるように選ばれ，$\beta^{(n)}$ は GRADY 法と同様に偏差自乗関数 $N^2(x_j^{(n+1)})$ が極小値をとるように選ばれる．以上の 6 つのアルゴリズムのうち，ISRA, ASIRT, および MSIRT 法に関しては各逐次近似ごとに $x_j^{(n+1)}$ が負値の場合はこれを 0 に修正し，かつ $x_j^{(n+1)}$ と y_i の j および i に関するそれぞれの総和を等しくするように規格化をする．これらのアルゴリズムの詳細については引用文献に譲り，以下ではアルゴリズム相互の相違点や類似点を分析する．

EM 法では (3) 式より初期画像 $x_j^{(0)}$ がいずれの画素でも負値でなければ，つねに $x_j^{(n)}$ は負値にならないことが明らかである．また，(3) 式の両辺を j について加算すると，(2) 式より次式が成立する．

$$\sum_{j=1}^{J}x_j^{(n+1)}=\sum_{j=1}^{J}x_j^{(n)}\cdot\left\{\sum_{i=1}^{I}(y_i a_{ij}/z_i^{(n)})\right\}$$

$$=\sum_{i=1}^{I}\left\{y_i\cdot\sum_{j=1}^{J}(a_{ij}x_j^{(n)}/z_i^{(n)})\right\}$$

$$=\sum_{i=1}^{I}y_i \quad (9)$$

上の式は逐次近似画像の総和がつねに測定投影データの総和に等しいことを保証している．(3) 式の右辺は (1), (2) 式を用いて次のように変形できる．

$$(3)\text{式の右辺}=x_j^{(n)}\cdot\left\{1-\sum_{i=1}^{I}a_{ij}+\sum_{i=1}^{I}(y_i a_{ij}/z_i^{(n)})\right\}$$

$$=x_j^{(n)}\cdot\left\{1+\sum_{i=1}^{I}(y_i-z_i^{(n)})\cdot a_{ij}/z_i^{(n)}\right\}$$

$$=x_j^{(n)}+\sum_{i=1}^{I}\left\{(y_i-z_i^{(n)})\cdot a_{ij}x_j^{(n)}\right.$$

$$\left.\Big/\sum_{j=1}^{J}a_{ij}x_j^{(n)}\right\} \quad (3')$$

(3′) 式は (5) 式の右辺と類似の関係にあることが認められる．すなわち，両者はともに補正項として投影データの推定値誤差 $(y_i-z_i^{(n)})$ を各画素に配分する式である．しかるに，(5) 式はその配分の重みが a_{ij} に比例するだけであるのに対して，(3′) 式では a_{ij} のみならず前回の逐次近似値 $x_j^{(n)}$ にも比例する．以上の考察より，前回の逐次近似画像も補正因子に寄与させる EM 法は ASIRT 法より良好な収束性を期待し得る．

また，(7) 式の左辺も $(y_i-z_i^{(n)})$ の成分を各画素に割り当てる式であり，GRADY 法も EM 法および ASIRT 法に類似している．ただし，(7) 式では平均自乗関数 $N^2(x_j^{(n+1)})$ が極小値をとるように補正項の係数が選ばれる．一方，CONGR 法は GRADY 法の変形である．(8) 式では単に $(y_i-z_i^{(n)})$ に比例する補正項のみではなく，前回の補正画像成分を考慮してその成分をあらかじめ取り除く．初期の補正が主に低周波成分の補正であることから，CONGR 法では誤差の高周波成分の補正を強調する効果が生じる．したがって，CONGR 法は GRADY 法より良好な収束性を期待し得る．

ISRA 法と MSIRT 法はアルゴリズムの式 (4) と (6) の比較により類似性の高いことが判明する．前者が y_i および $z_i^{(n)}$ の単純逆投影画像の比を補

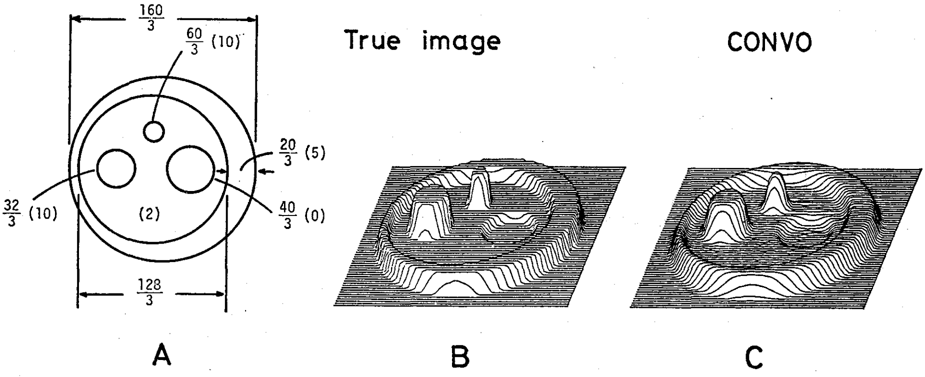

Fig. 2 The mathematical phantom used in the simulation (A) and its image (B). The values without parentheses are diameters or distances in terms of pixel number and the values in parentheses are relative emission densities. CONVO shows the reconstructed image using the convolution method (C).

正因子とするのに対して，後者は各逆投影方向の因子 a_{ij} の和 $\sum_{j=1}^{J} a_{ij}$ によって規格化した逆投影像で補正因子を形成する．すなわち ISRA 法は MSIRT 法のアルゴリズムを簡素化した画像再構成法である．

2. 逐次近似画像の比較

各種の逐次型画像再構成法によって作成される逐次近似画像を比較するために，計算機によるシミュレーション実験を行った．使用した数学的ファントムを Fig. 2 の A に示す．ファントムの形状は画素の辺の長さを単位とした円の直径等で与えられており，各領域ごとの線源濃度はカッコ内の相対値で示されている．

以下における画像再構成では具体例として高解像力 PET 装置を使用した場合を想定する．この PET 装置は 240 個の検出器が円環状ガントリーに 6 mm 間隔で等間隔配列されているものとし，投影データの標本化は画素の辺の長さ (1.5 mm) に等しい標本間隔で行うものとする．投影方向は 0.75度ごとに等間隔で240方向が得られる．以上の想定に基づいて，測定投影データ y_i $(i=1, \ldots, I)$ を計算した．

Figure 2 の B は，ファントム A の線源分布画像を鳥かん図で表示したものである．本論文中の鳥かん図表示はすべて 64×64 (=4,096) 画素数の正方形画面に内接する円形画面上で表示した．Fig. 2 の C は，通常の重畳積分法によって得られた再構成画像である．その重畳フィルタ関数には Shepp-Logan の関数[1)] を使用した．

逐次近似画像は逐次近似回数 n に依存するだけでなく，n=0 で与えられる初期推定画像にも依存する．以下の逐次近似画像で使われた初期画像はすべて同一であり，その画素値 $x_j^{(0)}$ は次式で与えた．

$$x_j^{(0)} = \frac{1}{J} \sum_{i=1}^{I} y_i \qquad \text{(for all } j) \qquad (10)$$

すなわち，初期画像は全画面上で一定の画素値をとり，その総和が測定投影データの総和に等しい．

Figure 3 の A1, A2 および A3 は，EM 法によって作成された画像であり，それぞれ逐次近似回数が n=4, 20 および 100 の逐次近似画像である．同様にして，B1, B2, B3 は ASIRT 法，C1, C2, C3 は GRADY 法による n=4, 20 および 100 の逐次近似画像である．Fig. 4 には ISRA 法 (D1, D2, D3), MSIRT 法 (E1, E2, E3) および CONGR 法 (F1, F2, F3) による逐次近似画像を例示した．これらの画像の逐次近似回数も同様にして，上から順に n=4, 20 および 100 である．

Figures 3 および 4 の上段の画像を見ると，n=4 の逐次近似画像は CONGR 法の場合 (F1) を除いてほとんど真の画像 (Fig. 2 の B) を復元できなか

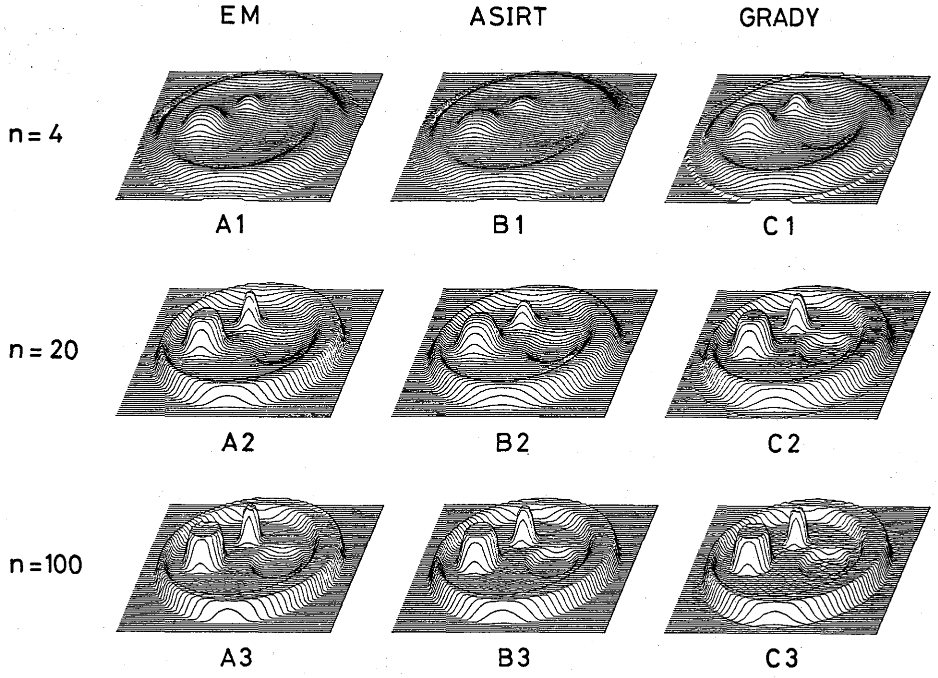

Fig. 3 Reconstructed images using EM method (A1, A2, A3), ASIRT method (B1, B2, B3), and GRADY method (C1, C2, C3). The top, middle, and bottom images have iteration numbers of n=4, 20, and 100, respectively.

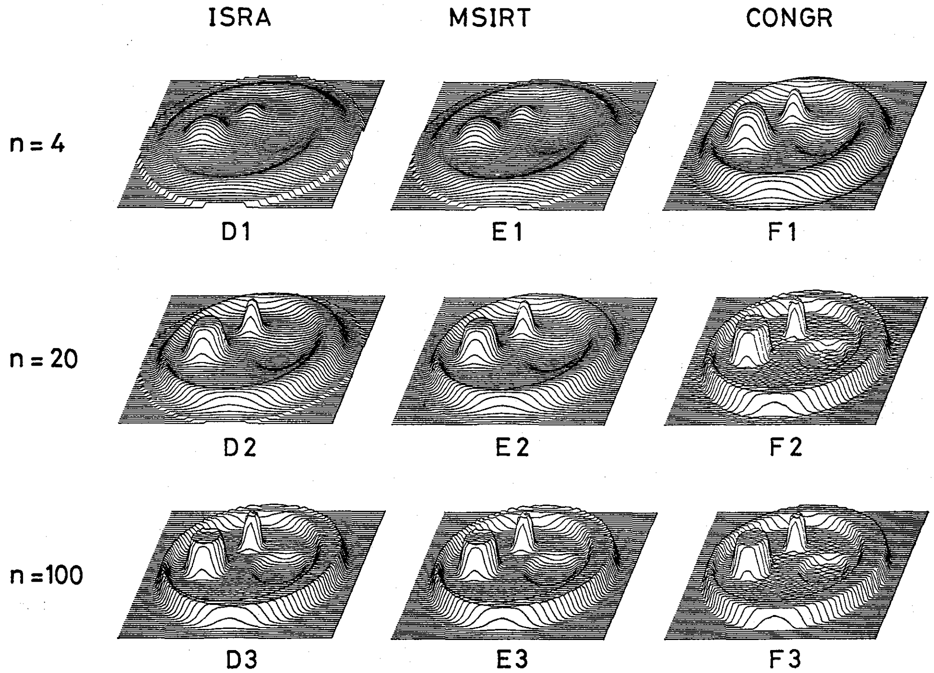

Fig. 4 Reconstructed images using ISRA method (D1, D2, D3), MSIRT method (E1, E2, E3), and CONGR method (F1, F2, F3). The top, middle, and bottom images have iteration numbers of n=4, 20, and 100, respectively.

った．しかも，重畳積分法で作成した再構成画像(Fig. 2 の C) に比べれば画像 F1 の復元度はまだ十分でなかった．

Figures 3 および 4 の中段の画像を見ると，どの再構成法でも復元性が向上しており，特に，CONGR 法 (F2) と GRADY 法 (B2) はホットおよびコールド領域で Fig. 2 の C に近い画像に復元されている．類似のアルゴリズムと考えられる EM, ASIRT, GRADY 法の中では A2, B2, C2 の画像の比較より，最も収束速度が良好であるのは GRADY 法であり，次に EM, ASIRT 法の順であるとみなすことができた．また，EM 法と ASIRT 法の共通する特徴として，画像の周辺において速くしかも安定に画素値が 0 の値へ収束することが認められた．画像 D2 と E2 はともに画像周辺部で 0 の値へ戻るのが遅く，特に D2 の方でその傾向が著しい．したがって，ISRA 法は MSIRT 法より収束速度が遅いと考えられた．

Figures 3 および 4 の下段の画像はいずれも Fig. 2 の C と同程度の画像に復元しており，逐次近似回数を 100 回以上に選ぶ必要はないと判断した．

III. 逐次近似回数の選択

いずれの画像再構成法を用いても，作成された画像 x_j が真の画像 T_j に正確に復元することは難しい．種々の画像再構成法の良否を判定するには，それぞれに作成された画像が真の画像にどれだけ近い像であるかを示す客観的な尺度(適合関数)が必要となる．特に，逐次型画像再構成法ではアルゴリズムの繰り返しによって各逐次近似ごとに作成画像が更新される．したがって，適当な再構成画像を選択することが不可欠となり，その選択の妥当性を評価するために何らかの適合関数を導入し，収束度を定量的に分析する必要がある．

最も信頼し得る適合関数は作成画像 x_j と真の画像 T_j の相対誤差のみで表されたもの（直接型適合関数と名づける）である．しかるに，実際の ECT 画像再構成においては真の画像 T_j が未知のため直接型適合関数の利用は不可能となる．その代わりに実測投影データ y_i と推定投影データ z_i の相対誤差で表された関数（間接型適合関数と名づける）を用いる．ここに (2) 式と同様に

$$z_i=\sum_{j=1}^{J} a_{ij}x_j$$

以下に代表的な直接型適合関数 1 つと間接型適合関数 3 つを列記する．

1) 平均誤差関数：$m(x_j)$

$$m(x_j)=\left(\sum_{j=1}^{J}|x_j-T_j|\right)\Big/\left(\sum_{j=1}^{J}T_i\right) \qquad (11)$$

2) 偏差自乗関数：$N^2(x_j)$

$$N^2(x_j)=\sum_{i=1}^{I}(y_i-z_i)^2 \qquad (12)$$

3) 対数尤度関数：$l(x_j)$

$$l(x_j)=\sum_{i=1}^{I}(y_i\log z_i-z_i) \qquad (13)$$

4) 平均補正因子誤差関数：$R(x_j)$

$$R(x_j)=\left\{\sum_{j=1}^{L}(E_j-1)^2/L\right\}^{1/2} \qquad (14)$$

ここに

$$E_j=\sum_{i=1}^{I}(y_i a_{ij}/z_i) \qquad (15)$$

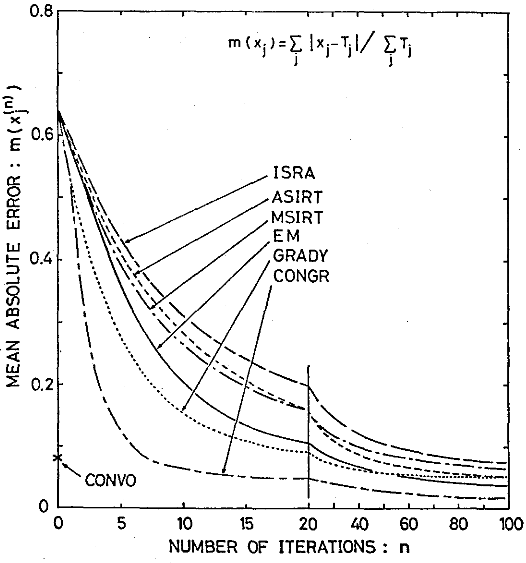

Fig. 5 Plots of the mean absolute error $m(x_j^{(n)})$ as a function of the iteration number n. The mean absolute error of the reconstructed image using the convolution method is marked by x.

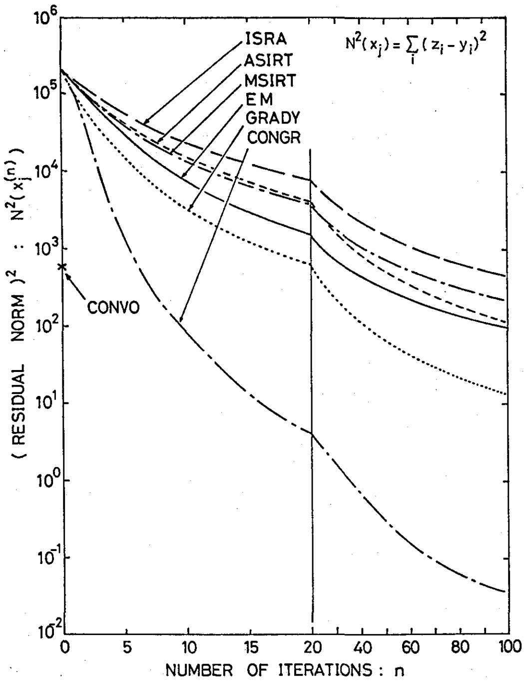

Fig. 6 Plots of the square norm of the residual, $N^2(x_J^{(n)})$ as a function of the iteration number n. The $N^2(x_J^{(n)})$ value of the reconstructed image using convolution method is marked by x.

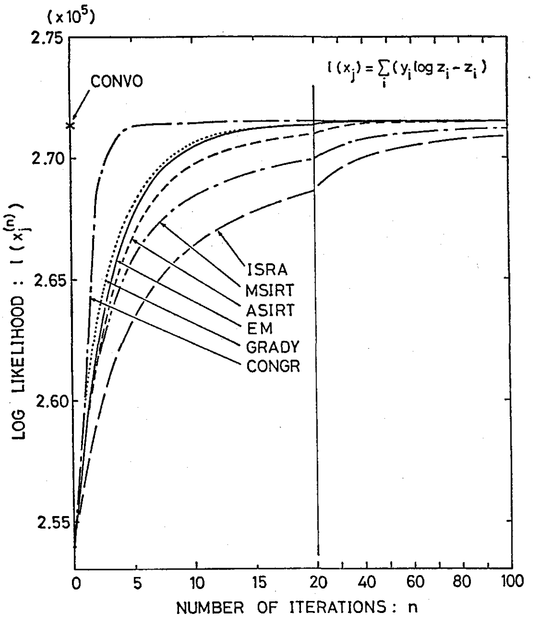

Fig. 7 Plots of the log-likelihood $l(x_J^{(n)})$ as a function of the iteration number n. The log-likelihood of the reconstructed image using the convolution method is marked by x.

(15) 式は (3) 式の右辺における中カッコ内の式と同一である．また，(14) 式の j に関する和は真の画像 T_J が 0 でない画素 (総数 L) のみに限定する．

6 つの逐次型画像再構成法のそれぞれの逐次近似画像に対する適合関数は逐次近似回数 n の関数として表すことができる．前節と同じ数学的ファントム (Fig. 2 の A) および初期画像 ((10) 式) に基づいて計算機によるシミュレーション実験を行い，それぞれの逐次近似画像 $x_J^{(n)}$ ごとに 4 つの適合関数 $m(x_J^{(n)})$, $N^2(x_J^{(n)})$, $l(x_J^{(n)})$, $R(x_J^{(n)})$ を求めた．

Figure 5 は $m(x_J^{(n)})$ を n の関数として表したグラフである．グラフを見やすくするために適合関数 $m(x_J^{(n)})$ は各画像再構成法の逐次近似画像ごとに線で結び，n=0 から 100 までを図に表示した．同様にして $N^2(x_J^{(n)})$, $l(x_J^{(n)})$ および $R(x_J^{(n)})$ を n の関数として各画像再構成法ごとにグラフで表したのが，それぞれ Figs. 6, 7 および 8 である．

$m(x_J)$, $N^2(x_J)$ および $R(x_J)$ は x_J が真の画像 T_J に近づくに従い減少し，0 に漸近するが，$l(x_J)$ は逆に増加し，一定の上限値に近づく．比較のために，重畳積分法の再構成画像 (Fig. 2 の C) に対する適合関数を Figs. 5–8 の縦軸 (n=0) 上に × 印で示した．

同一の逐次近似回数の画像の中では Figs. 5–8 のいずれの適合関数で見ても CONGR 法がつねに最良の収束性を示し，反対に，ISRA 法は最も遅い収束性を示した．また，EM 法と GRADY 法は両者とも ASIRT 法および MSIRT 法に比べてつねに収束性が良好であった．

EM 法と GRADY 法を互いに比較する場合，$N^2(x_J^{(n)})$ および $l(x_J^{(n)})$ (Figs. 6 と 7) のグラフで見る限り，GRADY 法の方がつねに収束性は良好であった．しかし，$m(x_J^{(n)})$ または $R(x_J^{(n)})$ (Figs. 5 と 8) のグラフで見ると，GRADY 法が EM 法より収束性が良いのは初期の逐次近似回数

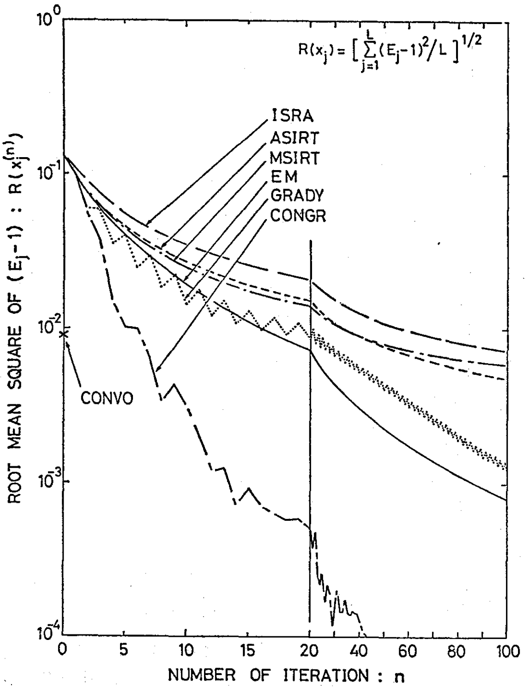

Fig. 8 Plots of the root mean square of (E_J-1), $R(x_J^{(n)})$ as a function of the iteration number n. The $R(x_J^{(n)})$ value of the reconstructed image using the convolution method is marked by x.

に対してのみであり，n が一定値より大きくなると逆に EM 法の方が良い収束性を示すようになった．

ASIRT 法と MSIRT 法を互いに比較すると，$1(x_J^{(n)})$ で見る限り前者の方がつねに良好な収束性を示した．しかし，$m(x_J^{(n)})$, $N^2(x_J^{(n)})$, $R(x_J^{(n)})$ のいずれのグラフで見ても，ASIRT 法が MSIRT 法より収束性に優るのは n=20 程度まででであり，n=40 以上では MSIRT 法の方が収束性は良好になった．以上のように画像再構成法の収束性を定量的に比較する場合は，使用する適合関数によって，その収束度の判定結果が依存することに注意する必要がある．

Table 1 Comparison of the iteration numbers for various iterative reconstruction methods with which the values of $m(x_J)$, $N^2(x_J)$, $l(x_J)$ and $R(x_J)$ are equivalent to the corresponding values of the reconstructed image with the convolution method, respectively

Method	Iteration number equivalent to CONVO			
	n(m)	n(N²)	n(l)	n(R)
CONGR	8	7	6	7
GRADY	25	21	20	20
EM	31	35	19	18
ASIRT	46	48	35	39
MSIRT	62	57	>100	39
ISRA	82	86	>100	66

重畳積分法の再構成画像よりも良好な適合関数を与える逐次近似回数 n の中で最小の n の値を CONVO 等価逐次近似回数と名づける．$m(x_J)$, $N^2(x_J)$, $1(x_J)$, $R(x_J)$ のそれぞれの CONVO 等価逐次近似回数をそれぞれ n(m), n(N²), n(1), n(R) で表し，これらの値を各画像再構成法ごとに求めて表としたものを Table 1 に示した．

n(m) の値の小さい方が良い収束性をもつとみなせば，画像再構成法の収束性は CONGR, GRADY, EM, ASIRT, MSIRT, ISRA 法の順に優劣の序列が得られる．他の 3 つの CONVO 等価逐次近似回数 n(N²), n(1), n(R) の中で，すべての画像再構成法に対して n(m) と近い値を与えるのは n(N²) であった．

n(1) は ISRA 法と MSIRT 法に対して n(m) より大幅に大きな値を示す傾向があった．これは，ISRA 法や MSIRT 法のように直流成分の補正が不十分な逐次近似画像に対して，対数尤度関数 $1(x_J)$ が容易にその上限値へ近づけないためである．また，n(R) の値が各画像再構成法の対応する n(m) の値と大きく異なるのは平均補正因子誤差関数 $R(x_J)$ の評価が画像の全領域ではなく，真の画素値 T_J が 0 でない領域内のみで行われることと，$R(x_J)$ の値が 0 に近い画素値の変動に大きく影響されることによるものと思われる．

IV. 考察と結論

本論文では ECT における連立逐次型画像再構成法を 6 つ取り上げて，これらのアルゴリズムを分析し，各画像再構成法の特徴を示すと同時に，相互の類似性および相違点を示した．EM 法は

ASIRT法およびGRADY法にアルゴリズムが類似していることを示すと同時に，補正項の因子を比較してEM法がASIRT法よりは収束性の良いことを推定できた．また，ISRA法はMSIRT法のアルゴリズムを簡素化した方法であり，CONGR法は誤差の高周波成分を強調する効果がアルゴリズムに含まれていることを示した．

計算機によるシミュレーション実験により，同一の数学的ファントムおよび初期画像を用いて逐次近似画像を作成した．これらの画像を鳥かん図表示で比較することにより，画像再構成法の収束性の比較を行い，アルゴリズムの分析による結果の正しいことを裏づけた．特にEM法とASIRT法は画像周辺において0の値に速く安定に収束することがわかり，反対にISRA法とMSIRT法は直流成分の収束性の遅いことが判明した．

逐次近似画像の収束性を定量的に分析するために$m(x_J)$, $N^2(x_J)$, $1(x_J)$および$R(x_J)$の4つの適合関数を導入した．前述と同じシミュレーション実験の結果を用いて，逐次近似回数nに関する適合関数のグラフを各画像再構成法ごとに求め，それらの比較を行うことによって収束性の定量的分析を行った．$m(x_J)$と$N^2(x_J)$は類似の性質を示す適合関数であり，これらに基づく収束性の比較ではCONGR, GRADY, EM, ASIRT, MSIRT, ISRA法の順で収束性の良いことが判明した．しかるに，$1(x_J)$や$R(x_J)$では別の序列が得られ，4つの適合関数がそれぞれに特徴をもつことを示した．

近年，計算機技術の進歩により，高速の演算装置が安価に入手できるようになってきた[14]．パイプライン処理を行う並列計算機やスーパーコンピュータがさらに普及すれば，今まで画像の作成に長時間を要するために利用されることの少なかった逐次型画像再構成法も臨床において使用できるようになるであろう．したがってECTに適した逐次型画像再構成法の特性を研究して，実用化をはかる努力が今後は重要となるであろう．

本論文中では各画像再構成法の特徴を分析するためにいくつかの仮定を設けて考察対象を簡素化した．第1に逐次近似の初期画像は全画面上で同一画素値をもつと仮定したが，実用的には重畳積分法の再構成画像を初期画像にするなどの方法が考えられ，収束性の向上がはかれるであろう[11]．

第2に測定投影データy_iが統計雑音を含まないことを仮定したが，実際のECTにおいては統計雑音の存在を無視できないので，この影響を考慮した収束性等の分析が今後必要であると考える．第3に，ファントムの形状はFig. 2のAのみを考えたが，ファントムの形状の違いにより各画像再構成法の特性が異なる場合もあり得るので，種種の形状のファントムによる実験も試みる必要がある．

最後に，本論文では一平面内に投影データを限定し，しかも不完全投影データの組ではないと仮定した．しかるに，逐次型画像再構成法が解析的方法に比べて有利となるのは，不完全投影データの条件下や3次元投影データによる3次元画像再構成の分野であり[20]，このような場合は重畳積分法のような解析的方法は適用が難しくなる．特に，3次元画像再構成においては計算機技術の進歩に依存するのみでなく，より収束性の良いアルゴリズムの開発が要求される．

稿を終えるにあたり，有益なご助言を頂いた筑波大学臨床医学系外山比南子博士に深謝致します．また，計算機の使用に際してご協力頂いた放射線医学総合研究所技術部福久健二郎データ処理室長に感謝致します．本研究の一部は厚生省がん助成金（松沢班60–28）および文部省科学研究費（がん特別研究(1)鳥塚班）によって行われた．

文　献

1) Shepp LA, Logan BF: Fourier reconstruction of a head section. IEEE Trans Nucl Sci **NS-21**: 21–43, 1974
2) Mersereau RM: Direct Fourier transform techniques in 3-D image reconstruction. Comput Biol Med **6**: 247–258, 1976
3) Shepp LA, Vardi Y: Maximum likelihood reconstruction for emission tomography. IEEE Trans Med Imag **MI-1**: 113–122, 1982
4) Vardi Y, Shepp LA, Kaufman L: A statistical model for positron emission tomography. J Amer Statist Assoc **80**: 8–37, 1985

5) Lange K, Carson R: EM reconstruction algorithms for emission and transmission tomography. J Comput Assist Tomogr **8**: 306–316, 1984

6) Shepp LA, Vardi Y, Ra JB, et al: Maximum likelihood PET with real data. IEEE Trans Nucl Sci **NS-31**: 910–913, 1984

7) Snyder DL, Politte DG: Image reconstruction from list-mode data in an emission tomography system having time-of-flight measurements. IEEE Trans Nucl Sci **NS-30**: 910–913, 1984

8) Snyder DL, Miller MI: The use of sieves to stabilize images produced with the EM algorithm for emission tomography. IEEE Trans Nucl Sci **NS-32**: 3864–3872, 1985

9) Vishampayan S, Stamos J, Mayans R, et al: Maximum likelihood image reconstruction for SPECT. J Nucl Med **26**: p 20, 1985

10) Miller MI, Snyder DL, Miller TR: Maximum-likelihood reconstruction for single-photon emission computed-tomography. IEEE Trans Nucl Sci **NS-32**: 769–778, 1985

11) Tanaka E, Nohara N, Tomitani T, et al: Utilization of non-negativity constraints in reconstruction of emission tomograms. In: Information processing medical imaging, ed. Bacharach SL, Martinus Nijhoff Publishers, Dordrecht, 1986, pp. 379–393

12) Lewitt RM, Muehllehner: An iterative reconstruction for positron emission tomography based on the EM algorithm for maximum likelihood estimation. IEEE Trans Med Imag **MI-5**: 16–22, 1986

13) Daube-Witherspoon ME, Muehllehner: An iterative image space reconstruction algorithm suitable for volume ECT. IEEE Trans Med Imag **MI-5**: 61–66, 1986

14) Floyed CE, Jaszczak RJ, Greer KL, et al: Inverse Monte Carlo as a unified reconstruction algorithm for ECT. J Nucl Med **27**: 1577–1585, 1986

15) Herman GT, Lent A: Iterative reconstruction algorithms. Comput Biol Med **6**: 273–294, 1976

16) Gilbert P: Iterative methods for the three-dimensional reconstruction of an object from projections. J theor Biol **36**: 105–117, 1972

17) Goitein M: Three-dimensional density reconstruction from a series of two-dimensional projections. Nucl Instr Meth **101**: 509–518, 1972

18) Budinger TF, Gullberg GT, Huesman RH: Image reconstruction from projection; Implementation and applications, ed. Herman GT, Spring-Verlag, New York, 1979, pp. 147–246

19) Huesman RH, Gullberg GT, Greenberg WL, et al: RECLBL library user's manual; Donner algorithms for reconstruction tomography. Publication PUB-214, Lawrence Berkeley Laboratory, 1977

20) Tanaka E: Recent progress on single photon and positron emission tomography; from detectors to algorithms. IEEE Trans Nucl Sci **NS-34**: 313–320, 1987

Summary

A Comparison of Several Iterative Reconstruction Methods for ECT

Hideo Murayama, Eiichi Tanaka, Norimasa Nohara,
Takehiro Tomitani and Mikio Yamamoto

Division of Physics, National Institute of Radiological Scienses, Chiba

Six iterative reconstruction methods appropriate for emission computed tomography were compared in regard to their algorithms. It was shown that the Expectation Maximization algorithm (EM) method is classified in an algorithmic type similar to the Additive Simultaneous Iterative Reconstruction Technique (ASIRT) method and the Gradient (GRADY) method, and that the Image Space Reconstruction Algorithm (ISRA) method has a simplified algorithm of the Multiplicative Simultaneous Iterative Reconstruction Technique (MSIRT) method.

The performances of the six methods were investigated by computer simulation generating their iterative reconstruction images of a mathematical phantom. Four fitness functions were introduced to analyze the convergence of the iterative reconstruction methods quantitatively. Each fitness function is a measure of the difference between the reconstruction image and the mathematical phantom, or a measure of the rate of covergence. The EM method achieved faster convergence than the ASIRT method, while the ISRA method gave slower convergence than the MSIRT method. Of the six methods, the fastest convergence was obtained using the Conjugate Gradient (CONGR) method, and the slowest was the ISRA method.

The characteristics of each fitness function were also analyzed by its behavior as a function of iteration number for the first 100 iterations of the six methods. These results suggest that the selection of the fitness function for a measure of the convergence is important to use any iterative reconstruction methods.

Key words: ECT, Image reconstruction, Iterative method, EM algorithm, Computer simulation.

《原　著》

POSITOLOGICA II による心電図同期ポジトロン CT

――加算パルス数と復元誤差の関係を中心に――

遠藤　真広*　　松本　　徹*　　氷見　寿治**　　飯沼　　武*
山崎統四郎*　　舘野　之男*　　吉田　勝哉**　　加賀谷秋彦**
増田　善昭**　　稲垣　義明**　　大串　　明***　　井上　愼一***

要旨　心ポジトロン CT における心臓の動きの影響を除去するため，POSITOLOGICA II を用いて心電図同期データ収集を行う方式を開発した．本方式では心電波形に同期して 2 つの時相 (例えば拡張末期と収縮末期) のデータが指定心拍数だけ収集され，画像復元される．データサンプリングの不均一性にもとづく復元誤差を評価するため，固定線源のパルス同期と非同期の撮像を行い，誤差の解析を行った．その結果，データサンプリングの不均一性にもとづく復元誤差は非常に少ない加算パルス数では支配的であるが，加算パルス数を増加すると急激に減少し，臨床使用条件では，統計ノイズに対して無視できることがわかった．正常例に N-13 アンモニアを投与して，心電図同期ポジトロン CT を施行したところ，壁運動と壁厚の時相による変化を検出できた．

I. はじめに

心臓を対象とするポジトロン CT では，心臓の運動はボケによる画質の劣化を招き，また定量解析を行う上で大きな障害となっている[1]．このような心臓の動きの影響を除去するためには，心電波形に同期してデータを収集する心電図同期ポジトロン CT を施行する必要がある．

心電図同期ポジトロン CT は，回転と線形走査を組み合わせた ECAT に対して，古くから開発が報告されている[2]が，最近の円形配列方式の装置についてはまとまった報告はない．この方式の装置で，心電図同期ポジトロン CT が開発されなかったのは，心電波形に同期したデータ収集と検出器走査 (ウォブリングや POSITOLOGICA 方式) との干渉の結果，データサンプリングが空間的に一様とならず，大きな復元誤差 (障害陰影) が発生する恐れがあることも一因と考えられる．

われわれは，円形方式の装置である POSITOLOGICA II[3] を用いて，心電図同期ポジトロン CT を行う方式を開発した．本報では，その概要と，特に加算パルス数を変えることにより復元誤差がどのように変化するかを実験的に検討したので，その結果を述べたい．

II. 心電図同期ポジトロン CT の原理と仕様

POSITOLOGICA II では，同時計数された検出器のアドレスはシノグラムの座標 (t, θ) に変換され，ヒストグラムモードでバッファメモリに書き込まれる．バッファメモリの大きさは 1 スライスあたり，256×256 ワードである．バッファメモリに書き込まれたデータは，スキャン終了後，ディスクに転送され画像再構成が行われる．

心電図同期ポジトロン CT では，Fig. 1 に示すように心電波形の R 波を基準として，一定時間おくれた時相で一定の時間幅のデータのみを収集

---

* 放射線医学総合研究所臨床研究部
** 千葉大学医学部第三内科学教室
*** ㈱日立メディコ

受付：62 年 11 月 24 日
最終稿受付：63 年 1 月 11 日

別刷請求先：千葉市穴川 4–9–1　(〒 260)
放射線医学総合研究所臨床研究部
遠　藤　真　広

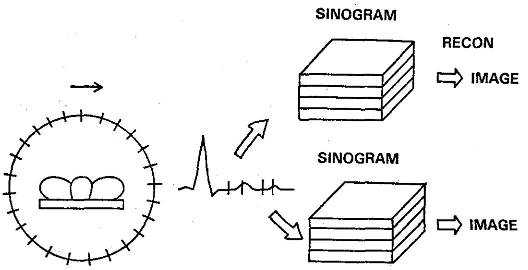

Fig. 1 Principle of ECG gated positron emission tomography. Coincidence events at two cardiac phases are collected during predetermined cardiac cycles and then reconstructed.

Table 1 Specifications of ECG gated positron emission tomography with POSITOLOGICA II

Number of cardiac phases	2
Data format ($t\times\theta$)	128×128/256×128
Number of cardiac cycles	1–9999
Delay time	0–999 msec
Sampling time	10–999 msec

しメモリに書き込み，これを指定された心拍数だけ繰り返す．スキャン終了後のデータ処理は，非同期の場合と同様に行う．同時に収集される時相の数は，メモリの読み出し時の性能により制限され，最大2である．したがって，例えば拡張末期，収縮末期の同時収集が可能である．収集データのマトリックス・サイズは$t\times\theta=128\times128$，または256×128が選択できる．Table 1に本方式の主な仕様を示す．

III. 性能評価の方法

本報の方式による心電図同期ポジトロンCTの性能を評価するため，以下の試験を行った．

1. 固定線源の撮像

POSITOLOGICA方式では検出器群の1回転(2 sec)により完全なデータが収集される．本方式のように心電波形に同期したデータ収集を行う場合，1心拍では一部を収集するだけである．したがって，加算する心拍数が少ない場合，収集データのサンプリングが不均等となり，結果として復元誤差が生じる．しかし，加算心拍数が多くなれば，収集データのサンプリングは近似的に一様となり，実用上，問題がなくなることが予想される．

このことを調べるため，固定線源を用いて次のような実験を行った．

1) 長さ11.6 cm，幅2.8 cm，厚さ0.3 cmの線源(放射能300 μCi)をスキャナ中心軸と長軸を一致して置き，800 msecごとのパルスに同期させて撮像した．遅延時間は0 msec，サンプリング時間は100 msecで一定とし，加算パルス数を1, 2, 5, 10, 20, 100, 500, 1,000と変化させた．なお，同時に用いるパルスは，III. 2で述べる線源回転装置で発生するものを用いた．

2) 1)と同一の線源を用い，パルスに非同期で通常の撮像を行った．撮像時間は2, 4, 6, 10, 20, 50, 100および1,000 secである．

3) 1)と同一形状で放射能が約1/20の線源を用い，パルスに非同期で通常の撮像を行った．撮像時間は2)と同様であった．

1)～3)を通じ，データ収集のマトリックスは256×128, 128×128の両方で行い，256×128は256×256(画素寸法1.2 mm)，128×128は128×128(画素寸法2.4 mm)の画像へ復元した．吸収補正は行わず，補正関数はShepp & Loganを用いた．この条件で復元像の空間分解能はそれぞれFWHM=10 mm, 11 mmであった．

1,000 sec非同期で得られた復元像を正しい画像と考え，次のようにして，他の画像のこの画像からの誤差を評価した．(なお，画像は全て，第3スライスのものを用いた．)

4) 線源の像に一致して12.0×28.8 mm²のROIを設定して，その内部のPET値を求めx_i ($i=1\sim n$)とする．実験1), 2)については同一のROIを用いることとし，実験2) 1,000 secの画像(これを0画像と呼ぶ)の画素値をx_{i0}とし

$$\mathrm{sd}\ 1=\sqrt{\frac{1}{n}\sum_{i=1}^{n}\left(\frac{N_{T0}}{N_T}x_i-x_{i0}\right)^2} \qquad (1)$$

を計算する．ここで，N_T, N_{T0}はそれぞれx_i, x_{i0}の画像を作る際のカウント数である．sd 1は，線源像内部の復元誤差を0画像の単位でみたものと考えられる．実験3)についても，同様の計算に

より誤差を求め，0画像と同じ単位にそろえる．

5) 線源像から10 cm下方に$4.8\times4.8\ \mathrm{cm}^2$のROIを設定し，その内部のPET値の標準偏差を求めsdとする．これは線源像外部の復元誤差を示すと考えられるので，

$$\mathrm{sd}\,2=\frac{N_{T0}}{N_T}\mathrm{sd} \qquad (2)$$

により，4)と単位をそろえる．実際には，sd 1, sd 2とも0画像のピーク値で除し，相対誤差で表すことにする．

2. 回転線源の撮像

パルスに同期したデータ収集が確実に行われているのを確かめるため，回転線源のパルス同期撮像を行った．線源回転装置はモータによるアルミ円板を回転させるもので，アルミ円板の外周部に体軸と平行に棒線源を固定する．回転装置の回転周期は500～2,000 msec可変であり，1回転ごとに同期パルスを出力する．また，線源の回転半径は10 cmである．

この装置に長さ2 cm, 直径3 mmの短棒状線源を装着し，第3スライスと線源の位置を一致させて，撮像を行った．線源の回転周期は800 msec, サンプリング時間は10 msec (最短のもの) を用い，データ収集を128×128のマトリックスで行い，500パルス分加算した．遅延期間を，0, 100, 200, 300, 400, 500, 600, 700 msecと変化させて，線源像が円周上の所定の位置にくるかを調べた．なお，画像復元のマトリックスは128×128 (画素寸法2.4 mm) とし，Shepp & Loganの補正関数を用いた．

3. 正常例の撮像

実際に臨床例の撮像が可能なことを次の実験により調べた．心電計は日本光電製ライフスコープ6を用い，心電図同期出力端子からすでに整形されたR波パルスを引き出し，これを同期信号として用いた．正常例に，N-13アンモニア約10 mCiを上腕静脈に投与してから，約15分後にデータ収集を開始した．拡張末期と収縮末期の2つの時相の撮像を行うため，遅延時間をそれぞれ，0, 250 msecに設定した．(このときの平均心拍数は毎分65である.) サンプリング時間は両時相とも50 msec, 加算心拍数は600とした．サンプリング時間は収縮末期像の動きを止めるため，また加算心拍数は画像ノイズとの兼ね合いで決められた．

データ収集のマトリックスは128×128, 画像マトリックスは128×128 (画素寸法2.4 mm) であった．補正関数はShepp & Loganをガウシアンで平滑化したものを用いた．この条件での復元像の空間分解能はFWHM＝13 mmである．心電図同期画像をその直後に撮像された非同期画像と比較した．

IV. 結　果

Figure 2 a, bは固定線源を撮像して，加算パルス数により復元誤差sd 1, sd 2がどのように変化するかを示したものである．図a, bとも×印はパルス同期画像 (サンプリング時間100 msec) から得られたものであり，横軸は加算パルス数および対応するスライスあたりの収集計数を示し，縦軸は0画像のピーク値で除した相対的な復元誤差を示す．

図の●印は弱線源，○印は強線源のパルス非同期画像から得られた同様な関係であり，これらの場合は，横軸として意味を持つのはスライスあたりの計数だけである．なお，強線源は方法の項で述べたとおり，パルス同期撮像に用いた線源と同じものであり，弱線源はそれと同一形状で強度が約1/20のものである．弱線源は20パルス以下のパルス同期画像と計数の等しい非同期画像を作るために用いられた．

Figure 2より非同期画像の復元誤差は全ての場合について，傾き－1/2の直線 (実線) に乗ってくることがわかる．これらの復元誤差の比については，図a, bとも線源像内の復元誤差sd 1は，線源像外の復元誤差sd 2の約4倍である．また，図bの復元誤差はsd 1, sd 2とも図aの約3倍であることもわかる．

一方，同期画像については，図a, bともsd 2は非同期画像と同じ傾き－1/2の直線 (実線) に乗る．sd 1は両図とも加算パルス数の小さいとこ

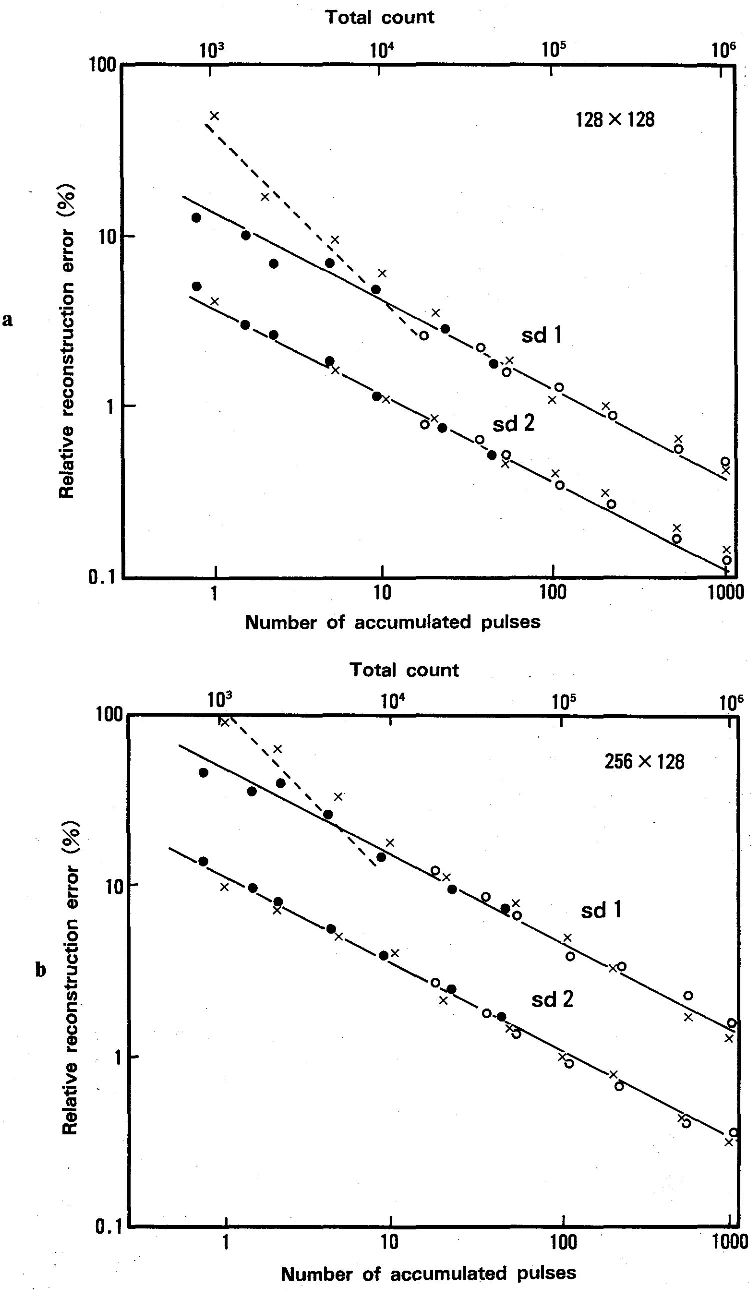

Fig. 2 Relationships between number of accumulated pulses (or total count) and relative reconstruction error. a) 128 × 128, b) 256 × 128 data collection. sd 1 and sd 2 indicate errors within the source image and out of it, respectively. Filled (●) and open (○) circles show errors calculated from the images of weak and strong radiation source taken without gating, respectively, while cross marks (×) show errors calculated from the images of strong source taken with gating. The solid lines, whose gradients are $-1/2$, correspond to statistical noise, while the broken lines errors due to non-uniform sampling caused by gated data acquisition.

ろでは傾き −1/2 の直線より上にあるが，加算パルス数を大きくしていくと，非同期画像と同じ直線に乗ってくる．図の破線は，同期画像の復元誤差より非同期画像の復元誤差の寄与を差し引いたもので，データサンプリングの不均一によるものと考えられるが，その詳細は考察において述べる．

次に Fig. 3 に回転線源を用いた実験の結果を示す．図は遅延時間を変化させて撮像した回転線源の画像を加算し，一つの画像として表したものである．線源像の横の数字はその画像を得るために用いた遅延時間 (msec) である．この図から，線源像は円周上に等間隔に配置され，パルスに同期したデータ収集が設定どおり確実に行われていることがわかる．

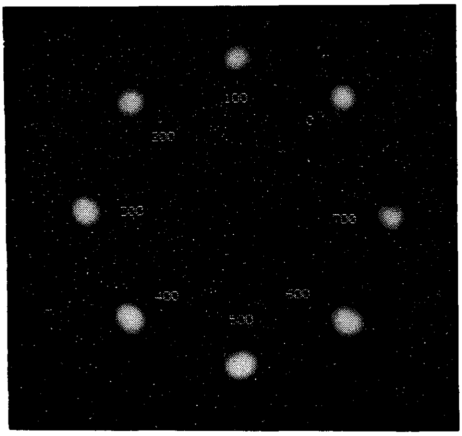

Fig. 3 Images of a rotating point source taken with varied delay time. The numbers next to the images show the delay time, while data sampling time was kept 10 msec for all images.

Figure 4 は正常例を撮像した結果を示している．図 a, b, c はそれぞれ拡張末期，収縮末期，非同期の画像である．これらの図から心筋の壁運動や壁厚の変化を検出することは容易である．

V. 考　察

本報では円形方式の装置である POSITOLOGICA II による心電図同期ポジトロン CT の基礎的特性を検討した．特に，データサンプリングの不均一性にもとづく復元誤差が加算パルス数によりどのように変化するかを調べた．この結果は Fig. 2 a, b にまとめられている．

Figure 2 a, b における非同期画像の復元誤差 (●印と○印) は，次のような考察から，sd 1, sd 2 とも検出光子数の統計的変動によるものと推定される．すなわち，第一にこれらの誤差は図で傾き −1/2 の直線に乗り，復元誤差は収集計数の平方根に逆比例することがわかる．

第二に図 a と図 b を比較すると，256×128 の復元誤差は 128×128 の復元誤差の約 3 倍である．エミッション CT の統計ノイズはサンプリング間隔の 3/2 乗に比例する[4]ので，全て統計ノイズを考えたときの理論値 $2\sqrt{2}\approx 2.8$ とほぼ一致する．第三に，sd 1 と sd 2 の比が約 4 になる点は次の

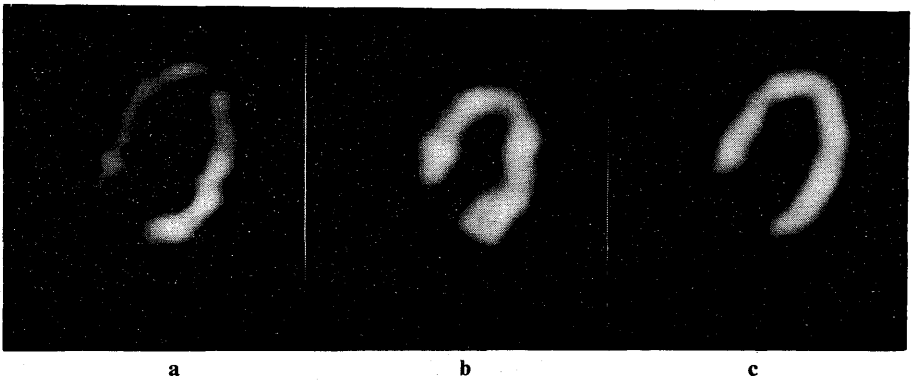

Fig. 4 Gated myocardial images of a normal case after intravenous injection of N-13 ammonia. a) end-diastolic, b) end-systolic and c) non-gated images. Left ventricular wall motion and changes of wall thickness are readily apparent.

ように説明できる．すなわち，Tanakaらによると統計ノイズの分散の空間的分布は，投影データをそのまま逆投影したもので近似できる$^{5)}$．この場合，線源像内部の分散にはシノグラム上の線源の軌跡全てが寄与するのに対し，線源像外部の分散にはその一部が寄与するだけである．後者の寄与の割合を外側のROIの中心から線源を見込みで角2.8/12.4 radとπ rad (＝180°) の比で近似するならば，分散の比は $(12.4\times\pi)/2.8\approx 14$ となり，したがって $\mathrm{sd}\,1/\mathrm{sd}\,2=\sqrt{14}\approx 3.7$. これは実験値とほぼ一致する．

次に，Fig. 2の同期画像の復元誤差 (×印) について考えてみる．まず，sd 2は非同期の場合と一致するので，同期画像についても線源像外部の復元誤差は統計ノイズによるものと推定できる．しかし，sd 1については，加算パルス数の小さいとき，同期画像の値は非同期の場合よりも大きくなり，統計ノイズ以外の要因が関与していることがわかる．この誤差は加算パルス数が小さくなるとき，急に大きくなることから，データサンプリングの不均一性によるものと考えられる．

今，統計ノイズとデータサンプリングの不均一性による復元誤差が独立なものとして，同期画像の復元誤差sd 1から統計ノイズ (非同期画像の誤差sd 1) の寄与を差し引く．Fig. 2 a, bの破線はこのようにして求めたものであり，データサンプリングの不均一性による復元誤差を表すものと考えられる．Fig. 2から破線の傾きは約 −1，また図bの方が図aより約2倍大きいことがわかる．

Figure 2にて上の実線と破線が交わる点は，二つの復元誤差の寄与が等しくなる加算パルス数と考えられるが，この値は図aでは約5パルス，図bでは10パルスである．これは回転数に換算するとそれぞれ0.25, 0.5に相当する．したがって，データサンプリングの不均一性にもとづく復元誤差 (障害陰影) は，加算パルス数の非常に小さい範囲では支配的であるが，1回転にも満たない相当に小さい加算パルス数で統計ノイズ以下となり，その影響は加算パルス数を増加させると急激に小さくなることがわかる．

Figure 2の破線と実線の交点の位置は，統計ノイズの大きさ，したがって線源の強度にもよると考えられる．本報で用いた線源強度は300 μCiであり，これを空間分解能を考慮した放射濃度に換算すると，

$$300\div(1.1\times 2.8\times 11.6)=8.4\ \mu\mathrm{Ci/cm}^3$$

となるが，通常，臨床で扱う放射能濃度はこれよりも低い．例えば，われわれが行っているうちでは，N-13アンモニアのダイナミック・スタディ$^{6)}$が最大の放射能濃度を与えるが，この場合の右心腔の最大放射能濃度が上記の値と同じ程度である．統計ノイズが大きくなると，Fig. 2の交点は左にシフトし，データサンプリングの不均一性にもとづく誤差の寄与は小さくなる．

Figure 4の心筋像の場合の放射能濃度は，上記の値の1/10程度と推定され，また600心拍 (15回転に相当) の加算を行っている．このような条件でデータサンプリングの不均一性は全く画像に影響を与えない．これは以上の考察からもまた画像上からも明らかである．心電図同期でスタティックな画像を得る場合，Fig. 4の撮像に用いたものと同じ位の条件を用いるので，データサンプリングの不均一性は全く画像に影響を与えないことが結論される．Fig. 4の画像からは心筋の壁運動や壁厚の変化が検出されるが，その臨床応用については別に報告する予定である．

心電図同期データ収集の目的の一つは，定量性を向上するため，心電波形に同期したダイナミック・スタディを行うことと考えられる．ある時相のデータのみを収集してダイナミック画像を構成すれば，心臓の動きの影響を考えずに，放射能の混じりの補正を行える．今回，開発したシステムには，そのような心電図同期ダイナミック・スタディの機能はない．しかし，本報の結果から，その場合に生じるデータサンプリングの不均一性にもとづく誤差の大きさを見つもることができる．例えば，われわれの行っている6 secごとのデータ収集で拡張期を中心としてその半分の3 sec (1.5回転) 程度集めれば，本報の考察によれば，デー

タサンプリングの不均一性は統計精度にくらべて十分小さくできる．今後はこのような開発も考えていきたい．また，本報で述べたことは POSITOLOGICA 方式のみならずウォブリング方式の装置に対しても基本的には成立するものと考えられる．

謝辞　稿を終えるにあたり貴重なご助言をいただいた放射線医学総合研究所物理研究部長田中栄一博士，同物理第一研究室長野原功全博士および同臨床研究部主任研究官福田寛博士に深く感謝いたします．本研究は同研究所の特別研究「重粒子線等の医学利用」(班長恒元博病院部長) の一部として行われました．特別研究関係者のご協力に感謝いたします．

文　献

1) Henze E, Huang SC, Ratib O, et al: Measurement of regional tissue and blood-pool radiotracer concentrations from serial tomographic images of the heart. J Nucl Med **24**: 987–996, 1983
2) Hoffman EJ, Phelps ME, Wisenberg G, et al: Electrocardiographic gating in positron emission computed tomography. J Comput Assist Tomog **3**: 733–739, 1979
3) Takami K, Ueda K, Tanaka E, et al: Performance of whole-body, multislice positron computed tomography—Positologica II—. IEEE Trans Nucl Sci **30**: 734–738, 1983
4) Brooks RA, DiChiro G: Principles of computer assisted tomography (CAT) in radiographic and radioisotope imaging. Phys Med Biol **21**: 689–732, 1976
5) Tanaka E, Murayama H: Properties of statistical noise in positron emission tomography. Proc International Workshop on Physics and Engineering in Medical Imaging, pp. 158–164, 1982
6) Yoshida K, Himi T, Shukuya M, et al: Fast dynamic study in cardiac positron CT using N-13-ammonia in man. Eur J Nucl Med **12**: 226–230, 1986

Summary

Electrocardiographic Gated Positron Emission Tomography with POSITOLOGICA II —Relationship between Accumulated Pulses and Reconstruction Errors—

Masahiro ENDO*, Toru MATSUMOTO*, Toshiharu HIMI**, Takeshi A. IINUMA*,
Toshiro YAMASAKI*, Yukio TATENO*, Katsuya YOSHIDA**,
Akihiko KAGAYA**, Yoshiaki MASUDA**, Yoshiaki INAGAKI**,
Akira OGUSHI*** and Sinichi INOUE***

**Division of Clinical Research, National Institute of Radiological Sciences*
***Third Department of Internal Medicine, Chiba University School of Medicine*
****Hitachi Medical Corporation*

Electrocardiographic (ECG) synchronized multiple gated data acquisition was employed with POSITOLOGICA II, a whole body positron emission tomograph to avoid blurring of cardiac image due to heart motion. Coincidence events at two cardiac phases (end-systole and end-diastole for example) are collected during predetermined cardiac cycles and then reconstructed. Delay time from triggering R-pulse can be varied 0–999 msec and data sampling time can be varied 10–999 msec. Fixed radiation sources were imaged with and without gating, and reconstruction errors of the both images were compared to evaluate the magnitude of errors due to non-uniform sampling caused by the gated data acquisition. The result was that although the reconstruction errors due to non-uniform sampling were dominant at very small numbers of accumulated pulses, they rapidly decreased with the increased number of pulses and became negligible to statistical noises at clinical conditions. Gated cardiac images of a normal case was taken after intravenous injection of N-13 ammonia solution. Left ventricular wall motion and changes of wall thickness were readily apparent in the gated images.

Key words: Positron emission tomography, Electrocardiographic gating, Reconstruction error.

Kinetics of [^{11}C]N,N-Dimethylphenylethylamine in Mice and Humans: Potential for Measurement of Brain MAO-B Activity

Hitoshi Shinotoh, Osamu Inoue, Kazutoshi Suzuki, Toshiro Yamasaki,
Masaomi Iyo, Kenji Hashimoto, Toshiyoshi Tominaga, Takashi Itoh, Yukio Tateno,
and Hiroo Ikehira

Division of Clinical Research, National Institute of Radiological Sciences, Section of Cyclotron, National Institute of Radiological Sciences, Japan

Carbon-11-labeled N,N-dimethylphenylethylamine ([^{11}C]DMPEA) was synthesized by the reaction of N-methylphenylethylamine with [^{11}C]methyl iodide. This newly synthesized radiotracer was developed for the purpose of in vivo measurement of monoamine oxidase-B activity in the brain using a metabolic trapping method. Initially, biodistribution was investigated in mice. The rapid and high uptake of ^{11}C radioactivity in the brain was observed following intravenous injection of [^{11}C]DMPEA, the peak of which was reached at 1 min, followed by a decrease at 1–5 min and slowly thereafter. The kinetics of [^{11}C]DMPEA in the human brain were determined using positron emission tomography (PET) and showed that ^{11}C radioactivity increased gradually over 60 min following initial rapid uptake of ^{11}C radioactivity, with basal ganglia and thalamus showing high accumulation.

J Nucl Med 28:1006–1011, 1987

Monoamine oxidase (MAO) is widely distributed throughout the body and catalyzes the oxidative deamination of a variety of monoamines (*1*). MAO has been classified into two main types: MAO-A and MAO-B. MAO-A deaminates serotonin (5-HT) and noradrenaline (NA) much better than phenylethylamine (PEA) or benzylamine, and is preferentially inhibited by clorgyline, whereas, MAO-B prefers PEA and benzylamine as substrates and is preferentially inhibited by 1-deprenyl (*2–4*).

Alterations of MAO-B activity in the brain has been implicated in aging, Alzheimer's disease, Huntington's disease, alcoholism, suicides, and affective illness (*5–11*).

If it were possible to measure MAO-B activity in the human brain by positron emission tomography (PET), it would offer valuable information about human brain function and neurochemical abnormalities in some neuropsychiatric disorders.

Recently, several attempts have been made to develop new tracers for in vivo estimation of brain MAO activity (*12–16*). One of our group (I.O.) developed labeled phenylethylamine derivatives as tracers for the study of the brain MAO activity using a metabolic trapping method (*14–16*). N-(methyl-^{14}C)N,N-dimethylphenylethylamine ([^{14}C]DMPEA) was found to be the most promising among them because of its high selectivity for MAO-B, its high brain uptake and its wide range of measurable brain MAO-B activity (*16*).

Kinetics of [^{14}C]DMPEA in mice have been reported as follows (*16*) (Fig. 1): [^{14}C]DMPEA enters the mouse brain rapidly following intravenous injection by first pass uptake because of its lipophilicity. A part of [^{14}C]DMPEA in the brain is deaminated selectively by the brain MAO-B. Its metabolite, ^{14}C-labeled dimethylamine, is trapped in the brain because its pKa value is very high (10.64) (*17*) and protonated dimethylamine cannot pass through the biologic membranes, including the blood–brain barrier. On the other hand, unmetabolized [^{14}C]DMPEA is eliminated from the brain rap-

---

Received Apr. 25, 1986; revision accepted Nov. 3, 1986.

For reprints contact: Hitoshi Shinotoh, MD, Div. of Clinical Research, National Institute of Radiological Sciences, 9-1 Anagawa-4-chome, Chiba-shi, CHIBA 260, Japan.

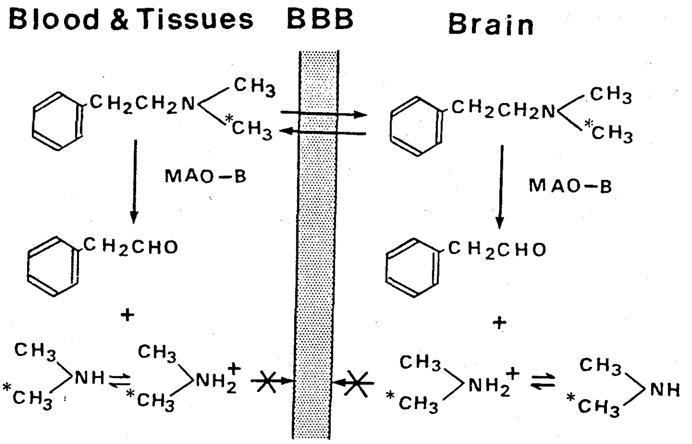

FIGURE 1
Proposed mechanism of metabolic trapping of labeled DMPEA in the brain. *: ^{14}C- or ^{11}C-labeled position. BBB: blood–brain barrier.

idly. Therefore, only [^{14}C]dimethylamine remains in the brain 60 min after injection. An inhibition experiment with l-deprenyl revealed that the initial uptake of [^{14}C] DMPEA was not altered but the clearance of ^{14}C radioactivity in the brain became faster as the dose of l-deprenyl pretreated was increased. [^{14}C]dimethylamine production in the mouse brain at 60 min after injection correlated well with remaining MAO-B activity after pretreatment with various doses of l-deprenyl.

These results indicate that relative MAO-B activity in the human brain could be measured by PET using ^{11}C-labeled DMPEA instead of [^{14}C]DMPEA.

In this report, we describe synthesis of [^{11}C]DMPEA, biodistribution of ^{11}C radioactivity, effects of MAO inhibitors on kinetics of ^{11}C radioactivity in mice following injection of [^{11}C]DMPEA, and kinetics of ^{11}C radioactivity in the human brain following injection of [^{11}C]DMPEA.

MATERIALS AND METHODS

Synthesis of [^{11}C]DMPEA

Carbon-11 was produced with 18 MeV protons from the NIRS cyclotron[*] by the ^{14}N (p, α)^{11}C reaction. The ^{11}C generated was converted to [^{11}C]CO$_2$ by passage through a CuO column at 800°C. Carbon-11 labeled methyl iodide was prepared from [^{11}C]CO$_2$ by reduction with LiAlH$_4$ and distillation of [^{11}C]methanol in a flow of nitrogen through refluxing concentrated hydroiodic acid. A mixture of 10–50 μl N-methylphenylethylamine,[†] [^{11}C]methyl iodide, and 5–20 μl 10 M NaOH in 0.5–1 ml of acetone was heated for 5 min at 70°C. The [^{11}C]DMPEA produced was purified by high-performance liquid chromatography with chloroform/methanol/ammonia (1500:50:1) as a solvent on a silica gel column (7.2 mm ϕ × 250 mm)[‡] at a flow rate of 5 ml/min. The retention time of the product and the substrate were 4 and 10 min, respectively. The fraction containing [^{11}C]DMPEA was collected and evaporated. The residue was dissolved in 10 ml of saline and passed through a sterile Millipore filter (0.22 μm). The time of preparation was ~35 min from the end of bombardment. The yield of [^{11}C]DMPEA for intravenous injection varied between 13 and 90 mCi, the radiochemical yield was ~20%, and the radiochemical purity was >99%. The specific activity was >100 mCi/μmol estimated from the detection limit of an ultraviolet detector. The product was sterile and pyrogen free.

Biodistribution in Mice

Male C3H mice (12 wk old) weighing 33 g were used. Mice were injected via the tail vein with no-carrier-added [^{11}C] DMPEA (50 μCi/0.2 ml, <2.3 μg/kg). Mice were killed 1, 5, 15, 30, and 60 min following injection. Tissues were removed, washed with saline, and weighed. The radioactivity was measured with a sodium-iodide scintillation counter. The uptake was expressed as percentage dose administered per gram organ.

Effect of MAO Inhibitors

Male C3H mice (12 wk old) were pretreated with various doses (0, 0.01, 0.1, 10 mg/kg, i.v.) of l-deprenyl[§] and a single dose of 10 mg/kg of clorgyline[¶] 60 min before injection of [^{11}C]DMPEA. Mice were killed 60 min after injection of [^{11}C] DMPEA and the radioactivity of the brain was measured as described above.

Experiments with [^{11}C]DMPEA in Human Subjects

Four male volunteers, varying in age from 48 to 70 yr took part in the study. These subjects were healthy at the time of physical and laboratory examination. Informed written consent was obtained from the subjects.

A three-ring PET system ("Positologia II") (*18*) was used to obtain quantitative data on the regional radioactivity within a section of the brain. The spatial resolution of the reconstructed images is 9.2 mm full width at half maximum (FWHM). The slice thickness is 10 mm (FWHM) for cross slices and 13 mm (FWHM) for direct slices.

Each subject lay supine with his head positioned in the PET scanner, so that the lowest slice corresponded to 10 mm above the canthomeatal line. A venous cannula was inserted into an antecubital vein for isotope injection. A dose of 9.1 ± 2.9 mCi (mean ± s.d. <18 μg) of no-carrier-added [^{11}C]DMPEA was administered over a period of 10 sec.

Serial PET images (each scan took 1–2 min) were obtained

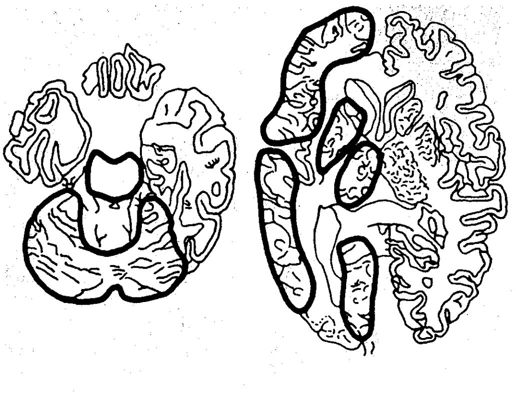

CML+10 **CML+46**

FIGURE 2
Regions of interest in the brain. ROI in the cerebrum were drawn in the left hemisphere.

for 30–60 min immediately following injection. Simultaneous venous blood samples were obtained at 1–10 min intervals during a period of 30–60 min, and the radioactivity in 1 ml of blood was measured with a sodium-iodide scintillation counter.

Regions of interest were the frontal cortex, temporal cortex, occipital cortex, basal ganglia (which included the caudate, putamen, and pallidum), thalamus, cerebellum, and brain stem (Fig. 2). Regional activity was measured for each sequential scan, corrected for ^{11}C decay, and plotted on a time basis. Partial volume effects were not corrected in this study. Regional activity and blood activity was expressed as percent injected dose per ml.

RESULTS

Biodistribution in Mice

Table 1 shows the biodistribution in mice. [^{11}C]DMPEA was well transported into many organs and was cleared rapidly from the blood. The highest uptake was observed in the kidney. A slightly lower uptake was observed in the brain and the lung. In the brain, the uptake of ^{11}C radioactivity reached its peak 1 min after injection, the clearance was rapid at 1–5 min and slow thereafter until the end of experiment. The activity in the blood decreased rapidly and reached a much lower level than that in the brain.

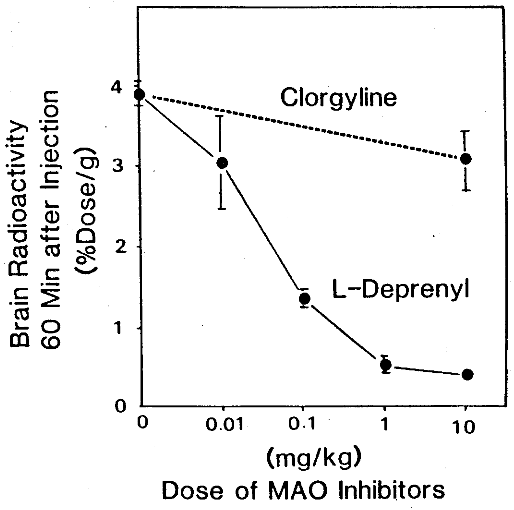

FIGURE 3
Effect of MAO inhibitors to the kinetics of [^{11}C]DMPEA in the mouse brain. The brain radioactivity 60 min after injection was expressed as percent dose administered per gram (mean ± s.d. of three mice).

Effects of MAO Inhibitors

The radioactivity in the brain 60 min after injection decreased in a dose-dependent mode with pretreatment of various doses of l-deprenyl, whereas, the radioactivity in the blood was not altered significantly. The blood radioactivity 60 min after injection with pretreatment of 10 mg/kg of l-deprenyl was 0.4 ± 0.4 %dose/g (mean ± s.d. of three mice); whereas, that of control mice was

TABLE 1
Tissue Distribution of Radioactivity in Mice After Intravenous Injection of [^{11}C]DMPEA

Tissue	1 min	5 min	15 min	30 min	60 min
Brain	7.9 ± 0.4	5.1 ± 1.0	3.9 ± 0.4	3.5 ± 0.1	2.8 ± 0.3
Heart	5.4 ± 0.3	2.9 ± 0.3	1.5 ± 0.1	0.8 ± 0.1	0.4 ± 0.1
Lung	7.9 ± 0.6	4.3 ± 0.5	2.0 ± 0.1	1.3 ± 0.0	0.7 ± 0.2
Liver	3.2 ± 0.9	4.2 ± 0.7	2.1 ± 0.1	1.4 ± 0.1	0.8 ± 0.1
Spleen	2.1 ± 0.6	3.9 ± 0.7	3.9 ± 0.3	2.5 ± 0.1	1.4 ± 0.4
Kidney	11.3 ± 1.7	12.0 ± 2.1	9.4 ± 1.5	5.7 ± 0.1	4.0 ± 1.0
Small intestine	4.8 ± 1.0	4.5 ± 0.3	2.1 ± 0.1	1.5 ± 0.4	0.9 ± 0.1
Testis	1.5 ± 0.2	1.9 ± 0.5	1.7 ± 0.2	1.3 ± 0.1	1.0 ± 0.1
Muscle	3.7 ± 0.7	2.3 ± 0.2	1.7 ± 0.3	0.9 ± 0.1	0.4 ± 0.1
Blood	2.3 ± 0.3	1.9 ± 0.1	1.0 ± 0.1	0.5 ± 0.1	0.2 ± 0.1

Mean uptake ± s.d. (% dose/g) of three mice.

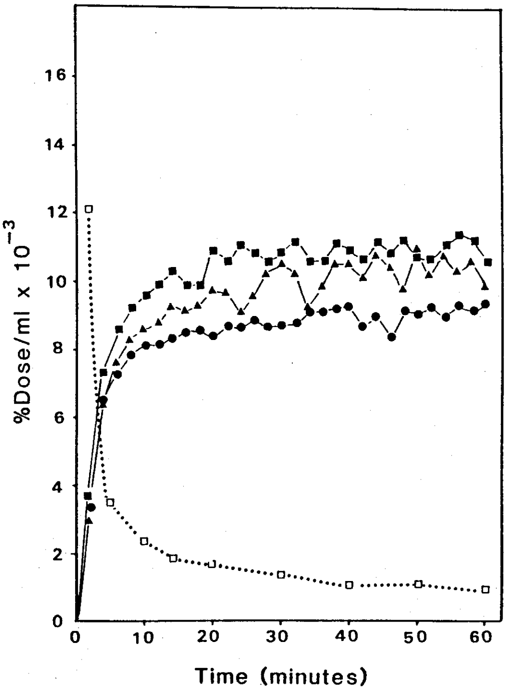

FIGURE 4
Kinetics of ^{11}C radioactivity in the human brain after intravenous injection of [^{11}C]DMPEA.

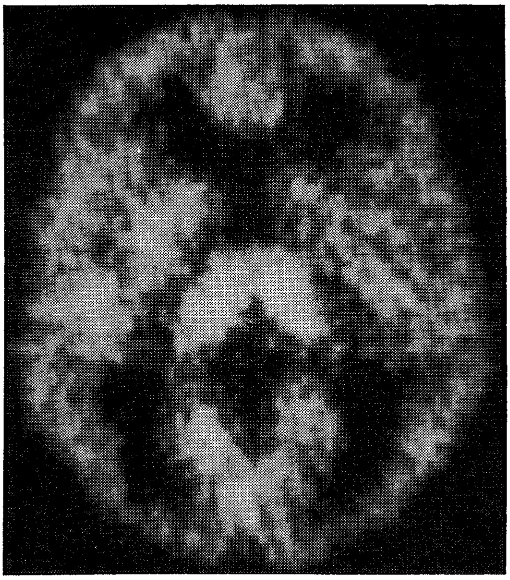

FIGURE 5
PET image of a volunteer at 3–30 min after intravenous injection of [^{11}C]DMPEA. This image was obtained at a level of 46 mm above the canthomeatal line.

0.2 ± 0.1 %dose/g. Pretreatment with clorgyline did not lower the radioactivity level significantly in the brain 60 min after injection (Fig. 3). These results indicate that [^{11}C]DMPEA is metabolized selectively by MAO-B and the radioactivity in the mouse brain 60 min after injection correlates well with MAO-B activity in the brain.

Kinetics in Humans

The accumulation of ^{11}C radioactivity in the brain was high and rapid within 4–6 min of intravenously injected [^{11}C]DMPEA and then increased gradually until the end of the experiment (Fig. 4). A high accumulation of ^{11}C radioactivity was observed in the thalamus, basal ganglia, cerebral cortex, and cerebellum (Fig. 5, Table 2). A moderate concentration of ^{11}C radioactivity was seen in the brain stem. The radioactivity in the blood decreased rapidly and was much lower than that in the brain.

DISCUSSION

The kinetics of [^{11}C]DMPEA in the mouse brain was the same as that of [^{14}C]DMPEA, which had been previously reported (*16*). Initial rapid clearance of ^{11}C radioactivity in the brain reflects the elimination of

TABLE 2
Distribution of Radioactivity in the Human Brain After Intravenous Injection of [^{11}C]DMPEA

Brain region	0–2 min	5–6 min	9–10 min	29–30 min	59–60 min*
Frontal cortex	4.2 ± 2.7	8.9 ± 2.8	9.4 ± 2.8	9.9 ± 2.7	11.7 ± 3.2
Temporal cortex	4.5 ± 2.4	8.9 ± 2.4	9.5 ± 2.3	9.6 ± 2.4	11.2 ± 1.6
Occipital cortex	4.6 ± 2.4	9.3 ± 1.9	9.8 ± 2.4	10.3 ± 2.9	10.9 ± 0.8
Basal ganglia	4.5 ± 2.5	9.0 ± 2.1	10.1 ± 2.1	11.6 ± 2.6	11.8 ± 2.7
Thalamus	4.7 ± 1.9	9.9 ± 2.7	11.1 ± 3.1	11.8 ± 3.0	12.1 ± 2.1
Cerebellum	4.2 ± 2.0	8.4 ± 2.2	8.9 ± 2.4	9.2 ± 2.6	9.8 ± 1.0
Brain stem	3.1 ± 2.1	5.1 ± 2.9	5.7 ± 3.0	6.0 ± 3.0	7.8 ± 1.5
Blood	9.5 ± 2.8	3.3 ± 0.3	2.4 ± 0.2	1.5 ± 0.1	1.1 ± 0.1

Mean uptake ± s.d. (% dose/ml × 10^{-3}) of four subjects (*two subjects) unmetabolized [^{11}C]DMPEA and slow clearance of ^{11}C radioactivity at 15–60 min following injection reflects retention of ^{11}C-labeled dimethylamine in the brain. The dose dependent decrease of ^{11}C radioactivity at 60 min after pretreatment with various doses of l-deprenyl suggests that MAO-B activity in the animal brain and also the human brain could be estimated by external detection method using PET.

However, kinetics of ^{11}C radioactivity in the human brain following intravenous injection of [^{11}C]DMPEA indicate that most of [^{11}C]DMPEA that entered the brain was trapped. This was probably because MAO-B activity in the human brain was much higher than that in the mouse brain. Although, to the best of our knowledge, there has been no comparative study of brain MAO-B activity between mice and humans, the MAO-B activity in the human brain has been reported to be higher than that in the rat brain (*5–7,11,19–20*).

The PET images of the human subjects showed a slightly higher accumulation of ^{11}C radioactivity in the thalamus and basal ganglia, although the difference was not statistically significant. This distribution of ^{11}C radioactivity seems to be different from that of the perfusion tracers. Because it has been reported that the MAO-B activity in the autopsied human brain is higher in the thalamus and basal ganglia than in the cerebral cortex (*8,10*), the distribution of ^{11}C radioactivity following intravenous injection of [^{11}C]DMPEA might reflect the regional distribution of MAO-B activity in the human brain.

If the MAO-B activity in the human brain is considerably higher than in the mouse brain, it may be necessary to modify the tracer to be metabolized by the brain MAO-B more slowly for the purpose of detecting the alterations of MAO-B activity in the human brain.

It has been reported that a considerable reduction in deamination occurred when the deuterium substitution was in the alpha position of beta-phenylethylamine and some other trace amines (*21*). Recently, we investigated deuterium isotope effects of [^{11}C]N,N-dimethylphenylethylamine-α,α-d_2 in vivo (*22*). The study revealed that the production rate of labeled metabolite ([^{11}C]dimethylamine) in mice was reduced significantly by substitution of the α-hydrogen of [^{11}C]DMPEA with deuterium. Thus, [^{11}C]DMPEA-α,α-d_2 is a promising tracer for in vivo measurement of MAO-B activity in the human brain.

Another possible cause for the long retention of ^{11}C radioactivity in the human brain following intravenous injection of [^{11}C]DMPEA is that unmetabolized [^{11}C] DMPEA and/or labeled metabolites was eliminated much slower in the human brain than in the mouse brain. So-called nonspecific binding sites of amines (*23*) might retain [^{11}C]DMPEA and/or labeled metabolites in the human brain and there might be large interspecies differences of nonspecific binding sites of amines between mice and humans.

In conclusion, whether or not [^{11}C]DMPEA is a suitable tracer for probing MAO-B in the human brain must await further experiments to elucidate the factors responsible for the observed irreversible trapping of ^{11}C radioactivity within brain structures.

Amine metabolism is an important aspect of human brain function and MAO plays an essential role in controlling the levels of biogenic amines. We are continuing in our attempts to devise methods by which it will be possible to measure MAO activity in the human brain.

NOTES

[*] CGR-MeV 960, CGR, Paris, France.

[†] Aldrich Chemical Co., Milwaukee, WI.

[‡] Megapak SIL, JASCO, Tokyo, Japan.

[§] Kindly provided by Dr. J. Knoll, Department of Pharmacology, Semmelweis University of Medicine, Budapest, Hungary.

[¶] May and Baker Ltd., Dagenham, UK.

ACKNOWLEDGMENTS

This work was supported by special coordination funds for promoting science and technology in Japan.

The authors are grateful to Dr. Y. Yoshida and T. Irie for their useful advice, K. Tamate for technical assistance in the preparation of [^{11}C]DMPEA, and K. Yoshida and S. Himi for their technical assistance in the PET study.

REFERENCES

1. Murphy DL, Garrick NA, Aulakh CS, et al. New contribution from basic science to understanding the effects of monoamine oxidase inhibiting antidepressants. *J Clin Psychiat* 1984; 47:37–43.
2. Johnston JP: Some observations upon a new inhibitor of monoamine oxidase in brain tissue. *Biochem Pharmacol* 1968; 17:1285–1297.
3. Knoll J, Magyar K. Some puzzling pharmacological effects of monoamine oxidase inhibitors. *Adv Biochem Psychopharmacol* 1972; 5:393–408.
4. Houslay MD, Tipton KF. Multiple forms of monoamine oxidase: Fact and artefact. *Life Sci* 1976; 19:467–478.
5. Shih JC. Monoamine oxidase in aging human brain. In: Singer TP, Von Korff RW, Murphy DL, eds. Monoamine oxidase; Structure, function, and altered functions. New York: Academic Press, 1979:413–421.
6. Oreland L, Fowler CJ. The activity of human brain and thrombocyte monoamine oxidase (MAO) in relation to various psychiatric disorders. II) The nature of the changed MAO activity. In: Singer TP, Von Korff RW, Murphy DL, eds. Monoamine oxidase; Structure, function, and altered functions. New York: Academic Press, 1979:389–396.
7. Fowler CJ, Wiberg A, Oreland L, et al. The effect of age on the activity and molecular properties of human

brain monoamine oxidase. *J Neural Transm* 1980; 49:1–20.

8. Eckert B, Gottfries CG, Von Knorring L, et al. Brain and platelet monoamine oxidase in mental disorders. 1. Schizophrenics and cycloid psychotics. *Prog Neuro-Psychopharmacol* 1980; 4:57–68.
9. Adolfsson R, Gottfries CG, Oreland L, et al. Increased activity of brain and platelet monoamine oxidase in dementia of Alzheimer type. *Life Sci* 1980; 27:1029–1034.
10. Oreland L, Arai Y, Stenström A, et al. Monoamine oxidase activity and localisation in the brain and the activity in relation to psychiatric disorders. *Mod Probl Pharmacopsychiat* 1983; 19:246–254.
11. Oreland L, Arai Y, Stenström A. Age, neuro-psychiatric diseases and brain monoamine oxidase. In: Tipton KF, Benedetti PD, Benedetti MS, eds. Monoamine oxidase and disease. London: Academic Press, 1984:291–297.
12. MacGregor RR, Halldin C, Fowler JS, et al. Selective, irreversible in vivo binding of [^{11}C]clorgyline and [^{11}C]-1-deprenyl in mice: potential for measurement of functional monoamine oxidase activity in brain imaging positron emission tomography. *Biochem Pharmacol* 1985; 34:3207–3210.
13. Ishiwata K, Ido T, Yanai K, et al. Biodistribution of a positron-emitting suicide inactivator of monoamine oxidase, carbon-11 pargyline, in mice and a rabbit. *J Nucl Med* 1985; 26:630–636.
14. Inoue O. A new metabolically trapped agent by brain monoamine oxidase: N-methyl labelled [^{14}C] N-methyl-phenylethylamine (^{14}C-MPEA). *Eur J Nucl Med* 1983; 8:385–388.
15. Inoue O, Tominaga T, Yamasaki T, et al. A new method for in vivo measurement of brain monoamine oxidase activity. *Prog Neuro-Psychopharmacol Biol Psychiat* 1984; 8:385–395.
16. Inoue O, Tominaga T, Yamasaki T, et al. Radioactive N,N-dimethylphenylethylamine: A selective radiotracer for in vivo measurement of monoamine oxidase-B activity in the brain. *J Neurochem* 1985; 44:210–216.
17. Hall HK. Correlation of the base strengths of amines. *J Am Chem Soc* 1957; 79:5441–5444.
18. Takami K, Ueda K, Okajima K, et al. Performance of whole-body, multislice positron computed tomograph—Positologica II—. *IEEE Trans Nucl Sci* 1983; 30:734–738.
19. Student AK, Edwards DJ. Subcellular localization of types A and B monoamine oxidase in rat brain. *Biochem Pharmacol* 1977; 26:2337–2342.
20. Benedetti MS, Kean PE. Differential changes in monoamine oxidase A and B activity in the aging rat brain. *J Neurochem* 1980; 35:1026–1032.
21. Yu PH, Barclay S, Davis B, et al. Deuterium isotope effects on the enzymatic oxidative deamination of trace amines. *Biochem Pharmacol* 1981; 30:3089–3094.
22. Hashimoto K, Inoue O, Suzuki K, et al. Deuterium isotope effect of [^{11}C]N,N-dimethylphenethyl-amine-α,α-d_2; Reduction in metabolic trapping rate in brain. *Int J Nucl Med Biol* 1986; 13:79–80.
23. Winchell HS, Baldwin RM, Lin TH. Development of I-123-labeled amines for brain studies: Localization of I-123 indophenylalkyl amines in rat brain. *J Nucl Med* 1980; 21:940–946.

Annals of Nuclear Medicine Vol. 1, No. 1, 1–6, 1987

Noninvasive quantification of regional myocardial blood flow and ammonia extraction fraction using Nitrogen-13 ammonia and positron emission tomography

Masahiro ENDO,* Katsuya YOSHIDA,** Takeshi A. IINUMA,* Toshiro YAMASAKI,*
Yukio TATENO,* Yoshiaki MASUDA** and Yoshiaki INAGAKI**

**National Institute of Radiological Sciences, Chiba, Japan*
***Chiba University School of Medicine, Chiba, Japan*

This report describes the theoretical basis and a method to quantitate regional myocardial blood flow (RMBF) and ammonia extraction fraction (E) in man, noninvasively, with N-13 ammonia and positron emission tomography (PET). Two patients with hypertrophic cardiomyopathy, whose left ventricular (LV) walls were markedly thick, were employed in this study to avoid partial volume effects and cross contamination between LV walls and blood pool. RMBF and E were calculated from time-activity curves of myocardial tissue and left atrium derived from serial 6-second PET images of the heart. The time-activity curve of left atrium was used as an arterial input function. The results were RMBF=67±4 ml/min/100 g, E=80±13% and 65±10 ml/min/100 g, 81±16% for each patient. The validity of the present method was discussed.

Key words: Dynamic positron emission tomography, Regional myocardial blood flow, N-13 ammonia, Hypertrophic cardiomyopathy

1. INTRODUCTION

NONINVASIVE QUANTIFICATION of regional myocardial blood flow (RMBF) is necessary to facilitate detection and evaluation of cardiac pathophysiology. In animal experiments the microsphere technique has been regarded as the "gold standard". However because of high invasiveness, it is not easily available for clinical use. A positron-emitting blood flow tracer, N-13 ammonia, exhibits properties which to some extent resemble those of the radioactive microsphere. Recently Shah et al[1] reported measurement of RMBF in dogs with N-13 ammonia and positron emission tomography (PET). Their method was much less invasive than the microsphere method, because it employed intravenous administration of N-13 ammonia and tissue radioactive concentration determined by PET scans. But it still needed withdrawal of arterial blood to calibrate arterial input function. The newer generation positron tomographs, with much higher temporal resolution, make it possible to determine the arterial input function directly from regions of interest assigned to the cardiac cavity, and thus make this approach largely noninvasive.

N-13 ammonia is extracted and fixed in myocardium in proportion to blood flow. However, a fraction of N-13 ammonia effectively retained in myocardium (net extraction fraction) is less than 100%, decreases with higher flows, and may be influenced by blood pH, disturbance of glutamine synthesis in myocardial cells, etc.[2,3] These findings need simultaneous determination of the RMBF and the extraction fraction of ammonia in myocardial tissue. The extraction fraction itself, if obtained, may provide an important physiologic and diagnostic indicator of the cellular viability in myocardium. Mullani et al[4] and Goldstein et al[5] suggested this possibility with rubidium extraction in dog.

It is the purpose of our study to develop a method of quantitating the RMBF and the extraction fraction

---

Received April 10, 1987; revision accepted June 8, 1987.
For reprints contact: Masahiro Endo, Division of Clinical Research, National Institute of Radiological Sciences, 9–1, 4-chome Anagawa, Chiba, 260 JAPAN.

of ammonia in man with time-activity curves of cardiac cavity and myocardium, determined by fast dynamic PET scans after intravenous injection of N-13 ammonia. To avoid partial volume effects and cross contaminations between left ventricular (LV) walls and blood pool in reconstructed images, patients with markedly thick LV walls were employed in the present study.

2. THEORY AND METHODS

2.1. Compartmental model

A model which characterizes physiologically correct processes of N-13 ammonia kinetics in myocardium seems to consist of at least three compartments, which are vascular, extravascular and cellular (metabolic) phases. But because of limited information obtained noninvasively by PET scans, analysis with the complicated models is difficult and it is necessary to employ an alternative simple functional model.

Schelbert et al[2] made intensive experimental studies on N-13 ammonia kinetics in canine myocardium and obtained conclusions as follows:

(1) N-13 ammonia freely crosses the capillary and is nearly 100% extracted during its initial capillary transit.

(2) The rate of metabolic fixation appears to be the rate-limiting step.

(3) N-13 ammonia is distributed in the extravascular space and back diffusion competes with metabolic trapping.

These findings suggest that the physiological complicated model can be simplified to a functional two-compartment model shown in Fig. 1, where the two compartments are free and trapped (metabolized) ammonia space. The present mokel is essentially the same as the one proposed by Mullani et al[4] on Rb-82 kinetics in myocardium. The release of ammonia metabolites from the trapped compartment can be neglected in the present study, because it is a very slow process (its half-time averaged 273 minutes at control flows[2]) and our observation time is only two minutes after injection of ammonia.

If amounts of N-13 ammonia in the free and trapped compartments for a unit volume of tissue are defined as $Q1$ and $Q2$ respectively, their relationships are given by,

$$\begin{aligned} dQ1/dt &= F\cdot Ca(t) - k\cdot Q1 - F\cdot Q1/Vd \\ dQ2/dt &= k\cdot Q1 \end{aligned} \qquad (1)$$

where we assume N-13 ammonia is 100% extracted during its initial capillary transit. k is a rate constant for the transport from the free to the trapped space. F is RMBF or perfusion and $Ca(t)$ is an input function, which is arterial activity concentration as a function of time. Vd is a distribution volume of N-13 ammonia in the free compartment, which is the volume of tissue space in which the tracer in the free compartment would have been distributed with the same concentration as in venous blood at equilibrium.

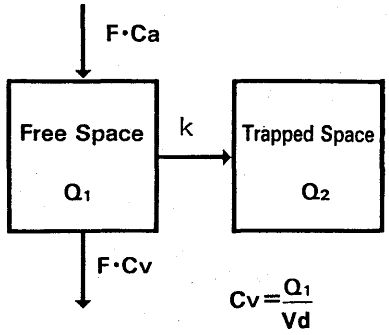

Fig. 1 Functional two-compartment model for N-13 ammonia kinetics in myocardium. F is regional myocardial blood flow (RMBF) or perfusion, $Ca(t)$ arterial concentration of N-13 ammonia, $Cv(t)$ venous concentration of N-13 ammonia. $Q1$ and $Q2$ are amounts of N-13 ammonia in the free and trapped compartments for a unit volume of tissue, respectively. $Cv(t)$ is approximated by $Q1/Vd$, where Vd is a distribution volume of N-13 ammonia in the free compartment.

A time-activity curve of myocardium is given by,

$$Q(t) = (1-fa)(Q1(t)+Q2(t)) + fa\cdot Ca(t) \qquad (2)$$

where fa is a fractional volume of arteries in the region of interest. From the solutions of eq. (1), $Q(t)$ can be expressed as,

$$Q(t) = (1-fa)(Ae^{-\alpha t}+B)\otimes Ca(t) + fa\cdot Ca(t) \qquad (3)$$

where,

$$\begin{aligned} A &= F\frac{F/Vd}{k+F/Vd} \\ B &= F\frac{F/Vd}{k+F/Vd} \\ \alpha &= k+F/p \end{aligned} \qquad (4)$$

and $\otimes$ denotes a convolution operation. From the eq. (4), RMBF is given by,

$$F = A+B \qquad (5)$$

Net extraction fraction of ammonia (E) is a ratio of myocardial uptake to the product of RMBF and the integral of input function. The myocardial uptake is

$$Q2(\infty) = \frac{kF}{k+F/Vd}\int_0^\infty Ca(t)dt \qquad (6)$$

Therefore the net extraction fraction is given by,

$$E = Q2(\infty)/F\int_0^\infty Ca(t)\,dt = F/(k+Vd) = B/(A+B) \qquad (7)$$

For simplicity the term "extraction fraction" is used instead of "net extraction fraction" in the rest of this paper.

2.2 Methods

N-13 was produced in the National Institute of Radiological Sciences medical cyclotron by the bombardment of pure water with proton beams by the $^{16}O(p,\alpha)^{13}N$ reaction. The product was reduced to ammonia and collected in physiological saline. Radiochemical purity of N-13 ammonia was greater than 99.5%.

Tomography was performed with POSITOLOGICA-II[6], which permitted serial acquisition of data in 6-second intervals and provided five transaxial sections simultaneously. Midpoints of the sections are separated by 18mm. Sensitivities for a 20 cm diameter phantom are 22.5 and 33.6 kcps/μCi/m*l* for in-plane and cross-plane, respectively.

About 10 mCi N-13 ammonia was injected intravenously as a bolus from the antecubital vein. Serial PET imaging was initiated at the time of tracer injection, and twenty 6-second PET scans were performed without gating of cardiac cycle. 44 to 180 k counts were obtained per slice. Tomographic data were collected and reconstructed in 128 × 128 matrix.

In the present study, the spatial resolution for reconstructed image was 13 mm FWHM at the center, and slice thicknesses were 13 mm and 10 mm for in-plane and cross-plane, respectively. To avoid partial volume effects and cross contaminations between left ventricular (LV) walls and blood pool, two patients with hypertrophic cardiomyopathy (HCM), whose LV wall thicknesses were more than twice the FWHM, were employed.

A time-activity curve of the myocardial tissue $Q(t)$ was determined by assigning a region of interest (ROI) over the myocardium. The number of slices was three for each patient, and the number of ROIs

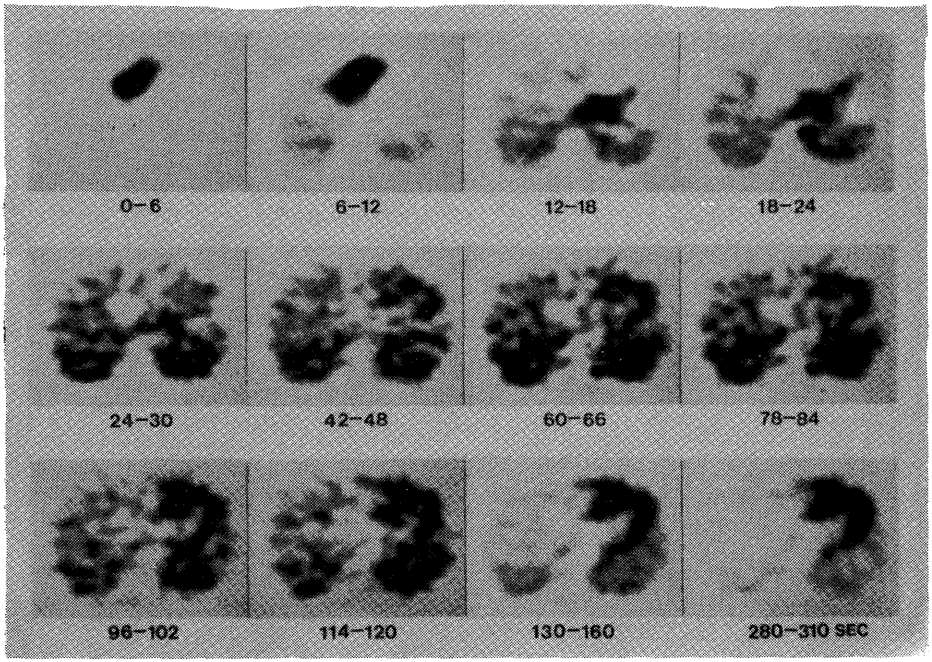

Fig. 2 6-sec serial PET imaging with N-13 ammonia at the midventricular level in a patient with hypertrophic cardiomyopathy (HCM). The numbers below the images show time (in sec) after intravenous injection of N-13 ammonia. The transit of N-13 activity through right ventricle, both lungs and left ventricle is visualized at the earlier images. Then occurs clearance of N-13 activity in the blood pools and lungs, and finally the myocardial image is delineated. The last two images represent 30-sec PET scans taken just after the initial twenty 6-sec PET were completed.

was three to five for each slice. An arterial input function $Ca(t)$ was determined noninvasively by assigning a ROI over the left atrium, which was large enough to avoid the partial volume effects and cross contaminations. The sizes of ROIs were about 10×10 mm. Count losses in high count rate were corrected whit an object-independent method using a single count rate.[7] Although the measured values were integrals of 6 second intervals, they showed enough temporal resolution for the present analysis. The parameters A, B, α and fa were estimated by fitting eq. (3) to the measured time-activity curve using a modified Gauss-Newton least-squares algorithm. The convolution in eq. (3) was calculated by a numerical integration. The curve-fitting algorithm was reproducible given the appropriate starting values for A, B, α and fa. Finally RMBF and extraction fraction of ammonia were calculated by the eqs. (5) and (7). Because RMBF thus obtained was in the unit volume of myocardium, it was corrected by a myocardial density (1.05 g/m*l*) and expressed as m*l*/min/100g.

3. RESULTS

Figure 2 shows a 6-sec serial PET imaging with N-13 ammonia at the midventricular level in one of the HCM patients (patient #1) employed in this study. The numbers below the images show time (in sec) after intravenous injection of N-13 ammonia. The transit of N-13 activity through right ventricle, both lungs and left ventricle is visualized at the earlier images. Then clearance of N-13 activity occurs in the blood pools and lungs, and finally the myocardial image is delineated. The last two images represent 30-second PET scans taken just after the initial twenty 6-second PET scans were completed.

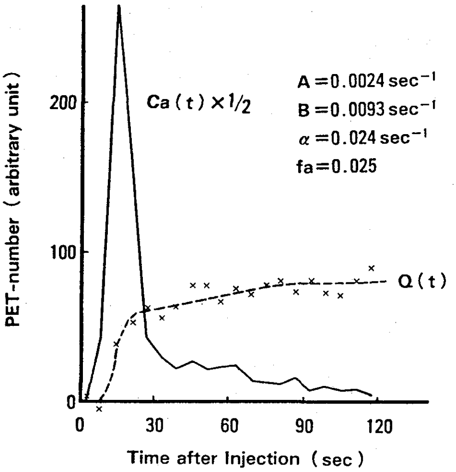

Fig. 3 Time-activity curves of septum ($Q(t)$) and left atrium ($Ca(t)$). The solid line shows $Ca(t)$, the cross marks (×) a measured time-activity curve of septum and the dotted line an estimated myocardial response with the parameter values listed above right. $Ca(t)$ is illustrated in a half of real PET-number.

Fig. 3 shows time-activity curves of septum and left atrium for patient #1. The solid line in the figure shows a time-activity curve of the left atrium which was used as an input function in the present analysis. The cross marks (×) show a measured time-activity curve of the myocardium, while the dotted line shows an estimated myocardial response.

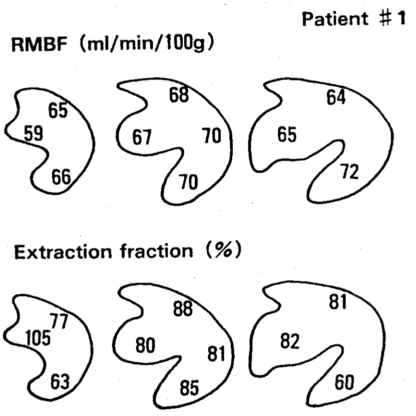

Fig. 4 Estimated values of RMBF (m*l*/min/100 g) and extraction fraction (%) of ammonia on the anatomical cross sections. The sections correspond to high ventricular (atrial), mid-ventricular and low ventricular levels from left to right.

Fig. 4 shows estimated values of RMBF and extraction fraction of ammonia on the anatomical cross sections in patient #1. The sections correspond to high ventricular (atrial), mid-ventricular and low ventricular levels from left to right. The upper panel shows RMBF and the lower shows extraction fraction. Table 1 summarizes the estimated results.

4. DISCUSSION

In this paper we estimated RMBF and extraction fraction in man with intravenous injection of N-13 ammonia and PET. To our knowledge this is the first report describing noninvasive measurements of such physiologic parameters in man. Although we have no direct evidence to judge whether the results obtained here are true or not, they seem consistent with values obtained in animal experiments[2] or by a much more invasive method in man.[8]

Schelbert et al[2] measured extraction fraction and

Table 1 Summary of parameter estimation

	F (ml/min/100 g)	E (%)	α (sec^{-1})	fa (%)
PT#1	67±4[a] (10)[b]	80±13 (10)	0.0231±0.0040 (9)[c]	3.5±2.0 (10)
PT#2	65±10 (12)	81±16 (12)	0.0205±0.0040 (9)	2.5±1.8 (12)

[a] Mean±Standard Deviation (SD)
[b] The number of ROIs
[c] The number of ROIs used for calculating means and SDs of α were smaller than others because ROIs in which E was greater than 90% were omitted.

clearance half-time of ammonia after coronary injection of N-13 ammonia in dog. Their results were summarized from our point of view as $E=82\%$ and $\alpha=0.027$ sec^{-1} at the control flow of $F=100$ ml/min/100g. Selwyn et al[8] measured RMBF in man with human albumin microspheres labeled with C-11 and PET. Their results showed that RMBF was 82.0 ±32.0 ml/min/100g in the normal myocardium. Although our results in Table 1 were obtained from the HCM patients, they seem to agree well with these values. The interpretation of this agreement needs further study. Fractional volume of vascular space in myocardium is usually about 10%.[9] fa in Table 1 is much smaller than this value. However fa is a fractional volume of arterial space in the field of view. Because it does not include capillaries and veins, the values in Table 1 seem reasonable.

As described before, the present model is essentially the same as the one proposed by Mullani et al,[4] and its validity might be further supported by the following discussion. From the eqs. (4), (5) and (7), k and Vd can be expressed as,

$$\begin{aligned} k &= E\alpha \\ Vd &= F/(1-E)\alpha \end{aligned} \tag{8}$$

If the average value of patient #1 is substituted in eq. (8), $k=0.019$ sec^{-1} (1.1 min^{-1}) and $Vd=2.5$.

Because Vd is the distribution volume of N-13 ammonia in the free compartment, the result ($Vd=2.5$) means that at equilibrium N-13 ammonia in the free compartment would occupy 2.5 times of actual tissue space if its concentration were the same as the venous concentration. Frank and Langer[10] measured extracellular space of perfused rabbit heart using radioactive La^{+++}, and found that if La were distributed in free solution it would occupy 194% of total tissue water, discussing that it was due to extensive binding of La^{+++} to polyanionic extracellular structures of myocardium. In extracellular space N-13 ammonia exists in the chemical equilibrium of NH_3 and NH_4^+, in which the prominent form is NH_4^+. The possibility of extracellular trapping of NH_4^+ just as La^{+++} suggests that N-13 ammonia concentration in the extracellular space may be greater than in veins, which supports our result of $Vd=2.5$ and the validity of the model. Further studies are required to interpret the values of k obtained here.

The present method employed a time-activity curve of left atrium measured with PET as an arterial input function. Iida et al[11] compared radial arterial curves with time-activity curves of left ventricle following intravenous injection of O-15 water, and concluded that the radial curve was significantly dispersed from the time-activity of left ventricle measured with PET. Their results suggest that the use of time-activity curve measured with PET as an input function not only is noninvasive but also may be more accurate, especially for arteries near the heart such as coronary artery.

Another problem on the input function is whether N-13 activity in the arterial blood is all due to ammonia or not. N-13 ammonia in the blood is rapidly uptaken and metabolized mainly by the liver, and its metabolites labeled with N-13 come into the blood. Lockwood et al[12] examined contents of N-13 activity in the arterial blood after intravenous injection of N-13 ammonia in man, and concluded that the labeled metabolites were not detectable until after 3 min of injection. Because our study utilized the activity changes up to 2 min after injection, N-13 activity observed in the arterial blood seems substantially due to ammonia.

In the present study to avoid partial volume effects and cross contamination of activity, we employed the HCM patients with a marked increase in LV mass and showed the reliable results as discussed so far. However we did not analyze normal cases and patients with ischemic heart diseases, which are the most important in clinical practice.

In order to apply the present method to these cases, we must correct the partial volume effects and cross contamination. Henze et al[9] proposed a deconvolution technique that permitted calculation of spillover fractions from geometric measurement of the imaged cross section and the spatial resolution of tomograph. Recently Carson[13] applied the EM (estimation maximum) algorithm to emission tomographic estimation of ROI activity and showed excellent results almost free from the partial volume effects. As the next step we will combine these techniques and the present method to analyze normal cases and patients with ischemic heart disease.

ACKNOWLEDGMENT

This research was done as a part of the research project 'Medical application of accelerated heavy particles' at the National Institute of Radiological Sciences (principal researcher Dr. H. Tsunemoto). The authors thank all the members of the project, especially Drs. N. Fukuda, T. Matsumoto and H. Shinoto for fruitful collaboration. They also thank Drs. T. Himi and A. Kagaya in the Chiba University School of Medicine for their clinical assistance.

REFERENCES

1. Shah A, Schelbert HR, Schwaiger M, et al: Measurement of regional myocardial blood flow with N-13 ammonia and positron-emission tomography in intact dogs. *J Am Coll Cardiol* 5: 92–100, 1985
2. Schelbert HR, Phelps ME, Huang SC, et al: N-13 ammonia as indicator of myocardial blood flow. *Circulation* 63: 1259–1272, 1981
3. Rauch B, Helus F, Grunze M, et al: Kinetics of ^{13}N-ammonia uptake in myocardial single cells indicating potential limitations in its applicability as a marker of myocardial blood flow. *Circulation* 71: 387–393, 1985
4. Mullani NA, Goldstein RA, Gould KL, et al: Myocardial perfusion with rubidium-82. I. Measurement of extraction and flow with external detectors. *J Nucl Med* 24: 898–906, 1983
5. Goldstein RA, Mullani NA, Marani SK, et al: Myocardial perfusion with rubidium-82. II. Effects of metabolic and pharmacologic interventions. *J Nucl Med* 24: 907–915, 1983
6. Tanaka E, Nohara N, Tomitani T, et al: A whole body positron tomograph, POSITOLOGICA-II —Design and performance evaluation—. In: Proceedings of the Third World Congress on Nuclear Medicine and Biology, August-September, 1982, Pergamon Press, Paris, pp. 535–538
7. Endo M, Nohara N, Iinuma TA, et al: Count rate characteristics and count loss correction of POSITOLOGICA II: a whole body positron emission tomograph. *Radioisotopes* 36: 227–231, 1987
8. Selwyn AP, Shea MJ, Foale R, et al: Regional myocardial and organ blood flow after myocardial infarction: Application of the microsphere principle in man. *Circulation* 73: 433–443, 1986
9. Henze E, Huang SC, Ratib O, et al: Measurements of regional tissue and blood-pool radiotracer concentrations from serial tomographic images of the heart. *J Nucl Med* 24: 987–996, 1983
10. Frank JS, Langer GA: The myocardial interstitium: Its structure and its role in ionic exchange. *J Cell Biol* 60: 586–601, 1974
11. Iida H, Kanno I, Miura S, et al: Error analysis of a quantitative CBF measurement using $H_2{}^{15}O$ autoradiography and positron emission tomography with respect to the dispersion of the input function. *J Cereb Blood Flow Metabol*, 1986: in press.
12. Lockwood AH, McDonald JM, Reiman RE: The dynamics of ammonia metabolism in man: Effects of liver disease and hyperammonemia. *J Clin Invest* 63: 449–460, 1979
13. Carson RE: A maximum likelihood method for region-of-interest evaluation in emission tomography. *J Comput Assist Tomogr* 10: 654–663, 1986

AMERICAN JOURNAL OF PHYSIOLOGIC IMAGING 3:7–9 (1988)

Fundamental Tumor Perfusion Analysis With Nuclear Magnetic Resonance Imaging Using Gadolinium-Diethylene Triamine Pentaacetic Acid

HIROO IKEHIRA, MD, TERUKO YAMANE, PhD, NOBUO FUKUDA, MD,
KOICHI ANDO, DDS, YOSHIRO AOKI, MD, SACHIKO KOIKE,
MASAHIRO ENDO, PhD, TORU MATUMOTO, PhD, TAKESHI IINUMA, PhD,
HIROSHI FUKUDA, MD, and YUKIO TATENO, MD
Division of Clinical Research (H.I., T.Y., N.F., K.A., S.K., M.E., T.M., T.I., H.F., Y.T.) and
Division of Hospital (Y.A.), National Institute of Radiological Sciences, Chiba, Japan

ABSTRACT **The measurement of blood perfusion is an important factor for both the diagnosis and follow-up of tumor lesions. However, noninvasive detection of this local blood flow factor is very difficult. To accomplish this, we tried to calculate tissue blood perfusion indexes with nuclear magnetic resonance imaging using gadolinium-diethylene triamine pentaacetic acid (Gd-DTPA).**

We experimentally applied this method to C3H mouse's tumor NFSa (fibrosarcoma) and its recurrence tumor R1137, whose experimental hypoxic cell fraction is different; that is, R1137 is more oxic than NFSa. Imaging pulse sequence was T1 (TR = 1,000 ms, TI = 300 ms), and longitudinal relaxation rate (R1 = 1/T1) values were calculated. Injected dose of Gd-DTPA was 0.1 mmol/kg.

The T1 images produced are from both the preinjection period from every 5 min postinjection for 30 min. Using two-exponential analysis and compartment analysis we calculated two fundamental parameters: uptake index and flow index as blood perfusion factors.

We found that this method has the possibility of differentiating the tissue's hypoxic cell fraction and is effective both for follow-up study after radiation therapy and for tissue characterization.

Key words: Gd-DTPA, tumor, blood perfusion, tissue characterization

INTRODUCTION

Blood perfusion of tumor tissue is the one of most important factors for both the diagnosis and assessment of treatment effects in parenchymal diseases and solid tumors. However, it is very difficult to measure the local blood perfusion factor directly and noninvasively. In this paper we proposed the method of blood perfusion factor analysis with NMRI using Gd-DTPA (gadolinium-diethylene triamine pentaacetic acid). We evaluated experimentally the effectiveness of this method with an animal model.

MATERIALS AND METHODS

A resistive type NMRI[1] was operated at 0.1 Tesla was used for imaging. The diameter of a head coil was 24 cm, and T1 (TR = 1,000 ms, TI = 300 ms) pulse sequence was used. It took 4 min to obtain a single T1 image. We calculated inversion T1 that was longitudinal relaxation rate (R1) and made R1 images [1].

Gd-DTPA, which was supplied commercially,[2] was used as a contrast enhancement medium. The injection dose was 0.1 mmol/kg as an intravascular injection. We took T1 images at before injection and every 5 min after injection for 30 min.

The animal tumor models employed were a NFSa (fibrosarcoma) and its recurrence tumor R1137 originated from C3H mice. The hypoxic cell fractions of these tumors are completely different. The NFSa has a 10% hypoxic cell fraction, but R1137 had no hypoxic cell fraction, so the NFSa is more oxic than R1137 [2,3].

The tumor cells were subcutaneously transplanted in the C3H mice's thighs. The tumors used had diameters between 1 and 1.5 cm with no central necroses as seen on the NMRI image.

Blood perfusion parameters were calculated from the dynamic change of the R1 values. These were measured in

---

[1] Asahi Mark-J: made by Asahichemical Co. Ltd.

[2] Schearing Co. Ltd.

Received September 3, 1987; accepted November 26, 1987.

Until October, 1988, Dr. Hiroo Ikehira will be at Lawrence Berkeley, Laboratory, Mail Stop 55-121, 1 Cyclotron Road, Berkeley, CA 94720. Address reprint requests there.

tumor tissue with a region of interest (ROI) (10 × 10 pixels) in the R1 images.

METHOD OF CALCULATION

We defined the uptake index and the flow index as tissue blood perfusion factors as follows.

In tumor tissue, which included both extravascular and intravascular spaces, the diffusion of Gd-DTPA from the intravascular space was very quick. This leads to the next equations using a compartment analysis,

$$\frac{dCex}{dt} = F \times Cin - \frac{Cex}{P2} \qquad (1)$$

$$Cin(t) = Cin(0) \times \exp(-t/P4) \qquad (2)$$

$$Cex(0) = 0 \qquad (3)$$

where F is the flow index, Cex and Cin indicate extra- and intravascular concentration of the Gd-DTPA, and P2 and P4 indicate the diffusion time constants between the extra- and intravascular space. P2 is the diffusion time constant for extravascular space to intravascular space, and P3 is another time constant. From these equations the next equation is obtained:

$$Cex(t) = Cin(0) \times F \times P2 \times P4 \times \frac{\exp(-t/P2) - \exp(-t/P4)}{P2 - P4} \qquad (4)$$

This is the two-exponential equation; therefore we can use a minimum square fitting to the change of R1 value with the next two-exponential equation,

$$Rt - R0 = P1 \times \exp(-t/P2) - P3 \times \exp(-t/P4) \qquad (5)$$

where Rt and R0 are R1 values of the tumor tissue at t min before and after injection; P1 and P2 are parameters.

In this case, Cex is a close approximation of the intravascular tissue's Gd-DTPA concentration. F (flow index) is calculated by the comparison of each parameter of the term exp(−t/P2) of equations 4 and 5.

$$F = \frac{P1 \times (P2 - P4)}{P2 \times P4 \times Cin(0) \times B} \qquad (6)$$

where B is the proportional constant between the R1 value and Gd-DTPA concentration in the tissue [4]; B was decided experimentally. The B-value is 3,000 ml/mmol/s, but here ml indicates ml tissue volume [5].

The uptake index is defined by the next equation,

$$Ui = \frac{P1}{Cin(0) \times B} \qquad (7)$$

where Ui is the experimental relative enhancement ratio of the tissue.

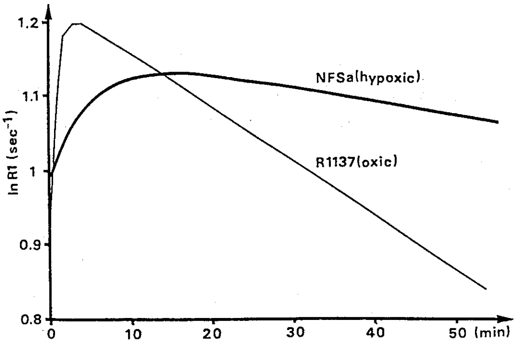

Fig. 1. Semilogarithmic plots of mean R1 value changes after Gd-DTPA injection for experimental tumor NFSa (hypoxic tumor) and R1137 (oxic tumor). Pattern of the oxic tumor indicates early uptake and quick clearance of the contrast medium.

TABLE I. Calculated values of parameters for NFSa and R1137[a]

	NFSa (n = 5)	R1137 (n = 7)	Significant
R0	2.64 ± 0.340	2.35 ± 0.130	−
P1	0.535 ± 0.089	1.02 ± 0.144	−
P2	536 ± 692	138 ± 31.4	+
P3	0.547 ± 0.170	1.02 ± 0.281	+
P4	5.56 ± 8.08	0.920 ± 0.719	−
U_i	0.115 ± 0.038	0.189 ± 0.052	+
F	0.140 ± 0.175	0.504 ± 0.241	+

[a] R0, the R1 value of the tumor before Gd-DTPA injection; P1 to P4, parameters of the fitting equation 5; Ui, uptake index; F, flow index. "Significant" indicates over 95% probability using Wilcoxon's method. The units are as follows: R0, P1, P3 (sec^{-1}); P2, P4 (min); Ui (no unit); F (ml/min/ml tissue volume).

The units for P1 and P3 are s^{-1}, and for P2 and P4 are min; Ui has no units, and the units of F are ml/min/ml tissue volume.

RESULTS

Data of calculated parameters and blood perfusion factors are shown in Table I. P2 is the time constant of the contrast media clearance from the tumor tissue; mean P2 value of R1137 (oxic tumor) is 138 min, and it is significantly shorter ($P < .05$) than the mean P2 value of NFSa (hypoxic tumor) 536 min. The uptake constant P4 has a mean value for R1137 of 0.92 min and for NFSa of 5.56 min, so R1137 has a shorter P4 value than NFSa, although not significant. The enhancement effect with Gd-DTPA indicates quick uptake and rapid clearance in the tissue of R1137. Standard deviations of P2 and P4 value are large, because some large values are included in data.

The uptake index and the flow index of R1137 are significantly higher as compared with those of NFSa.

We plotted the change of R1 value after Gd-DTPA injection, using mean values of P1 to P4 of NFSa and R1137. As shown in Figure 1, the changing patterns of Gd-DTPA concentration or R1 value in tumor tissue represent the difference of enhancement pattern between R1137 and NFSa. That is, in the case of R1137 (oxic tumor) its curve indicates quick enhancement and more rapid clearance when compared with the pattern of NFSa (hypoxic tumor).

DISCUSSION

In this study we have experimentally produced a calculation method for analyzing tumor blood perfusion by using a very simple model of a tumor tissue as an extra- and intravascular space two-compartment model. With this method we can easily and clearly separate the tissue by characteristic differences of the hypoxic cell fraction between NFSa and R1137.

It is very difficult to detect in vivo the differences in local tumor tissue blood perfusion, but by this method, which uses Gd-DTPA with NMRI, it is indicated that the differences in hypoxic cell fractions are partly dependent upon the differences in blood perfusion factor. This fact is very significant for radiation biology.

One problem of this method is the proportional constant, which is decided by the relaxivity of Gd-DTPA in the renal cortex. At this time this is the most reasonable method to decide in vivo proportional constant between Gd-DTPA concentration and the longitudinal relaxation rate.

Another point is the signal/noise ratio of NMRI equipment itself. This leads to calculated blood perfusion factors as a relative value, which can be applied to each model as its own control.

CONCLUSIONS

We developed tumor tissue blood perfusion factor analysis using Gd-DTPA with NMRI and evaluated this method by an animal model. It was indicated by this method that the differences in hypoxic cell fractions of each tumor possibly depended on the differences in in vivo blood perfusion factor.

Our next step is to apply this method to patients and to evaluate the usefulness of this method for tumor tissue characteristic diagnosis and for detectability of treatment effect.

ACKNOWLEDGMENTS

This study was partially supported by grants Koseisho showa 62 nendo joseikin (61-16) Japan.

REFERENCES

1. Ikehira H, Torii S, Yamane T, Fukuda N, Shibata S, Endo M, Matumoto T, Shinotoh H, Iinuma T, Tateno Y: Evaluation of the renal kinetic function, using NMR-CT by gadolinium-DTPA (report 2), NMR-CT regional renogram and glomerular filtration ratio. Jpn J Nucl Med 22:1615-1624, 1985.
2. Ando K, Koike S, Fukuda N, Kanehira C: Independent effect of a mixed-beam regimen of fast neurons and gamma rays on a murine fibrosarcoma. Radiat Res 98:96-106, 1984.
3. Ando K, Koike S, Shikita M, Hayata I, Otsu H, Satoh S: Radiosensitivity of late recurrences following radiotherapy of murine fibrosarcomas. Radiat Res: in press.
4. Strich G, Hagan PL, Slutsky RS: Tissue distribution and magnetic resonance spin lattice relaxation effects of gadolinium-DTPA. Radiology 154:723-726, 1985.
5. Ikehira H: Experimental renal kinetic function analysis using Gd-DTPA enhanced MRI—the separation analysis of glomerular and tubular functions. Jpn J Nucl Med 24:263-272, 1987.

シンポジウム 4　新しい画像診断法の癌診療への応用

ポジトロン CT のがん診療への応用の可能性

福田　寛[*1]　舘野　之男[*1]　松澤　大樹[*2]

要旨　ポジトロン CT 法は，ポジトロン標識薬剤を用いて生きている人間の代謝情報を映像化できる優れた診断技術である。一方，癌は糖，蛋白代謝などが高進しているので，ポジトロン CT 法により癌の代謝を指標とする質的な診断が可能である。このことはヒト癌の生物学的理解を深めるのみならず，癌診療においても有用である。すなわち，1）癌の検出，2）悪性度の診断，3）癌の生物学的性格付け，4）治療効果の判定などが挙げられる。これらの観点から肝癌，肺癌および脳腫瘍のポジトロン CT による診断研究が行われているが，肝癌，肺癌の組織別診断が可能であること，脳腫瘍のポジトロン CT による grading が，予後と良い相関を示すことなど有望な結果が得られている。しかしポジトロン CT 法は臨床診断技術としては未だ成熟しておらず，今後の研究の充実が望まれる。

〔癌と化学療法　15(4): *PART-II*, 860-865, 1988.〕

はじめに

ポジトロン CT 法は短寿命のポジトロン放出核種で標識された化合物を用いて，生体の代謝情報を定量的な画像として表示する優れた手段である。「機能の変化は形態の変化に先行する」といわれており，この意味ではポジトロン CT は病態生理の研究に重要な役割を果たすと考えられる

一方，癌は正常組織に比べて代謝が亢進しており，糖，アミノ酸，核酸などを多量に必要としている。またこれらの代謝の程度と癌の悪性度はおおむね比例していることが知られている。癌の糖代謝については Warburg1) 以来，半世紀に及ぶ研究の歴史があり癌の増殖速度と解糖活性との相関が指摘されている。また癌の各種アミノ酸とりこみについては，Busch2) の詳細な報告がある。癌の増殖と DNA 合成能については，さらに多くの報告がある。したがって，これらの化合物をポジトロン核種で標識してポジトロン CT で撮像すれば，癌の検出のみならず癌の代謝量を映像化することができる。

癌診断用ポジトロン標識化合物

表1に癌診断に用いられるポジトロン標識化合物を示した。エネルギー代謝の指標である糖のトレーサーとしてはグルコースの類似化合物である 2-デオキシ-2-[^{18}F] フルオロ-D-グルコース (^{18}FDG) が最もよく用いられている。他に，^{11}C-グルコース，TCA サイクルで直接利用される ^{11}C-ピルビン酸3) などが用いられている。またガラクトースの類似体である，2-デオキシ-2-[^{18}F] フルオロ-D-ガラクトース (^{18}FDGal) は肝のガラクトース代謝のトレーサーであるが4)，肝細胞癌に特異的に集積することから肝癌の診断薬として用いられる。

アミノ酸は癌の増殖に必要な蛋白合成の原料である。われわれは種々のポジトロン標識アミノ酸の腫瘍集積性についてスクリーニングを行ったが，生理的アミノ酸としては ^{11}C-メチオニン，^{11}C-トリプトファンまた非生理的アミノ酸としては ^{11}C-

---

[*1] 放射線医学総合研究所・臨床研究部
[*2] 東北大学抗酸菌病研究所・放射線医学部門

表 1 癌診断用ポジトロン標識化合物

[1] 糖代謝
　^{18}F-デオキシフルオログルコース (^{18}FDG)
　^{18}F-デオキシフルオロガラクトース (^{18}FDGal)
　^{11}C-グルコース
　^{11}C-ピルビン酸
[2] アミノ酸代謝
　^{11}C-メチオニン
　^{11}C-トリプトファン
　^{11}C-ACPC
　^{13}N-グルタミン酸
[3] 核酸代謝（ピリミジン）
　^{18}F-デオキシフルオロウリジン (^{18}FdUr)
[4] 血流
　$H_2{}^{15}O$，$C^{15}O2$
　$^{13}NH_3$
　^{11}C-ブタノール
[5] ポリアミン
　^{11}C-メチルプトレッシン
　^{11}C-メチルスペルミン
　^{11}C-メチルスペルミジン
[6] 薬物代謝
　^{11}C-BCNU

ACPC が最も癌診断薬として優れていることがわかった5)。

DNA 合成，RNA 合成の指標としては，^{18}F-デオキシフルオロウリジンがある6)。この化合物は核に取り込まれるのは約50％で完全な核酸合成のトレーサーではないが，きわめて悪性の腫瘍だけに集積する性質を持っており，興味深い化合物である。

一方，腫瘍の血流量も重要な因子であり，^{15}O-二酸化炭素，^{15}O-水，^{11}C-ブタノールなどがこの目的にもちいられている。また^{15}O-二酸化炭素と^{15}O-酸素を用いて腫瘍の血流と酸素消費量が測定された7)。

癌診療におけるポジトロン CT の役割

ポジトロン CT が癌の臨床の場で果たし得る役割およびこれらの分野で行われている研究を表2に示した。癌の検出，癌の質的診断および癌の治療効果の判定などが主な役割と考えられる。この中のいくつかについて，具体的に説明を加える。しかしポジトロン CT 検査法は臨床的診断技術としてはまだ成熟していないので，この方法の将来の可能性を含めて論ずることにする。

表 2 ポジトロン CT の癌診療における役割（可能性）

[1] 癌の検出（存在診断）
[2] 癌の悪性度の診断・性格付け
　(1) ^{18}FDG によるグリオーマの grading
　(2) ^{18}FDG によるメニンギオーマのgrading と予後の関係
　(3) 肺癌の組織型分類と ^{18}FDG，^{11}C-L-メチオニンの取り込み
　(4) ^{18}FDG，^{18}FDGal による肝癌の診断
　(5) 各種トレーサーの組み合わせによる脳腫瘍の診断
　(6) $^{15}CO_2$，$^{15}O_2$ による脳血流・エネルギー代謝測定
　(7) ^{11}C-ピルビン酸による脳腫瘍の診断
　(8) ^{18}FDG による眼窩腫瘍の診断
[3] 癌治療効果の判定
　(1) ^{18}FDG による放射線治療の効果判定
　(2) ^{18}FDG による化学療法の効果判定
[4] 再発の判定
　(1) 脳腫瘍の再発の判定

^{18}FDG と ^{18}FDGal による肝癌の診断

2-デオキシ-2-［^{18}F］フルオロ-D-グルコース（^{18}FDG）はグルコースの類似体で代謝されずに癌細胞に蓄積する。しかも正常の肝臓からは排出されるので肝内の癌を陽性像として描出することができる8,9)。このことは通常の腫瘍核医学で用いられているクエン酸-^{67}Ga では困難である。図1に肝細胞の ^{18}FDG によるポジトロン CT 像を示

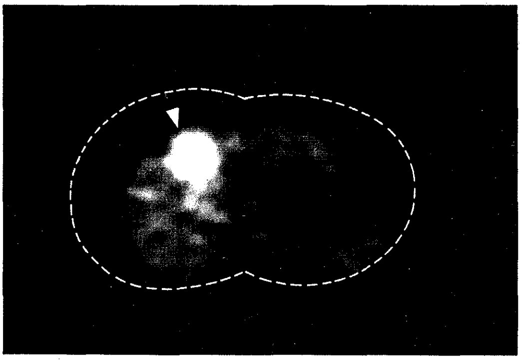

図 1 ^{18}FDG による肝細胞癌のポジトロン CT 像(50分後)。腫瘍部（矢印）に ^{18}FDG の高い集積がみられる。

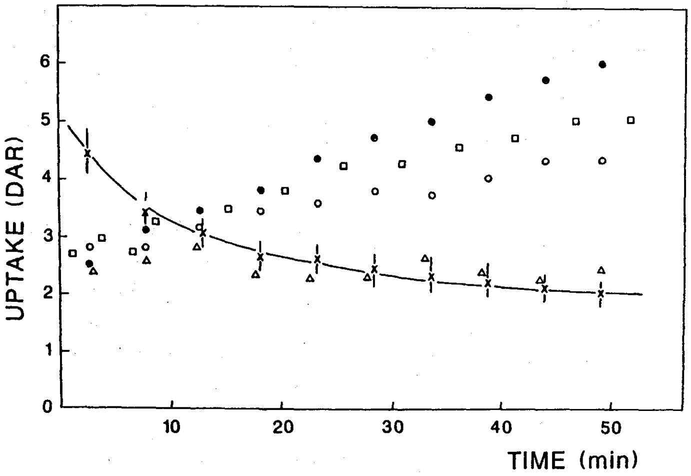

図 2　肝細胞癌の ^{18}FDG とりこみ曲線。肝細胞癌には，時間とともに ^{18}FDG が集積するが，正常肝からは排泄される。
×；正常肝，□，○，●，△；肝細胞癌症例

した。静注早期は RI は肝全体に分布しているが，時間とともに腫瘍部に集積が増加していく。肝細胞癌，転移性肝癌の数例について，腫瘍部の時間—放射能曲線を示したのが図2である。腫瘍の放射能は時間とともに増加していくのに対して正常肝は時間とともに減少する。したがって，静注30〜50分後には腫瘍の明瞭な陽性画像がえられる。また糖代謝活性の程度は悪性度を示すことが動物実験では証明されているので，^{18}FDG の相対的取り込み値から肝癌の悪性度（未分化度）を判定できるはずである。しかしまだ十分なデータが蓄積していないので，今後，病理所見と対応させた臨床研究が必要である。

一方，2-デオキシ-2-［^{18}F］フルオロ-D-ガラクトース（^{18}FDGal）は肝細胞に特異的に存在するガラクトキナーゼによりリン酸化されるが，代謝されずにトラップされる。したがって，肝のガラクトース代謝のトレーサーとして用いられる[4)]。^{18}FDGal によるポジトロン CT では正常肝への集積は極めて高いのに対して，肝硬変では著しい低下を示す。また，^{18}FDGal の癌集積性については，興味深い事実が明らかとなった。すなわち肝細胞由来の原発性肝癌（HCC）では正常肝の60〜80％高集積を示した。また HCC が肝以外の部位に転移した症例でも著しい高集積を示した[10)]。ところが他の組織由来の転移性肝癌への集積はきわめて低かった（山口ら[11,12)]）。このことは，肝細胞癌は発生母地である肝細胞のマーカー酵素-ガラクトキナーゼを保持しているのに対して，他の臓器由来の転移性肝癌は持っていないことを示唆している。また肝細胞癌のなかでも集積の多いものと低いものがあることから，その癌が正常の肝細胞の形質をどれだけ保持しているか，すなわち分化度（良性度）を示している可能性がある。以上のように，^{18}FDGal は肝細胞癌の分化度を，^{18}FDG は悪性度を示すと考えられるので両者を組み合わせることにより，肝癌の質的診断および癌の治療・予後に直結する癌分類が可能であろうとわれわれは考えている。

^{11}C-L-メチオニン，^{18}FDG による肺癌の診断

肺は含気量が多く，バックグラウンドが低いので良好な腫瘍イメージを得ることができる。われわれは，ポジトロン標識アミノ酸である ^{11}C-L-メチオニンと糖の類似化合物である ^{18}FDG を肺癌の診断に用いている。図3は ^{11}C-L-メチオニンによる肺癌（偏平上皮癌）のポジトロン CT 像を示したものである。静注直後は血中濃度が高いので，血液プールがみえているが，約20分後には主病巣および縦隔転移リンパ節が明瞭に描出されている。窪田らは ^{11}C-L-メチオニンが肺癌には高集積を示すが，結核腫などの良性腫瘍，炎症にはあまり集

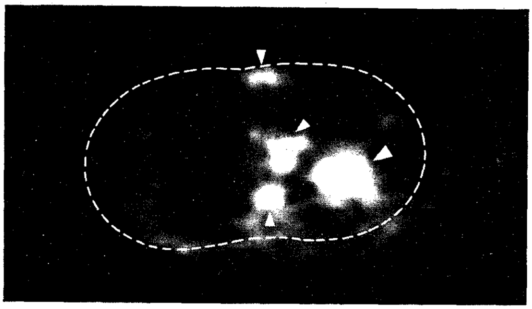

図 3 ^{11}C-L-メチオニンによる肺癌のポジトロン CT像（20分後）．主病巣（大矢印）および縦隔の転移リンパ節（矢印）が明瞭に描画されている。また^{11}C-L-メチオニンは，正常骨髄に集積する（小矢印）。

まらないことを示した[13,14]。また藤原ら[15]は^{11}C-L-メチオニンの取り込みと肺癌の組織像の違いによる相関をしらべた。その結果，大細胞癌がもっとも高く，偏平上皮腺癌，小細胞癌がこれにつぎ，腺癌が最も低い値を示した。

図4は^{18}FDGによる肺癌のポジトロンCT像である。^{18}FDGは肺，縦隔への取り込みが少ないので静注30〜50分後にはきわめてコントラストの良い腫瘍像が得られる。肺癌の組織像と^{18}FDGとりこみの相関を調べたところ^{11}C-L-メチオニンと同様に大細胞癌が最も高く，腺癌が最も低い値であった。小細胞癌は増殖が早いにもかかわらず^{11}C-L-メチオニンおよび^{18}FDGの集積はあまり多くなかった。この結果は腫瘍の増殖速度と必ずしも一致しておらず興味深い結果である。今後，予後との対応など十分に検討して臨床的評価を下す必要がある。

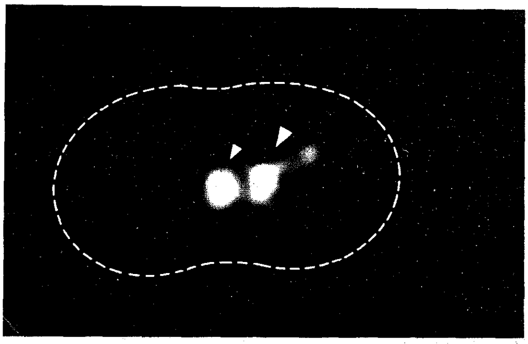

図 4 ^{18}FDGによる肺癌のポジトロン CT像．主病巣（大矢印）および縦隔リンパ節（小矢印）に高度の集積がある。このため，胸郭の輪郭はほとんど見えない（破線で示してある）。

^{18}FDGによる脳腫瘍の診断

脳においては，^{18}FDGの集積程度からソコロフの数学的モデルにより組織グルコース消費量を計算できる。Di Chiroら（米国，NIH）はグリオーマの悪性度と^{18}FDGによって求めたグルコース消費量とがよく一致することを示した[16]。またDi Chiro，畑沢ら[17]は^{18}FDGの取り込みの多いメニンギオーマほど治療後の再発が多く，低いものはほとんど再発しなかったことを示した。また組織像との対応ではおおむね一致していたが，同じ組織像を示すメニンギオーマでも再発する悪性のものとそうでないのものがあり，^{18}FDGの取り込みのほうがむしろ相関があったとしている。癌の代謝活性を見るポジトロンCTのほうが，癌の予後と相関が高いのは当然であるが，これについても臨床的評価はまだ不十分であり，今後の臨床研究に期待したい。

ポジトロン CTによる治療効果の判定

従来，癌の治療効果の判定は形態学的手段または免疫学的手段（腫瘍マーカーなど）によって行われてきた。しかし，前者は癌の見た目の大きさだけでは生き死にを判定できないし，後者はすべての腫瘍に適応できるわけではないという欠点がある。一方，ポジトロンCTはRIの集積程度が代謝活性（viability）をあらわしているので，癌の治療効果を直接あらわしていると考えられる。阿部ら[18]は，放射線治療後の腫瘍の増殖動態とよく一致することを実験的に示した。また高橋ら[19]は胃癌，転移性肝癌などの腹部領域癌を対象にして，化学療法の臨床的効果判定とポジトロンCTによる^{18}FDGの取り込み値の増減がよく一致することを示した。ポジトロンCTにより腫瘍の位置と広がりおよび代謝活性を知ることができるので治療効果判定法としては理想的である。しかし，分解能に限りがあることから，どれだけの感度で物をいうことができるか問題であり，見きわめが必要である。

おわりに

ポジトロンCT法は生体の代謝情報を定量的な画像として示す優れた手段であり，癌診療に貢献する潜在能力はきわめて大きいと考えられる。しかし，種々の制約のために一般臨床の場では行いにくい手段であるため臨床診断技術としては成熟していないのが現状である。幸いにしてわが国ではポジトロンCT施設に恵まれており，さらに増加しつつあるので十分な臨床研究が行われるのを期待する。

謝辞：本論文で紹介した研究の大部分は東北大学抗酸菌研究所放射線医学部門の諸先生，同薬理学部門–多田雅夫博士，臨床癌化学療法部門–高橋弘博士および東北大学サイクロトロンラジオアイソトープセンター–井戸達雄博士はじめ教室の諸先生との共同研究の成果である。本研究は文部省科学研究費，および厚生省がん研究助成金の援助をうけた。

文献

1) Warburg, O.:On the origin of cancer cells. *Science* **123**:309–314, 1956.
2) Busch, H., Daruis, L. R., Hoing, G. R. *et al*: The uptake of a variety of amino acids into nuclear proteins of tumors and other tissues. *Cancer Res.* **19**:1030–1039, 1959.
3) Tsukiyama, T., Hara, T., Iio, M. *et al*:Preferential accumulation of ^{11}C in human brain tumors after intraveous injection of C–11 pyruvate. *Eur. J. Nucl. Med.* **12**:244–248, 1986.
4) Fukuda, H., Matsuzawa, T., Tada, M. *et al*: 2–deoxy–2–[^{18}F]fluoro–D–galactose:A new tracer for the measurement of galactose metabolism in the liver by positron emission tomography. *Eur. J. Nucl. Med.* **11**:444–448, 1986.
5) Kubota, K., Yamada, K., Fukuda, H. *et al*: Tumor deteciton with carbon–11–labeled amino acids. *Eur. J. Nucl. Med.* **9**:136–140, 1984.
6) Abe, Y., Fukuda, H., Yamada, K. *et al*:Studies on(F–18)–labeled pyrimidines:tumor uptekes of (F–18)–5–fluorouracil, (F–18)–fluorouridine and (F–18)–fluoro–deoxyuridine in animal studies. *Eur. J. Nucl. Med.* **8**:258–261, 1983.
7) Itoh, M., Lammertsma, A. A., Wise, R. J. *et al*:Measurement of regional cerebral blood flow and oxygen utilization in patients with cerebral tumors using ^{15}O and positron emision tomography:analytical techniques and preliminary results. *Neuroradiology* **23**:63–74, 1982.
8) Fukuda, H., Matsuzawa, T., Abe, Y. *et al*: Experimental study for cancer diagnosis with positron labeled fluorinated glucose analogs:[^{18}F]–2–fluoro–2–deoxy–D–mannose:A new tracer for cancer detection. *Eur. J. Nucl. Med.* **7**:294–297, 1982.
9) Yonekura, Y., Benau, R. S., Brill, A. B. *et al*: Increased accumulation of 2–deoxy–2–[^{18}F]fluoro–D–glucose in liver metastases form colon carcinoma. *J. Nucl. Med.* **23**:1133–1137, 1982.
10) Fukuda, H., Yamaguchi, K., Matsuzawa, T. *et al*:Imaging of hepatoma with 2–deoxy–2–[^{18}F]fluoro–D–galactose by positron emission tomographpy. Proceedings of the International Symposium on Current and Future Aspects of Cancer Diagnosis with Positron Emission Tomography(PET–85), p. 24–27 1986.
11) Fukuda, H., Yamaguchi, K., Matsuzawa, T. *et al*:Imaging of hepatoma with 2–deoxy–2–[$^{1}{}_{8}$F]fluoro–D–galactose by PET(abstr). 34th Annual Meeting of SNM, 3–8 June, 1987, Toronto, Canada.
12) Yamaguchi, K., Fukuda, H., Matsuzawa, T. *et al*:Differential diagnosis between hepatocellular carcinoma and metastatic liver tumor using 2–deoxy–2–(18F) fluoro–D–galactose with positron emission tomography. CYRIC Annual Report 1986, Tohoku University:303–311, 1987.
13) Kubota, K., Matsuzawa, T., Itoh, M. *et al*: Lung tumor imaging by positron emission tomography using C–11 L–methionine. *J. Nucl. Med.* **26**:37–42, 1985.
14) 窪田和雄，松澤大樹，藤原竹彦・他：^{11}C–メチオニンによる癌と炎症の鑑別診断の基礎的研究．核医学 **22**：1327–1332, 1985.
15) 松澤大樹，藤原竹彦，阿部由直・他：ポジトロンCTによる肺癌の診断．呼吸と循環 **35**:15–20, 1987.
16) Di Chiro, G., DeLaPaz, R. L., Brooks, R. A., *et al*:Glucose utilization of cerebral gliomas measured by [^{18}F]fluorodeoxyglucose and positron emission tomography. *Neuroradiology* **32**:1323–1329, 1982.
17) Di Chiro, G., Hatazawa, J., Katz, D. A. *et al*:Glucose utilization by intracranial meningiomas as an index of tumor aggressivity and probability of recurrence:a PET study. *Radiology* **164**:521–526, 1987.
18) Abe, Y., Matsuzawa, T., Fujiwara, T. *et al*: Assessment of radiotherapeutic effects on experimental tumors using ^{18}F–2–fluoro–2–deoxy–D–glucose. *Eur. J. Nucl. Med.* **12**:325–328, 1986.
19) Takahashi, H., Yamaguchi, K., Wakui, A. *et al*:New approach to clinical evaluation of cancer chemotherapy using positron emission tomography with ^{18}FDG (2–deoxy–2[^{18}F] fluoro–D–glucose).

Sci. Rep. Res. Inst. Tohoku Univ-C 11(1-4): 38-43, 1986.

Summary

〔*Jpn J Cancer Chemother* 15(4):*PART-II*, 860-865, *April*, 1988.〕

POTENTIAL USE OF POSITRON-EMISSION TOMOGRAPHY IN CLINICAL ONCOLOGY

Hiroshi Fukuda*1, Taiju Matsuzawa*2 and Yukio Tateno*1

*1 *Div. of Clinical Research, National Institute of Radiological Sciences,* *2 *Dept. of Radiology and Nuclear Medicine, The Research Institute for Tuberculosis and Cancer, Tohoku University*

Positron-emission tomography (PET) is an excellent technique, utilizing positron-labeled radiopharmaceuticals which provide a quantitative image of tissue metabolism in the living body. Cancer tissue is characterized by increased forms of metabolism, such as glycolysis and protein synthesis. Consequently, PET makes it possible to evaluate the metabolic activity of cancer tissue. Such information is useful not only for a better understanding of human cancer biology but for utilization in cancer clinics. The potential use of the PET technique for clinical oncology are cancer detection, cancer grading, biological characterization of tumors, and evaluation of therapeutic effectiveness. From this viewpoint, much clinical research has been done and good results obtained in both the characterization of hepatoma and lung cancer, and the grading of brain tumor, showing good correlation with prognosis after cancer therapy. However, PET is not commonly available and has not yet been established as a diagnostic technique in cancer clinics. Further extensive studies will thus be necessary in order to achieve these aspects.

Key words:Positron-emission tomography, Clinical oncology

《研究速報》

Gd-DTPAによるMRI腎ファンクショナルイメージ作成の試み

池平　博夫*　青木　芳朗**　長原　陽子***　山根　昭子*
福田　信男*　松本　徹*　遠藤　真広*　飯沼　武*
福田　寛*　舘野　之男*

I. はじめに

われわれはこれまでに，MRI造影剤であるGd-DTPA (gadolinium-diethylene triamin penta-acetic acid) がGFR (glomerular filtration ratio) 物質であることに着目して，MRIによる腎動態機能検査法を考案し，動物実験によりその基礎的検討と有効性の評価を行い報告してきた[1,2]．ところが今回シェーリング社よりGd-DTPAの提供を受ける機会を得たので，6名の腎機能正常ボランティアを対象としてヒトの正常腎機能評価の目的でわれわれがすでに報告した手法を応用して，その有効性の確認を行った．さらに局所腎機能評価のために，腎ファンクショナルイメージの作成を試み，腎動態機能の可視化と局所腎機能評価に有効であるという示唆が得られたので報告する．

II. 対象と方法

対象は腎機能正常の25歳から61歳，平均45歳の女性5名と18歳男性1名，計6名のボランティアとした．造影剤はシェーリング社製のGd-DTPAを使用し，投与量は0.05 mmol/kgを肘静脈よりボーラス静注とした．ただし投与前後での体位を同じ状態に保つために，留置針による血管確保の上で検査を行った．

MRI装置は0.1 Tesla常伝導型旭Mark-Jで，パルス系列はTl系列 (Tr=1,000 msec, Td=300 msec) を用い，造影剤投与前および投与後5分ごとに30分間，両側の腎臓を含む前額断面にて連続撮像を行った．なお心ゲート，呼吸ゲートは使用しなかった．

造影効果の観察には1/T1の逆数変換により縦緩和速度R1(1/T1)画像を作成し，R1画像上で腎中央部付近の皮質部および髄質部でROI (region of interest) 処理を行って，すでに報告した方法に従ってGFR値，尿流値，逆拡散値および尿細管容積値を算出した[1,2]．ただし今回はボランティアに対して本法を応用したので，各個人に対して他のGFR測定法は行えなかった．

腎ファンクショナルイメージについては，同様にR1画像上で両側腎臓全体をそれぞれ含む領域をROIとして，ROI内の各絵素ごとにGFR値算出法を適用することにより作成を試みた．

III. 結　果

25歳の女性のR1画像の経時的変化をFig. 1に示す．Fig. 1のa, b, c, dはそれぞれ造影剤投与前，投与後5分，15分，25分の画像である．またこれらのR1画像はmean 5 sec^{-1}, width 10 sec^{-1}と標準化して表示したものである．このR1画像上の変化は，造影剤投与前の画像では腎皮質部と髄質部の分離も明らかで，腎全体の形態も腎周囲脂肪組織とのコントラストが明瞭で良く把握

---

* 放射線医学総合研究所臨床研究部
** 同　病院部
*** 旭メディカル(株)

受付：62年8月19日
最終稿受付：62年9月3日
別刷請求先：千葉市穴川4-9-1 (〒260)
放射線医学総合研究所臨床研究部
池平博夫

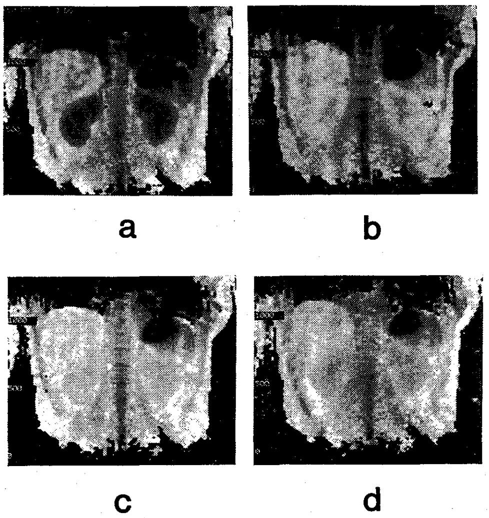

Fig. 1 Longitudinal relaxation rate (R1) images of 25 years old female volunteer, bilateral kidneyes' level colonal section. Gd-DTPA 0.05 mmol/kg) injected, a. preinjection, b., c. and d. are postinjection images, b. 5 min later, c. 15 min later and d. 25 min later.

できる．しかし造影剤投与直後の画像では腎皮質部と髄質部の区別は可能であるが，周囲脂肪組織とは分離し得ないほどの R1 値の上昇を認めた．15分後，25分後の画像では皮質部と髄質部の区別は付きにくくなっているが，次第に周囲の脂肪組織と腎臓の区別が明瞭となっている．

そこで右腎臓中央付近の皮質部および髄質部に ROI (10×10 絵素) 処理をして，その R1 値の平均値をプロットしたいわゆる MRI レノグラムが Fig. 2 である．Fig. 2 で分かるように，造影剤投与後の R1 値の経時的変化は投与直後にピークとなり，投与後は半減期約 20 分で減少していくことが分かる．また髄質部の R1 値は投与直後やはりピークとなるが一般的に皮質部のピーク値より低値であった．ただし造影剤投与前の組織の R1 値からの変化は，皮質部と髄質部でほぼ同じ値であった．なお，他の 5 例についてもほぼ同様の造影剤排泄パターンを示した．

各腎臓において，Fig. 2 のような MRI レノグラムを作成し，すでに報告した方法[1,2]により

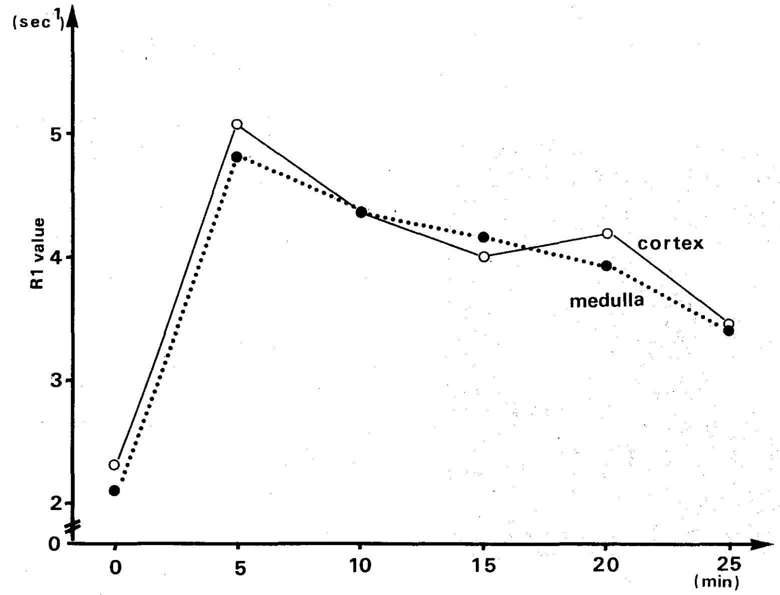

Fig. 2 MRI renogram, the change in longitudinal relaxation rates of the renal cortex and the renal medulla, pre- and post-injection of Gd-DTPA (0.05 mmol/kg) in the same volunteer of the Fig. 1.

MRIレノグラムの排泄相の部分から算出したGFR値，尿流値，逆拡散値および尿細管容積値の各ボランティアごとの両側腎臓における値を平均した計6名の測定値について，その平均値と標準偏差をTable 1に表示した．

GFR値は79.2±16.1 (ml/min), 尿流値は68.7±21.5 (ml/min), 逆拡散値は1.98±6.61 (μmol/min), 尿細管容積値は0.148±0.719 (ml) であり逆拡散値と尿細管容積値は健常ボランティアではいずれもほぼ0値を示した．

GFR値算出法を適用し，各絵素ごとに算出した値をプロットしたMRI腎ファンクショナルイメージの例をFig. 3に示した．症例は41歳女性でROIによるGFR値の平均は65.3 ml/minであった．ファンクショナルイメージの表示は，mean 40 ml/min, width 80 ml/minとした，画像でのGFR値言い換えれば造影剤クリアランスの分布パターンを見ると右腎臓では上下両極部で高値を示し，左腎臓では中央部で高値を示しており，両腎臓ともGFR値の分布は不均一パターンであった．また両側腎臓のGFR値を比較すると全体として右側腎臓のGFR値が左側腎臓に比べて大きいパターンを示した．

Table 1 Calculated renal functional parameter values of normal healthy six volunteers

	Volunteers (n=6)
GFR value (ml/min)	79.2±16.1
U. Flow value (ml/min)	68.7±21.5
B. Diff. value (μmol/min)	1.98±6.61
Vol. value (ml)	0.148±0.719

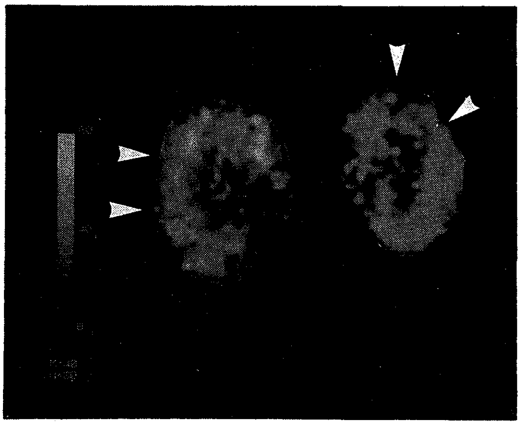

Fig. 3 Renal functional GFR of 41 years old female volunteer, mean value is 40 ml/min and width range is 80 ml/min. This image suggests irregular pattern of the intra renal blood flow, arrowheads indicate relatively low perfusion area.

IV. 考　察

家兎による動物実験から考察したGFR測定法および腎動態機能検査法を，ヒトの腎動態機能検査法に応用を行ったところ，腎局所ROIによるMRIレノグラムのパターンおよびGFR値等正常腎機能者についてほぼ矛盾のない結果であった．

すなわち，ヒトの正常機能腎臓で求めたGFR値79.2±16.1 ml/minという値は正常GFR値の正常限界がクレアチニンクリアランス等では一般に70～130 ml/min[3]であるのに比較して矛盾のない値であった．ただし今回われわれが行ったGFR値の測定は，血中造影剤濃度の変化ではなく，MR画像上における腎臓局所の造影剤濃度の変化について求めたものであるため腎局所血流分布の影響により標準偏差が大きくなったものと考えられた．

すなわち，ROI測定の結果およびファンクショナルイメージの造影剤クリアランス分布から，健常者であっても腎臓全体が同じ血流分布をしているのではなく，腎内血流分布には腎神経やrenin-angiotensin系のコントロールを受けて，局所ごとに血流の多い所，少ない所が存在する[4,5]ことを示していると考えられた．このような局所血流動態あるいは，局所尿細管機能の観察にはFig. 1に示したようなMRI腎動態レノグラフィーも有効であるが，腎局所における造影剤のクリアランスをより明瞭に観察するためにはFig. 3に示したファンクショナル画像のように腎局所におけるクリアランス値をプロットした画像が有効であろう．Fig. 3では造影剤クリアランス値をGFR値として標準化したものであるため皮質部のパターンはほぼGFR値の分布を示しており，腎髄質部

のパターンはほぼ尿流値の相対的分布に相当したものと考えられよう．

腎の呼吸性移動については，ゲートを使用していないので，MRI 画像作成法から，位置はほぼ呼気時の状態を示していると考えられる．

なお Table 1 に示したように，健常者の尿流値は 68.7±21.5 (ml/min)，逆拡散値は 1.98±6.61 (μmol/min)，尿細管容積値は 0.148±0.719 (ml) という値を示したが，尿流値についてはほぼ GFR 値に比例した値を示しており，逆拡散値および尿細管容積値は健常者であるためいずれもほぼ0となったものであり，病的状態においては，GFR 値および尿流値の低下や逆拡散値，尿細管容積値の増加が生じると推定される[2]．

V. 結　語

動物実験により基礎的検討を行ってきた Gd-DTPA を用いた MRI 腎動態機能検査法を，健常ボランティアに応用してヒトの腎機能評価への妥当性について検討を行った．さらに断層像での腎動態機能検査法としての特徴を生かすために，経時的に撮像された MRI レノグラフィーを基にして，MRI 腎ファンクショナルイメージとして GFR 画像を試作した．

算出された GFR 値その他のパラメータについては，一般に使用されている正常値などと矛盾のない値であり，MRI 腎ファンクショナルイメージについては，正常機能腎においても腎局所血流分布の不均一性を視覚的に捉え得る可能性を示唆する興味ある結果が得られた．ただし今まで述べた方法では，測定時間がかかり，早い時期の測定ができないので，新しい MRI の登場に期待するところが大きい．

今後本法の臨床的有効性を確認するために腎機能の実質障害例や局所性病変の早期定量診断や病期判定あるいは経過観察に対する有効性評価を行う必要がある．

なお本研究の一部は文部省昭和61年度科学研究費補助金（奨励研究〈A〉）課題番号 61770813，および厚生省がん研究助成金（有水班）61-16の援助を受けた．

文　献

1) 池平博夫，山根昭子，福田信男，他：ガドリニウム DTPA による NMR-CT 腎動態機能検査法の試み．核医学 **22**: 219-224, 1985
2) 池平博夫：MRI による腎動態機能検査法の実験的検討——糸球体機能と尿細管機能の分離評価法について——．核医学 **24**: 263-272, 1987
3) 金井　泉，金井正光，編著：臨床検査法提要，改訂第28版，腎機能検査法 XIV，金原出版，東京，1978
4) Thurau K: The dependency of intrarenal distribution of single nephron filtration rates on dietary salt intake (micropuncture studies). Proc Roy Soc Med **62**: 1118-1122, 1969
5) Barger AC, Herd JA: The renal circulation. New Engl J Med **284**: 482-490, 1971

Summary

Experimental Production of MRI Renal Functional Image Using Gd-DTPA

Hiroo IKEHIRA*, Yoshiro AOKI**, Yoko NAGAHARA***, Teruko YAMANE*,
Nobuo FUKUDA*, Toru MATUMOTO*, Masahiro ENDO*, Takeshi IINUMA*,
Hiroshi FUKUDA* and Yukio TATENO*

**Division of Clinical Research, **Division of Hospital,*
National Institute of Radiological Sciences, Chiba, Japan
****Asahimedical Co. Ltd., Tokyo, Japan*

We already developed and reported the MRI renal kinetic function study method using Gd-DTPA as a magnetopharmaceutical for the GFR substance. These trials were evaluated as a experimental studies. But these days we could get Gd-DTPA supply from Schering Co. Ltd., so we applied this method to the human being for the purpose of normal human renal kinetic function analysis. Normal six volunteers' examinations were done, six volunteers were 25 to 61 years average 45 years old females and 18 years old male.

In this paper we evaluated normal human renal kinetic function to get GFR value, tubular urine flow value, tubular back diffusion value and tubular volume parameters and also we had tried to make the GFR functional image.

We got these normal values as follows, GFR value was 79.2±16.1 m*l*/min, tubular urin flow value was 68.7±21.5 m*l*/min, tubular back diffusion value was 1.98±6.61 μmol/min and tubular volume value was 0.148±0.719 m*l*, but last two values, tubular back diffusion value and tubular volume value were almost 0 values in the cases of normal volunteers.

Intra renal local blood flow (GFR) pattern was visualized with MRI GFR functional image. This GFR image indicated the irregular pattern of intra renal local blood flow, even if in the case of normal function kidney.

Key words: Gd-DTPA, MRI, Renal function, Functional image.

昭和62年度第1回粒子線治療研究委員会議事概要

日　時：昭和62年8月1日(土) 10：00～14：00
場　所：霞山会館　(東京都千代田区霞が関)
出席者：委員長　恒元　博
　委　員　梅垣洋一郎(特別研究員)，稲田哲雄，入江五郎，尾内能夫，鎌田力三郎，北川俊夫，津屋　旭，田中栄一，平尾泰男，松田忠義，森田皓三
　研究説明　堀　佑司，森田新六，丸山隆司，川島勝弘，大原　弘，河内清光，金井達明，中村　譲，遠藤真広，佐藤眞一郎，小池幸子，松本健

配布資料：

1. 昭和62年度研究計画
   a．医用重粒子線加速器に関する研究
   b．重粒子線治療に関する臨床的研究
   (原発巣に対する初回放射線治療の内訳，及び陽子線治療患者名簿)
   c．重粒子線治療に関する技術的研究
   (垂直陽子線治療設備)
   d．重粒子線治療に関する生物学的研究
   e．重粒子線治療計画に関する研究
2. 重粒子線がん治療装置建設年次計画

議事概要：

1. 研究の経過に関して以下の報告が行われた。
   a．垂直陽子線治療ポートの整備が進み，治療に必要な物理測定が行われた。
   b．重粒子線がん治療装置の詳細設計が昭和62年度行われる。
   c．医用重粒子線研究部が新設され，加速器建設等に関する責任体制が整った。
2. 昭和62年度における研究計画がグループリーダーよりそれぞれ紹介され，討議が行われた。その内容は以下のとおりである。
   a．医用重粒子線加速器の研究に関しては，荷電変換装置，ビーム，監視試験装置等の試作研究を医用重粒子線研究部と協力して行う。
   b．速中性子線，及び陽子線治療の対象となる症例を明らかにすると共に，重粒子線治療システム（陽子ビームの wobbler scanning 法）の技術的研究を行う。

   Lawrence Berkeley 研究所において安藤興一（臨床）が行ったアルゴンイオンの実験結果が報告された。アルゴンイオンのプラトー部の RBE は，速中性子線(30 MeV d→Be)と略同じ値である。

   治療計画に関する研究分野では，計画装置の導入により研究の前進が期待される。
3. 重粒子線がん治療装置の建設年次計画が報告された。

   昭和68年度に重粒子線治療臨床トライアルを開始する予定であり，治療室の整備方針が紹介された。
4. 研究成果の報告は昭和63年3月の第2回委員会において行われる予定である。

昭和62年度第2回粒子線治療研究委員会ならびに第1回粒子線治療臨床部会議事概要

1. 日　時：昭和63年3月5日(土)10：00～15：00
2. 場　所：霞山会館（東京都千代田区霞が関）
3. 出席者：委員長　恒元　博

委　員　梅垣洋一郎，柄川　順，尾内能夫，岡田重文，田崎瑛生，春日，孟，平尾泰男，松田忠義，田中栄一，飯野　祐，鎌田力三郎

部会委員　尾形佳郎，笠松達弘，森田新六，高田典彦，花岡英弥，井坂茂夫(島崎代)，小出義雄(小野田代)

研究説明　堀　佑司，大原　弘，川島勝弘，河内清光，野原功全，遠藤真広，久保田進，丸山隆司，中野隆史，石井　猛，松井正典

4. 配布資料：

(1)　重粒子線がん治療装置建設年次計画

(2)　重粒子線がん治療装置概略図

(3)　研究報告・粒子線治療

(4)　研究報告・医用重粒子加速器に関する研究

(5)　研究報告・重粒子線治療に関する技術的研究（垂直陽子線治療装置）

(6)　研究報告・重粒子線治療に関する生物学的研究

(7)　研究報告・重粒子線治療計画に関する調査研究

(8)　臨床部会報告・子宮頸がんの速中性子線治療

(9)　臨床部会報告・前立腺がん・膀胱がんに対する速中性子線治療

(10)　臨床部会報告・食道がんの放射線治療

(11)　臨床部会報告・軟部悪性腫瘍に対する粒子線治療法とLINAC療法の対照

(12)　重粒子線がん治療装置・照射装置全体組立図

5. 議事概要：

昭和62年度に行われた特別研究の経過と成果が報告され，その内容につき討議が行われた。

a．経過報告

重粒子線がん治療装置の着工が昭和62年度からはじまり，臨床トライアルは昭和68年度中に開始される予定であること，並びに重粒子線治療室は3室整備されること等が紹介された。

b．研究報告

1）臨床的研究

昭和50年11月より昭和62年12月までに1,623名の患者が速中性子線治療を受けた。速中性子線に対して著効を示した腫瘍は耳下腺がん，パンコースト型肺がん，骨肉腫，悪性黒色腫等である。

陽子線治療の垂直ビームラインが完成し，眼球の悪性腫瘍の治療が垂直ビームを用いて行えるようになった。昭和54年10月から昭和62年10月までに，水平陽子線ビームを用いて治療を行った患者は45例である。

昭和62年10月から昭和63年2月まで4例が垂直ビームによる治療を受けた。

2）基礎的研究

陽子線垂直ビームにはWobbler法による

ビーム照射システムが採用され，高線量率・短時間照射が可能になった（6 cm φの照射野で60 Gy/m）。治療計画研究については念願の計算機システム，VAX-8250，の導入が決まり，これからの研究に発展が期待されている。

医用重粒子線加速器の研究に関しては，荷電変換試験装置とビーム監視試験装置の試作研究が進められた。

炭素ビーム（230 KeV/u 及び400 KeV/u）をV-79細胞に照射した時のdose-cell-survival曲線は直線減弱型となっている。

重粒子線がん治療装置が完成するまでは他施設の協力を得て，基礎研究を進める必要があると強調された。

3） 臨床部会報告

骨肉腫，泌尿器系のがん，子宮頸部がん，食道がん，及び軟部組織肉腫の速中性子線治療症例について追跡調査の経過が報告された。

高LET放射線の特徴を悪性腫瘍の治療に生かすためには線量分布の改善が重要な課題である。

c．重粒子線がん治療装置の詳細設計

重粒子線がん治療装置の詳細設計の経過が紹介された。

重粒子線治療適応症例を自ら選択できる規模を有する総合病院は臨床トライアルを進める上で貴重であるとの意見があった。

昭和62年度第1回短寿命及び陽電子RIの診断利用に関する研究委員会議事概要

日　時：昭和62年3月18日（金）10：00～14：00
場　所：霞山会館　松の間
出席者：舘野（委員長），山崎，福田（英），村山，
　寺尾，黒沢，樫田，高橋，野崎，宇野，
　蓑島，（以上委員）
　野原，井上，入江，福田（信），福田（寛），
　篠遠，鈴木，玉手，三門他（研究説明員）

配布資料：

1. ^{11}C-PK 11195注射液の前臨床段階における評価
2. ^{11}C-N-メチルスピペロン注射液の前臨床段階における評価
3. ^{11}Cシアノイミプラミン注射液の前臨床段階における評価
4. 発熱性物質試験法について

議事概要：

1. 舘野委員長より委員会の主旨説明が行われた後，山崎より，放医研のポジトロンCT研究の現状について，研究内容，新規設備・施設等について説明があった。次いで，野原より近日中に設置予定の高分解能頭部専用ポジトロンCTについて，補足説明があった。
2. 新規薬剤について

井上より，^{11}C-N-メチルスピペロン，^{11}C-PK 11195，および^{11}C-シアノイミプラミンの医学的有用性，安全性，および被曝線量に関する説明があった。

次いで鈴木より，^{11}C-N-メチルスピペロン，^{11}C-PK 11195，および^{11}C-シアノイミプラミンの製法，品質管理法，および最終製剤の生産量，純度比放射能等について説明があった。

質疑応答：

福田委員…メチルスピペロンは，ドーパミン D_2 レセプターに結合する以外にセロトニンレセプターにも一部結合すると聞いているがどの程度か

井上…in vitro では 1/10 程度で無視できると考えている。in vivo では，データはない。

福田委員…^{11}C-PK 11195 の副腎への集積が極めて多いが，集積機序は，わかっているか。

井上…副腎ではレセプターが多いことが知られているが，集積機序はよくわからない面もある。

野崎委員…レセプター研究においては，優れた薬剤を大量に投与して，検査するのが良い訳であるが，被曝線量の問題が出てくる。何かガイドラインはあるのか。

井上…アイソトープ協会で検討したものがある。

野崎委員…^{3}HPK 11195 を用いた実験でキャリアフリーとはどういう意味か

井上…担体無添加という意味である。

^{3}H 化合物の比放射能は，87 mCi/μmole である。

寺尾委員…^{11}C-PK 11195 を溶解するのに，Twin 80 とエタノールを用いているが，エタノールは局方エタノールか。

また，Twin 80 は，医薬品用か。

鈴木…エタノールは試薬特級を用いている。今後は局方エタノールの使用を考える。

井上…Twin 80 は，^{133}I-アドステロール等で実際に使用されている。

我々は，Twin 80 エタノールとも 1/2 の濃度で使用した。

寺尾…高速液体クロストグラムの測定の際，すべて 254 μm で固定して測定しているがそれでよいか。

井上…この範囲で十分可能であった。

鈴木…他の波長ではやっていない。

村山委員…被曝線量の計算に用いたマウスの体重がすべて 32 g というのはおかしい。

井上…この週齢のマウスは，体重のバラツキが少なく 31-33 g である。各群の平均値は大体 32 g になる。

以上の質疑応答の後，三種の新規薬剤の使用が承認された。

3. 発熱性物質試験の改良法について

玉手より，発熱性物質試験について従来法（パイロジエント法）の欠点，および改良法（トキシノメータ ET 201 法）の利点について説明があった。また，同一の検体を従来法と改良法で測定した結果，同じ結果が得られたので，今後改良法に変更したい旨提案があった。樫田より従来法の欠点について補足説明があった。質疑応答の後，試験法を変更することが承認された。

4. 臨床研究成果の報告

篠遠より，前回の本委員会で承認された ^{11}C-MMBA による臨床研究の成果について報告があった。

5. その他

特になし

昭和62年度第1回重粒子線がん治療装置建設委員会議事概要

1. 日　時　4月14日(火) 13：30～16：20

2. 場　所　放医研　第1会議室

3. 出席者　田中委員長，恒元副委員長，久保井，平尾，塚田，門田，堀，河内，松本，大原，飯沼，黒沢，新井，吉川，（以上委員）
土屋(関東地建)，富田，井上，奥原，中山，山田，佐藤(以上オブザーバー)

4. 配付資料
   - 1-1　重粒子線がん治療装置建設委員会名簿
   - 1-2　昭和61年度第2回重粒子線がん治療装置建設準備委員会議事概要（案）
   - 1-3　重粒子線がん治療装置の建設に係わる経費
   - 1-4　基本設計技術検討報告書（案）
   - 1-5　建屋配置について

5. 議事概要

(1)　委員長挨拶

重粒子線がん治療装置建設委員会及び関連部会の目的と，建設計画作業推進の組織について説明

(2)　各委員の自己紹介

(3)　昭和61年度第2回重粒子線がん治療装置建設準備委員会議事概要の確認

(4)　基本設計発注以後の経過について河内委員が報告

(5)　昭和62年度重粒子線がん治療装置建設に係わる経費について堀委員が説明

(6)　基本設計技術検討報告書（案）の内容報告。以下，下記の議論があった。

①　基本設計としては，おおむね満足できると思うが放医研における検討事項がかなりある。

②　今後，メーカーに対する放医研側からの指導が重要であり，仕様の真意をメーカーに正しく伝えていく必要がある。

③　中エネルギービーム，6 MeV/u，の使い方について利用者の意見を出してほしい。

④　ユーザー側での中エネルギービームの知識が足りない。中エネルギー域における研究テーマについては，ユーザー側と加速器側との意見交換が必要である。

⑤　どのコースで800 MeV/uのエネルギーが必要か議論する必要がある。

⑥　2 ring方式による同時照射の可能な施設は，国際的にも将来にわたってユニークであると言える。

⑦今後ユーザーを国際的にも拡げる必要がある。

(7)　建設の配置について

①　建設配置について土屋設計官より説明
垂直ビーム棟が近隣に近く，「安全性，美観性」に問題がありレイアウトの変更を検討して欲しい。

②　さらに黒沢委員より補足説明
サイクロトロン棟建設，内ばく棟建設を通じて周辺住民との交渉の経緯があり，問題をさけるために仕方がない。

③　恒元副委員長より，環境上の問題から病院棟を敷地の北側に建てることを前提とした加速器棟の配置を検討して欲しいとの要望が出された。

④　その他，幾つか案が出されたので次回に下記の点を主として検討することとなっ

た。

・関東地建の提案を南側へ寄せる案。

・南北180°反転する案。

・ビームラインの変更案。

6. 次　回

5月7日　13：30～

昭和62年度第2回重粒子線がん治療装置建設委員会議事概要

1. 日　時　5月7日(木) 13：30～15：00

2. 場　所　放医研　第1会議室

3. 出席者　田中委員長，恒元副委員長，久保井，平尾，石塚，塚田，門田，川島，丸山，河内，松本，飯沼，黒沢，新井，吉川，山田(隆)(以上委員)

土屋，古田，寺川(以上関東地建)

井上，山田(聡)，佐藤(幸)(以上オブザーバー)

4. 配付資料

4-1　昭和62年度第1回建設委員会議事概要(案)

4-2　建屋工事工程表

4-3　建屋配置案

5. 議事概要

(1) 第1回議事概要の確認

・表現について若干修正することとして，了承された。

(2) 建屋工事に関する工程表について石塚委員より説明があった。

(3) 上記工程表にともなう重粒子線がん治療装置建設年次計画表について，河内委員の説明があった。

(4) 関東地建　古田氏より，建屋配置案に対する経過説明と模型を用いた新配置案（途中経過）の説明があり，以下のような議論があった。

① 基本設計の配置案の東西を反転する案については，治療施設建設予定地の確保が必ずしも十分とは言えない。

② 基本設計の配置案を180°回転する案は，治療施設が将来設計される40ｍ道路から十分離れるなど環境はよくなるものの，北側斜線の高さ規制により，建物の高層化が難しくなると共に眺望も良いとは言えず，40ｍ道路からのアプローチが遠くなるなどの問題が残る。

③ 治療施設を北側に置く案を詰めてほしい。また，敷地が許すなら外来棟と治療施設は分けておいてほしい。

④ 関東財務局は，もし180°回転案を採用するなら，評価に時間を要するので至急知らせてほしいと言っている。

⑤ 180°回転案では，垂直ビーム棟と研究棟に挾まれた狭い空間を通って外来棟にアプローチしなければならないことに強い抵抗感がある。世界に唯一という施設にふさわしい建物外観・配置にしたいので，さらに検討を進めたい。今日結論を出すのはまだ待ってほしい。

⑥ どちらの案を採用するにしても装置側としては，最適化を至急詰める必要がある。

昭和62年度第3回重粒子線がん治療装置建設委員会議事概要

1. 日　時　昭和63年1月21日(木)13：30～16：00
2. 場　所　放医研　第1会議室
3. 出席者　田中委員長，恒元副委員長，平尾，黒沢，門田，堀，川島，松本，大原，新井，吉川，河内(以上委員)，松尾管理部長
4. 配布資料
   - 4-1　昭和62年度第2回建設委員会議事概要
   - 4-2　昭和62年度第1回装置製作総合検討部会議事概要
   - 4-3　放医研重粒子線がん治療装置詳細設計仕様書
5. 議事概要

(1) 第2回議事概要の確認

(2) 重粒子線がん治療装置建設に係る経過報告

① 平尾委員より，医用重粒子線研究部の現状と，重粒子線がん治療装置建設推進本部の体制及びその役割等について説明があった。

② 堀委員より，昭和63年度重粒子関係予算の概要について報告があり，装置，建屋を合わせた総枠が決まったこと，年次計画等について説明があった。

年次計画については，臨床試行開始の時期，予算総枠の確実性についての質疑があった。

③ 昭和62年度第1回装置製作総合検討部会について概要報告があり，詳細設計仕様に対するコメントの説明があった。

(3) 河内委員より，装置レイアウト案と詳細設計仕様について説明があり，それらを基本線において了承した。下記の質疑，コメントがあった。

① 照射室のビームコースの記述で，β関数値についての質問があった。

② 建屋の遮蔽壁は，中性子線に対する線質係数の評価が変わっても，対応できるか否かの質問があった。

- 遮蔽設計では，安全係数にかなり余裕を見ているので充分と思われるが，それでも不可能な場合は運用面で制限を設けるしかない。

③ レイアウトと地上階に予想される建屋について質問があった。

- 現段階では，装置とその関連施設(電源・空調・冷却) 等を優先して考える。
- 次の段階で，61年度に利用者の要望をまとめたリストで検討し，必要度の高いものから順次取り上げる。

④ 本装置では，国内のみならず国際的研究協力が重要であり，必要な共同研究施設を充実しておくべきである。

(4) 装置詳細設計の発注と，イオン源及び前段加速器製作発注の時期と手続きについて，門田委員より報告があった。

(5) 今年度の委員会とその開連する部会のスケジュールについて，河内委員より報告があった。

特別研究「重粒子線等の医学利用に関する調査研究」
昭和62年度　班員名簿

（班長）	恒元博	病院長
（副班長）	舘野之男	臨床研究部長
（顧問）	梅垣洋一郎	特別研究員
	松沢秀夫	〃
	櫻田義彦	〃
	市川龍資	医用サイクロトロン委員会委員長
	吉川元之	技術部放射線安全課長
	山田隆	技術部サイクロトロン管理課長

1.　医用重粒子加速器に関する調査研究

丸山隆司	物理研究部第３研究室長
田中栄一	物理研究部長
野原功全	物理研究部第１研究室長
川島勝弘	〃　第２研究室長
星野一雄	〃　第２研究室
平岡武	〃　〃
野田豊	〃　第３研究室
中島敏行	〃　第４研究室長
喜多尾憲助	〃　第４研究室
江藤久美	生物研究部第１研究室長
大原弘	生理病理研究部生理第２研究室
飯沼武	臨床研究部第２研究室長
中村譲	〃　第２研究室
遠藤真広	〃　〃
佐藤真一郎	〃　第４研究室
河内清光	医用重粒子線研究部第２研究室長
金井達明	〃　第２研究室
佐藤幸夫	〃　第１研究室
板野明史	〃　〃
恒元博	病院部長
森田新六	病院部医務課長
松本健	〃　医務課

（技術部サイクロトロン管理課）

（技術部技術課）

（技術部放射線安全課）

2. 重粒子線治療システムに関する臨床研究

(1) 重粒子線治療に関する臨床的研究

安藤興一	臨床研究部第4研究室長
古川重夫	〃　第4研究室
佐藤真一郎	〃　〃
小池幸子	〃　〃
恒元博	病院部長
森田新六	〃　医務課長
青木芳朗	〃　医務課
五味弘道	〃　〃
久保田進	〃　〃
向井稔	〃　〃

(2) 重粒子線治療に関する技術的研究

川島勝弘	物理研究部第2研究室長
星野一雄	〃　第2研究室
平岡武	〃　〃
野田豊	〃　第3研究室
中島敏行	〃　第4研究室長
古川重夫	臨床研究部第4研究室
佐藤真一郎	〃　〃
中村譲	〃　第2研究室
福田寛	〃　第3研究室
河内清光	医用重粒子線研究部第2研究室長
金井達明	〃　第2研究室
森田新六	病院部医務課長
久保田進	〃　医務課
松本健	〃　〃
坂下邦雄	〃　〃
熊谷和正	〃　〃

(3) 重粒子線治療に関する生物学的研究

大原弘	生理病理研究部生理第2研究室
安藤興一	臨床研究部第4研究室長
小池幸子	〃　第4研究室
小島栄一	障害基礎研究部第1研究室

金井達明	医用重粒子線研究部第２研究室
山口寛	物理研究部第３研究室

(4)　重粒子線治療計画に関する研究

舘野之男	臨床研究部長
飯沼武	臨床研究部第２研究室長
中村譲	〃　第２研究室
松本徹	〃　〃
遠藤真広	〃　〃
福田信男	〃　第３研究室長
福田寛	〃　第３研究室
池平博夫	〃　〃
古川重夫	〃　第４研究室

3.　重粒子線治療のための医学診断に関する研究

(1)　診断用核医学薬剤の開発に関する研究

山崎統四郎	臨床研究部第１研究室長
福士清	〃　第１研究室
入江俊章	〃　〃
大野茂	〃　〃
福田寛	〃　第３研究室
鈴木和年	技術部サイクロトロン管理課

(2)　核医学の測定技術の開発に関する研究

田中栄一	物理研究部長
野原功全	〃　第１研究室長
富谷武浩	〃　〃
山本幹男	〃　〃
村山秀雄	〃　〃
舘野之男	臨床研究部長
山崎統四郎	臨床研究部第１研究室長
飯沼武	〃　第２研究室長

(3)　画像診断の臨床応用に関する研究

舘野之男	臨床研究部長
山崎統四郎	臨床研究部第１研究室長
福田信男	〃　第３研究室
池平博夫	〃　〃
福田寛	〃　〃
飯沼武	臨床研究部第２研究室長

松本　徹	臨床研究部	第２研究室
遠藤真広	〃	〃

特別研究「重粒子線等の医学利用に
関する調査研究」論文集　第４集

平成元年３月
千葉市穴川４－９－１
放射線医学総合研究所
Tel. 0472—51—2111(代)